博　士　論　文

Modeling of Pozzolanic Reaction of Siliceous Fly Ash in Cement System based on its Material Characterization

（クリンカーとの相互作用を考慮した物理化学キャラクターに基づくフライアッシュのポゾラン反応モデル）

王　眺

WANG Tiao

A dissertation submitted to

The University of Tokyo

In partial fulfillment of the requirement for

The Degree of Doctor of Philosophy

Supervisor

Prof. Dr. ISHIDA Tetsuya

Department of Civil Engineering

The University of Tokyo

October 2017

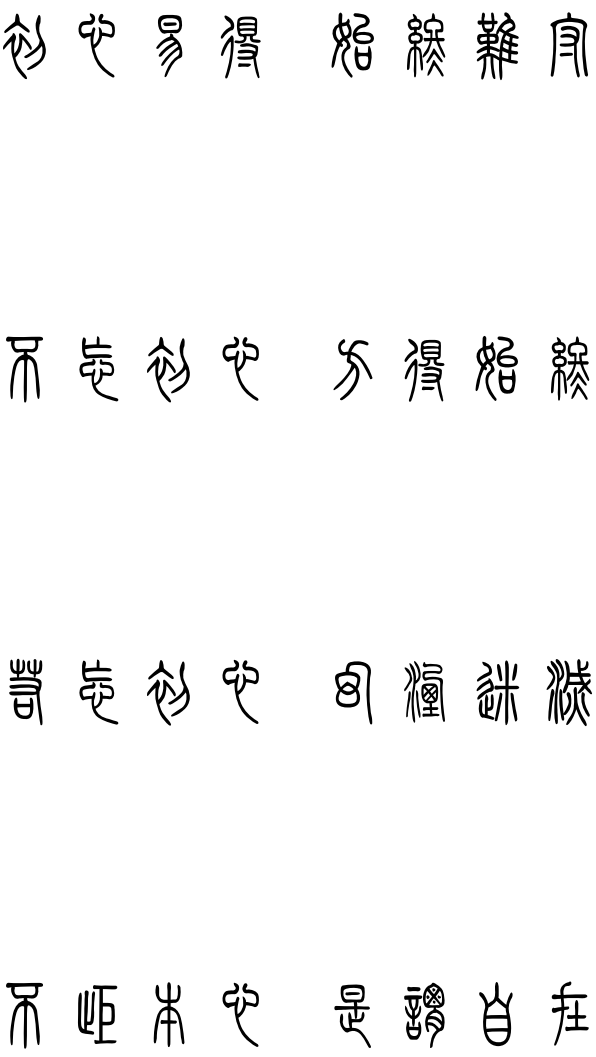

初心易得，始終難守。不忘初心，方得始終。若忘初心，幻湮迷滅。不拒本心，是謂自在。

Acknowledgements

Very Special Thanks to Dr. ISHIDA Tetsuya, my lovely supervisor, the professor of Concrete Laboratory of Tokyo University. Thank you for giving me the precious opportunity to allow me to pursue the Ph.D. degree in Tokyo University. Thank you for taking care of me since the first day I had entered the Concrete Laboratory to the date when this thesis is completed. Thank you for your patience, energy and flexibility towards my endless new ideas. Thank you for supervising my research, for your support, suggestions, guidance and comments to streamline my work. You make me know how to do research and how to explain my ideas simply, clearly and concisely. Thank you for your financial support on my experiment and international conference. These three years are extraordinary experience. Thank you again!

Particular and Great Thanks to Dr. Gu Rui, the researcher at Material Research Center of Southern University of Science and Technology. You kindly allow me to use your lab advanced and expensive experiment machine and personally help me to carry out various experiments. You always discussed with me without any words. Without you, this thesis cannot be completed. I don't know how to express my appreciation and gratitude to you. I just can wish you best as well as your unborn baby. I am really looking forward to seeing him or her in next year.

I would like to thank my committee: Prof. Dr. Maekawa Koichi, Prof. Dr. Kishi Toshiharu, Prof. Dr. Noguchi Takafumi, Assoc. Prof. Dr. Nagai Kohei. This thesis cannot be completed without your fruitful advices and comments.

I would like to express my sincere appreciation to my previous boss Assoc. Prof. Dr. Dai Jian-Guo at Hong Kong Polytechnic University. You help me a lot. Thank you for training me to become a researcher, helping me to write my first SCI paper and recommending me to Tokyo University. Thank you for your suggestions and financial support over the last three years.

I would like to thank Dr. Takahashi Yuya and our secretary Ms. Tabata Izumi and Ms. Takeuchi Naoko for their support on my research and my life in life. I always asked you questions and help, especially for purchasing experiment materials and devices. Thank you for your patience, your time and your flexibility.

I would like to thank Assoc. Prof. Dr. Sagawa Takahiro at Maebashi Institute of Technology. Thank you for teaching me how to carry out the XRD test and Rietveld refinement analysis. Without you, I cannot study the retarded effect of fly ash on cement hydration. Thank you.

I would like to thank my dear senpai, Assoc. Prof. Dr. Asamoto Shingo and Assist. Prof. Dr. Luan Yao at Saitama University. Thank you for allowing me to carry out the TGA test in your laboratory. Your kind assistance greatly helps me to finish the cement model. I also would like to thank my senpai Dr. Yoneda Taiju. Although my topic finally changed to fly ash, I never forgot your help and suggestions on the shrinkage model in my first Ph.D. year.

I would like to give special thanks to my dear foreign senpai, Dr. Mohammed Youssef, Dr. Ali Ahmed, Dr. Zhu Xiaoxu, Dr. Gong Fuyuan and Dr. Rungrawee Wattanapornprom (Jing san). Thank you for the jokes and comfort when I was in troubles. Thank you for taking care of my life and study in Japan over these years. You guys are so nice. It is my great pleasure to know you.

I would like to thank my kouhai, Mr. Mr. Fang Jie, Mr. Hosoi Yusuke, Mr. Maruno Mikito, Mr. Nishigaki Yuya, Mr. Yamazaki Takahiro, Mr. Iwaya Nozomi, Mr. Ogawa Shimpei, Mr. Koleneath Pen and Mr. Amirfarkhan Radzali and all the peoples in concrete labs. Thank you for your help on my study and life. Thank you for giving me so warm working environment, especially for my tutor Mr. Hosoi Yusuke. Your kind warmness makes me go further. Thanks!

I would like to thank the Assoc. Prof. Dr. Shashank Bishnoi from Indian Institute of Technology Delhi, India. Thanks you for your precious time on discussing my modelling. Thank you very much.

I also would like to thank my Indian friend, Satya Chaitanya Medepalli, the exchange student from IIT. Although you were just in Tokyo University for 6 months, we have become good friends. Thank you for your constructive comments. Thank your for recommending so many good materials to me. They are so helpful to my study. Thank you!

Very special thanks for financial support from Monbukagakusho and every Japanese people who paid tax for my study in Japan. Thank you for delicious food, accommodation and facilities.

Finally, my deepest gratitude goes to my beloved mother. Thank you for bringing me into this world and giving me everything. Thank you for your unconditional love and grace I didn't deserve it. Thank you for your believing and understanding. I know that is very hard for a mother to allow her only son to study abroad for so many years. And, my beloved father, I miss you so much today as I did the day you passed away. Are you everything fine? I greatly hope that you will love my thesis. If you cannot understand English, please call me to explain. I really want to talk to you.

Abstracts

Fly ash is a by-product of burning pulverized coal in thermal power plants. It is a high potential supplementary cementitious material to improve concrete performance. However, the application of fly ash is hindered in due to its intrinsic and significant heterogeneity and variability. Moreover, its slow pozzolanic reaction compared to cement also limits its application in engineering practices. Therefore, high temperature curing is often used in fly ash concrete to accelerate its pozzolanic reaction.

However, current information regarding the material characterization, the pozzolanic reactivity and the temperature dependence of fly ash is insufficient to understand the behavior of fly ash and to model its effect in cement systems. In this study, three different types of low-calcium (Class F) fly ashes were selected based on their solubility in NaOH solution at 20 and 60 °C. A new material characterization technology based on SEM-EDS full element mapping method and image analysis was developed to comprehensively characterize chemical composition and mineralogical phases of these fly ashes in a micro-scale and determine their accurate specific surface area. The temperature-dependent dissolution processes of these three fly ashes was long-term observed in alkaline systems. These three fly ashes were further studied in ordinary portland cement systems by preparing blended cement pastes under sealed curing conditions at 20 and 60 °C. The extent of pozzolanic reaction for these fly ashes and cement hydration degrees were subsequently measured by selective dissolution tests and XRD Rietveld refinement analysis respectively.

Experimental results showed that reactive phases of siliceous fly ash are mainly composed of amorphous silicate and Al-silicate; amorphous Al-silicate is more reactive than silicate but less sensitive to temperature. The pozzolanic reactivity of fly ash depends on its amount of amorphous phase assemblage, surface areas and intrinsic reactivity of amorphous phase. The reactivity of amorphous phase can be described by the amorphous-crystal ratios. Compared to the dilute effect and filler effect of fly ash which promotes the cement hydration rate at early age, the later hydration process will be retarded in fly ash blended cement paste because C-S-H gel becomes denser with continuous consumption of calcium hydroxide of fly ash.

Based on these works, a temperature-dependent two-phase pozzolanic reaction model, amorphous silicate and Al-silicate, considering fly ash material variations was proposed to predict the pozzolanic reaction and therefore degree of reaction at different temperatures. The cement and fly ash interaction was taken into account. The model was validated by the experimental results. With the help of this model, parametric analyses are presented to show how the pozzolanic activity and temperature dependence of fly ash affects the concrete performance.

Key words: Material characterization; Pozzolanic reactivity; Intrinsic reactivity; Amorphous silicate; Amorphous Al-silicate; Specific surface area; SEM-EDS mapping; Image analysis; C-S-H gel morphology; Two-phase reaction model

Contents

Acknowledgements ..... **I**

Abstracts ..... **V**

List of abbreviations ..... **XIII**

List of Figures ..... **XV**

List of Tables ..... **XXI**

1. Introduction **1**

2. Literature review and research methodology **5**

2.1 Fly ash application in concrete **6**

2.1.1 Benefits of fly ash in concrete 6

2.1.2 Application difficulties of fly ash in concrete 7

2.2 The nature of fly ash and its formation mechanism **9**

2.2.1 Chemical composition of fly ash 9

2.2.2 Crystalline and amorphous solids of fly ash 12

2.2.3 Morphology of fly ash 17

2.3 Fly ash material properties characterization methods **19**

2.3.1 Mineralogical properties 19

2.3.2 Chemical properties 20

2.3.3 Morphology properties 21

2.4 Fly ash temperature-dependent activity **22**

2.5 Interaction between cement and fly ash 22
2.6 Underlying questions and research methodology 24
2.6.1 Underlying questions 24
2.6.2 Research methodology 24

3. Principal Materials and Test Methods 27
3.1 Principal materials 28
3.2 Test methods 29
3.2.1 Inductively coupled plasma optical emission spectrometry (ICP-OES) 29
3.2.2 X-ray fluorescence (XRF) 29
3.2.3 X-ray powder diffraction (XRD) 30
3.2.4 Air permeability fineness (Blaine fineness) 31
3.2.5 Particle size distribution (PSD) 31
3.2.6 Nitrogen absorption test 32
3.2.7 Scanning electron microscopy (SEM) 32
3.2.8 Energy-dispersive X-ray spectroscopy (EDS) 33
3.2.9 Thermo-gravimetric analysis (TGA) 33

4. Fly ash material properties characterization 35
4.1 Introduction 36
4.2 Fly ash chemical properties characterization 37
4.2.1 Bulk chemical compositions 37
4.2.2 Micro-scale characterization of fly ash chemical properties 37
4.3 Fly ash mineralogical properties characterization 47
4.3.1 Bulk mineralogical phases 48
4.3.2 Micro-scale characterization of fly ash mineralogical properties 48
4.4 Fly ash specific surface area 61
4.4.1 Conventional test methods 61
4.4.2 Image analysis 68
4.5 Summary and conclusions 71

5. Temperature-dependent reactivity of fly ash in alkaline system 73

5.1 Introduction 74
5.1.1 Sample preparation procedures 75
5.1.2 Experiment procedures of ICP measurement [55] 76
5.2 Temperature-dependent alkali dissolution test result 79
5.2.1 Element concentrations 79
5.2.2 Induvial composition dissolution process 81
5.2.3 Composite dissolution process 85
5.3 Microscopic evaluation on fly ash after alkali dissolution test 86
5.3.1 Dissolution mechanism of fly ash 86
5.3.2 SEM-EDS mapping result and discussions 89
5.4 Fly ash reactivity and its material properties 97
5.4.1 Introduction 97
5.4.2 Intrinsic reactivity of amorphous phase 98
5.4.3 Explanation on the reactivity variation of studied fly ashes 100
5.5 Summary and conclusions 100

6. Temperature-dependent reactivity of fly ash in cement system 103
6.1 Introduction 104
6.2 Sample preparation 105
6.3 Fly ash reaction degree 107
6.3.1 Selective dissolution test procedures 107
6.3.2 Selective dissolution test results 109
6.4 Calcium hydroxide and bound water content 111
6.4.1 TGA test procedures and analysis method 112
6.4.2 TGA test result 119
6.5 Hydration degrees of cement clinkers 122
6.5.1 XRD test and Rietveld refinement analysis procedures 123
6.5.2 Cement clinkers hydration degrees 123
6.5.3 Interaction between cement clinkers and fly ash 125
6.6 Summary and conclusions 133

7. Modeling of pozzolanic reaction of fly ash in cement systems 135

7.1 Introduction **136**
7.2 Current DuCOM multi-heat model **137**
7.2.1 Multi-component hydration model of Portland cement 137
7.2.2 Current fly ash pozzolanic reaction model in cement systems 139
7.2.3 Current model verification on cement paste tests 141
7.3 Modified multi-heat model **147**
7.3.1 Modified multi-component hydration model of Portland cement 147
7.3.2 Modified fly ash pozzolanic reaction model 150
7.4 Modified model verification **158**
7.4.1 Cement paste test 158
7.4.2 Hanehara's experiment [14] 168
7.5 Parameter analysis **169**
7.6 Summary and conclusions **172**

8. Conclusions and perspectives **175**
8.1 Conclusions **175**
8.1.1 Fly ash material characterization 175
8.1.2 Reactivity of siliceous fly ash 176
8.1.3 Interaction between cement and fly ash 177
8.1.4 Modelling of pozzolanic reaction of siliceous fly ash 177
8.2 Perspectives **178**

A. Two-dimension hamming window smooth method **179**

B. Thermogravimetric curves **181**
B.1 Cement paste 182
B.2 FA1 blended cement paste 183
B.3 FA2 blended cement paste 184
B.4 FA3 blended cement paste 185

C. Hydration degrees **187**
C.1 Cement paste 188
C.2 FA1 blended cement paste 189

C.3 FA2 blended cement paste 190
C.4 FA3 blended cement paste 191

D. Regression analyses for alkali dissolution tests 193
D.1 Introduction 194
D.2 Linear regression analyses result 194

Bibliography 197

List of abbreviations

Cement notation of oxide compounds:

C: Cao S: SiO_2 A: Al_2O_3 M: MgO F: Fe_2O_3 F: Fe_3O_4 $: SO_3
c: CO_2 H: H_2O

Notation of the main anhydrous and hydrated phases:

C_3S	$3CaO·SiO_2$	Tricalcium silicate (Alite)
C_2S	$2CaO·SiO_2$	Dicalcium silicate (Belite)
C_3A	$3CaO·Al_2O_3$	Tricalcium aluminate
C_4AF	$4CaO·Al_2O_3·Fe_2O_3$	Ferrite
Cc	$CaCO_3$	Calcite
CH	Ca(OH)2	Calcium hydroxide (Portlandite)
C-S-H	$CaO-SiO_2-H_2O$	Calcium silicate hydrate
$C_3A·3C\$·H_{32}$	$3CaO·Al_2O_3·3CaSO_4·32H_2O$	Ettringite
$C_3A·C\$·H_{12}$	$3CaO·Al_2O_3·CaSO_4·12H_2O$	Monosulfate
$C_3A·Cc_{0.5}·H_{12}$	$3CaO·Al_2O_3·0.5CaCO_3·12H_2O$	Hemicarbonate
$C_3A·Cc·H_{11}$	$3CaO·Al_2O_3·CaCO_3·11H_2O$	Monocarbonate
C_3AH_6	$3CaO·Al_2O_3·6H_2O$	Katoite
$C_3A·S_{2.16}·H_{1.68}$	$3CaO·Al_2O_3·2.16SiO_2·1.68H_2O$	Silicated katoite
3A·2S	$3Al_2O_3·2SiO_2$	Mullite

Materials:

LPC:	Low heat cement
OPC:	Ordinary portland cement
FA:	Fly ash
CFA:	Celerons fly ash
SFA:	Siliceous fly ash

Techniques:

SE:	Secondary electrons
AFM:	Atomic force microscope
BSE:	Back scattered electron
EDS:	Energy-dispersive x-ray spectroscopy
SEM:	Scanning electron microscopy
XRD:	X-Ray powder diffraction
XRF:	X-Ray fluorescence
TGA:	Thermal gravimetric analysis
DTG:	Differential thermogravimetric curve
DDTG:	Second differential thermogravimetric curve
EBSD:	Electron backscatter diffraction
ICP-OES:	Inductively coupled plasma optical emission spectrometry

Others:

mass %:	Mass fraction percentage
at. %:	Atomic percentage
Mt:	Million ton
NBO:	Non-bridging oxygen
PSD:	Particle size distribution
SSA:	Specific surface area

List of Figures

Fig. 2.1 Chloride profiles into marine-exposed concrete at 10 years 6
Fig. 2.2 Benefits of fly ash concrete 7
Fig. 2.3 Long-term monitoring on compression strength of fly ash cement paste 8
Fig. 2.4 Fly ash replacement effect on compression strength 9
Fig. 2.5 Filed survey on chemical compositions of fly ash produced in North America . 10
Fig. 2.6 Al-Si-Ca atomic-% ternary frequency plots of fly ashes in Durdzinski's work .. 11
Fig. 2.7 Atoms arragement of cytalline and amorhopus silica 12
Fig. 2.8 BSE images of Takahashi experiments 13
Fig. 2.9 Temperature effect on solids crystallization..... 14
Fig. 2.10 Two-dimensional representation of polymeric network substitution of Al for Si 15
Fig. 2.11 Two-dimensional representation of polymeric network modifier addition of Na 15
Fig. 2.12 Schematic representation of step-wise phase separation in amorphous solids .. 16
Fig. 2.13 BSE images of Takahashi experiments 18
Fig. 2.14 Schematic representation of fly ash bloating and its dependency on melt viscosity 19
Fig. 2.15 Dissolution process of synthetic glasses in alkaline solution..... 21
Fig. 2.16 Retarded hydration of belite in fly ash blended cement paste..... 23
Fig. 2.17 Durdziński's experiemtn work 23
Fig. 2.18 Research methodology in this thesis 26

Fig. 4.1 SEM-EDS epoxy sample preparation 38
Fig. 4.2 The simulation result of electron trajectories and its energy distribution with respect to FA1 predicated by Casino software. 39
Fig. 4.3 Comparison of element mapping result between before and after data processing 40
Fig. 4.4 Visual representation of fly ash element distributions measured by SEM-EDS .. 44
Fig. 4.5 Al-Si-Ca ternary frequency plot of fly ashes measured by SEM-EDS..... 45
Fig. 4.6 Al-Si-Fe ternary frequency plot of fly ashes measured by SEM-EDS 46
Fig. 4.7 Al-Si element distribution of fly ashes measured by SEM-EDS..... 47
Fig. 4.8 X-ray diffractograms of the siliceous fly ashes studied..... 48
Fig. 4.9 BSE image of typical crystal-amorphous particle of fly ashes studied 50
Fig. 4.10 BSE images with different amorphous and crystalline solids 51
Fig. 4.11 Proposed segmentation criteria for crystalline phases based on element distributions..... 52
Fig. 4.12 Selected particles with crystalline mullite solids for SEM-EDS mapping analysis 54
Fig. 4.13 Masked image of selected particles with crystalline mullite solids..... 54
Fig. 4.14 Solids mapping result of selected particles with crystalline mullite solids 55
Fig. 4.15 Proposed segmentation criteria between Al-silicate and semi-mullite..... 55
Fig. 4.16 Proposed segmentation criteria between amorphous silicate and Al-silicate 56
Fig. 4.17 Illustration of the segmentation criteria among different mineralogical phases. 57
Fig. 4.18 Mineralogical mapping result of fly ashes..... 60
Fig. 4.19 Illustrations on formation mechanism of crystalline phases..... 60
Fig. 4.20 Laser diffraction test result 62
Fig. 4.21 Comparison between two refractive models..... 65
Fig. 4.22 Comparisons among different test conditions 67
Fig. 4.23 SE Images of fly ash particles before heating and after heating..... 67
Fig. 4.24 SE Images of fly ash particles before water washing and after water washing.. 67
Fig. 4.25 Illustration of edge classification in image analysis 69
Fig. 4.26 Detected boundaries of Al-silicate and semi-mullite of FA1 69

Fig. 5.1 Illustration of matrix interference of Na ion 76
Fig. 5.2 Comparison between axial and radial viewing 77
Fig. 5.3 Measurement result of dissolved element concentrations in alkaline dissolution test 80
Fig. 5.4 Dissolution processes of individual oxide chemical composition of fly ash 82
Fig. 5.5 Dissolution processes of individual oxide chemical composition of amorphous solid 84
Fig. 5.6 Dissolution processes of fly ashes in alkaline system 85
Fig. 5.7 BSE pictures of fly ash particles after alkali dissolution test of 210 day at 20 °C 87
Fig. 5.8 BSE pictures of fly ash particles after alkali dissolution test of 210 day at 20 °C 88
Fig. 5.9 Proposed dissolution mechanism of fly ash particles 88
Fig. 5.10 Mineralogical mapping result of FA1 after alkali dissolution test 90
Fig. 5.11 Mineralogical mapping result of FA2 after alkali dissolution test 91
Fig. 5.12 Mineralogical mapping result of FA3 after alkali dissolution test 92
Fig. 5.13 Comparisons of different mineralogical passes at different temperatures 96
Fig. 5.14 Dissolution process of synthetic glasses in alkaline solution 96
Fig. 5.15 Redrawing of dissolution processes of fly ashes in alkaline system 97
Fig. 5.16 Schematic representation of the relationships between the intrinsic reactivity of amorphous phases and the combustion conditions 98
Fig. 5.17 Comparisons between FA2 and FA3 for amorphous silicate and Al-silicate 99

Fig. 6.1 Comparison of fly ash reaction degrees among different fly ashes 110
Fig. 6.2 Comparison of fly ash reaction degrees between OPC and LPC 111
Fig. 6.3 Comparison of TGA test result with and without degassing 112
Fig. 6.4 Comparison of TGA test result before and after data smoothing 113
Fig. 6.5 Comparison of different analysis method for TGA tests 114
Fig. 6.6 Interpretation of calculation method of calcium hydroxide content in TGA tests 115
Fig. 6.7 Verification of the proposed tangential method in determining decomposed calcium hydroxide content in TGA test 118
Fig. 6.8 Experiment result of TGA-FTIR test 118

Fig. 6.9 Calcium hydroxide content of cement pastes 120
Fig. 6.10 Calcium hydroxide content of blended FA cement pastes 120
Fig. 6.11 Bound water content of cement pastes 121
Fig. 6.12 Bound water content of FA blended cement pastes..... 122
Fig. 6.13 Comparison of Alite hydration processes between cement and FA blended paste 124
Fig. 6.14 Comparison of Belite hydration processes between cement and FA blended paste 125
Fig. 6.15 Comparison of hydration processes of synthetic belite and alite in different calcium hydroxide concentrations 126
Fig. 6.16 Morphologies of C-S-H on the surface of synthetic tricalcium silicate 127
Fig. 6.17 Surface representation of C-S-H on the surface of synthetic tricalcium silicate gel measured by AFM 127
Fig. 6.18 Interaction forces of C-S-H gel and the schematic illustration..... 128
Fig. 6.19 Maximum adhesion force in different conditions..... 128
Fig. 6.20 Simulated bond representations of C-S-H at low and high pH by MD methods. The color code corresponds to the particle coordination number 129
Fig. 6.21 Simulated hydration processes at low and high pH by MD methods..... 129
Fig. 6.22 Collected C-S-H gel from different pH conditions..... 130
Fig. 6.23 Micro observation of C-S-H gel from different pH conditions 131
Fig. 6.24 Schematic illustration on influence of fly ash on cement hydration process.... 133

Fig. 7.1 Comparison of fly ash reaction degrees between cement paste test result and current model simulations 142
Fig. 7.2 Comparison of hydration processes between cement paste test result and current model simulations at room temperature of 20 °C 143
Fig. 7.3 Comparison of hydration processes between cement paste test result and current model simulations at high temperature of 60 °C..... 143
Fig. 7.4 Comparison of calcium hydroxide content between cement paste test result and current model simulations 144

Fig. 7.5 Comparison of calcium hydroxide content between FA blended cement paste test result and current model simulations 145
Fig. 7.6 Comparison of bound water content between cement paste test result and current model simulations 146
Fig. 7.7 Comparison of bound water content between FA cement paste test result and current model simulations 146
Fig. 7.8 Proposed Ca/Si ratio of C-S-H gel with temperature 148
Fig. 7.9 Comparison of calcium hydroxide content between cement paste test result and modified model predictions 149
Fig. 7.10 Comparison of bound water content between cement paste test result and modified model predictions 149
Fig. 7.11 Illustration of two dissolution stages of fly ash 151
Fig. 7.12 Comparison of two different reactivity indexed of fly ash 153
Fig. 7.13 Relationship between factors χ_{mor} and R_{paste}^{CH} 157
Fig. 7.14 Comparison of fly ash reaction degrees predicted by current and modified model 160
Fig. 7.15 Comparison of alite and belite hydration degrees at 20 °C predicted by current model and modified model 162
Fig. 7.16 Comparison of free water content of fly ash blended cement paste at 20 °C predicted by current and modified model 162
Fig. 7.17 Comparison of alite and belite hydration degrees at 60 °C predicted by current model and modified model 164
Fig. 7.18 C-S-H gel morphology factor χ_{mor} in fly ash blended cement paste at 60 °C.. 164
Fig. 7.19 Comparison of calcium hydroxide content predicted by current model and modified model 166
Fig. 7.20 Comparison of bound water content predicted by current model and modified model 167
Fig. 7.21 Trial-error simulation for determination of fly ash material parameters of Hanehara's experiment used in the modified model 168
Fig. 7.22 Comparison between simulation predictions and Hanehara's experimental results 169

Fig. 7.23 Parametric analyses on pozzolanic reaction degree of fly ash at 20 °C 170
Fig. 7.24 Parametric analyses on pozzolanic reaction degree of fly ash at 60 °C 171
Fig. 7.25 Parametric analyses on compression strength of fly ash concrete at 20 °C..... 171
Fig. 7.26 Parametric analyses on compression strength of fly ash concrete at 60 °C 172

Fig. A.1 Schematic illustration on dimension-reduction algorithm of hamming window 179
Fig. A.2 Schematic illustration on algorithm of hamming window smooth method..... 180

Fig. B.1 Differential thermogravimetric curves of cement paste..... 182
Fig. B.2 Differential thermogravimetric curves of FA1 blended cement paste 183
Fig. B.3 Differential thermogravimetric curves of FA2 blended cement paste 184
Fig. B.4 Differential thermogravimetric curves of FA3 blended cement paste 185

Fig. C.1 Hydration degrees of cement paste 188
Fig. C.2 Hydration degrees of FA1 blended cement paste 189
Fig. C.3 Hydration degrees of FA2 blended cement paste 190
Fig. C.4 Hydration degrees of FA3 blended cement paste 191

Fig. D.1 Linear regression analyses result for intimal stage..... 195
Fig. D.2 Linear regression analyses result for intimal stage..... 196

List of Tables

Table. 2.1 Summary of physical testing of fly ashes in Schlorholtz's work 8

Table. 3.1 Physical and chemical compositions of cement and fly ash 28
Table. 3.2 Mineralogical phase of cement and fly ash 28

Table. 4.1 XRF-analysis result (mass %)..... 37
Table. 4.2 Chemical oxide compositions of fly ash calculated by SEM-EDS mapping (mass %)..... 41
Table. 4.3 Normalized chemical oxide compositions of fly ash calculated by XRF test (mass %)..... 41
Table. 4.4 Comparison between SEM-EDS mapping and XRF test (SEM-EDS/XRF %) 41
Table. 4.5 Comparison of chemical oxide compositions of studied fly ashes between SEM-EDS mapping and XRF result in the Al-Si-Ca-Fe system..... 42
Table. 4.6 Mineralogical phase composition determined by XRD-Rietveld analysis (mass %) 48
Table. 4.7 EDS analysis result of quartz and amorphous solid in Fig. 4.10 (a) (at. %)..... 52
Table. 4.8 EDS analysis result of magnetite and amorphous solid in Fig. 4.10 (b) (at. %)52
Table. 4.9 EDS analysis result of fly ash particle with crystalline mullite solids (at. %).. 54
Table. 4.10 Segmentation criteria on different mineralogical phases (at. %)..... 56
Table. 4.11 Area fractions of different phases determined by SEM-EDS mapping analysis (%)..... 57

Table. 4.12 Specific gravities of crystalline phases and fly ashes 57
Table. 4.13 Mineralogical phases contents determined by SEM-EDS mapping analysis and the comparison with XRD tests (wt.%)..... 58
Table. 4.14 Specific surface area of fly ash measured by Blaine air permeability test (cm^2/g) 61
Table. 4.15 Real components *n* used for laser diffraction test 62
Table. 4.16 Specific surface area of fly ash measured by laser diffraction test (cm^2/g) 63
Table. 4.17 Specific surface area of fly ash measured by nitrogen absorption test (cm^2/g) 63
Table. 4.18 Summary of specific surface areas determined by different methods (cm^2/g) 64
Table. 4.19 Comparison of specific surface area of fly ashes determined by different material refractive index 65
Table. 4.20 Comparison of SSA between laser diffraction and nitrogen gas absorption .. 66
Table. 4.21 Specific surface areas of different phase determined by image analysis (cm^2/g) 70
Table. 4.22 Comparison of specific surface areas between laser diffraction and image analysis 71

Table. 5.1 Details of verification samples..... 78
Table. 5.2 Measurement results of verification samples (ppm) 78
Table. 5.3 Oxide chemical compositions of amorphous solid (mass %) 83
Table. 5.4 Mass percentages of remained fly ash powders after alkali dissolution test (%) 89
Table. 5.5 Phase assemblage of fly ashes after alkali dissolution tests (mass %)..... 89
Table. 5.6 Mass fractions of each phase of fly ashes before and after alkali dissolution tests (%)..... 93
Table. 5.7 Comparison of dissolution degrees between Al-silicate and semi-mullite at 60 °C 93
Table. 5.8 Summarization of fly ash material properties 97
Table. 5.9 Material properties of amorphous silicate and Al-silicate phases in FA2 and FA3 99

Table. 6.1 Material properties of cement 105
Table. 6.2 Residue of raw material to initial mass after selective dissolution test 107
Table. 6.3 Residue of hydrated products to anhydrous cement after selective dissolution test 107
Table. 6.4 Loss of ignition of raw material at 1000 °C..... 108
Table. 6.5 Ca/Si ratio of C-S-H gel for cement paste (CEM I 42.5R)..... 119

Table. 7.1 Fineness values used for model simulation 141
Table. 7.2 Dissolution degrees of amorphous phases at 20 °C in alkaline system..... 150
Table. 7.3 Thermal activity energies of different stages (WK/kg) 152
Table. 7.4 Fly ash material properties used in proposed model..... 158
Table. 7.5 Fly ash material properties used in proposed model..... 168

1 Introduction

Fly ash is a by-product of burning pulverized coal in thermal power plants. It is a great potential supplementary cementitious material to improve concrete performance. For example, fly ash could not only modify the workability of concrete and reduce its water demand but also chemically react with calcium hydroxide to form cementitious compounds and further enhance concrete strength and durability [1, 4]. On the other hand, as the most widely used construction material, cement contributes up to 5 mass % of man-made CO_2 emissions [5]. Therefore, it is also an efficient way to reduce the CO_2 emissions to protect environment through replacing part of the cement clinker by supplementary cementitious material, such as fly ash.

Although these potential benefits for using fly ash as a supplementary cementitious material with cement has been well known since the start of the last century, it has not yet been widely applied in concrete constructions and only around 30 mass % of produced fly ash is used right now [6]. The primary reason is due to fly ash itself intrinsic and significant heterogeneity and variability. Its properties are highly affected by the coal type, combustion temperature, production processing, and other factors [4, 7, 8]. Therefore, the reactivity of fly ash inherently and significantly varies even produced in the same power plant but from different batches [9]. Schlorholtz et al. monitored the compression strength variation of fly ash cement paste produced at same thermal power plant over 2 years and drastic differences were markedly and unexpectedly observed. As a result, around 70 mass % of fly ash is recycled to produce cement clinkers in Japan but only 2 mass % of that is mixed with cement to cast concrete due to these concerns on material variations [10]. However, the utilization of fly ash

recently becomes more desirable in Japan because more electric power will be provided by thermal power plant instead of nuclear power after the violent earthquake in 2011.

Another drawback of fly ash is its slow reaction rate compared to cement, especially for siliceous fly ash. At high fly ash replacement ratio engineering problems may be encountered with extended setting time and slow strength development, resulting in low early-age strengths and delays in the rate of construction. This shortcoming becomes particularly pronounced in winter construction. Therefore, high temperature curing is often used in fly ash concrete to accelerate its reaction. Unfortunately, current information is still insufficient to understand the temperature-dependent behavior of fly ash and the corresponding effect on concrete performance as well.

In conclusion, it is promising and desirable to study and model pozzolanic reaction of fly ash in different cement systems. Therefore, based on current multi-heat model, this study is aim to develop a more unified model which is capable of covering different siliceous fly ashes and predicting their temperature-dependent pozzolanic reaction in different cement systems. This thesis is organized in the following order:

Chapter 2 presented a summarization of recent research progress of understanding material properties of siliceous fly ash and reviewed the current state of the art on material properties characterization method on fly ash;

Chapter 3 briefly described the materials and test methods used in this study;

Chapter 4 introduced the complexity of the fly ash microstructure and composition. Different methods were used to characterize the selected fly ashes. In this chapter, a developed phase segmentation criteria was proposed based on SEM-EDS full element mapping test to provide a visible and quantitative description of phase separation within fly ash particles. A new image analysis technique was also developed to determine the specific surface areas of different phases;

Chapter 5 studied the temperature-dependent activities of selected fly ashes in alkali conditions. The temperature-dependent reactivity of amorphous phases was studied by SEM-EDS full element mapping analysis. Based on these new findings together with material characterization conducted in chapter 4, the temperature-dependent reactivity of fly ashes was

comprehensively reviewed and discussed and corresponding mechanism was subsequently proposed to explain the reactivity variations;

Chapter 6 presented all experiment results of cement paste tests. The extent of pozzolanic reaction of these fly ashes were determined by selective dissolution tests and calcium hydroxide consumption were estimated by thermogravimetric test respectively. The interaction between cement and fly ash was investigated and the corresponding mechanism was discussed as well;

Chapter 7 reviewed all research progresses on fly ash reactivity in this study and developed a two-phase reaction model both considering fly ash material variations and cement and fly ash interaction to predict the temperature-dependent pozzolanic reaction of siliceous fly ash in different cement systems. This model was validated by the experimental results. With the help of this model, parametric analyses are presented to show how the pozzolanic reactivity and temperature dependence of fly ash affects the concrete performance; and

Chapter 8 summarizes all works and conclusions in this study and then gives perspectives for further research.

2 Literature review and research methodology

Contents:

2.1 Fly ash application in concrete 6
2.1.1 Benefits of fly ash in concrete 6
2.1.2 Application difficulties of fly ash in concrete 7
2.2 The nature of fly ash and its formation mechanism 9
2.2.1 Chemical composition of fly ash 9
2.2.2 Crystalline and amorphous solids of fly ash 12
2.2.3 Morphology of fly ash 17
2.3 Fly ash material properties characterization methods 19
2.3.1 Mineralogical properties 19
2.3.2 Chemical properties 20
2.3.3 Morphology properties 21
2.4 Fly ash temperature-dependent activity 22
2.5 Interaction between cement and fly ash 22
2.6 Underlying questions and research methodology 24
2.6.1 Underlying questions 24
2.6.2 Research methodology 24

2.1 Fly ash application in concrete

2.1.1 Benefits of fly ash in concrete

Fly ash is a by-product of burning pulverized coal in thermal power plants, which mainly consists of small, spherical particles of alumina-glass solids. It can improve concrete performance in many respects when it mixes with cement. For example, a well-proportioned fly ash concrete mixture will have improved its workability and reduced hydration heat when compared to the portland cement concrete with the same slump. These benefits greatly facilitate the construction of massive concrete in engineering practice. On the other hand, with the latent pozzolanic reaction that amorphous solids reacts with the calcium hydroxide to produce various calcium-silicate hydrates (C-S-H) and calcium-aluminate hydrates (C-S-A-H), the micro-structure of fly ash concrete will be continuously improved in long-term period, which suppresses the the long-term creep and shrinkage and strengths the resistance of concrete to various environment attacks, such as freezing and thawing, alkali-silica reaction, sulfate attack, chloride ingression etc. [1, 4].

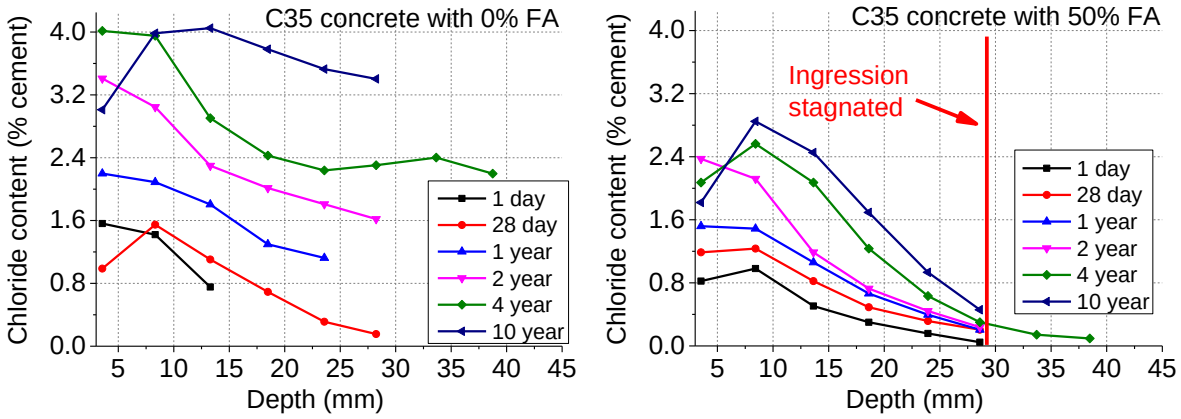

(a) C35 concrete with 0% FA (b) C35 concrete with 50% FA

Fig. 2.1 Chloride profiles into marine-exposed concrete at 10 years [4]

Besides laboratory studies, these superior performances of fly ash concrete also have been verified in real conditions. For instance, Mehta and Langley described the impressive performance of a large fly ash concrete foundation designed to endure for at least one thousand years. The foundation consists of a massive, unreinforced, monolith structure composed of two parallel slabs and each slab was cast with a well-proportioned 20-MPa mixture containing 60

mass % siliceous fly ash that registered only 13 °C maximum temperature rise. After 5 year inspection, the exposed surfaces did not reveal a single crack in the concrete and the strength was nearly double the designed value [1, 11].

Moreover, it is also reported that fly ash concrete exhibits an excellent resistance of chloride ingression in marine environment. Thomas studied chloride concentration profiles at different ages for fly ash concrete exposed in a marine tidal zone for up to 10 years. Compared to the referenced ingression profiles of normal OPC concrete with same strength at 28 day (i.e. C35), the rate of chloride penetration decreased significantly with fly ash content and the chloride content at this depth barely increased at all beyond the initial 28-day period for the concrete with 50% fly ash [4].

At last but not least, as the widely used construction material, cement contributes up to 5% of man-made carbon dioxide emissions every year, therefore, fly ash concrete also provides a promising and efficient way to reduce the carbon dioxide emissions and protect environment through replacing part of cement.

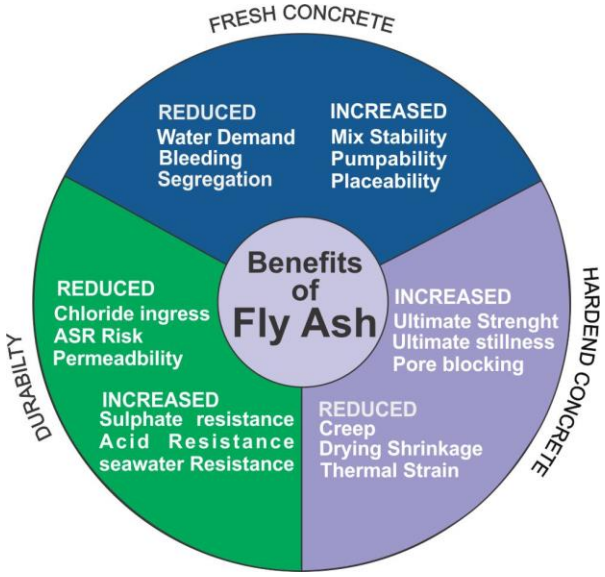

Fig. 2.2 Benefits of fly ash concrete [2]

In conclusion, fly ash is a great potential supplementary cementitious material to improve concrete performance in many aspects, which were comprehensively summarized in Fig. 2.2. These superior benefits make fly ash concrete becomes a promising and powerful approach by which we can build far more durable and resource-efficient concrete structures in the future.

2.1.2 Application difficulties of fly ash in concrete

These benefits for using fly ash in concrete has been well known for a long time, however, compared to the annual production of 670 Mt, only 30 mass % of them is used in concrete right now and most of them is discarded [6]. Japan is a representative example. Although the

efficient utilization of coal ash was up to 98 mass % in 2016, still only 1.5 mass % of them was directly used to be mixed with cement and casted concrete [10]. That is because there are several application difficulties that limits and hinders the applications of fly ash in engineering practices, which will be briefly discussed in following sections.

2.1.2.1 Material properties variation of fly ash

The primary application difficulty and major concern on fly ash comes from its intrinsic and significant heterogeneity and variability. Their physical, mineralogical and chemical properties actually can be profoundly different among coal types, combustion conditions and collection methods in thermal power plants, which highly influences the performance of fly ash concrete. Schlorholtz et al. monitored the material properties variation of fly ash produced in the same plant (Table. 2.1) and its effect on compression strength of cement paste for up to 2 years (Fig. 2.3). It is found that the compression strength of fly ash cement paste were dramatically different although the physical testing result of these fly ashes were similar [3].

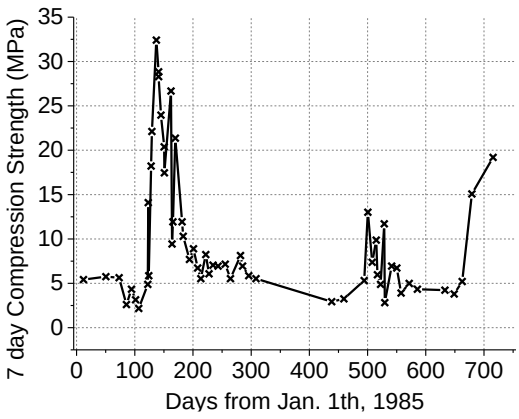

Fig. 2.3 Long-term monitoring on compression strength of fly ash cement paste (modified from [3])

Table. 2.1 Summary of physical testing of fly ashes in Schlorholtz's work [3]

	1985 sample number : 85			1986 sample number : 75		
	Avg.	Stv.	R	Avg.	Stv.	R
Moisture content. (%)	0.03	0.02	0.10	0.03	0.03	0.11
Loss on ignition (%)	0.24	0.06	0.24	0.31	0.06	0.28
Fineness (normalized %)	9.83	0.81	3.90	9.47	0.92	4.70

2.1.2.2 Low compression strength at early age

Another utilization difficulty of fly ash is its slow reaction rate compared to cement, especially

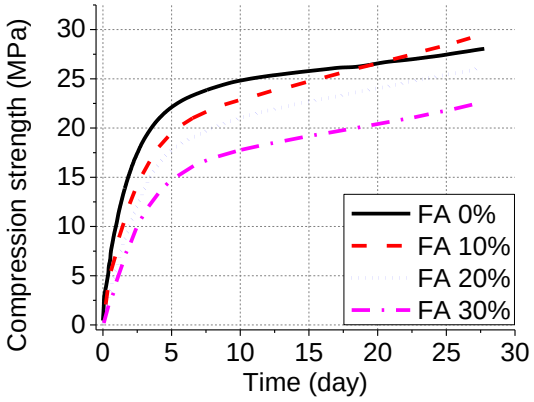

Fig. 2.4 Fly ash replacement effect on compression strength [1]

for siliceous fly ash. As a result, the early-age strength of fly ash concrete decreases as fly ash replacement ration increase (Fig. 2.4), which usually results in delays in the rate of construction. This shortcoming becomes particularly pronounced in winter construction. This problems could be solved by selecting a lower water-to-cement ratio for fly ash concrete. However, construction designs usually have some specific requirements on mixture slump and hydrated heat and reducing water-to-cement ratio is accordingly impracticable, especially for massive concrete. Therefore, high temperature curing is often used in fly ash concrete to accelerate its reaction and then achieve a certain minimum strength at early age.

Unfortunately, although considerable studies had been carried out to investigate the temperature-dependent pozzolanic reactivity of fly ash [12-16], current information and knowledge is still far from enough to understand the temperature-dependent behavior of fly ash and the corresponding effect on concrete performance. As a result, the guidance for high temperature curing is currently insufficient and most engineers more rely on their experience.

2.2 The nature of fly ash and its formation mechanism

As mentioned before, the material properties of fly ash are intrinsically and significantly heterogeneous and variable since they are highly affected by coal types, combustion conditions and collection methods in thermal power plants. This section is going to summarize recent progress on the fly ash material properties and the corresponding formation mechanism, which will help us better understand the reactivity of fly ash.

2.2.1 Chemical composition of fly ash

2.2.1.1 Bulk chemical composition

The reactivity of fly ash highly depends on its chemical composition. Generally, high-calcium

fly ashes are more reactive than low-calcium ones. Fly ash chemical properties are dependent to a large extent on the composition of the coal. High-calcium (calcareous) fly ashes are usually originated from younger lignite or sub-bituminous coal. In contrast, the harder, older anthracite and bituminous coal typically produces the low-calcium (siliceous) fly ashes.

Since a wide range of worldwide coal are burned in the thermal power plant, the fly ash chemical properties can be very different when their sources are different. So far, considerable efforts have been made to investigate material property variations of fly ash. Fig. 2.5 was a survey on the calcium content variation of fly ashes from 110 commercially-available sources in North America. It showed that the chemical compositions of commercial fly ashes actually fell into a wide range of categories if their producer are different [17].

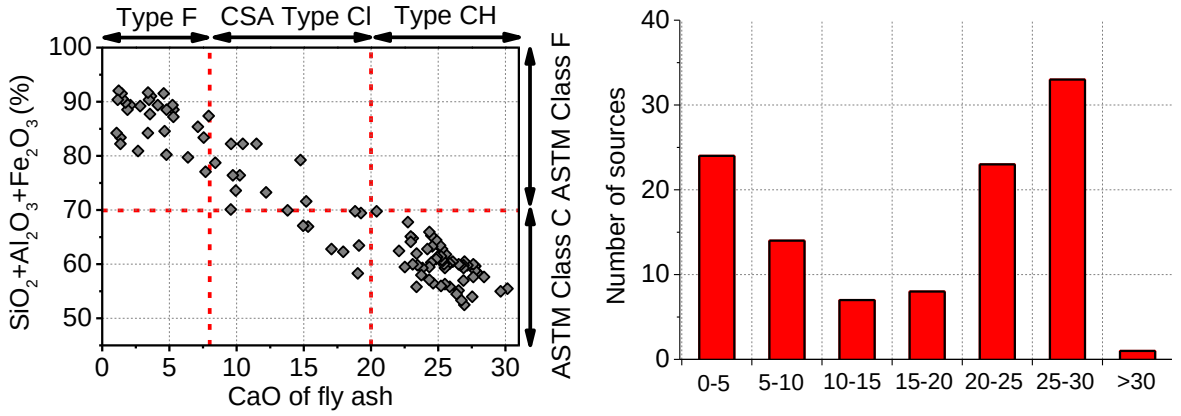

(a) oxides composition (b) calcium content distributions

Fig. 2.5 Filed survey on chemical compositions of fly ash produced in North America (modified from [17])

2.2.1.2 Element distribution

Although bulk oxide composition is widely used to accesses fly ash reactivity, this information is still insufficient to describe it since their element distributions can be significantly varied in micro-scale as well. Recently, Durdzinski et al used SEM-EDS to access the Ca-Si-Al element distribution fly ashes. They found that siliceous fly ash mainly consists of silicate and Al-silicate groups, as shown in Fig. 2.6 (a) and (b). However, compared to siliceous fly ash, the distribution of calcareous fly ash is more complicated. The element distributions of two

calcareous fly ash CFA4-1 and CFA4-2 were also shown in Fig. 2.6. These two calcareous fly ash were produced in the same plant but from different batches. Although the oxide compositions of these two fly ashes are very similar, their element distributions actually were significantly different. CFA4-1 tended to concentrate on Al-Si group but CFA4-2 had a wider distribution and a considerable amount of Ca-Al-Si solids [9].

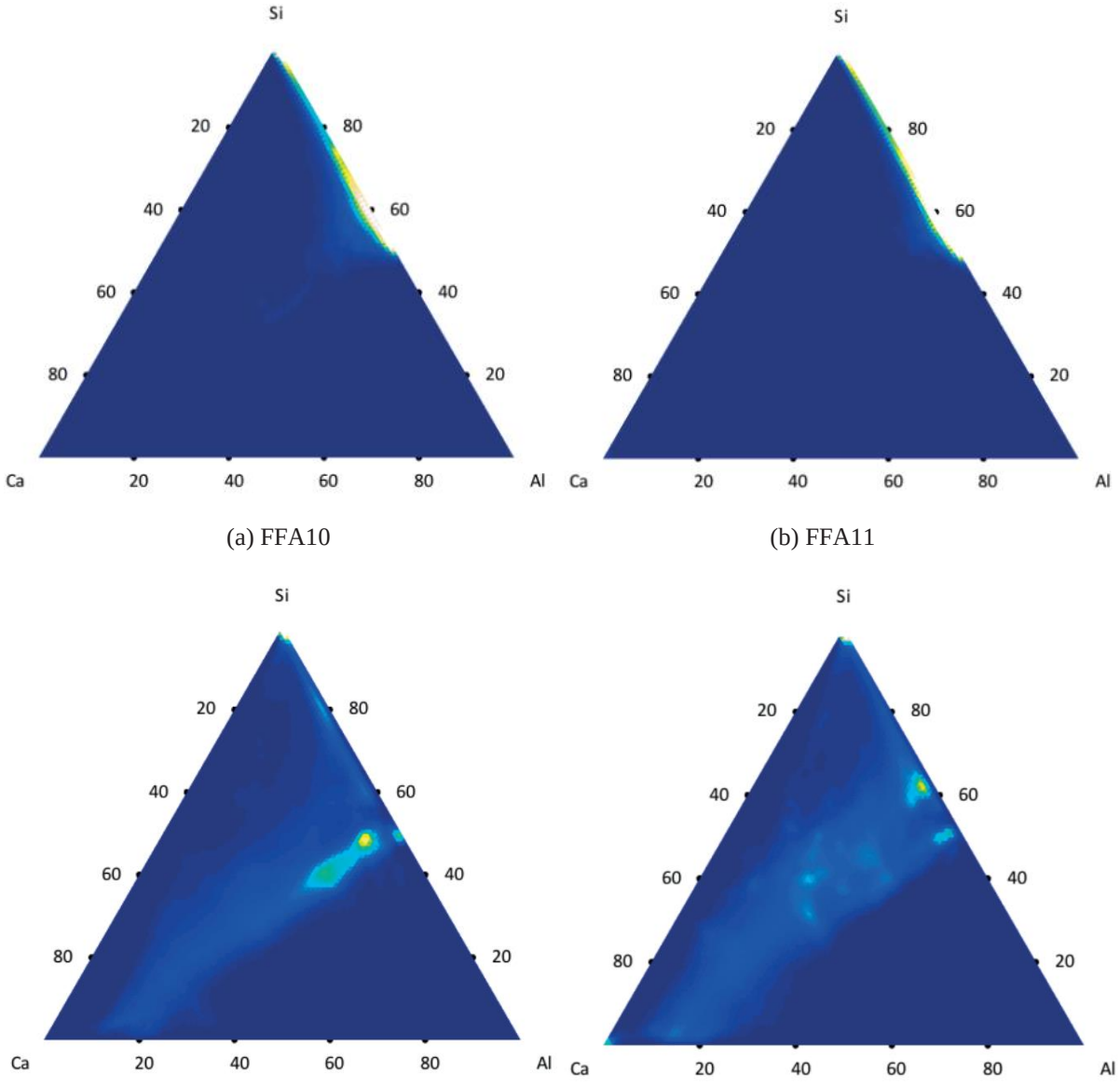

(a) FFA10 (b) FFA11

(c) CFA4-1 (d) CFA4-2

Fig. 2.6 Al-Si-Ca atomic-% ternary frequency plots of fly ashes in Durdzinski's work [9]

The element distribution of a specific fly ash is depended on the coal combustion conditions. Generally speaking, when the crystal phases are more completely molten and less viscous, phase-interchange and element diffusion therefore are more easily happened and the chemical composition is more homogenous. It is noted that the melting degree of coal mineral constituents also depends on their composition, especially on the amount of glass-modifying elements, such as iron, calcium, sodium, and potassium. These elements act as fluxing agents and then facilitate the melting of crystal phase, resulting in more homogenous phases [18, 19].

2.2.2 Crystalline and amorphous solids of fly ash

Solid materials exist as either crystalline solids or amorphous solids. They are distinguished by the degree of geometric order of the constituent molecules is repeated or systematic or not. A graphical representation of both the crystalline and amorphous atoms arrangement of silica (SiO_2) is schematically shown in Fig. 2.7 for illustration. Crystalline structure has a repeating molecular pattern but the pattern for amorphous silica is random and disordered. Because the most reactive content of fly ash are the amorphous phases, this section is going to address the material properties of crystalline and amorphous phases and its corresponding formation mechanism.

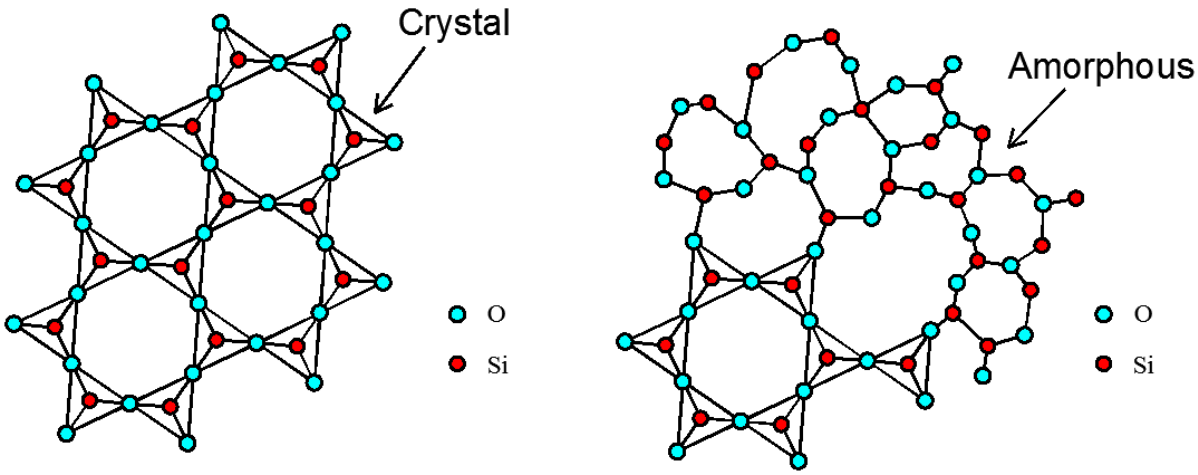

(a) crystalline silica (b) amorphous silica

Fig. 2.7 Atoms arragement of cytalline and amorhopus silica

2.2.2.1 Phase assemblage of fly ash

As mentioned before, fly ash has both of amorphous and crystalline phases. The fraction between amorphous and crystalline phases in fly ash is depended on combustion conditions and the chemical and mineral composition of coal. The typical content of amorphous phases of fly ash can be varied from 30 ~ 80 mass % in different fly ashes. Generally, hematite, magnetite and other Ca-richer crystalline phases, like gehlenite, anorthite and akermanite will present in high calcium fly ashes. In contrast, the mineralogy of siliceous fly ash is simpler and it principally contains mullite and quartz due to its high Al and Si and low Ca content [18].

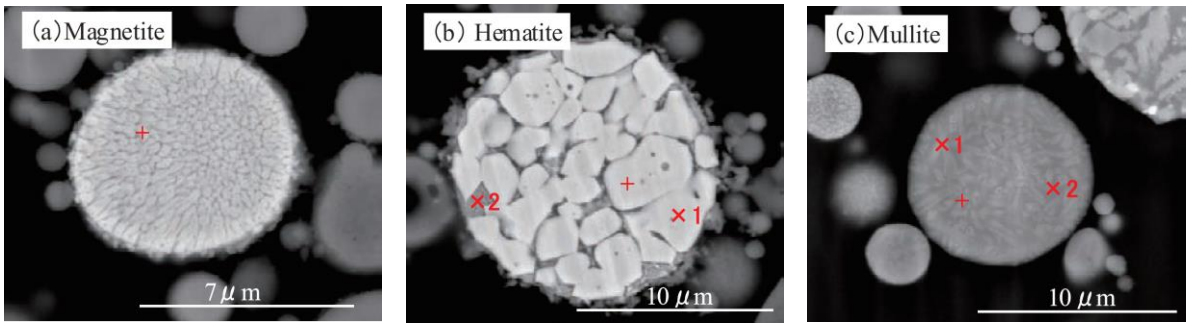

(a) magnetite (b) hematite (c) mulllite

Fig. 2.8 BSE images of Takahashi experiments [20, 21]

Recent researches showed that the mineralogical phase assemblage of fly ash is varied and heterogeneous in micro-scale as well. Takahashi et al. using SEM-EDS and Electron backscatter diffraction (EBSD) to study the microstructure of fly ash, as shown in Fig. 2.8 [20, 21]. It can be clearly seen that fly ash particles are not homogenous solids but complicated mixtures of various crystalline and amorphous solids. It is also found that, unlike common crystal phases (i.e. magnetite, hematite, quartz etc.), crystalline mullite usually existed as small solids and widely distributed in fly ash particles (e.g. Fig. 2.8 (c)). Under this consideration, they named these particles as “mullite-rich” and inferred that the reactivity of these particles are highly depended on its surface area by analyzing the suppression effect of alkali-silicate reaction [20, 21].

2.2.2.2 Heterogeneous phase formation mechanism

It is known that mineralogical phase assemblage of fly ash are actually heterogeneous in micro-

scale. It is believed as the one of the major reasons for the variations of reactivity of fly ash. Therefore, this section is going to summarize the both formation mechanism of crystalline and amorphous solids. The stepwise separation phase processes will be introduced to explain the micro phase assemblage of fly ash as well.

(a) Crystalline phase

When coal is burned in power furnace, partial mineral of coal will be molten. At the melting point, vibrating lattice elements of molten solids will no longer return to sites belong to their neighbors. During the cooling, the vibrating intensity of lattice elements reduces as the internal energy of the material decreases and the material then begins to re-solidify [18, 22]. According to principles of thermodynamic, such a system always tends toward its lowest free energy state, in other words, transfers to crystal solids. This re-crystallization takes place if the cooling liquid spends a sufficient amount of time in the transition temperature range conducive to nucleation and growth of crystals [19]. The time required for crystallization is highly depended on the combustion temperature, which shifts very little for lower volume fraction, as shown in Fig. 2.9. However, it should be noted that this theoretical nucleation time is for pure material and the "critical rate" can be strongly promoted 5 ~ 10 times if the micro-heterogeneities are present as initial nucleation [18]. In conclusion, the crystalline solids of fly ash comes from the unmolten mineral and the re-crystallization of molten mineral, which is strongly depends on combustion conditions of coal and its chemical compositions.

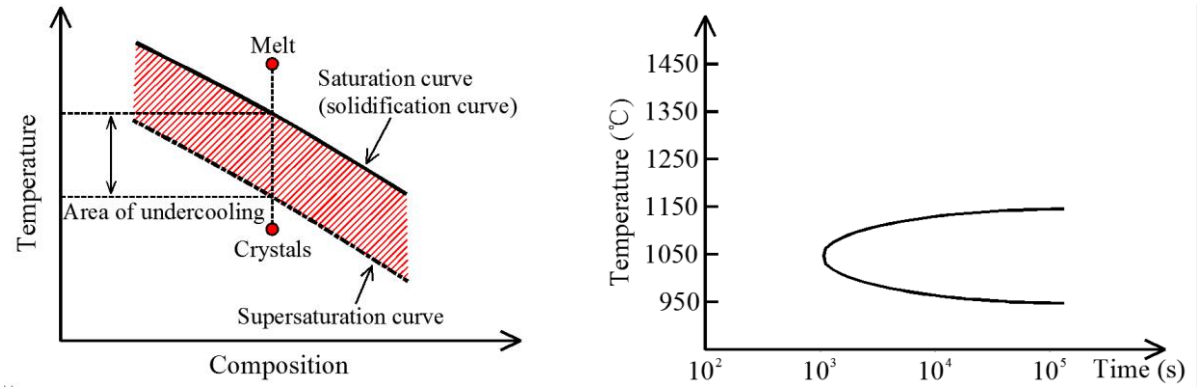

(a) transition region (b) time required for crystallization

Fig. 2.9 Temperature effect on solids crystallization

(b) Amorphous phase

Compared to re-crystallization, when molten material is cooled rapidly, it forms an amorphous solid that lacks the long-range order which is characteristic of a crystal. This process most notably affects the aluminosilicate minerals present in coal, which dissociate and form various amorphous Al-silicate phases upon cooling processes [18, 19].

Regarding to siliceous fly ash, it mainly contains pure Al-silicate glass and modified Al-silicate glasses formed as a result of aluminosilicate minerals co-melting with other oxides. For siliceous fly ashes, typical amorphous elements are Si and Al and typical modifier elements are Ca, Al, Na Fe and Mg. This modification may occur as either a polymeric network substitution or as a polymeric network modifier addition. The higher the modifier concentration, the more matrix will be depolymerized [18, 19].

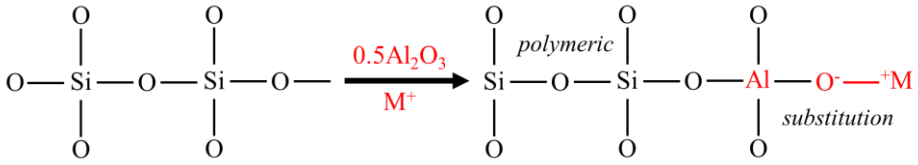

Fig. 2.10 Two-dimensional representation of polymeric network substitution of Al for Si (modified from [19])

More specifically, in case of network substitution, some elements are capable of replacing Si in the polymeric network to form another amorphous phase. For example, the tetravalent Si^{4+} can be replaced by trivalent Al^{3+} and then the amorphous silicate transfers to amorphous Al-silicate, as shown in Fig. 2.10. It is noted that this amorphous Al-silicate is also modified because a univalent cation M^+ is introduced to balance the net negative charge of O^- during this substitution as well [18, 19].

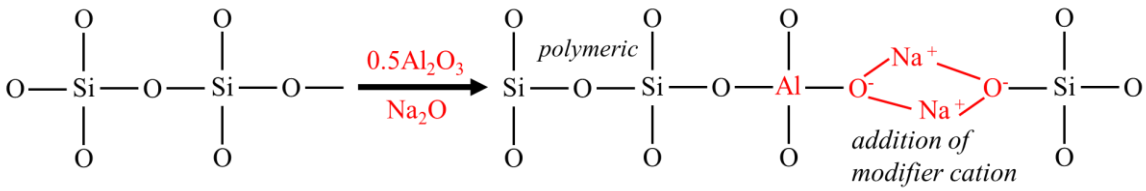

Fig. 2.11 Two-dimensional representation of polymeric network modifier addition of Na (modified from [19])

In addition to substitution, the amorphous phase can be modified by addition of a polymeric modifier as well. Fig. 2.11 is an example. After the substation of Al for Si, the Na_2O can precipitate to build the network and connect two polymer by bridge bond, resulting in fewer pure silicate oligomers and a high number of terminal non-bridging oxygen atoms [19].

(c) Stepwise separation phase processes

It is well known that the micro-phases of fly ash is heterogeneous. That is because coal has different composition materials and the unburned residue experiences a series of complicated combustion and cooling processes in power furnace. They both together lead to a separated phase assemblage as shown in Fig. 2.8. This processes called multiphase separation or step wise separation, which is schematically illustrated in Fig. 2.12 by a two phase system.

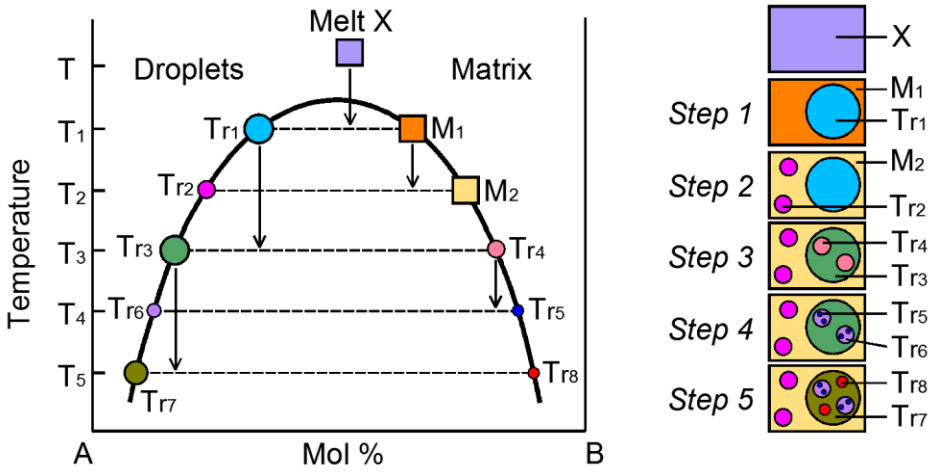

Fig. 2.12 Schematic representation of step-wise phase separation in amorphous solids (modified from [18])

Specifically, during cooling, a mineral solids with composition of X was first separated by matrix M_1 and droplet Tr_1 at temperature T_1 (step1). After this primary separation, these two phases of different viscosity behaved as almost two different systems and each of them displayed their own processes. For example, matrix M_1 was further separated into matrix M_2 and Tr_2 at temperature T_2 (step 2) and droplet Tr_1 became droplets Tr_3 and Tr_4 at temperature T_3 (step 3). Finally, the homogenous matrix matrix X transferred to a multiphase mixture that contains 8 phases (step 5).

2.2.3 Morphology of fly ash

2.2.3.1 Morphology of fly ash particle

Compared to previous properties, the fineness of fly ash may be the best known effect with respect to the application of fly ash in concrete. In general, high fineness usually means high reactivity; thus by using finer fly ash, the fly ash concrete can archive a higher strength and better performance. All standards therefore have some specifications on fineness. For example, Japan specifies that coal ash cannot be categorized into fly ash when its specific surface area (SSA) is lower than 1500 cm^2/g [23].

Although fly ash is made up of very fine, predominantly spherical particles, most of conventional methods fails to accurately estimate the fineness of fly ash because of the unburned coal and irregularly shape particles. Fig. 2.13 showed some BSE observations on fly ash particles. It can be seen that, besides the solid and sphere particle, fly ash also consists a considerable amount of irregularly shape particles, such as angular, cenospheres (hollow spherical bodies), vacuolated spherical and plerosphere (sphere in sphere) parties, which make the SSA is analytical troublesome. Moreover, the morphology of fly ash also affects the performance of fly ash concrete in other aspects. For example, when applying fly ash into cement or concrete, the small, smooth, spherical particles can effectively improve the rheology of mixture and then reduce the amount of required water and suppress the bleeding; however, the irregularly shaped particle may have an opposite effect. In conclusion, the morphology of fly ash is an important property related to its performance in concrete.

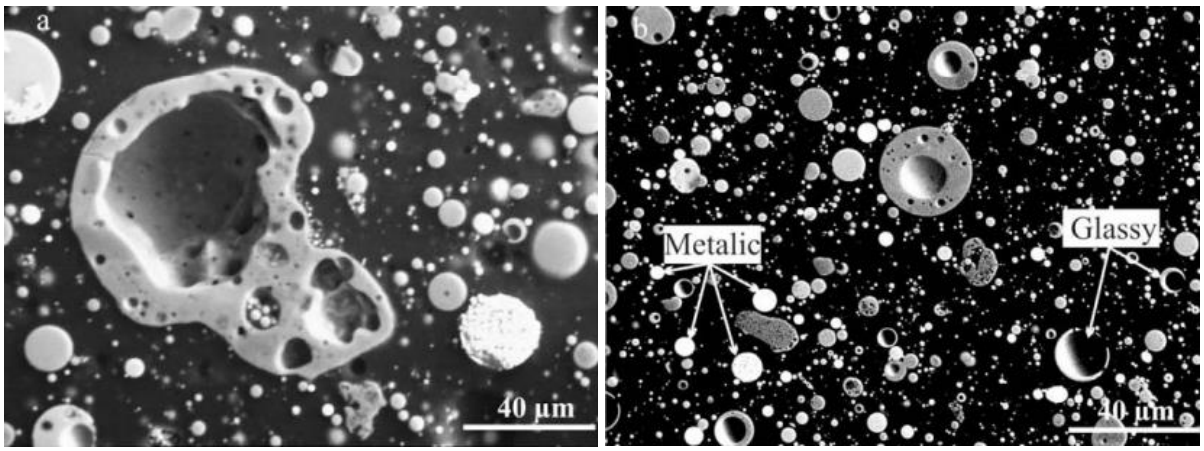

(a) angular (b) cenospheres

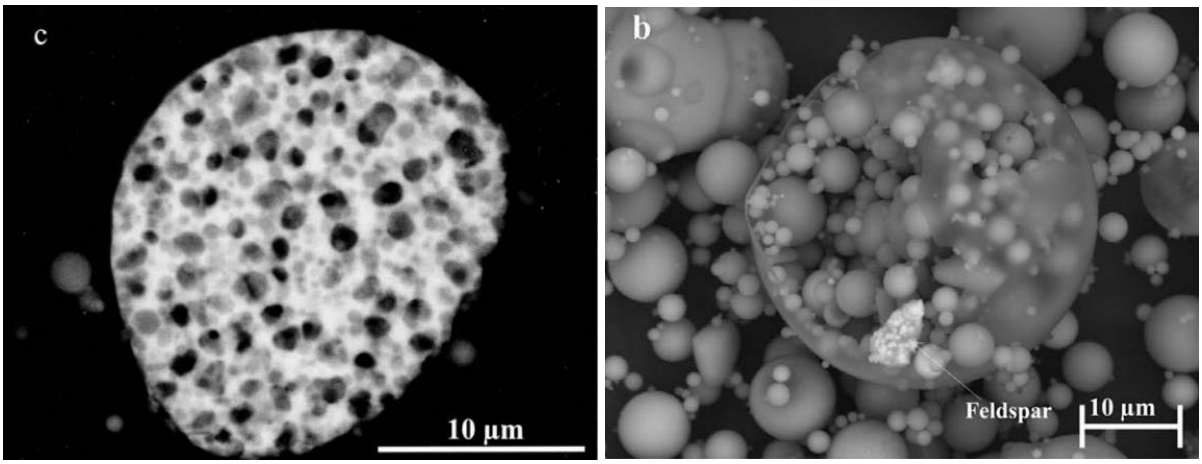

(c) vacuolated spherical (d) plerosphere

Fig. 2.13 BSE images of Takahashi experiments [20, 21]

2.2.3.2 Morphology formation mechanism

Besides it is well known that the size distribution of fly ash strongly correlates with the size distribution of coal and highly depends on the collecting separators used in the thermal power plants, considerable effect also has been made on the formation mechanism of hollow particles of fly ash in last serval decades.

Current research believes the morphology particle origins from the chemical and physical properties of the ash-formatting molten constituents [18]. Because coal actually is a combustible sedimentary rock always containing hydrate and carbonate products, melting of minerals is always accompanied with gas decomposition (e.g. H_2O and C_2O) during the combustion of coal. If the viscosity of the glass melt is low enough to expand but high enough to preserve the spherical form during the reaction sequence of fly ash particles, the holes will consequently form because the glass melt is blew by the decomposition gas [18]. Because this glass-blowing can be only effectively done between the softening point and melting point of minerals and the glass viscosity decreases with increasing modifier content, the morphology of fly ahs particles is accordingly affected by the modifier contents as well [18]. If the modification content is enough, the viscosity will be lower than a critical value and the holes can be filled by glass melt and particles become solid again. This relationship is well summarized by Pietersen as shown in Fig. 2.14 [18].

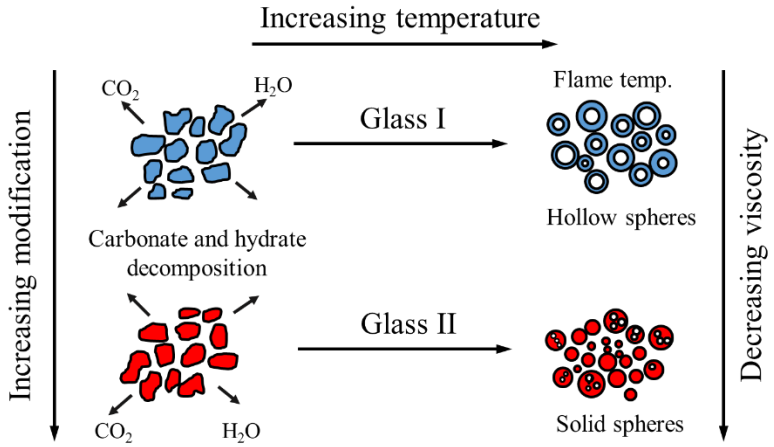

Fig. 2.14 Schematic representation of fly ash bloating and its dependency on melt viscosity (modified from [18])

2.3 Fly ash material properties characterization methods

The essential point to understand the reactivity of siliceous fly ash lies in accurate material properties characterization. However because fly ash chemical, mineralogical, physical and morphology are significantly affected by coal properties and combustion conditions, numerous methods have been developed to characterize the fly ash material properties in describing the reactivity of fly ash. This section is going to briefly review these characterization methods and their application limitations.

2.3.1 Mineralogical properties

Because crystalline materials usually exist in a low energy state as result of re-solidification products of glass melt at a slow cooling rate, they are always considered as unreactive or inert solids compared to the higher energy state amorphous solids of the same elemental composition. Therefore amorphous (glass) content is usually used to describe the reactivity and potential reaction degree of fly ash in cement systems.

X-Ray powder diffraction (XRD) is the most widely used method to identify and quantify mineralogical phases of fly ash. However, this method just only provides the bulk

information on the mineralogical properties and therefore fails to distinguish the differences of the amorphous phases of fly ash [24].

Considering these limitations, Chancey et al tried to characterize and quantity the mineralogy phases of siliceous fly ash by SEM-EDS with software MultiSpec [19, 25]. However, this analysis method highly depends on the software itself clustering algorithm and user mutually operating without reasonable theoretical background. That limits the accuracy of analysis result and the analysis result is very difficult to be used for modelling as well.

Later on, Takahashi et al. used SEM-EDS and electron backscatter diffraction (EBSD) to study siliceous fly ash and found that fly ash particles are heterogeneous multiphase mixtures of amorphous and crystalline solids, especially for mullite [20, 21]. They consequently proposed some different amorphous solids, such as mullite-rich, Al-Si-Ca glass Fe-rich etc [20, 21]. However, this method needs the operator to analyze the particle chemical composition one by one and then classify the particles, it is therefore arduous, expensive and time-consuming and not suitable for engineering practice.

2.3.2 Chemical properties

The reactivity of fly ash highly depends on its chemical composition. Generally, high-calcium fly ashes are more reactive than low-calcium ones because some content of calcareous fly ashes will display cementitious behavior by reacting with water. So far, the most widely used specifications for fly ash, such as EN 197-1 [26] and ASTM C618 [27], are consequently all based on their bulk chemical composition. The EN standard divides fly ashes into siliceous ($CaO_{reactive}$ < 10 mass %) and calcareous ($CaO_{reactive}$ > 10 mass %) fly ashes. Similarly, ASTM standard divides them into class F ($SiO_2 + Al_2O_3 + Fe_2O_3$ > 70 mass %) and class C ($SiO_2 + Al_2O_3 + Fe_2O_3$ < 50 mass %) as well.

X-Ray fluorescence (XRF) test is the most widely used approach to characterize fly ash chemical composition. It can provide the element contents of interested materials in their oxide forms. However, similar to XRD, XRF only provides the bulk chemical composition of fly ash but fails to distinguish variations of amorphous contents. Recently, a new advanced technique of SEM-EDS full element mapping was proposed by École polytechnique fédérale

de Lausanne (EPFL) to identify and characterize fly ash chemical composition [9, 24, 28]. They found that the reactivity of amorphous solid are related to itself chemical composition by investigating the dissolution rate of amorphous solids with different chemical compositions in alkaline system (Fig. 2.15) [9, 24, 28]. Therefore, they proposed a segmentation criteria based on chemical composition to identify and distinguish different amorphous groups. This work does make a great process on characterization of fly ash material properties and reveal the relationship between reactivity of amorphous solids and their chemical compositions. However, this method only focuses on the chemical composition of fly ash but ignores the mineralogical effect as previous section discussed.

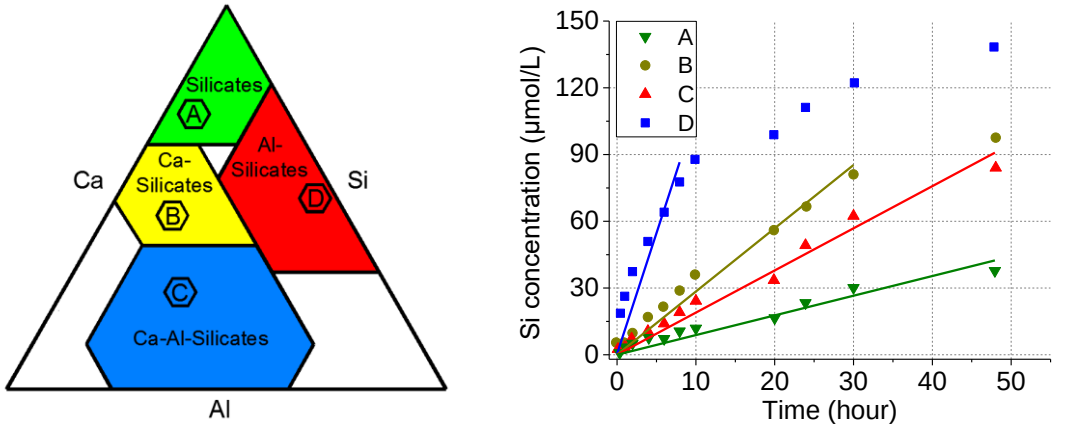

(a) segmentation criteria (b) silicon concentrations in alkali dissolution test

Fig. 2.15 Dissolution process of synthetic glasses in alkaline solution [28]

2.3.3 Morphology properties

The specific surface area (SSA) or fineness is another important property influencing the reactivity of fly ashes as well. Currently, there are three major methods to measure the SSA of fly ashes, Blaine air permeability, laser diffraction and gas adsorption[29, 30]. The first two methods involve the assumption of the perfect spherical particle geometry and they are not preferred by academics [30]. Compared with these two semi-empirical methods, nitrogen absorption test is believed more reliable since it can access the cracks, crevices and pores of materials that water can access. However, this method is sensitive to degassing conditions and material properties and its consistency largely suffers criticism as well [30]. Therefore, these

three methods will be carefully studied in this study. More detailed discussion can be referred to section 4.4.1.

2.4 Fly ash temperature-dependent activity

The pozzolanic reaction rate of fly ash is slow at room temperature but can be significantly promoted at high temperature. Therefore, high temperature curing is often used in fly ash concrete to accelerate its pozzolanic reaction. However, compared to the numerous studies on normal temperature, the information on fly ash concrete at high temperature curing is limited.

Pietersen et al studied the dissolution rate of fly ash in a NaOH alkali condition with with a pH ranging from 13.0 to 13.7 and temperatures between 20 and 40 °C. They found that dissolution rate of fly ash was promoted as pH and temperature increased [18].

Narmluk also studied the studied the extent of temperature-dependent pozzolanic reaction degrees with a low-binder ratio and proposed a kinetic model to simulate fly ash reaction [15, 16, 31].

Hanehara et al. studied the extent of temperature-dependent pozzolanic reaction degrees in cement systems from 20 to 40 ℃ with different water-binder ratios and fly ash replacement ratios. They concluded that the pozzolanic reaction can be promoted by high temperature curing; the extent of reaction degrees decreased as fly ash replacement ratio increased and water-binder-ratio decreased; and the maximum replacement ratio of fly ash is approximately 40% [14].

2.5 Interaction between cement and fly ash

Previous research pointed out that, besides filler and dilute effect, pozzolanic reactions of fly ash may suppress cement hydration as well. Sakai et al. found that although cement hydration was promoted by filler and dilute effect of fly ash at early age, the later hydration process was retarded in fly ash blended cement paste, as shown in Fig. 2.16 (a) [32]. Kawabata et al further found that the retarded effect on belite hydration was more significantly at high temperature

curing (Fig. 2.16 (b)). However, it is interesting found that the belite hydration was promoted in Class C fly ash blended cement paste, which is abounded with Ca-Si-Al glass. [28].

This phenomena is believed to origins from the morphology of C-S-H gel variation induced by the continuous consumption of calcium hydroxide for pozzolanic reaction of fly ash. Nonat et al. found that the C-S-H gel prefers to growth parallel to the surface of anhydrous cement grains at low calcium hydroxide content but to perpendicularly at high calcium hydroxide content [33-36], therefore the diffusion process is more difficult at low calcium hydroxide content due to the continuous pozzolanic reaction of fly ash. This retarded effect is also investigated in this test and more detailed discussion will be done in section 6.5.3.

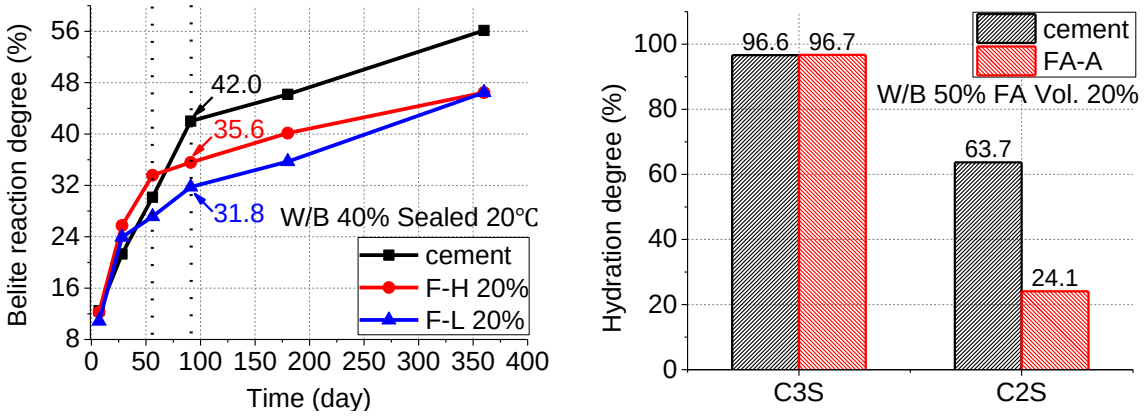

(a) Sakai's experiment [32] (b) Kawabata's experiment [37]

Fig. 2.16 Retarded hydration of belite in fly ash blended cement paste

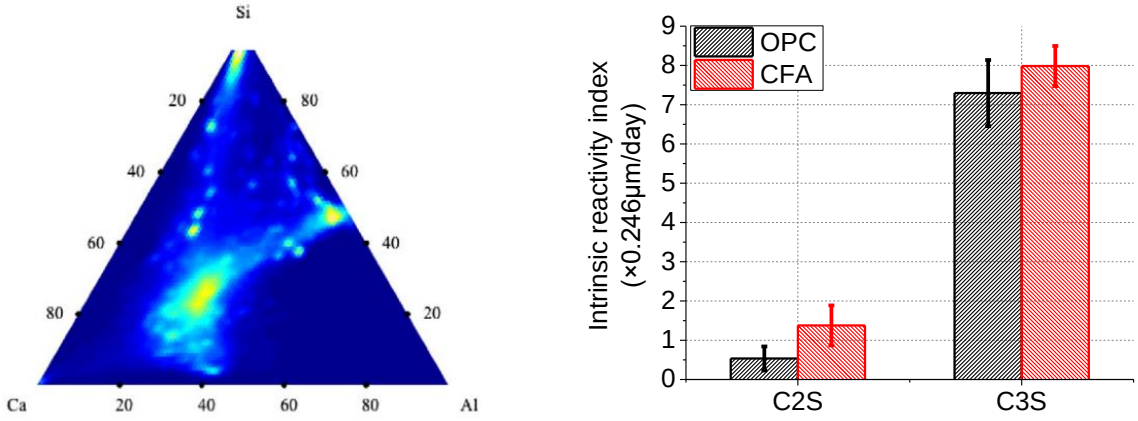

(a) ternary frequency plot of CFA (b) intrinsic reactivity of C2S and C2S

Fig. 2.17 Durdziński's experiemtn work [28]

2.6 Underlying questions and research methodology

2.6.1 Underlying questions

According to previous discussions, it can be known that the material properties are highly affected by combustion conditions, properties of coal and production process and they can be significantly varied in different fly ashes. Although considerable efforts have been made on that, most of them were more focus on studying some specific parameters of some specific fly ashes (e.g. finesse, water-binder ratio etc.) and these information are insufficient and difficult to provide a fundamental understanding on pozzolanic reaction of fly ash with us to build a unified model considering different fly ashes. Compared to them, a more comprehensive and fundamental approach is to distinguish and quantify the amount of reactive phases of fly ash and then characterize their temperature-dependent kinetic properties. If so, similar to the cement kinetic models, a more unified and comprehensive model can be accordingly proposed to cover different fly ashes, which is also easily extended to other supplementary materials, such as slag, silica fume etc. Moreover, the interaction between cement clinkers and cement can be accordingly more easily discussed and modeled. To archive this goal, some underlying questions should be solved first as follows:

(1) What is the exact phase assemblage of siliceous fly ash? Which phase is reactive and which phase is not reactive;

(2) What is and how to determine the reactivity properties of reactive phases of siliceous fly ash, including intrinsic reactivity, thermal activation energy and specific surface area? ;

(3) What is relationship between the reactivity of integral fly ash and induvial phase? ;

(4) What is the impact of siliceous fly ash on the hydration of cement clinkers? ; and

(5) With all the information, how to build a unified model both considering fly ash material variations and cement and fly ash interaction to predict the temperature-dependent pozzolanic reaction of siliceous fly ash in cement systems?

2.6.2 Research methodology

To comprehensively characterize fly ash material properties, fundamentally understand pozzolanic reaction of fly ash in cement systems and finally build a unified model to consider the variation of fly ash material properties, a research methodology was proposed and schematically illustrated in Fig. 2.18. Considering low calcium fly ash is dominated and popular in Japan and time and resource is limited, the interest of this study is only focus on siliceous fly ash.

More specifically, three different types of siliceous fly ashes were first selected based on its solubility in alkaline condition. The material properties characterization of these fly ashes, including phase assemblage and specific surface area, was studied by SEM-EDS (Scanning Electron Microscopy; Energy-Dispersive x-ray Spectroscopy) full element mapping test and image analysis method with a developed phase segmentation criteria. Subsequently, the temperature-dependent reactivity of these fly ashes were investigated in NaOH solution and further studied in cement systems by preparing blended cement pastes under sealed curing conditions at 20 and 60 °C. The extent of pozzolanic reaction of these fly ashes were measured by selective dissolution tests. The interaction between fly ash and cement and calcium hydroxide consumption were also investigated and estimated in this study.

Based on all information, a temperature-dependent two-phase reaction model both considering fly ash material variations and cement and fly ash interaction was finally proposed to predict the temperature-dependent pozzolanic reaction of siliceous fly ash in cement systems and validated by the experimental results.

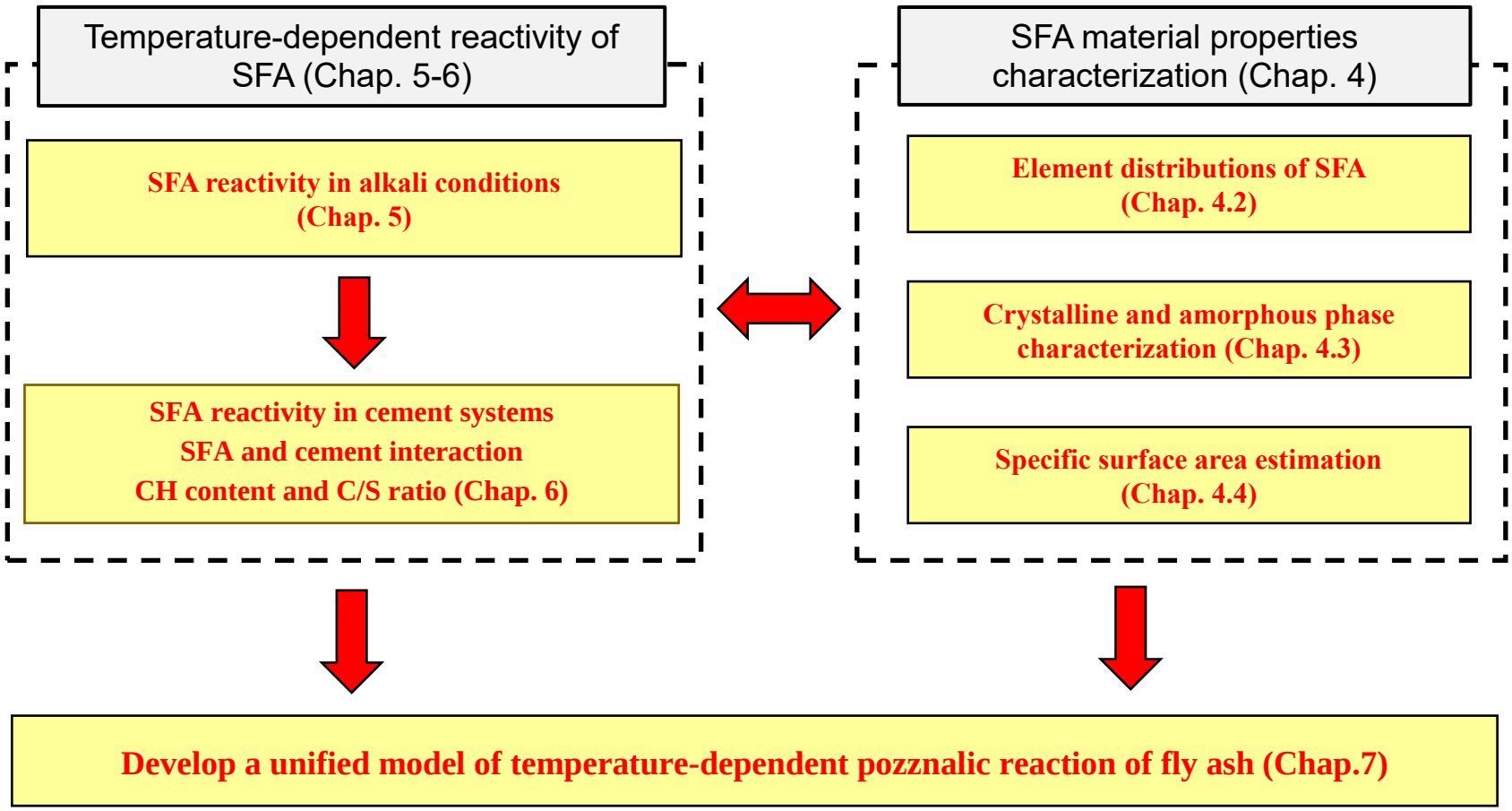

Fig. 2.18 Research methodology in this thesis

3 Principal materials and test methods

Contents:

3.1 Principal materials 28
3.2 Test methods 29
3.2.1 Inductively coupled plasma optical emission spectrometry (ICP-OES)..... 29
3.2.2 X-ray fluorescence (XRF)..... 29
3.2.3 X-ray powder diffraction (XRD) 30
3.2.4 Air permeability fineness (Blaine fineness)..... 31
3.2.5 Particle size distribution (PSD)..... 31
3.2.6 Nitrogen absorption test..... 32
3.2.7 Scanning electron microscopy (SEM) 32
3.2.8 Energy-dispersive X-ray spectroscopy (EDS)..... 33
3.2.9 Thermo-gravimetric analysis (TGA) 33

3.1 Principal materials

Three different types of low-calcium (Class F) fly ashes, ordinary portlaned cement (OPC) and low heat cement (LPC) were used in this experiment. These three fly ashes were all commercial JIS II fly ashes and selected from 11 types fly ashes according to their solubility in NaOH solution at 20 and 60 °C.

The bulk chemical and physical properties of fly ash and cement were summarized in Table. 3.1 and the phase compositions listed in Table. 3.2. The specific surface areas determined by blain test and laser diffraction test were both provided in Table. 3.1. These three types of low-calcium (Class F) fly ashes have different crystallize compositions and different solubility in NaOH solution but similar physical and chemical oxide result.

Table. 3.1 Physical properties and chemical compositions of cement and fly ash

	OPC	LPC	FA1	FA2	FA3
Specific gravity	3.15	3.24	2.23	2.29	2.29
Blaine fineness, cm2/g	3350	3750	3940	3730	4070
Surface area*, cm2/g	– –	– –	5893	5803	5567
SiO2, mass %	– –	– –	64.10	60.57	63.78
Al2O3, mass %	– –	– –	20.23	21.35	19.78
CaO, mass %	– –	– –	2.19	2.01	4.65
MgO, mass %	– –	– –	0.70	0.75	0.69
Na2O, mass %	– –	– –	0.58	0.68	0.54
K2O, mass %	– –	– –	1.24	1.40	1.07
TiO2, mass %	– –	– –	1.40	1.18	1.24
Fe2O3, mass %	– –	– –	4.17	5.20	4.12

Note: – – means not measured items; and * is estimated by laser diffraction test

Table. 3.2 Mineralogical phase of cement and fly ash

	OPC	LPC	FA1	FA2	FA3
C_2S, mass %	15.90	62.53	– –	– –	– –
C_3S, mass %	65.50	26.33	– –	– –	– –
C_3A, mass %	8.07	2.10	– –	– –	– –
C_4AF, mass %	8.77	6.30	– –	– –	– –
Mullite, mass %	– –	– –	11.40	6.49	15.28
Quartz, mass %	– –	– –	7.09	4.94	10.64
Free lime, mass %	– –	– –	0.02	0.06	0.24
Magnetite, mass %	– –	– –	0.43	0.61	0.82
Amorphous, mass %	– –	– –	81.07	87.90	73.03

Note: – – means not existed items according test result

3.2 Test methods

3.2.1 Inductively coupled plasma optical emission spectrometry (ICP-OES)

ICP-OES is stand for Inductively Coupled Plasma Optical Emission Spectrometry. It is a commonly used instrument in modern laboratories in quantitative measurement of trace metal element in liquid. It is based on atomic emission spectroscopy, where the metal element of sample at high temperature plasma up to 8000 Kelvin converted to free, excited or ionized ions [38].

During measuring, ICP-OES generates an intense electromagnetic field in the torch. When the argon gas flows through the torch, the argon element is ionized and a stable, high temperature plasma is then generated as the result of the inelastic collisions created between the neutral argon atoms and the charged particles [39]. The element in the liquid is then exited as well and emits electromagnetic radiation at wavelengths characteristic of a particular element. The radiation passes through grating monochromator and only specific wavelength passes to the photomultiplier detector. The intensity of this emission is indicative of the amount of the element within the liquid and the concentration can be accordingly determined by comparing the intensity of standard solution prepared for measurement [39].

In this study, ICP-OES (ICPS-7000 Shimadzu) was used to measure the amount of dissolved element of fly ash in alkaline system, such as Si, Al and Ca.

3.2.2 X-ray fluorescence (XRF)

X-ray fluorescence (XRF) spectrometry is a common approach used to identify elements in a substance and quantify the amount of those elements present to ultimately determine the elemental composition of a material, which is widely used in cement industry [40].

In XRF spectrometry, high-energy primary X-ray photons are emitted from a source (X-ray tube) and strike the sample and knock electrons out of the innermost K or L, orbitals. When this occurs, the atoms become ions and unstable. The electrons from outer orbitals therefore will move into the newly vacant space at the inner orbital to make the atoms regain stability. During this process, an energy known as a secondary X-ray photon is according

emitted from these moved electrons. This phenomena is called fluorescence. Because the secondary X-ray produced is characteristic of a specific element and its energy is proportional to the content of the element as well, the elemental composition of a material can be quantified by measuring the intensity of its characteristic emission [40].

In this study, X-ray Fluorescence analyzer Range 2 (Buker) at Material Research Center of Southern University of Science and Technology (SUSTech) was used to determine the chemical composition of studied fly ashes.

3.2.3 X-ray powder diffraction (XRD)

X-ray powder diffraction (XRD) is a rapid analytical approach primarily used for identification and quantitative measurement of crystalline phase of a material. X-ray diffraction is based on constructive interference of monochromatic X-rays and a crystalline sample. These X-rays are generated by a cathode ray tube, filtered to produce monochromatic radiation, collimated to concentrate, and directed toward the sample. The interaction of the incident rays with the sample produces constructive interference when conditions satisfy Bragg's law [38]

$$n\lambda = 2d\sin\theta \tag{3.1}$$

where n is the order of the interference band; λ is the wavelength of X-rays; d is the spacing between crystal planes; and θ is the incident beam angle.

Because XRD samples were usually grinded into sample crystal, every crystal plane gets an opportunity to diffract X-rays when X-ray beams hit the sample. Scanning over a range of angles produces a pattern characteristic for mineralogical phase assemblage of tested sample. Individual phases of multiphase that can be identified and quantitatively determined by comparing standard pattern database.

In this study, the X-ray diffraction test was conducted by X-ray diffractometer of Shimadzu XRD 6100 under these conditions: Cu-Kα X-ray source, 40 kv tube voltage, 30 mA tube current, 2θ=5 ~ 70° scanning range, 0.02° step width and 2 second step measurement speed. The fly ashes were mixed with around 10 mass % corundum (α-Al_2O_3) as internal standard material and carefully front-loaded in an alumina holding cell. Rietveld analysis was carried out after measurement by software Siroquant version 3.

$$f^{A} = 100\left(f_{cor}^{cal} - f_{cor}^{mix} \right) \Big/ \left\{ f_{cor}^{cal} \left(1 - \frac{f_{cor}^{mix}}{100} \right) \right\} \tag{3.2}$$

$$f_i^{C} = f_i^{cal} f_{cor}^{mix} \Big/ \left\{ f_{cor}^{cal} \left(1 - \frac{f_{cor}^{mix}}{100} \right) \right\} \tag{3.3}$$

where f^{A} is the actual amorphous fraction of tested sample; f_{cor}^{cal} is the Rietveld analysis fraction of internal standard material; f_{cor}^{mix} is the actual mixed fraction of internal standard material in the tested sample; f_i^{cal} is the the Rietveld analysis content of crystalline phase *i*; and f_i^{C} is the actual fraction of crystalline phase *i* of tested sample.

3.2.4 Air permeability fineness (Blaine fineness)

The Baline air permeability test is the most widely used method to determine the SSA of a powder in cement industry. In this method, the time needed for a fixed volume of air to pass through a well packed bed of powder of known dimensions is measured by an air permeability apparatus that had been empirically calibrated as described in ASTM C204 [41, 42]. By taking the measured time, the specific surface area of a material therefore can be determined with the Kozeny-Carman theory that assumes a mono-seized and spherical shape of particles [42].

In this study, Baline air permeability test was conducted by fly ash producer to access the fineness of studied fly ashes.

3.2.5 Particle size distribution (PSD)

The laser diffraction test (LD) is another common method to determine the SSA of a powder in cement industry. In laser diffraction test, a laser passes through a dilute suspension with a dispersed particulate sample and the scattering intensities is collected at low angles with respect to the incident light. Generally, large particles scatter light at small angles relative to the laser beam and small particles scatter light at large angles. The angular scattering intensity result is then analyzed to deduce the size distribution responsible for creating the scattering pattern based on diffraction theories, such as Mie theory or Fraunhofer theory [43]. The SSA

of tested powder therefore can be determined with the PSD result if the particles are all considered as solid spheres.

In this study, the PSD of studied fly ashes was measured by Mastersizer 3000 (Malvern Instruments) at SUSTech as well.

3.2.6 Nitrogen absorption test

The nitrogen adsorption method is based on quantifying the volume of nitrogen molecules needed to cover the sample surface. The specific surface area of tested material is calculated using the BET (Brunauer–Emmett–Teller) model. Compared to other methods, gas adsorption test does not postulate the particle shape or include semi-empirical equations and gas can access any pores, cracks and crevices that water can access as well. Therefore, this method is widely believed more reliable and preferred by academics. Because the molecule size of nitrogen is close to water, nitrogen is the most commonly employed gaseous adsorbate used for surface probing by BET methods.

In this study, the nitrogen absorption test were carried out by ASAP 2020 Plus Physisorption (Micromeritics) at SUSTech as well.

3.2.7 Scanning electron microscopy (SEM)

Scanning electron microscope (SEM) is a powerful electron microscope to produces images of a sample by scanning the surface with a focused beam of electrons. The electrons interact with atoms on the sample surface, producing various signals that contain information about the sample's surface topography and composition.

Among various signals, secondary electrons (SE) and back-scattered electrons (BSE) are the most common signals used for observation [44]. The SE are emitted from very close to the specimen surface. Therefore, SE can produce high-resolution images of a sample surface, revealing details less than 1 nm in size [44]. Compared to SE, BSE are beam electrons that are reflected from the sample by elastic scattering. They emerge from deeper locations within the specimen and consequently the resolution of BSE images is less than SE images [44]. However,

because the intensity of BSE signal are related to the atomic number of the specimen, this image are also often used in qualitative analysis of the element distributions and therefore mineralogical phase assemblage in the sample.

In this study, the scanning electron microscope we used was ZEISS Merlin at SUSTech as well.

3.2.8 Energy-dispersive X-ray spectroscopy (EDS)

Energy-dispersive X-ray spectroscopy is an analytical technique used for the elemental analysis or chemical characterization of a sample. The principle of EDS is similar to XRF and it also relies on the interaction of X-ray excitation and tested sample. Because it usually couples with the SEM, it can provide the spatial chemistry analysis on samples. Recently, a new technology named faster silicon-drift detectors is developed for EDS. With this new technology, full element mapping analysis can be done in several hours and make the comprehensive chemical characterization on tested sample become feasible in a micro-scale.

The EDS used in this study was a high speed detector of EDAX Octane Pro with 10 mm^2 active surface at SUSTech as well.

3.2.9 Thermo-gravimetric analysis (TGA)

Thermal gravimetric analysis (TGA) is a method of thermal analysis in which the mass of a sample is measured over time as the temperature changes. TGA allowed the identification of phases as different phases decompose within specific temperature ranges according its characteristic decomposition equations. In cementitious material studies, measurements of bound water and calcium hydroxide content by TGA are often used to evaluate the pozzolanic reactivity of fly ash. However, it should be noted the TGA test results substantially depend on the sample preparation procedures and experiment setups. A strict protocol on test method was developed and followed to ensure the comparability of test results. The modified analysis method was also develop to more accurately and reasonably estimate the calcium hydroxide content and bound water content. More detailed information can be referred to section 6.4.1.

In this study, the calcium hydroxide and bound water content of cement paste will be determined by TGA test. The general range of major phase decomposition are listed for reference [9, 45]:

- 60 - 150 °C Ettringite
- 150 - 180 °C Hemicarbonate and monocarbonate
- 180 - 200 °C Monosulfate
- 250 - 280 °C Hemicarbonate and monocarbonate
- 290 - 310 °C Hydrogarnet
- 350 - 550 °C Portlandite
- 700 - 800 °C Calcite, hemicarbonate and monocarbonat

4 Fly ash material properties characterization

Contents:

4.1 Introduction 36
4.2 Fly ash chemical properties characterization 37
4.2.1 Bulk chemical compositions 37
4.2.2 Micro-scale characterization of fly ash chemical properties 37
4.3 Fly ash mineralogical properties characterization 47
4.3.1 Bulk mineralogical phases 48
4.3.2 Micro-scale characterization of fly ash mineralogical properties 48
4.4 Fly ash specific surface area 61
4.4.1 Conventional test methods 61
4.4.2 Image analysis 68
4.5 Summary and conclusions 71

4.1 Introduction

In last several decades, considerable methods has been developed to characterize fly ahs material properties but they all have their own disadvantages. For example, X-Ray fluorescence (XRF) and X-Ray powder diffraction (XRD) are usually used to identify and quantify chemical compositions and mineralogical phases of fly ashes respectively. However, because fly ash has multiple glassy components and their particles are complicated mixture of amorphous and crystalline solids as well [9, 19-21, 24, 25], these methods are useful but insufficient to describe fly ash material properties. They are just able to provide the bulk information of fly ashes but cannot resolve and distinguish the material property variation within micro-scale [24, 25].

Fineness is another difficult issue to be estimated. Because fly ash has certain amount of irregular particles and unburned carbon, conventional methods, such as Blaine air permeability, laser diffraction, nitrogen absorption, all are not capable of accurately accessing the fineness of fly ash [29, 30].

Besides such shortcomings mentioned above, these methods are all independent and just focus on one specific parameter. However, fly ashes as a complicated by-product of coal combustion in thermal power plant, their chemical, physical, mineralogical properties and fineness will be significantly varied as type of coal, combustion condition changes. That makes these method application limited and incapable of covering different types of fly ash.

Compare to these conventional methods, a more comprehensive and fundamental approach to consider the variety of fly ash is to identify the basic reactive phases of pozzolanic materials and characterize the corresponding kinetic properties. If so, similar to cement can be described different clinkers like Alite, Belite ect., various fly ashes can be easily taken into account and then described by limited basic phases without further information as well. Furthermore, this framework can be easily extended to apply for other supplementary materials, such as slag, silica fume etc. in the further as well.

To achieve this goal, a comprehensive material properties characterization method and a reasonable phase segmentation criteria are essential. Therefore, based on full element SEM-EDS mapping analysis, this chapter is going to develop a new method to separate different phases and characterize their material properties. Specifically, the major elements distributions

will be first determined by SEM-EDS mapping test. Based on these element distributions, a phase segmentations criteria was subsequently proposed according the characteristic chemical compositions of different phases and therefore the whole phase assemblage including crystalline and amorphous phases can be identified and quantitatively analyzed. At last, a new image analysis method will be also proposed based on SEM-EDS mapping and the specific surface area of induvial phase and the whole particles can be accurately estimated without the morphology influence. The reliability of other fineness estimation methods will be also discussed in this chapter. It is hoped that these material characterization will help us reveal the pozzolanic reaction mechanism of siliceous fly ash in cement systems.

4.2 Fly ash chemical properties characterization

4.2.1 Bulk chemical compositions

As introduced in Chapter. 2, the reactivity of fly ash depends on it chemical composition and high calcium fly ash are usually more reactive than low-calcium fly ash. XRF test (Range 2, Buker, SUSTech) is therefore used to characterize fly ash bulk chemical composition. The quantification of elements was determined by fitting target profile with element standard profiles and assuming all unknown characteristic intensities comes from carbon. Table. 4.1 summarizes the XRF results of the fly ashes used in this study.

Table. 4.1 XRF-analysis result (mass %)

Item	Al_2O_3	SiO_2	CaO	Fe_2O_3	Na_2O	MgO	K_2O	TiO_2	Sum
FA1	20.23	64.10	2.19	4.17	0.58	0.70	1.24	1.40	94.61
FA2	21.35	60.57	2.01	5.20	0.68	0.75	1.40	1.18	93.12
FA3	19.78	63.78	4.65	4.12	0.54	0.69	1.07	1.24	95.87

It can be seen that these three fly ashes are all siliceous fly ashes and mainly composed of Si, Al and Fe oxides. The Ca content was a few mass %. Magnesium and alkali oxides did not exceed 3 mass %. The differences in bulk chemical composition between these siliceous ashes were generally rather small, around several mass %.

4.2.2 Micro-scale characterization of fly ash chemical properties

As discussed before, the SEM-EDS full element mapping test is carried out in this study to investigate the chemical properties of above fly ashes. Based on this SEM-EDS mapping analysis, a new phase segmentations criteria is proposed to identify and quantitatively analyze phase assemblage of fly ash in next section.

4.2.2.1 Sample preparation and microscope setup

A flat and smooth surface wiht abundant fly ash particle exposed is essential to conduct a successful SEM-EDS test. Therefore, an easily operated method without pellet press machine was developed in this study to prepare a proper sample with abundant particles as follows. The fly ash powder was first mixed with pure water and set down on a filter paper by vacuum filtration. The sample was subsequently dried in oven at 105℃ for 4 hours to remove all the physically absorbed water. Then the fly ash together with filter paper were impregnated into transparent epoxy resin (Epofix™ 1232) at a silicon mold under vacuum condition.

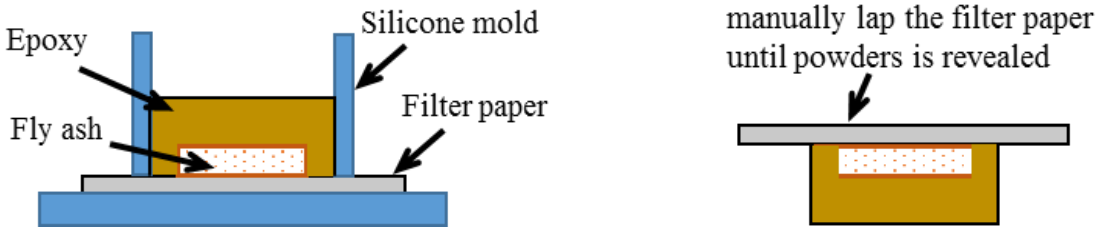

(a) setting epoxy (b) lapping filter paper

Fig. 4.1 SEM-EDS epoxy sample preparation

After epoxy resin become harden the side of sample with filter was manually lapped by silicon paper #40, #80, #200, #400 and #1000 successively until powders were clearly revealed without any visible notch. (see Fig. 4.1). Next, the sample was further polished by polishing machine (Metallography, QualiPol) down to ¼ μm with diamond spray and alcohol (as lubricant). After polishing, the sample was cleaned by alcohol ultrasonic bath and coated with a thin conductive layer of carbon (around 10 nm).

The SEM-EDS mapping test was carried out at SUSTech. The scanning electron microscope used in this test was ZEISS Merlin. EDS detector was EDAX Octane Pro with 10 mm^2 active surface. The microscope was operated at 15 kV accelerating voltage and 9.0 mm

working distance. The magnification of microscope was 450 and field view was 242×189 μm. The image resolution was 1024×800 and then pixel size was 0.236×0.236 μm.

Thanks to the high speed EDS doctor, a high EDS count rate of 60,000~70,000 counts per second was maintained during the test and dead time was between 0 and 5%. In order to balance poor measurement at high speed and potential risk of sample damage at low speed, a dwell time of 200 μs was adopted to keep the scanning speed at a moderate rate.

Because Al, Si and Ca is the major interest of fly ashes, these three elements standard spectra was first verified and calibrated by analytical grade Al_2O_3, SiO_2 and $CaCO_3$ based on the Winter's suggestions [46].

After all preparations and locating a proper measurement position in BSE image, an automated routine started to analyze four frames per sample. The total acquisition time was around 12 hour per sample.

4.2.2.2 SEM-EDS mapping and analysis algorithm

In this study, following elements were quantified from the spectra: Al, Si, Ca, Na, K, Mg, Fe, Ti and P during the EDS measurements. The quantification of elements content was determined by Genesis software through fitting target profile with element standard profile and PhiRhoZ matrix corrections. All results were saved as atomic percent (at. %).

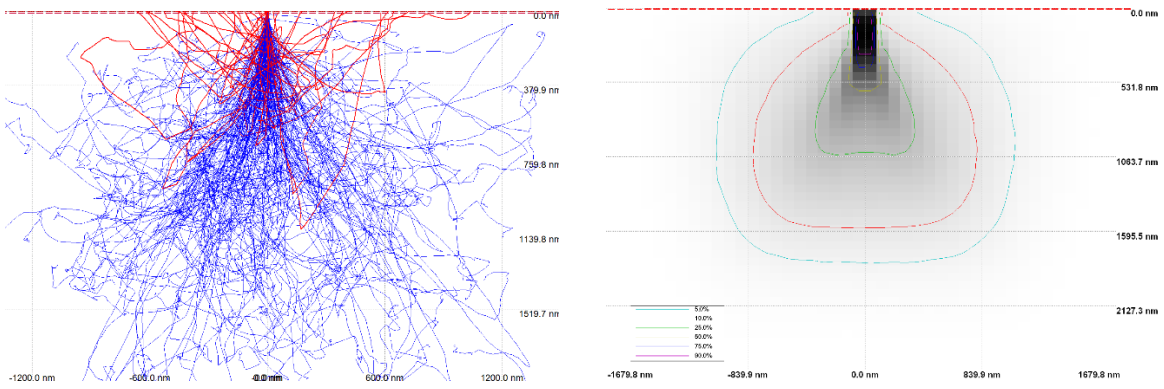

(a) electron trajectory (b) energy distribution

Fig. 4.2 The simulation result of electron trajectories and its energy distribution with respect to FA1 predicated by Casino software.

However, the raw data cannot be directly analyzed because it is not accurate and precise enough and full with noises. Fig. 4.2 is the simulation result of electron trajectories and its energy distribution with respect to FA1 predicted by Casino Monte Carlo simulation software (version 2.48, www.gel.usherbrooke.ca/casino/index.html), where the simulation parameters all followed the bulk chemical compositions of FA1 (Table. 4.1) and microscope setup used in this study. It can be seen that electrons usually travel a finite distance through the tested specimen, typically a few microns, before being absorbed or backscattered (Fig. 4.2 (a)). Over at least some of this distance until the electrons have lost all their energy, signals excited by electrons are all detected and collected by EDS detector of microscope (Fig. 4.2 (b)). The region that electrons travelled through is the so called interaction volume. Therefore, every EDS data is affected by the proximity of epoxy resin and the adjacent particles with different chemical composition and consequently full with noises.

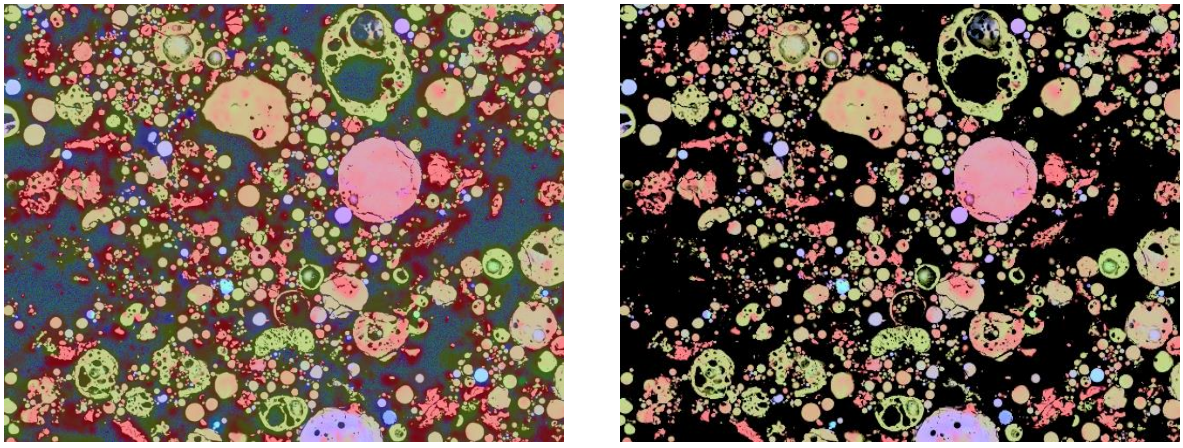

(a) before post-data processing (b) after post-data processing

Fig. 4.3 Comparison of element mapping result between before and after data processing

To account of this effect the raw data was smoothed by two-dimensional hamming window, which was developed by author based on Durdziński's work[24]. Further technical details on this method is illustrated in Appendix A. After smoothing, the background was removed by a mask from the threshold grey level of BSE image. Fig. 4.3 is the comparison of element mapping result between before and after post-data processing. It can be seen that background and noise was satisfactorily removed and and boundary of particles becomes more smooth and clear after post-data processing.

4.2.2.3 SEM-EDS element mapping result and discussions

(a) Bulk chemical composition

Table. 4.2 and Table. 4.3 shows the normalized chemical oxide compositions calculated by SEM-EDS mapping and XRF test respectively. Table. 4.4 presents the comparison between those two methods. It can be seen that Al_2O_3, CaO and Fe_2O_3 are good in agreement between two methods. However, the content of SiO_2 tended to be underestimated but other minor elements seemed to be overestimated in SEM-EDS compared to XRF tests.

Table. 4.2 Chemical oxide compositions of fly ash calculated by SEM-EDS mapping (mass %)

Item	Al_2O_3	SiO_2	CaO	Fe_2O_3	Na_2O	MgO	K_2O	TiO_2	SO_3	P_2O_5	Sum
FA1	21.52	57.98	2.38	4.53	1.39	2.08	2.08	2.59	2.33	3.13	100.00
FA2	21.53	55.95	2.52	5.80	1.43	2.11	2.50	2.53	2.41	3.23	100.00
FA3	19.55	58.92	3.58	4.41	1.21	1.98	1.88	2.56	2.36	3.57	100.00

Table. 4.3 Normalized chemical oxide compositions of fly ash calculated by XRF test (mass %)

Item	Al_2O_3	SiO_2	CaO	Fe_2O_3	Na_2O	MgO	K_2O	TiO_2	SO_3	P_2O_5	Sum
FA1	21.19	67.16	2.30	4.37	0.60	0.73	1.30	1.47	0.31	0.57	100.00
FA2	22.60	64.13	2.12	5.50	0.72	0.79	1.46	1.25	0.57	0.82	100.00
FA3	20.41	65.83	4.80	4.26	0.55	0.71	1.13	1.27	0.46	0.62	100.00

Table. 4.4 Comparison between SEM-EDS mapping and XRF test (SEM-EDS/XRF %)

Item	Al_2O_3	SiO_2	CaO	Fe_2O_3	Na_2O	MgO	K_2O	TiO_2	SO_3	P_2O_5
FA1	101.54	86.34	103.38	103.59	231.47	285.13	160.29	175.87	751.32	548.85
FA2	95.28	87.24	119.10	105.54	198.21	266.65	170.90	202.13	422.56	393.49
FA3	95.79	89.50	74.58	103.52	220.00	278.87	166.37	201.57	513.04	575.81

These differences probably came from different sample preparation methods and different measuring conditions. For example, the fly ash in XRF test was compressed into holding cell. But in SEM-EDS mapping, fly ash was set into epoxy and the surface was finally polished down to ¼ μm. Therefore, the minor elements may be more likely exposed and then more easily measured in SEM-EDS mapping.

Another reason may be the measurement time and data amount of SEM-EDS mapping is significantly longer and larger than XRF test and then the minor element is more easily detected by EDS.

The different analysis assumptions and calculation methods used in these two techniques may be another reasons contributed to the differences. The Genesis software in SEM-EDS mapping only considers the elements selected before measurement. Although XRF considers the whole profile, it assumes that all unknown characteristic intensities comes from carbon, which may actually come form water or other organic matter existed in fly ash, and some errors may be then introduced [47].

In spite of that there are some differences in the full element systems, in the Al-Si-Ca-Fe system we most concerned, SEM-EDS mapping is satisfactorily consistent with XRF test. Table. 4.5 is the comparison of the chemical oxide compositions of fly ashes between SEM-EDS mapping and XRF result in the Al-Si-Ca-Fe system. It can be seen that all elements contents are in good agreement. Therefore, SEM-EDS mapping test is feasible and reliable and it can be used to further study the chemical distribution of fly ash.

Table. 4.5 Comparison of chemical oxide compositions of studied fly ashes between SEM-EDS mapping and XRF result in the Al-Si-Ca-Fe system

	SEM-EDS Mapping (1) (wt.%)				XRF (2) (wt.%)				(1)/(2) (%)			
	Al_2O_3	SiO_2	CaO	Fe_2O_3	Al_2O_3	SiO_2	CaO	Fe_2O_3	Al_2O_3	SiO_2	CaO	Fe_2O_3
FA1	24.91	66.99	2.81	5.29	22.30	70.68	2.42	4.60	111.7	94.8	116.2	115.0
FA2	25.13	64.96	3.05	6.87	23.95	67.97	2.25	5.83	104.9	95.6	135.6	117.8
FA3	22.63	67.90	4.29	5.18	21.42	69.08	5.04	4.47	105.7	98.3	85.2	115.8

(b) Micro-sale chemistry analysis of fly ash based on SEM-EDS mapping method

EDS data of main interest elements of Al, Si and Ca is displayed in Fig. 4.4 with a false color attributed to each element atomic content (i.e. Al×1.5, Si×1.0 and Ca×8), where red-Al, green-Si and blue-Ca. It can be seen that fly ashes have different composition groups and particles are composed of multiple phases. This heterogeneity is due to the composition differences of source coals and combustion conditions in thermal power plant.

The corresponding chemical distributions of these fly ashes were further illustrated in a ternary element frequency plot (Fig. 4.5) proposed by Durdziński et al [24] for discussion. Since Fe element also takes a certain amount of weight (see Table. 4.2) in these three fly ashes, the chemical distributions of Al-Si-Fe systems also studied and presented in Fig. 4.6 for comparisons as well.

It can be seen form Fig. 4.5 that siliceous fly ashes mostly composed of amorphous silicate and alumino-silicate components and the peak of its intensity is around 60 % of silicon due to their low calcium content. These results are in good agreement with Durdziński et al works on European siliceous fly ashes as well [24].

In Al-Si-Fe system (Fig. 4.6), the element distributions are very similar to the ones in Al-Si-Ca system. However, compared to Ca element, Fe element seems to have a wider distribution range. That is probably because Fe ion is a fluxing agent and it is therefore more easy to melt and combine with other elements [19].

Because the main component of these three fly ashes are amorphous alumino-silicate, their chemical distributions was further displayed into normalized Al-Si system (Fig. 4.7) to study their differences. A comparison is made in Fig. 4.7 (d), which shows that the differences of Al-Si distribution for these three fly ashes are slight. More specially, FA2 has more amorphous alumino-silicate component and FA3 has more amorphous silicate. FA1 is the medium one between them.

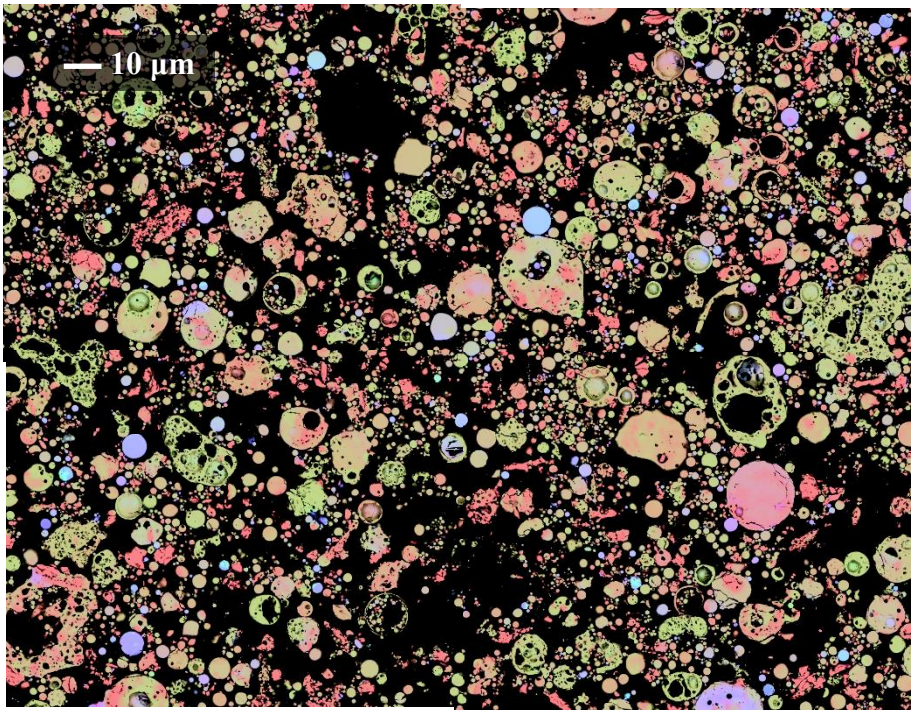

(a) SEM-EDS mapping result of FA1

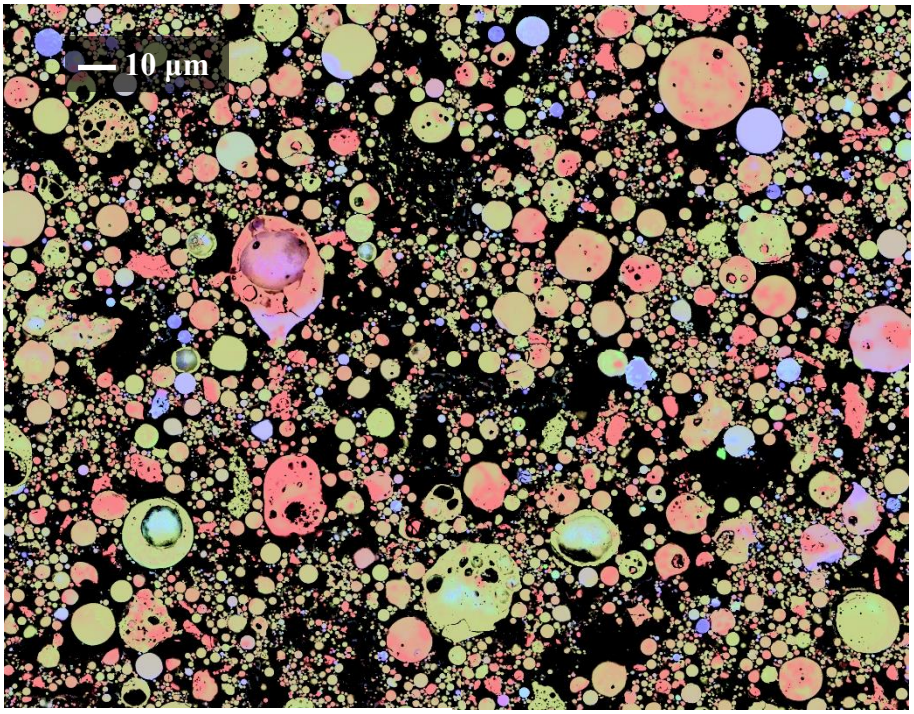

(b) SEM-EDS mapping result of FA2

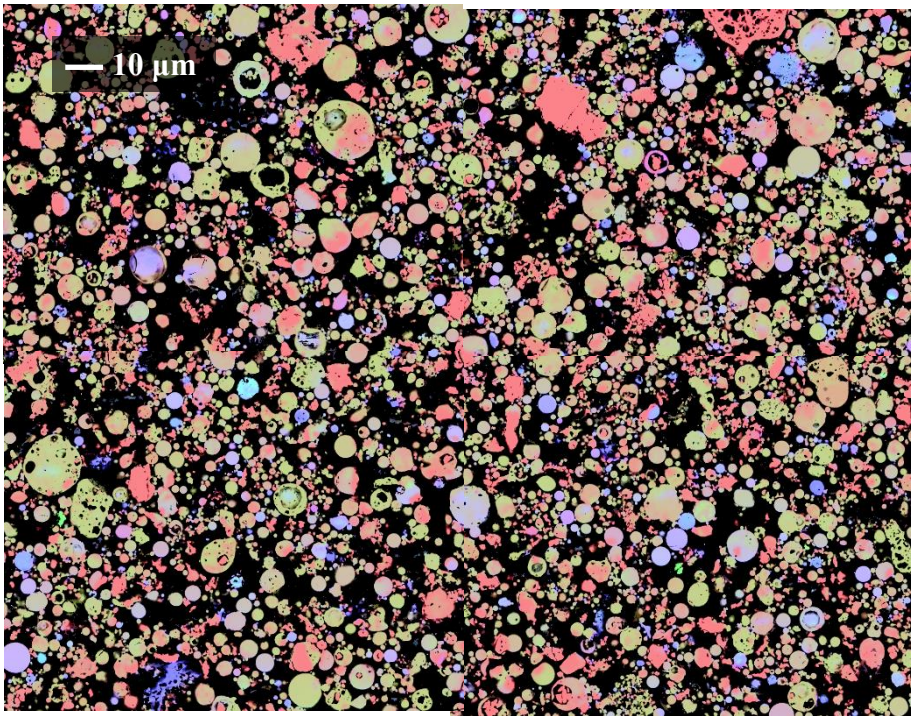

(c) SEM-EDS mapping result of FA3

Fig. 4.4 Visual representation of fly ash element distributions measured by SEM-EDS

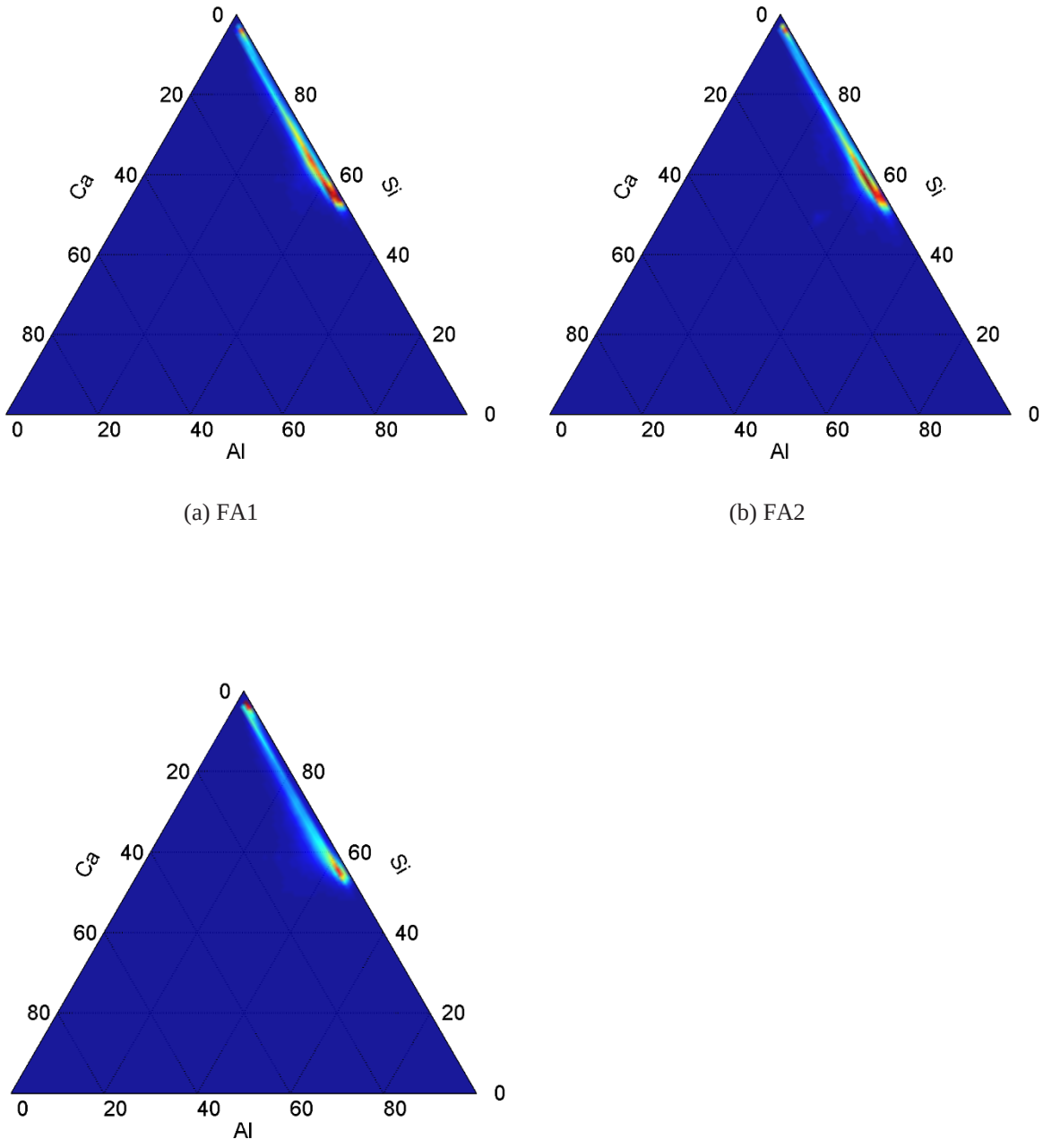

(a) FA1

(b) FA2

(c) FA3

Fig. 4.5 Al-Si-Ca ternary frequency plot of fly ashes measured by SEM-EDS

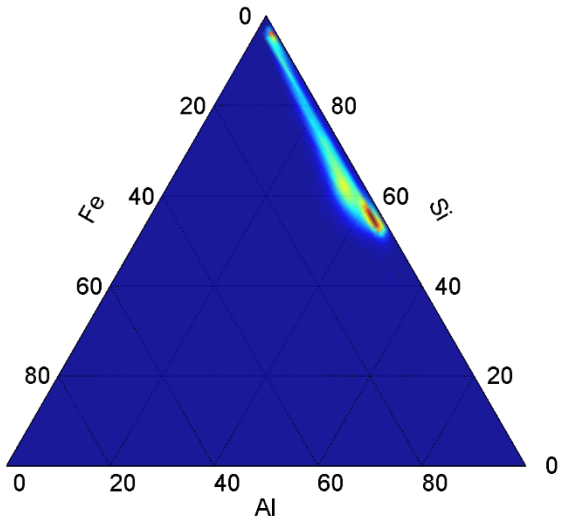

(a) FA1

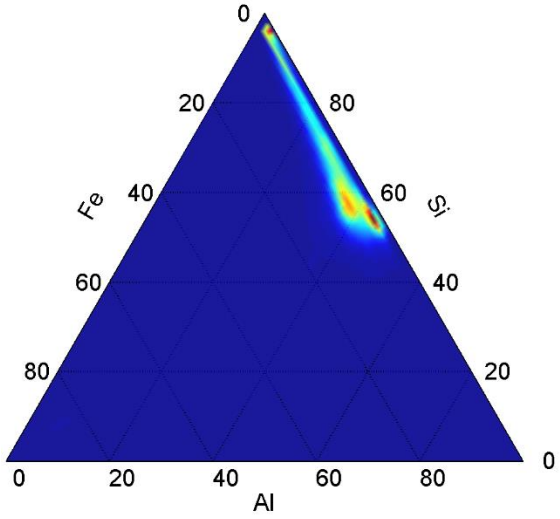

(b) FA2

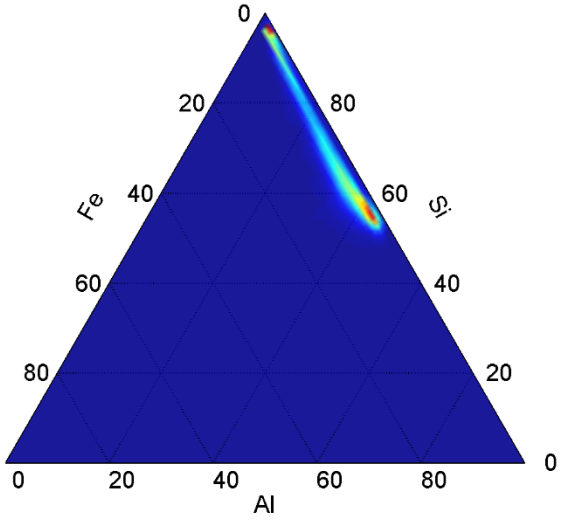

(c) FA3

Fig. 4.6 Al-Si-Fe ternary frequency plot of fly ashes measured by SEM-EDS

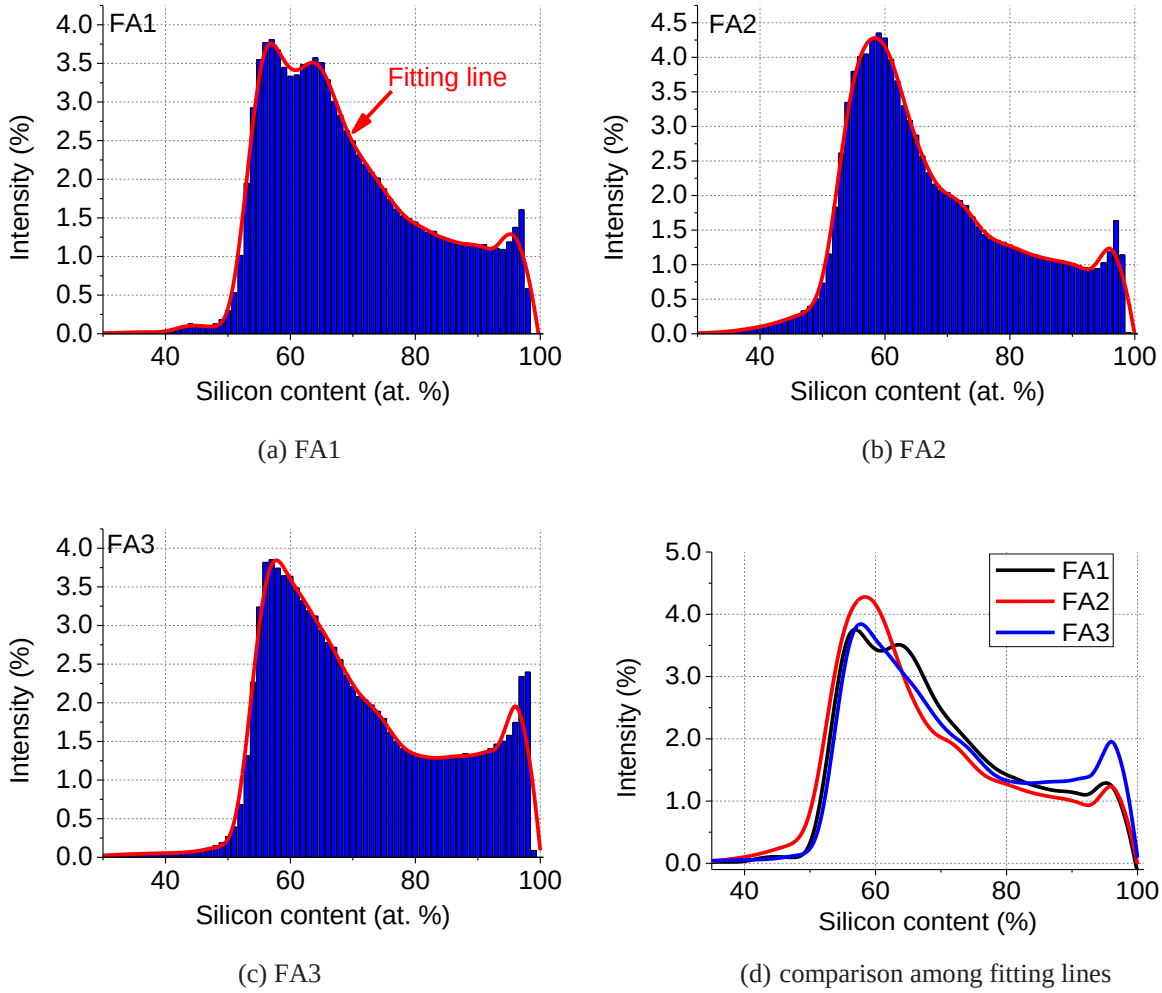

(a) FA1 (b) FA2

(c) FA3 (d) comparison among fitting lines

Fig. 4.7 Al-Si element distribution of fly ashes measured by SEM-EDS

4.3 Fly ash mineralogical properties characterization

Siliceous fly ashes are usually produced from anthracite or bituminous coals and are predominantly composed of alumino-silicate glasses with varying amounts of crystalline quartz, mullite, hematite and magnetite[4]. These crystalline phases are essentially inert in concrete and only the glass will react with alkali or lime (for example, $Ca(OH)_2$) to form cementitious hydrates. Therefore, mineralogical properties is another important parameter to affect fly ashes activities and it will be studied in this section.

4.3.1 Bulk mineralogical phases

X-ray diffraction with Rietveld refinement analysis is the most widely used method to identify and quantify the crystalline phases of fly ashes. In this study, XRD tests on powdered sample mixed with 10 mass % corundum as internal standard was conducted by X-ray diffractometer of Shimadzu XRD 6100 under test conditions mentioned in section 3.2.2. According to X-ray diffraction diagrams of fly ashes (Fig. 4.8), mullite ($3Al_2O_3{\cdot}2SiO_2$), quartz (SiO_2), free-lime (CaO), magnetite (Fe_3O_4) and corundum (Al_2O_3) were selected into Rietveld refinement analysis. Based on the result of Rietveld refinement analysis, the amounts of amorphous and crystalline phases was determined by Eqs. (3.2) and (3.3). More technician details can be referred to section 3.2.3.

Table. 4.6 is the XRD-Rietveld analysis result of siliceous fly ashes studied in this thesis. It can be seen that these fly ashes have different amount of mullite and quartz. The amorphous phases are the dominated component and they are all over 70 mass %.

Table. 4.6 Mineralogical phase composition determined by XRD-Rietveld analysis (mass %)

Item	Mullite	Quartz	Lime	Magnetite	Amorphous
FA1	11.40	7.09	0.02	0.43	81.07
FA2	6.49	4.94	0.06	0.61	87.90
FA3	15.28	10.64	0.24	0.82	73.03

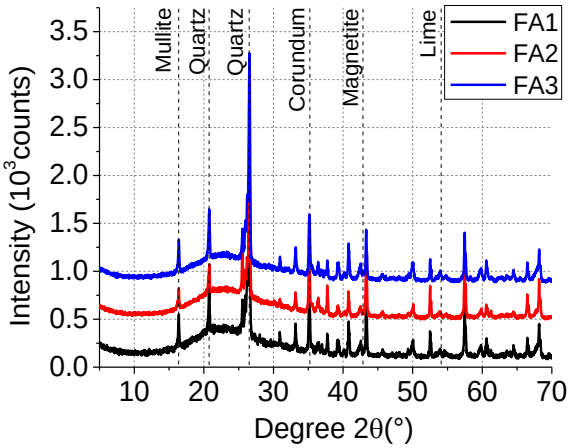

Fig. 4.8 X-ray diffractograms of the siliceous fly ashes studied

4.3.2 Micro-scale characterization of fly ash mineralogical properties

4.3.2.1 Fly ash mineralogical phases characterization

As introduced in chapter 2, fly ash usually shows significant heterogeneity in mineralogy and its particles are usually complicated mixtures of crystal and amorphous solids [19, 20]. Fig. 4.9 are some SEM pictures of typical crystal-amorphous fly ash particle in the three fly ashes we studied, which clearly showed the mineralogical heterogeneity of fly ash.

Since XRD method are only able to provide the bulk amount of crystal and amorphous phases, it fails to identify these crystal-amorphous particles and further quantify the amount of different within particles, as shown in Fig. 4.9. Although different crystalline and amorphous phases can be identified by grey levels (Fig. 4.9) in BSE images, this method is difficult to be directly applied to determine the relative proportion of each phase because the number of grey levels in BSE image is limited and different phases with different compositions may have similar levels as well. Therefore, a new method is desired and necessary to distinguish and quantify the amount of different mineralogical phases.

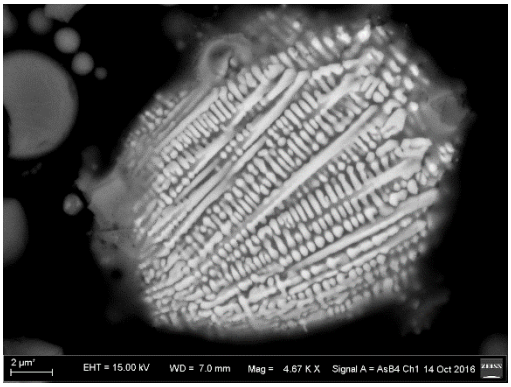

(a) FA1

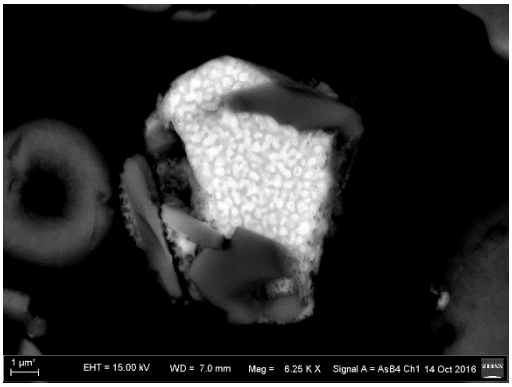

(b) FA1

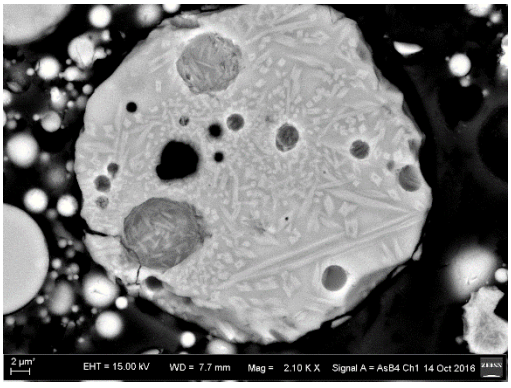

(c) FA2

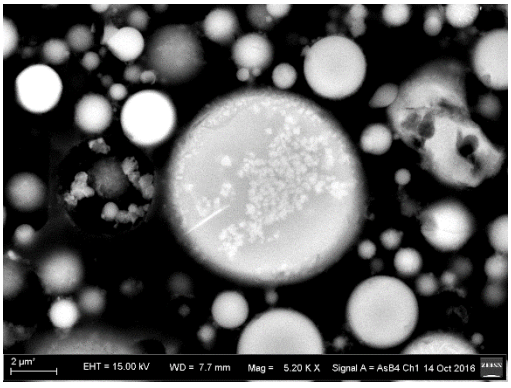

(d) FA2

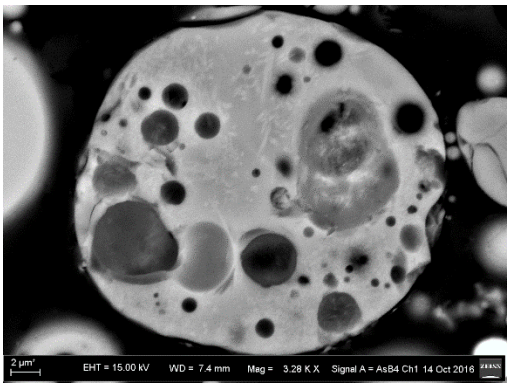

(e) FA3

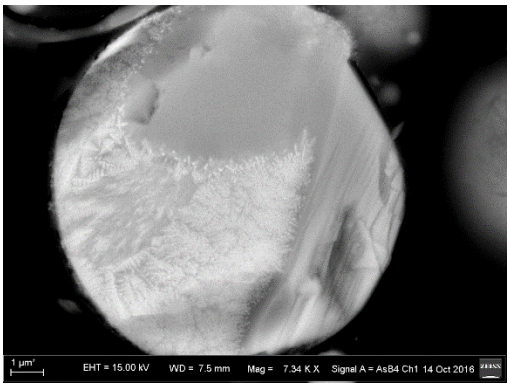

(f) FA3

Fig. 4.9 BSE image of typical crystal-amorphous particle of fly ashes studied

Rather than grey levels, element analysis method is more feasible and practical to distinguish different mineralogical phases because different crystalline and amorphous phases have different chemical compositions. For example, quartz (SiO_2) and mullite ($3Al_2O_3{\cdot}2SiO_2$) generally have higher Si content and Al content than common amorphous solid. Therefore, if a reasonable segmentation criteria of mineralogical phases is built, taking advantage of the SEM-EDS elements mapping result mentioned in last section, we could identify and quantify the amorphous phases within fly ash particles. A tentative work had been done by Chancey et al. They tried to characterize and quantity the mineralogy phases of siliceous fly ash by SEM-EDS. However, this method is entirely based on the software itself segmentation algorithm without any orientations, which limits control over the analysis and may have unexpected influence on the results[9]. Therefore, this section is going to to build a reasonable and practical segmentation criteria among these different phases based on material properties and knowledges we had known.

4.3.2.2 Segmentation criteria of mineralogical phases

Because fly ashes are both heterogeneous in chemical and mineralogical properties and the resolution of EDS is limited (around 1 μm), the result of EDS analysis is usually different from the ideal conditions. Therefore, it is impractical and improper to directly build the segmentation criteria by the standard chemical composition of crystal solids. Considering this situation, the method used in this study is first to find out the representative phases in SEM and then analyze their chemical composition by EDS. Based on these analysis result, a

segmentation criteria was further built on the characteristic element distribution of different phases. Since the major crystal phases in these three studied siliceous fly ash are mullite ($3Al_2O_3 \cdot 2SiO_2$), quartz (SiO_2), magnetite (Fe_3O_4) and lime (CaO), the segmentation criteria on crystalline phase are just focus on these crystalline phases this time. All the SEM-EDS mapping analysis therefore will be discussed in the Al-Si-Ca-Fe system as well.

(a) Segmentation criteria on quartz, magnetite and lime

As motioned before, amorphous phases are the solids lack of systematic structural arrangement and their chemical compositions usually varies in a certain range. In contrast to amorphous phases, crystalline solids have repeated atoms arrangement and their chemical compositions are more unique and concentrated.

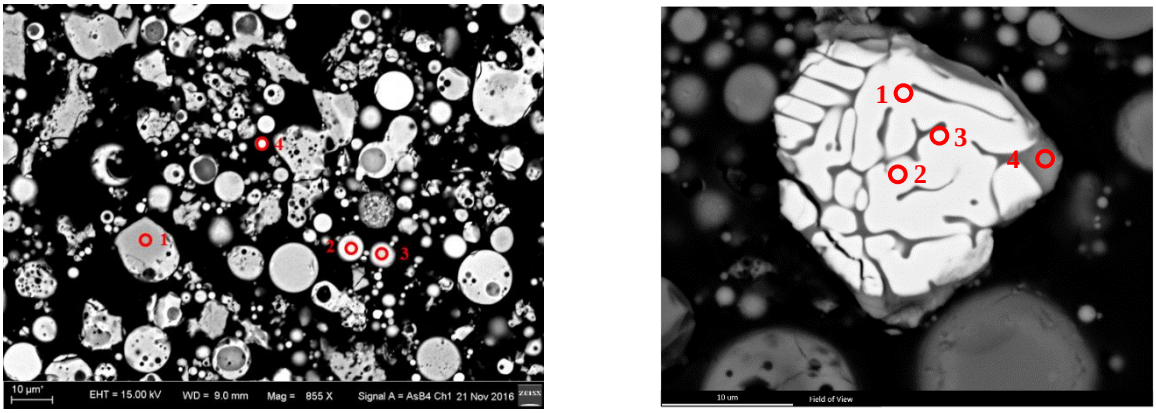

(a) quartz and amorphous solid (b) magnetite and amorphous solid

Fig. 4.10 BSE images with different amorphous and crystalline solids

Fig. 4.10 (a) and (b) are the reprehensive BSE images that amorphous solids and quartz solids and magnetite solids respectively. Table. 4.7 and Table. 4.8 are the EDS analysis result of these solids. It can be seen that the atomic ratio was significant different between amorphous and crystalline solids. The Si atomic ratio of quartz was up to 98.5% but amorphous solids are just around 60%. Similarly, the Fe atomic ratio of magnetite is also significant higher than the amorphous solid (see Table. 4.8). Therefore, quartz, magnetite and lime can be distinguished by their reprehensive elements contents (i.e. Si, Fe and Ca) respectively.

Table. 4.7 EDS analysis result of quartz and amorphous solid in Fig. 4.10 (a) (at. %)

	Phase	Al (at. %)	Si (at. %)	Ca (at. %)	Fe (at. %)	Other (%)
Point 1	Quartz	——	98.50	1.50	——	0.00
Point 2	Amorphous	24.11	57.88	1.93	7.38	8.70
Point 3	Amorphous	25.90	63.00	1.88	2.22	7.00
Point 4	Amorphous	27.54	63.14	3.34	4.67	1.31

Table. 4.8 EDS analysis result of magnetite and amorphous solid in Fig. 4.10 (b) (at. %)

	Phase	Al (at. %)	Si (at. %)	Ca (at. %)	Fe (at. %)	Other (%)
Point 1	Magnetite	4.63	6.57	2.04	81.70	5.06
Point 2	Magnetite	4.80	2.09	0.94	89.12	3.05
Point 3	Magnetite	3.90	4.80	0.73	85.33	5.24
Point 4	Amorphous	11.11	44.99	18.80	14.57	10.53

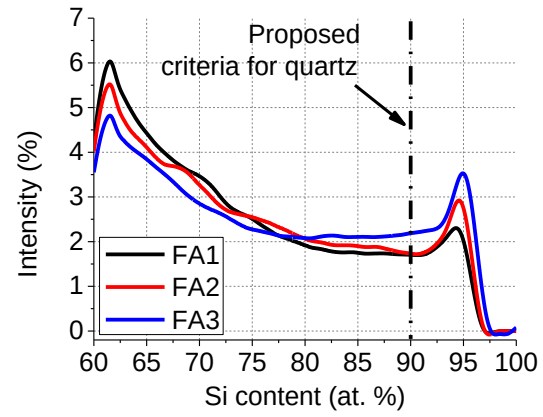

(a) Si element content distribution

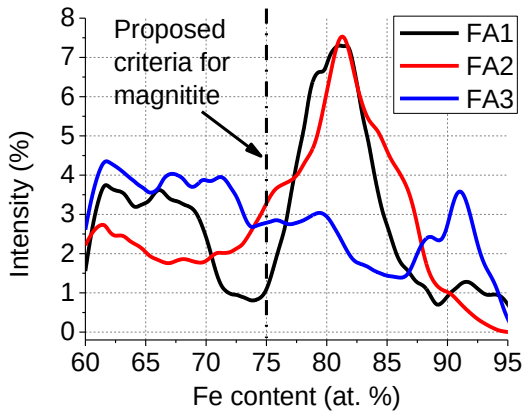

(b) Fe element content distribution

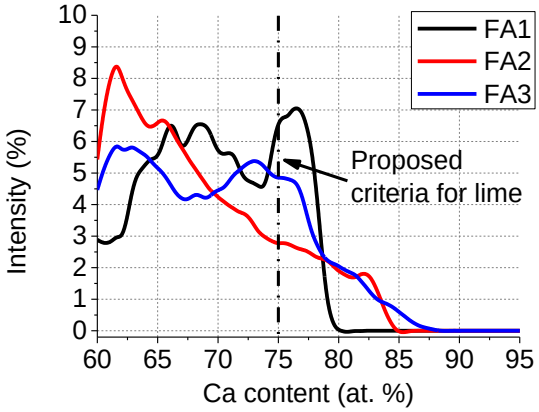

(c) Ca element content distribution

Fig. 4.11 Proposed segmentation criteria for crystalline phases based on element distributions

To find out the proper criteria, the normalized distribution of elements (the normalized

region is from 60 ~ 100 % of interested element) on Si, Fe, Ca were studied and illustrated in Fig. 4.11. It can seen from Fig. 4.11 (a) that the there is a characteristic peak over 90% of silicon in all three fly ashes, which is very likely contributed by crystalline quartz. Generalizing this idea to magnetite and lime, it was also found that a characteristic peak also appeared after 75% of Fe element distribution, which is very likely contributed from magnetite (see Fig. 4.11 (b)). Due to the low content of lime, the characteristic peak of crystalline lime is not so obvious in Ca element distribution compared to quartz and magnetite but we still find a peak around 75% of Ca in FA1 (Fig. 4.11 (c)). Therefore, in this study, the 90% of Si, 75% of Fe and 75% of Ca was proposed for the segmentation of crystalline quartz, magnetite and lime respectively.

It is noted that element content of characteristic peak of quartz is higher than lime and magnetite. That might because that these elements, such as, calcium, iron, sodium, and potassium, act as fluxing agents and facilitate the melting of the constituents at lower temperatures, resulting in higher proportions of amorphous material upon cooling [19]. Therefore, crystalline lime and magnetite usually co-melts with other amorphous material and the purity is consequently lower than crystalline quartz.

(b) Segmentation criteria between semi-mullite and mullite

Mullite is a crystalline compound in siliceous fly ash. Although it has considerable amount in all fly ashes, the situation is far more complicated than previous crystalline solids because most mullite exists as a small solid and widely distributes in fly ash particles. Fig. 4.12 is the BSE image of two common particles with abundant small mullite solids found in FA2 and FA3. Apparently this kind of particles cannot be simply separated form pure amorphous and mullite phase. Therefore, a transitional phases, between pure mullite and amorphous alumino-silicate (Al-silicate), the semi-mullite phases (e.g. point 5 at Fig. 4.12 (a)) were proposed herein for distinction. Although it is difficult to measure the accurate atomic ratios of these phases since resolution of EDS is limited (0.5~1μm, see Fig. 4.2), it still can be seen from Table. 4.9 that the Al atomic ratio of the typical mullilte solids is significantly higher than amorphous solids.

Therefore, the SEM-EDS mapping analyses were carried out on these two particles to find out a proper segmentation criteria between semi-mullite and amorphous Al-silicate. The SEM-EDS mapping field view of these particles was 34×27 μm. The image resolution was

512×400 and then pixel size was 0.67×0.67 μm. Other parameters were used the same ones mentioned in section 4.2.2.1. To eliminate the influence of other irrelevant solids, the nearby particles and background (i.e. grey level <=50) were masked during data analysis, as shown in Fig. 4.13.

Table. 4.9 EDS analysis result of fly ash particle with crystalline mullite solids (at. %)

	Phases	Al	Si	Ca	Fe	Other
Point 1	Al-silicate	33.96	60.65	1.33	3.02	1.04
Point 2	Al-silicate	30.51	63.41	1.54	2.86	1.68
Point 3	Al-silicate	33.35	61.44	2.33	2.07	0.81
Point 4	Al-silicate	32.18	62.70	3.22	1.02	0.88
Point 5	Semi-mullite	43.52	49.37	1.73	1.43	3.95
Point 6	Semi-mullite	45.24	48.91	2.31	1.22	2.32
Point 7	Semi-mullite	47.31	46.11	1.67	2.56	2.35
Point 8	Semi-mullite	42.38	50.66	2.34	2.01	2.61

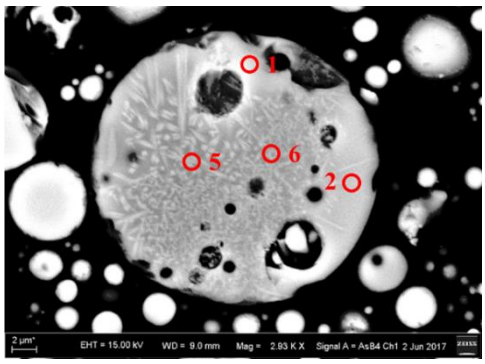

(a) particle found in FA2

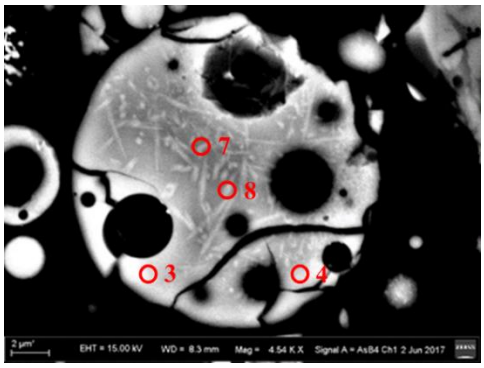

(b) particle found in FA3

Fig. 4.12 Selected particles with crystalline mullite solids for SEM-EDS mapping analysis

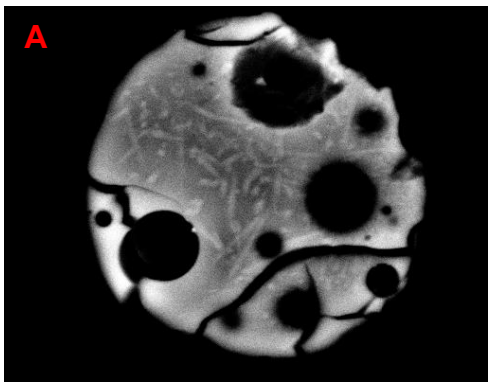

(a) particle found in FA2

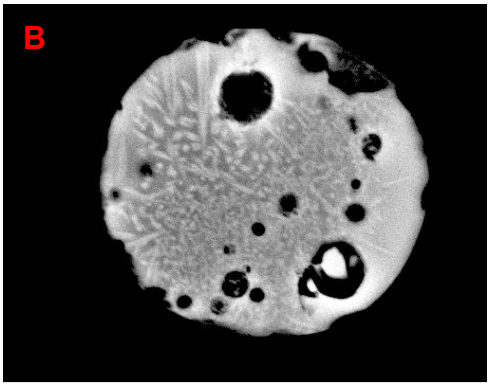

(b) particle found in FA3

Fig. 4.13 Masked image of selected particles with crystalline mullite solids

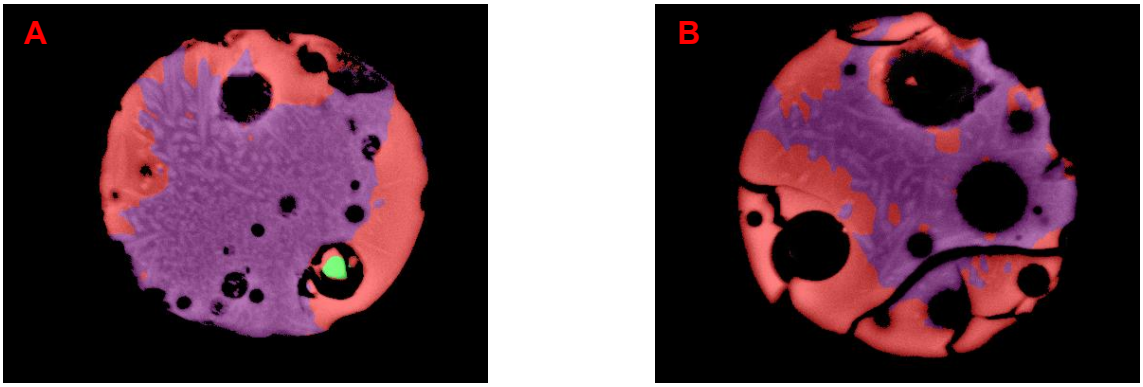

(a) particle found in FA2 (b) particle found in FA3

Fig. 4.14 Solids mapping result of selected particles with crystalline mullite solids

The element Al distributions of these two particles are provided in Fig. 4.15. It can be seen that there is a characteristic peak over 35% of Al in both two particles. Referring to point analysis in Table. 4.9, this peak is very likely to represent the solids of semi-mullite. Therefore, the 35% of Al content was used for segmentation criteria between amorphous Al-silicate and semi-mullite. Based on this criteria, the amorphous Al-silicate (red) and semi-mullite (violet) were satisfactorily distinguished, as shown in Fig. 4.14. It is also interesting to find out that there is quartz solid (green) existed in Fig. 4.14 (a) too.

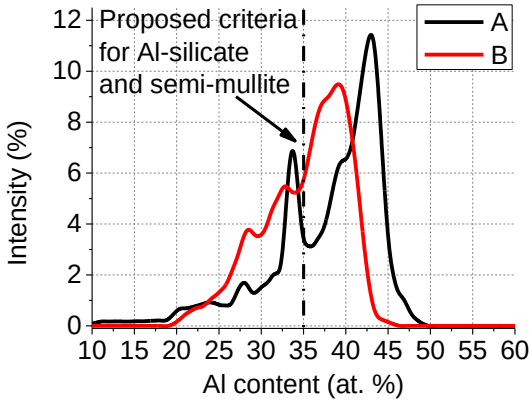

Fig. 4.15 Proposed segmentation criteria between Al-silicate and semi-mullite

The next issue is about pure mullite. Although it is still very difficult to find out the pure mullite solid to be analyzed since it usually mixed with amorphous Al-silicate solids, recent research points out that it displays various Al to Si ratios (referring $Al_{4+2x}Si_{2-2x}O_{10-x}$, with x ranging between about 0.2 and 0.9) and its Al atomic ratio is not less than 73.33%[48]. Therefore, solids would be considered as crystalline mullite if its Al atomic ratio is over 70% in this study.

(c) Segmentation criteria on amorphous silicate and amorphous Al-silicate

All crystalline phases segmentation criteria had been studied in previous sections and this section is going to discuss the classifications of amorphous solids. In previous researches, Durdziński et al. proposed that the amorphous solids of siliceous fly ash can be classified by amorphous silicate and amorphous Al-silicate [24]. Later on, they further proved that these two amorphous solids have different reactivity by examining the initial dissolution rates of the synthetic glasses in alkaline condition [28]. Therefore, these classifications for amorphous solids were also used in this study for discussions.

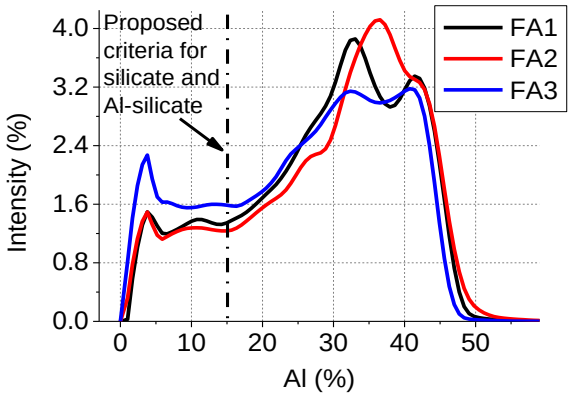

Fig. 4.16 Proposed segmentation criteria between amorphous silicate and Al-silicate

The normalized distribution of element Al is showed in Fig. 4.16. It can be seen that some characteristic peak appear after 15% of Al, which is likely contributed by Al-silicate and semi-mullite. The 15% of Al was therefore used the segmentation criteria for the amorphous silicate and Al-silicate, which is also similar to the segmentation criteria proposed by Durdziński [24].

4.3.2.3 Mineralogical phases segmentation mapping result and discussions

Summarizing the discussions in section 4.3.2.2, all segmentation criteria is listed in Table. 4.10 and further schematically illustrated in ternary element plot Fig. 4.17.

Table. 4.10 Segmentation criteria on different mineralogical phases (at. %)

Phases	Al (at. %)	Si (at. %)	Ca (at. %)	Fe (at. %)	Color
Silicate	≤15	<90	<75	<75	
Al-silicate	15～35	<90	<75	<75	
Semi-mullite	35～70	<90	<75	<75	
Mullite	≥70	<30	<30	<30	
Quartz	<10	≥90	<10	<10	
Magnetite	<25	<25	<25	≥75	
Lime	<25	<25	≥75	<25	

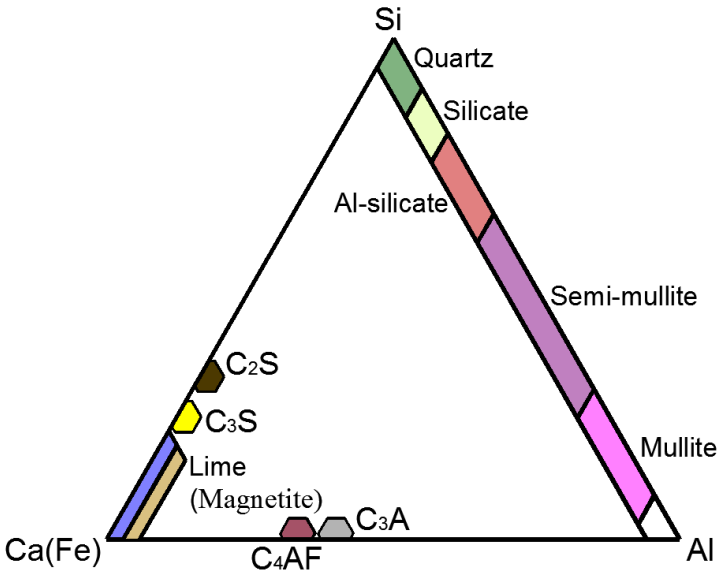

Fig. 4.17 Illustration of the segmentation criteria among different mineralogical phases

Based on this segmentation criteria and SEM-EDS data, different mineralogical phases were distinguished from SEM-EDS analysis. Table. 4.11 is the area fraction of different mineralogical phases determined by SEM-EDS mapping. According to fundamental stereology (Delesse's principle), the volume fraction of each type of phases approaches its corresponding area fraction. Given area fraction of different solids is already known (see Table. 4.11), the mass faction can be further determined if the specific gravities of different phases are known. Since the specific gravities of crystalline phases and fly ashes are known (see Table. 4.12), if we simply assumed densities of amorphous silicate, Al-silicate and semi-mullite are all same considering the atomic weight of Al and Ca are close, the mass fraction of different solids can be determined according to the area fraction (Table. 4.11).

Table. 4.11 Area fractions of different phases determined by SEM-EDS mapping analysis (%)

	Amorphous silicate	Amorphous Al-silicate	Semi-mullite	Mullite	Quartz	Magnetite	Lime
FA1	10.94	48.70	33.92	0.00	6.36	0.06	0.01
FA2	10.47	45.38	37.28	0.03	6.40	0.38	0.06
FA3	13.85	46.60	29.83	0.04	9.48	0.12	0.09

Table. 4.12 Specific gravities of crystalline phases and fly ashes

Mullite	Quartz	Magnetite	Lime	FA1	FA2	FA3
3.05	2.65	5.18	3.35	2.23	2.29	2.29

Table. 4.13 summarizes the mineralogical phases contents determined by SEM-EDS mapping analysis. The result of XRD-Rietveld analysis is also listed for comparison. A good agreement can be found on this table among quartz, magnetite and lime. It demonstrates that the proposed SEM-EDS mapping method can be used to characterize the mineralogical properties of a fly ash. However, for the crystalline mullite, the content in SEM-EDS mapping is significant smaller than XRD-Rietveld analysis and almost close to zero. That is because mullite exists as a small solid and widely distributes in fly ash particles (see Fig. 4.12). Therefore, EDS categorizes them into semi-mullite phase.

Table. 4.13 Mineralogical phases contents determined by SEM-EDS mapping analysis and the comparison with XRD tests (wt.%)

Phases	FA1		FA2		FA3	
	SEM-EDS	XRD	SEM-EDS	XRD	SEM-EDS	XRD
Total amorphous	80.88	81.07	85.16	87.90	73.35	73.03
Silicate	10.79	— —	10.30	— —	13.59	— —
Al-silicate	48.03	— —	44.64	— —	45.72	— —
Semi-mullite	33.46	— —	36.67	— —	29.27	— —
Mullite	0.01	11.40	0.05	6.49	0.05	15.28
Quartz	7.56	7.09	7.41	4.94	10.97	10.64
Magnetite	0.14	0.43	0.85	0.61	0.26	0.82
Lime	0.02	0.02	0.08	0.06	0.13	0.24

To further investigate the mineralogical properties of these three fly ashes, the SEM-EDS data was re-mapped back to BSE images, as shown in Fig. 4.18. The representations of image color can be found in Table. 4.10. These re-mapping images satisfactorily illustrate the detailed assembly of different mineralogical phases of fly ashes, which provides us a new way to further observe fly ash and then distinguish different phases in a micro-scale.

These re-mapping figures clearly show that fly ash particles are complicated mixtures of different mineralogical phases. More specifically, crystalline mullite usually exists as a small solid and widely distributes in amorphous Al-silicate solids. The reason is because mullite is the crystallization product of Al-silicate amorphous solids[19]. Since the combustion and cooling processes is very complicated in furnace, local crystallization commonly occurs inside Al-silicate amorphous solids and some Al-silicate amorphous solids would crystallize to mullite and finally remained inside particles (Fig. 4.19).

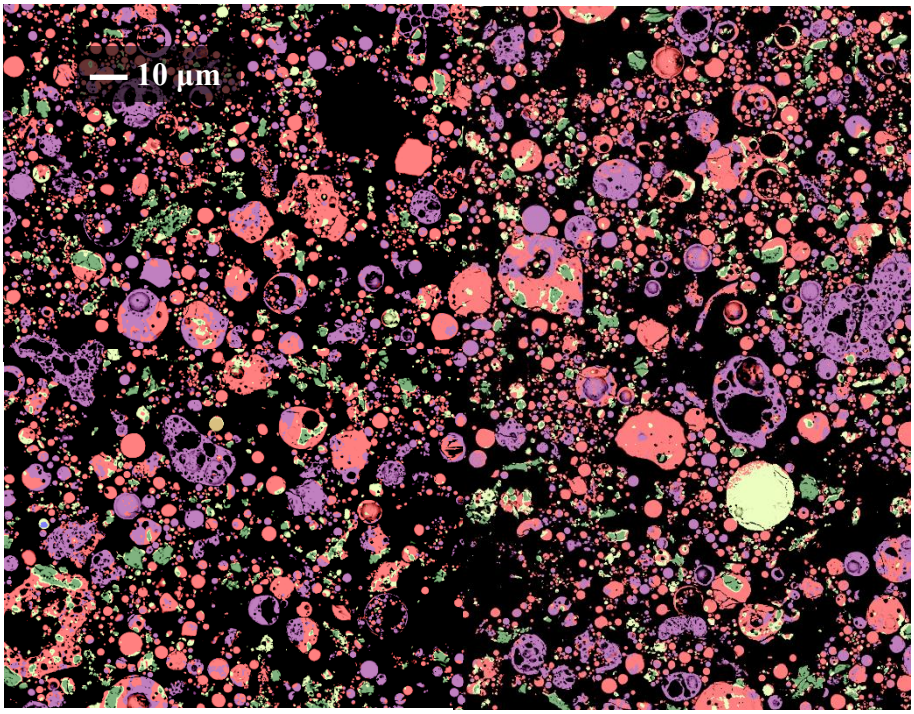

(a) Mineralogical mapping result of FA1

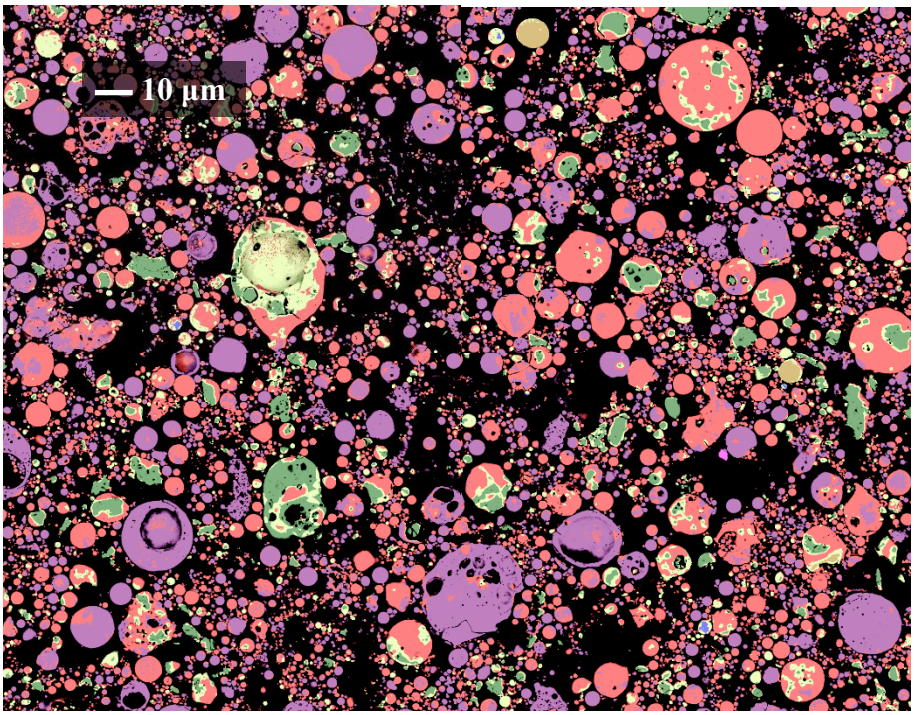

(b) Mineralogical mapping result of FA2

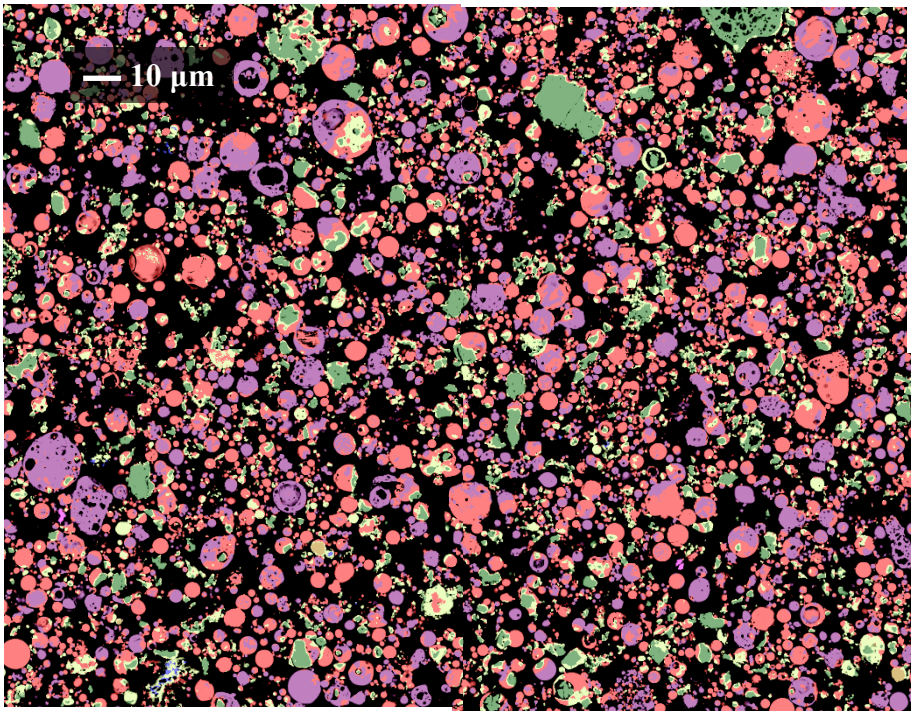

(c) Mineralogical mapping result of FA3

Fig. 4.18 Mineralogical mapping result of fly ashes

Compared to mullite, quartz tends to exist along and and it is usually covered by amorphous silicate. That is due to quartz is not crystalized from Al-silicate amorphous solids. Actually, quartz is the only crystalline phase in fly ash which comes from the parent coal. It is estimated that only 75% of quartz reaches melting temperature in the furnace and the remaining inside crystalline quartz keeps just intact since the combustion temperature is not enough high [18]. Therefore, the outside part of quartz is melted and becomes amorphous silicate and finally cover the inside crystalline quartz core, as shown in Fig. 4.19.

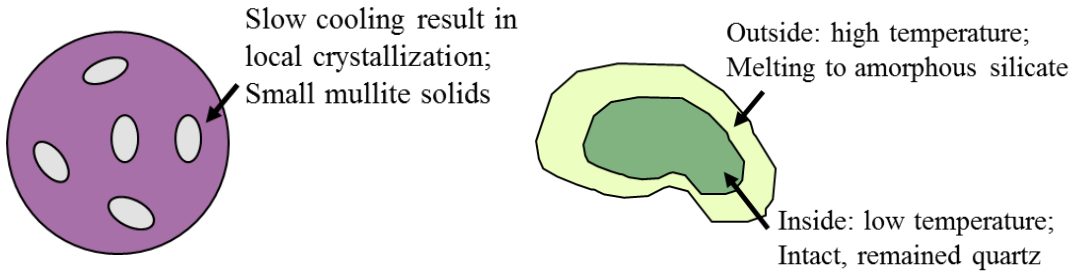

(a) mullite and Al-silicate (b) Quartz and silicate

Fig. 4.19 Illustrations on formation mechanism of crystalline phases

4.4 Fly ash specific surface area

The specific surface area (SSA) or particle size distribution (PSD) is a complementary parameter that provide information about the fineness of a power. It is, after the chemical and mineralogical properties, the main charactering property of a fly ash that influence the reaction kinetics of a fly ash, the rheology of a cement pastes and finally the performance of a concrete. Therefore, an accurate and reliable measurement of specific surface area is essential to characterize its fly ash material properties and it will be studied in this section.

4.4.1 Conventional test methods

4.4.1.1 Blaine air permeability test

The Baline air permeability test is the most widely used method to determine the specific surface area of a powder in cement industry. In this study, the Blaine air permeability tests were conducted by fly ash providers and the result is shown in Table. 4.14.

Table. 4.14 Specific surface area of fly ash measured by Blaine air permeability test (cm^2/g)

FA1	FA2	FA3
3940	3730	4070

4.4.1.2 Laser diffraction test

The laser diffraction test (LD) is another common method to determine the specific finesse of a powder in cement industry. In this study, the particle size distribution of fly ashes was measured by Mastersizer 3000 (Malvern Instruments) at SUSTech.

The powders were first dispersed in alcohol by ultrasonic bath. After that, this suspension was placed into a sample cell and irradiated by a laser beam. The diffracted beams on particles were continuously recorded by laser detector. Based on optical model, the particle size distribution can be deduced by laser signal. In this test, Mie optical model (i.e. Eq. (4.1)) was adopted:

$$m = n - ik \tag{4.1}$$

where n is the real component and k is the imaginary component. In this test, the real component n was determined by the normalized mass fraction of Al_2O_3 and SiO_2 of the specific fly ash. The imaginary component k and the refractive index of alcohol is used 0.1 and 1.360 respectively.

Table. 4.15 Real components n used for laser diffraction test

Item	Al_2O_3	SiO_2	n
FA1	23.99	76.01	1.534
FA2	26.06	73.94	1.541
FA3	23.67	76.33	1.533

Note: 1. The normalized mass fraction of Al_2O_3 and SiO_2 was determined by the result of XRF tests (Table. 4.1).

2. The real component of Al_2O_3 and SiO_2 was 1.77 and 1.46 respectively.

Fig. 4.20 is the result of particle size distribution and cumulative volume size distribution for test fly ashes. According to PSD result, the theoretical geometrical specific surface area (SSA) can be calculated by Eq. (4.2):

$$SSA_{LD} = \frac{1\times10^4 \times F}{\rho} \sum \frac{6f}{d} \tag{4.2}$$

where: f is the volume fraction of grains whose diameter is d (μm) and ρ is density (g/cm^3) and F is an empirical correction factor 1.13 to consider the article and surface shape[49]. The theoretical geometrical specific surface areas of test fly ashes were determined and listed in Table. 4.16.

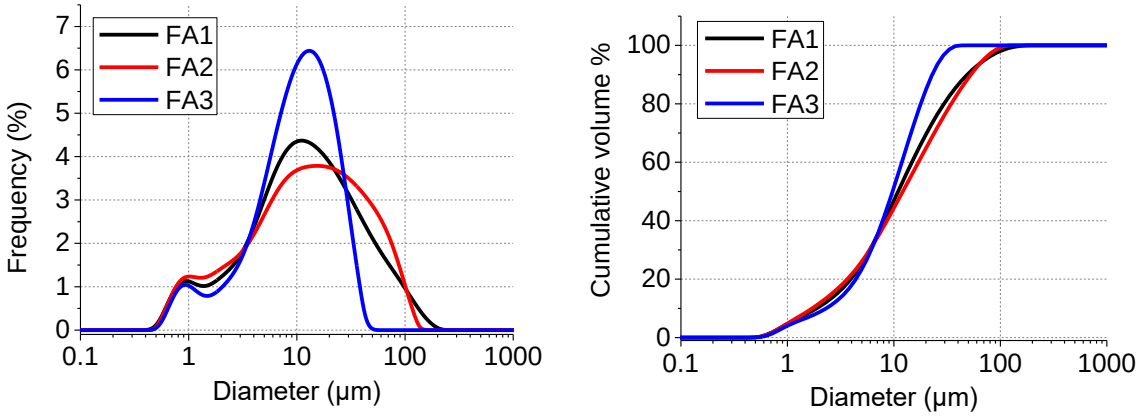

(a) particle size distribution (b) cumulative volume of size distribution

Fig. 4.20 Laser diffraction test result

Table. 4.16 Specific surface area of fly ash measured by laser diffraction test (cm^2/g)

FA1	FA2	FA3
5893	5803	5567

4.4.1.3 Nitrogen absorption test

The specific surface area can be determined by Bliane air permeability and laser diffraction test. However, these two methods often suffers strong criticisms from academics on their improper assumption that particles are all perfectly sphere solid, especially for fly ash whose particles are usually irregular, porous and cracked (e.g. Fig. 4.4). In contrast, academics tend to prefer nitrogen adsorption tests because of their more fundamental basis [30]. Therefore, the nitrogen absorption tests were also conducted in this study for comparison. These tests were carried out by ASAP 2020 Plus Physisorption (Micromeritics) at SUSTech as well.

Nitrogen was used in this test as adsorbate gas because its size is close to water molecule. Before measurement, samples must be degassed to remove physisorbed molecules so that the nitrogen can directly interact with the sample along its small cavities. In this test, fly ashes powders (around 2 g) was vacuum degassing at 40 °C for 24 hours. After that, the powder was cooled down to cryogenic temperature (-196 °C) and a known amount of pure nitrogen (99.9%) was continuously added into sample cell. During this time, the adsorption and desorption isotherm was recorded by machine. Based on the the BET theory, the adsorption isotherm was used to determine the SSA through Eq. (4.3)

$$SSA_{BET} = \frac{N_A V_m A_N}{V_o} \tag{4.3}$$

where: N_A is the Avogadro constant; V_m is the amount of gas needed to cover surface with a monolayer; V_0 is the molar volume of gas; A_N is the area of surface occupied by a single adsorbed gas molecule. For nitrogen, it is usually assumed as 16.2×10^{-20} m^2. The nitrogen absorption test result was listed in Table. 4.17.

Table. 4.17 Specific surface area of fly ash measured by nitrogen absorption test (cm^2/g)

FA1	FA2	FA3
12709	16475	8855

4.4.1.4 Comparisons and discussions

Table. 4.18 summarizes all the measurement result in previous sections. It can be seen that different methods gives different results and different fineness ranks among these three fly ashes. Blaine air permeability gives the lowest value of specific surface area, where the finest fly ash is FA3 and the coarsest one is FA2. Laser diffraction result is the medium one among these three methods but the finest fly ash is FA1 and the coarsest one is FA3. Compared to these two methods, nitrogen gas absorption test provides the highest value, where the finest fly ash becomes FA2 and the coarsest one is FA3.

Table. 4.18 Summary of specific surface areas determined by different methods (cm^2/g)

	Blaine's fineness	Laser diffraction	Nitrogen gas absorption
FA1	3940	5893	12709
FA2	3730	5803	16475
FA3	4070	5567	8855

(a) Laser diffraction

The Blaine air permeability test is the most common one in cement industry. However, this method suffers from various weakness and limitations. First, this method needs empirical calibration, which is highly influenced by the test operator. In addition, fly ash particles are not mono-sized and spherical solids that Blaine fineness assumes (e.g. Fig. 4.4) [30].

Compared to Blaine air permeability method, laser diffraction method is more reliable than Blaine air permeability method. This method does not depend on volumetric flow rate and the amount of particles and therefore it does not need any empirical calibration. However, this method still involves the assumption of the perfect spherical particle geometry as like as Blaine air permeability method used.

Moreover, laser diffraction method is significantly affected by material refractive index m (see Eq.(4.1)). Fig. 4.21 shows the PSD result of three fly ashes with different material refractive index (Model A: the parameters are same to the ones in section 4.4.1.2; Model B: n = 1.61, k = 0.1). Table. 4.19 compares the specific surface are of fly ashes determined by these different material refractive index. It can be seen that the PSD result of Model A estimates the fly ashes to have a higher fineness than Model B. A similar result is also found in the work of Arvaniti et al. [29]. As we know, fly ashes are intrinsically heterogeneous in chemistry and

mineralogy, therefore, it is controversial to use one constant parameter in laser diffraction test even we take the bulk chemical composition into account (e.g. Table. 4.15).

Table. 4.19 Comparison of specific surface area of fly ashes determined by different material refractive index

	FA1	FA2	FA3
Model A	5893	5803	5567
Model B	4755	5435	4848
Comparison	1.24	1.07	1.15

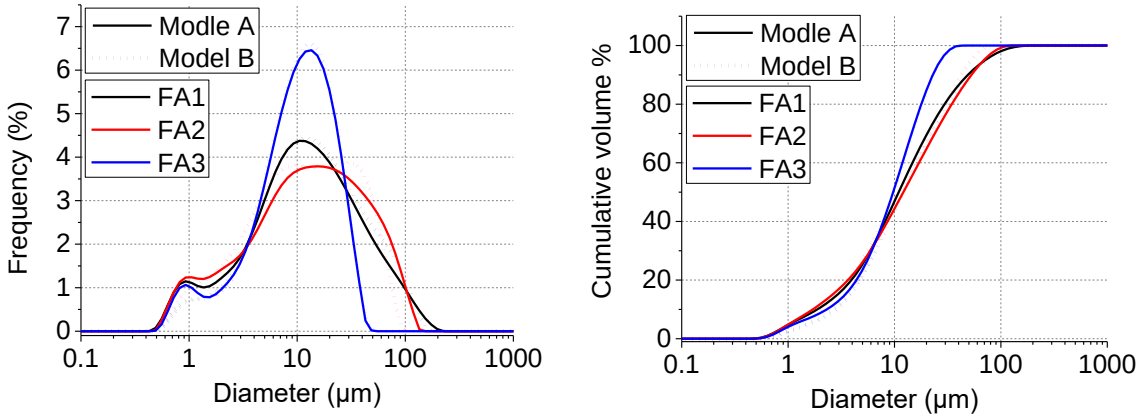

(a) particle size distribution (b) cumulative volume of size distribution

Fig. 4.21 Comparison between two refractive models

(b) Nitrogen gas absorption

In contrast with Blaine method and laser diffraction method, the gas absorption method does not postulate any assumptions on material properties and it can consider irregularities and porosity of particle, therefore, this method is usually preferred by academics. However, the accuracy of this method highly depends on the degassing condition and material itself purity. For fly ashes, the by-product of coal combustion in thermal power plant, it always contains unburned carbon such kind of porous material that has much higher surface area (e.g. 1×10^6 ~ 4×10^6 cm^2/g) [50] than fly ashes (3000 ~ 6000 cm^2/g). Therefore, even there is a slight amount of carbon existed in fly ashes (e.g. 0.5%), the nitrogen gas absorption method may result in a significant overestimation on SSA of fly ashes because nitrogen can assess any types of micro-pores, including unburned carbon. Table. 4.20 shows a comparison between laser diffraction

and nitrogen gas absorption. It can be seen that Nitrogen gas absorption method does give a higher estimation on SSA than laser diffraction and this overestimation is proportional to the carbon content which is determined by XRF test as well.

Table. 4.20 Comparison of SSA between laser diffraction and nitrogen gas absorption

Item	Laser diffraction (1) (cm^2/g)	Nitrogen absorption (2) (cm^2/g)	Comparison (2)/(1)	Carbon content (wt. %)
FA1	5893	12709	2.16	4.43
FA2	5803	16475	2.84	5.56
FA3	5567	8855	1.59	2.89

To further investigate the carbon effect on nitrogen gas absorption method, two additional series test were conducted in this study. One series was high temperature degassing that samples were degassed at 350 °C for 3 hours. This temperature usually is the starting point of decomposition of carbon [50]. The other series was water washing. The fly ashes samples were first immersed into water. The floated material above water was taken away to remove the unburned carbon. The precipitate fly ash powders was collected again and dried under vacuum for 1 days. After that, these precipitate fly ash powders was degassed at the same conditions as descried in section 4.4.1.3.

Fig. 4.22 shows the comparison of nitrogen gas absorption tests among these different test conditions. It can be seen that high temperature degassing gives a higher estimation of specific surface area compared to room temperature degassing. That reason is that the unburned carbon decomposed at high temperature and some pores appeared on carbon surface resulting in a high surface area (see Fig. 4.23). Another possible reason may be that samples somewhat expend at high temperature degassing and then the surface area increases.

However, it is interesting to find that the specific surface area of fly ash also increased after water washing. In the washing series, unburned carbon actually cannot be completely removed and a lot of carbon still remained. With regard to the remaining unburned carbon, its exposed surface unexpectedly increased since the originally attached particles were washed out by water, as shown in Fig. 4.24. Thus the measurement result increased.

In conclusion, the unburned carbon inside fly ashes has a significant effect on nitrogen gas absorption method and this method is not suitable to determine the fineness of a fly ash.

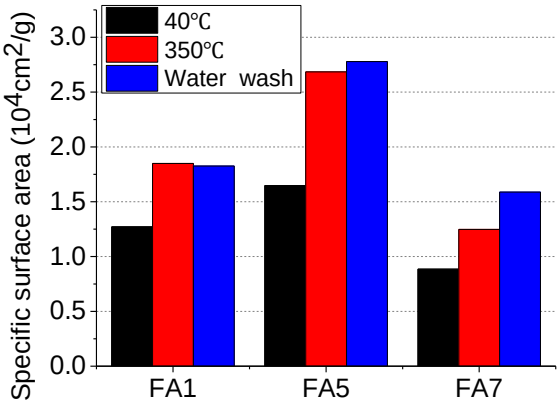

Fig. 4.22 Comparisons among different test conditions

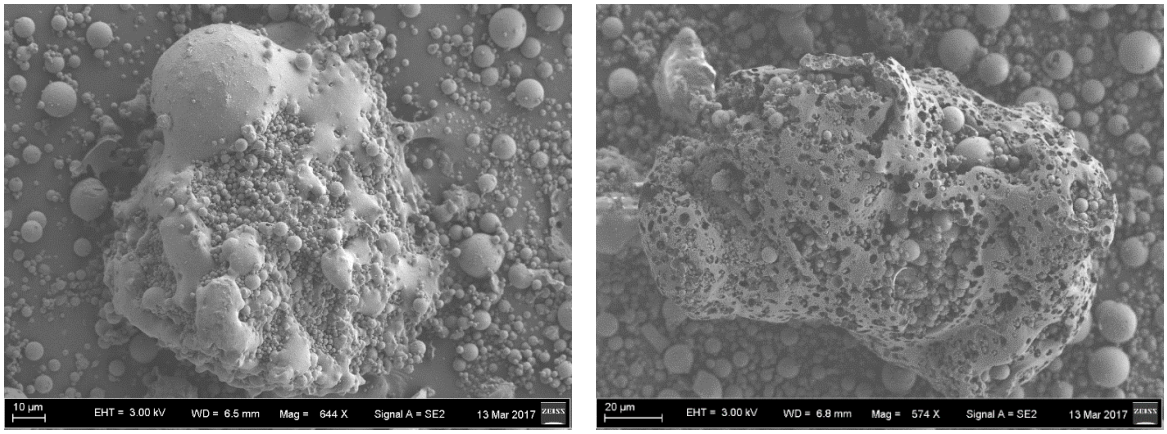

(a) before heating at 350 °C (b) after heating at 350 °C

Fig. 4.23 SE Images of fly ash particles before heating and after heating

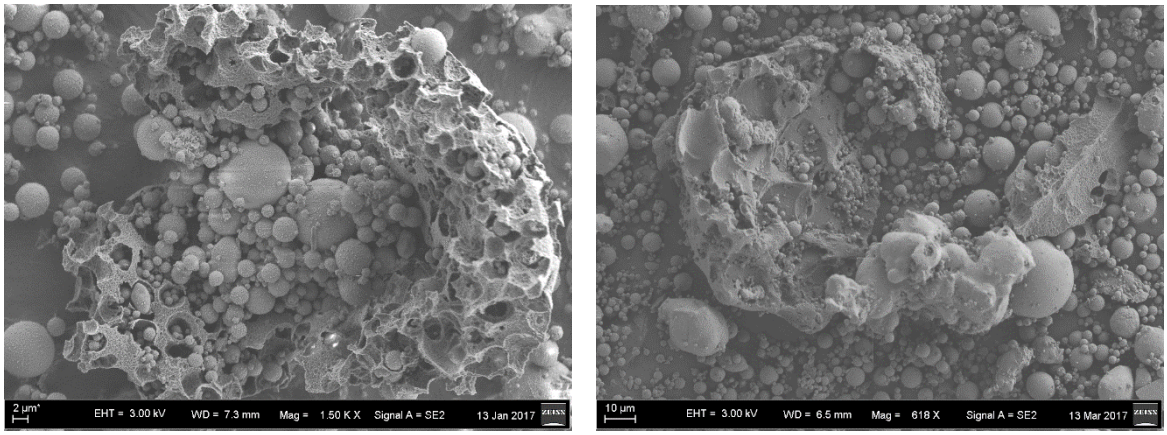

(a) before water washing (b) after water washing

Fig. 4.24 SE Images of fly ash particles before water washing and after water washing

4.4.2 Image analysis

4.4.2.1 Introduction

As described in last section above, conventional methods all have their drawbacks on estimation of specific surface area of a fly ash. Blaine air permeability method is semi-empirical and assumes all particles are perfectly spherical solid. Compared to Blaine air permeability method, laser diffraction does not need any empirical calibration but it still cannot consider different particle geometries. In addition, the accuracy and reliability of this method depends on material refractive index and therefore it is not suitable for heterogeneous material, like fly ash. Nitrogen gas absorption method is the most sophisticated but it is very sensitive to degassing condition and material purity. This method is therefore not suitable to fly ash such kind of material usually contains unburned carbon. At last but not least, it had been shown that fly ashes have different composition groups and particles are composed of multiple phases. Therefore, all above conventional methods accordingly fail to identify these multiple phases and quantity their specific surface areas as well.

To solve all the drawbacks described above, an image analysis method based on SEM-EDS mapping result is developed to determine the specific areas of different phases in this study. This method has serval advantages as follows. First, it is a direct visual analysis method compared to other conventional methods. Therefore, it can consider any cracks, crevices, pores and geometrical shapes and it will be not affected by material chemical composition as well. Second, carbon is usually considered as background and almost invisible in BSE image due to its light atomic number and the weak signal in BSE. Therefore, the influence of carbon can be easily eliminated by background masking in post-data process. At last, based on the analysis result of mineralogical phase identification, this method can be easily extended to be applied for different phases and further quantity their specific surface areas. Therefore, this section is going to explain how to develop the image analysis method based on SEM-EDS mapping to determine the specific areas of different phases.

4.4.2.2 Algorithm of image analysis

As discussed before, fly ash particles are composed of multiple phases and it have pores,

crevices and crack as well. Therefore, the essential point of image analysis it how to successfully identify the external boundary, internal boundary and phase boundary, as shown in Fig. 4.25.

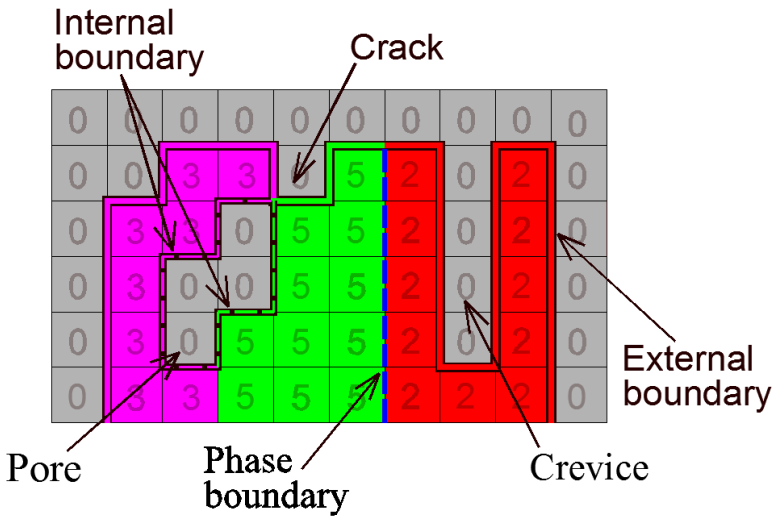

Fig. 4.25 Illustration of edge classification in image analysis

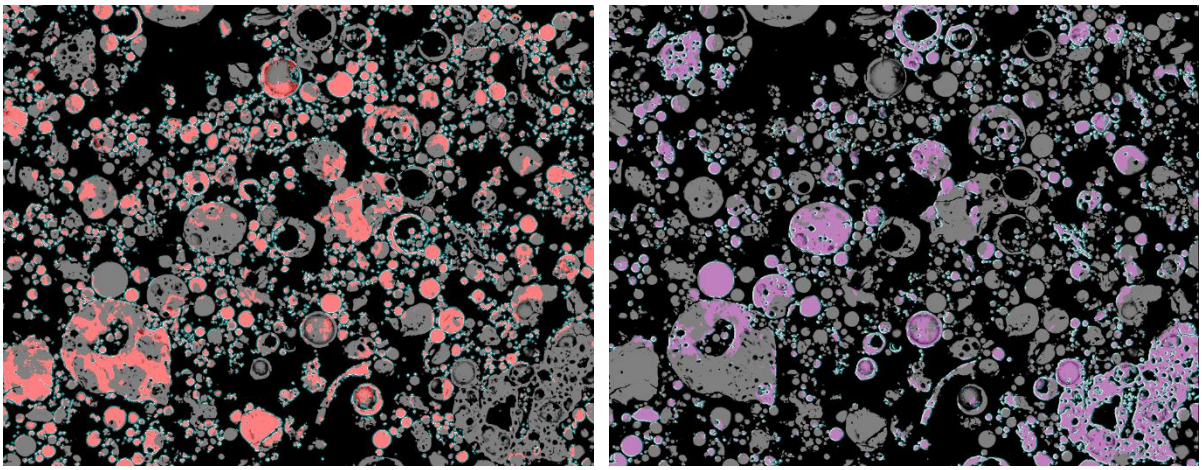

(a) Al-silicate (b) semi-mullite

Fig. 4.26 Detected boundaries of Al-silicate and semi-mullite of FA1

This can be easily solved by edge classification based on SEM-EDS mapping analysis. Because different mineralogical phases had been already identified, every element in the pixel matrix can be labeled with different numbers, for example, background as 0, Al-silicate as 2, semi-mullite as 3, quartz as 5, ,etc. With the help of these labels, we can easily determine

whether the edge of an element is an external boundary, internal boundary or phase boundary by checking the labels of connected elements and this boundary belongs to which phase, as shown in Fig. 4.25. Repeating this procedure to all elements of pixel matrix, all boundaries of a specific phase can be finally detected. Fig. 4.26 shows two cases of amorphous Al-silicate and smei-mullite of FA1 respectively. It can be seen that all external and internal boundaries were satisfactorily detected.

4.4.2.3 Image analysis results and discussions

If assuming the above statistical information are unbiased, the specific surface area of a phase SSA_{Img}^{I} can be determine through its density of boundary length of section area B_A^I with a constant value $4/\pi$ deduced by Smith and Guttman [51, 52]:

$$SSA_{Img}^{I} = \frac{4}{\pi\rho} B_A^I \tag{4.4}$$

Because the all element of pixel matrix had been known, the density B_A^I of phase *I* can be easily determined by the total the boundary length and area of phase *I* from image analysis, as Eq. (4.5) shows:

$$B_A = \frac{N_P^I}{N_A^I L_s} \tag{4.5}$$

where: N_P^I is the number of external boundary and internal edge belonged to phase *I*; N_A^I is the number of element belonged belonged to phase *I*; ρ is the density of fly ash and d_s is the edge length of pixel and is 0.236 μm in this study. It is noted that the phase boundary is not taken into account in this study because it is not exposed and then not contributed to the reactivity of fly ash.

Table. 4.21 Specific surface areas of different phase determined by image analysis (cm^2/g)

	Amorphous silicate	Amorphous Al-silicate	Semi-Mullite	Mullite	Quartz	Magnetite	Lime	Total
FA1	8810	8283	7400	6472	6036	2063	137	7894
FA2	5202	6510	5323	6099	2425	1298	1646	5648
FA3	6926	6296	4780	6967	3080	1897	9017	5623

Table. 4.22 Comparison of specific surface areas between laser diffraction and image analysis

	FA1	FA2	FA3
Image analysis (cm^2/g)	7894	5648	5623
Laser diffraction (cm^2/g)	5893	5803	5567
Comparison	1.34	0.97	1.01

Table. 4.21 summarized all specific surface areas of different phase determined by image analysis. The comparison between laser diffraction and image analysis is made in Table. 4.22 as well. It can be seen that image analysis gives the same ranking orders of SSA_{LD} and a good agreement between FA2 and FA3. However, image analysis gives a higher estimation of FA1. That is because FA1 is the most porous fly ash (see Fig. 4.4) and the correction factor F in Eq. (4.2) is not enough to cover the the shape effect introduced by cracks, crevices and pores. Therefore, Laser diffraction method gives an underestimation of FA1.

In conclusion, the image analysis gives the most reliable and detailed results of specific surface area of a fly ash.

4.5 Summary and conclusions

A comprehensive and accurate characterization of fly ash material properties is the essential point to understand the behavior of fly ash and its effect in cement systems. To achieve this goal, a phase segmentation criteria both considering chemical and mineralogical effect were proposed. Taking this segmentation criteria with SEM-EDS full element mapping analysis, the phase assemblage of the three siliceous fly ashes can be directly observed and quantitatively analyzed in a micro-scale now. At last, a new image analysis method was also proposed. With this new method, the specific surface area of induvial phase and the whole particles can be accurately estimated without the morphology influence. Based on these works, the conclusions of this chapter are summarized in the following points:

1. Siliceous fly ashes mostly composed of amorphous silicate and Al-silicate phases;

2. Fly ash particles are a complicated mixture of crystalline and amorphous solid;

3. Crystalline mullite usually exists as a small solid and widely distributes in fly ash particles. A transition phase semi-mullite was therefore proposed for distinction;

4. A new phase segmentation criteria based on SEM-EDS full element mapping analysis was developed in this study. This criteria both considers chemical and mineralogical effect. Experiment results showed that this proposed method can be used to characterize the mineralogical properties and distinguish different phases of a fly ash in a micro-scale; and

5. Experiment results showed that Blaine air permeability method, laser diffraction method and nitrogen absorption method all have their own drawbacks on estimation of fly ash fineness. Therefore, a new image analysis method based on mineralogical characterization was developed in this chapter. With this new image analysis method, the specific surface area of induvial phase and the whole particles can be accurately estimated without the morphology influence.

5 Temperature-dependent reactivity of fly ash in alkaline system

Contents:

5.1 Introduction 74
5.1.1 Sample preparation procedures 75
5.1.2 Experiment procedures of ICP measurement [55] 76
5.2 Temperature-dependent alkali dissolution test result 79
5.2.1 Element concentrations 79
5.2.2 Induvial composition dissolution process 81
5.2.3 Composite dissolution process 85
5.3 Microscopic evaluation on fly ash after alkali dissolution test 86
5.3.1 Dissolution mechanism of fly ash 86
5.3.2 SEM-EDS mapping result and discussions 89
5.4 Fly ash reactivity and its material properties 97
5.4.1 Introduction 97
5.4.2 Intrinsic reactivity of amorphous phase 98
5.4.3 Explanation on the reactivity variation of studied fly ashes 100
5.5 Summary and conclusions 100

5.1 Introduction

In chapter 4, comprehensive material characterizations had been carried out on the three different siliceous fly ashes, including chemical composition, phase assemblage and specific surface areas. Experiment result shows that these three fly ashes have different physical and chemical properties. Therefore, it is desirable to investigate how these material properties affect the reactivity of a fly ash.

There are several methods to study the reactivity of a fly ash. The chemical composition is usually used to indicate the fly ash reactivity. For example, hydraulic or basicity indices comparing the glass polymerization degree expressed as the amount of network modifying to network forming elements such as (CaO + MgO) / SiO_2 (EN197-1) are commonly used as normative requirements for slags or fly ashes [53].

Selective dissolution method is another commonly used techniques. It aims at dissolving the hydrates and the unhydrated clinkers without dissolving the unreacted fly ash. This allows a direct determination of the reaction degree of a fly ash in a hardened cement paste as the unreacted fly ash remains as residue and can be quantified [54]. However, these result are difficult to directly reveal the fly ash itself reactivity and to model its behavior in cement system because it goes through complicated reaction in cement system and it affects clinker hydration processes as well, like filler effect, etc.

A more theoretical approach to study the reactivity of a fly ash is to investigate the dissolution process by analyzing element content (e.g. Al, Si, Ca etc.) in a alkaline condition [13]. As the pozzolanic reaction of a fly ash can be considered as a series of coupled reactions involving dissolution of reactants and precipitation of products, analysis of the reaction kinetics as individual steps is instrumental in delivering a more fundamental understanding on fly ash reactivity [53]. Moreover, with the SEM-EDS mapping analysis, alkali dissolution test also facilitate the studying on kinetics parameters of induvial phase of a fly ash by examining their dissolution degrees.

Considerable works had bee done to establish the links between dissolution rates of a fly ash and its reactivity. Pietersen et al studied the dissolution rate of fly ashes in NaOH alkali conditions with with a pH ranging from 13.0 to 13.7 and temperatures between 20 and 40 °C

[12, 13]. Snellings studied the reactivity of synthesized calcium alumino-silicate glasses in NaOH solution (pH 13.0) [53]. Durdziński et al. study the chemical composition effect on glasses reactivity in alkaline conditions recently.

Therefore, this chapter is going to examine the reactivity of the three different siliceous fly ashes in alkaline conditions. The temperature-dependent effect will be investigated in different temperatures of 20 and 60 °C. The detailed kinetics parameters of induvial phase will be studied through observing its dissolution process with the help of SEM-EDS mapping analysis. It is hoped that these result could deliver a more fundamental understanding on fly ash reactivity and the modelling in cement systems.

5.1.1 Sample preparation procedures

To investigate the reactivity and temperature dependence of fly ash, three different types of fly ash were selected to measure their long term dissolution processes in NaOH solution at 20 and 60 °C. Material properties characterization on these three types of fly ash had been done in chapter 4.

To avoid any contamination, all experiment bottles, glass wares and pipettes were cleaned by detergent, nitric acid (2 mol/L) and deionized water three times successively before tests. Experiments were carried out in a 1500 mL polypropylene air-tight bottles. The NaOH solution (0.14 mol/L) was prepared with 5.6 g of analytical-grade NaOH in 1 L deionized water (18.2 MΩ×cm) that was decarbonated by boiling. The theoretical pH of this alkaline solution is 13.2 at 20 °C, which corresponds to pore solution of common portland cement paste. The batch of NaOH solution at high temperature was pre-heated to 60 °C by storing in an environment chamber of 60 ± 0.1 °C for 2 days in advance.

In the experiment day, around 0.5 g fly ash was added into the prepared NaOH solution of 1 L (i.e. water-solid ratio is 2000). Such a high water-solid ratio used in this test was to ensure far-from-equilibrium conditions and limit precipitation of hydrates during long term measurement. Then solutions were manually and gently stirred with a plastic spoon for around 15 seconds to make sure that fly ashes evenly deposited on the bottom of bottles and fully contacted with NaOH solution. After that, all bottles were stored in a curing room of 20 ± 2 °C

and an environment chamber of 60 ± 0.1 °C respectively.

At the designated sampling days (0.25~126 days), NaOH solutions were disturbed in advance by a plastic spoon from bottom to top to ensure the solution homogenous. These actions were carefully and smoothly taken to avoid any unwished abrasion of the bottom fly ash powders. Waiting for around 15 minutes until the suspended particles precipitated again, aliquots of 10 ml were sampled from NaOH solutions and stored in a small, polypropylene, air-tight bottles at 20 and 60° C, At last, 10 ml of the NaOH (0.14 mol/L) solution was added back again to keep the same volume in the reactor constant. The dilution effect was accounted for during data analysis.

5.1.2 Experiment procedures of ICP measurement [55]

The element aqueous concentrations in the samples collected in last sections cannot be directly measured by ICP because these raw samples have some problems as follows. First, these samples are high Na concentration solutions. The Na element is easily ionizable and it produces a strong wake flame in plasma, which makes other elements invisible and suppresses the signals, as shown in Fig. 5.1. Therefore, the content of elements interested in high-salt solution will be underestimated in ICP-OES due to this matrix interference of Na. Second, because solutions contains Ca ion, some calcium-silicate-hydrate (C-S-H) gel inevitably forms in long-term alkali dissolution test. These C-S-H gel cannot be detected by ICP and aqueous concentrations are consequently underestimated. At last but not least, the raw solution is alkali solution. It probably damages the glass apparatus of ICP machine, such as nebulizer, quartz and spray chamber if the raw solution is directly measured. Therefore, a proper ICP sample treatment method is desirable and indispensable as well to obtain an accurate element aqueous concentrations.

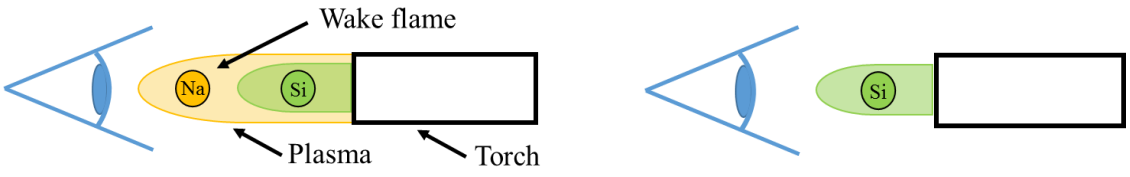

(a) high-salt solution (b) common solution

Fig. 5.1 Illustration of matrix interference of Na ion

To account of above problems a sample treatment method is developed in this chapter for ICP measurement. Portions of 2 ml of raw sample of 60 °C was taken and diluted 5 times with 8 ml nitric acid of 0.5 mol/L (for atomic absorption spectrometry grade) in a volumetric flask of 10 ml. Considering the element aqueous concentrations of samples of 20 °C is relatively lower, the dilution ratio for samples at 20 °C reduced by half, in other words, 4 ml of raw sample of 20 °C was diluted in 6 ml nitric acid of 0.5 mol/L. The advantages of these acidification procedures have fours: 1. to limit the matrix interference of Na by dilution; 2. to dissolved the C-S-H gel formed in the NaOH solution by nitric acid; 3 to stabilize the element condition for better measurement, like Al; and to change the pH of solution to avoid the potential damages on ICP glass apparatus. To limit the matrix interference effect, the radial viewing is adopted in this tests as well. Compared to axial viewing, this observation angel could significantly suppress the matrix interference introduced by ionizable ion and improve the accuracy and repeatability of measurement result in high-salt solutions due to its shorter interference region (Fig. 5.2). At last, to further consider the matrix interference, the matrix chemical proportions of calibration solutions was adjusted to same as the measurement sample by mixing different volume of NaOH solution and nitric acid, i.e. 20 ml NaOH of 0.14 mol/L mixed with 80 ml nitric acid of 0.5 mol/L for samples of 60 °C.

(a) axial viewing (b) radial viewing

Fig. 5.2 Comparison between axial and radial viewing

A verification experiment was conducted to confirm the reliability of above methods. Three verification samples were prepared by adding specific amount of element standard solutions into NaOH solution of 0.14 mol/L and storing at 20 and 60 °C for 1 day.

Corresponding details is listed in Table. 5.1. Following the proposed procedures, the element aqueous concentrations of verification samples were measured by ICP-OES (ICPS 7000 Shimadzu).

Table. 5.1 Details of verification samples

	Al (ppm)	Si (ppm)	Ca (ppm)	Temperature (°C)
Sample 1	5.00	10.00	5.00	20.0
Sample 2	0.50	1.00	0.50	60.0
Sample 3	50.00	100.00	10.00	60.0

Table. 5.2 Measurement results of verification samples (ppm)

	Sample 1			Sample 2			Sample 3	
	Expected	4 hour	12 hour	Expected	4 hour	12 hour	Expected	12 hour
Al	2.00	2.03496	2.07457	0.20	0.177223	0.23516	10.00	10.0819
Si	4.00	3.65501	3.90259	0.40	0.448639	0.47726	20.00	20.0971
Ca	2.00	1.66068	2.11996	0.20	0.134123	0.17957	2.00	1.98777

A comparison between expected values and measurement results is made in Table. 5.2. The results for different standing time were also listed for comparison. It can be seen from sample 1 that the element concentrations is a little underestimated after sample treatment for 4 hour. That is because the time is not enough for acid to completely dissolve the C-S-H gel inside the verification sample. After 12 hour, the the C-S-H gel can be completely dissolved and the results of sample 2 and sample 3 are in good agreement with the expected values. However, when we compare to sample 2 and sample 3, the result of sample 2 is worse. That is probably because the element concentration is quite low and almost closed to the resolution limitation of the machine. In conclusion, the proposed sample treatment method is feasible and reliable.

At last, to ensure the quality of the measurement data, other supplementary methods and procedures were also used in this test as follows.

(1) Before measurement, the machine conditions is verified and calibrated by spectrometry of argon and the experiments start only if the variance is less than 10. The background of element spectrometry will be also correspondingly adjusted according to tested samples before measurement;

(2) Five points calibration line was used in this test and the linear correlation coefficient

is higher than 0.99995 for Al and Si and 0.99980 for Ca respectively. Calibration solutions were stored in a constant temperature room of 20 ℃ without light and replaced by a new one every month;

(3) The ICP machine was frequently cleaned by nebulizing a mildly-acidic blank solution (HCl of 1 mol/L) during measurement (3 samples) and starting and closing machine. Each time after 3 sample measurements, the machine conditions were checked by standard solution. If the error is more than 5%, the experiment would stop and the glass apparatus and the sucking tube would be cleaned again; and

(4) The tests would be conducted in 24 hours after sample treatment to avoid the additional formation of silica-gel due to Na ion.

5.2 Temperature-dependent alkali dissolution test result

5.2.1 Element concentrations

Fig. 5.3 presents all the measurement results at 20 and 60 °C respectively. It can be seen that different fly ashes had different dissolution processes. More specifically, at room temperature of 20 °C, FA1 and FA2 had a similar concentration of Si but the Al concentration of FA2 was higher than FA1. In contrast, the concentrations of Si and Al of FA3 were significantly smaller than FA1 and FA2 but it had a higher concentration of Ca, which was consistent with the bulk chemical compositions of fly ashes (Table. 4.1).

At high temperature of 60 °C, the general trends were same to the room temperature of 20 °C but the dissolution processes of fly ashes were significantly promoted. It is noted that the concentration of dissolved Ca decreased after half a day (Fig. 5.3 (f)). It is likely that some calcium-silicon-hydrate (C-S-H) gel formed and precipitated on the surface of fly ash particles. Therefore, even the nitric acid is used to dissolve the C-S-H gel, the Ca concentration still decreased. However, considering Ca ion concentration was significantly smaller than Si and Al (comparing Fig. 5.3 (f) to (d) and (e)), it is believed that this error induced by C-S-H gel was limited and can be negligible.

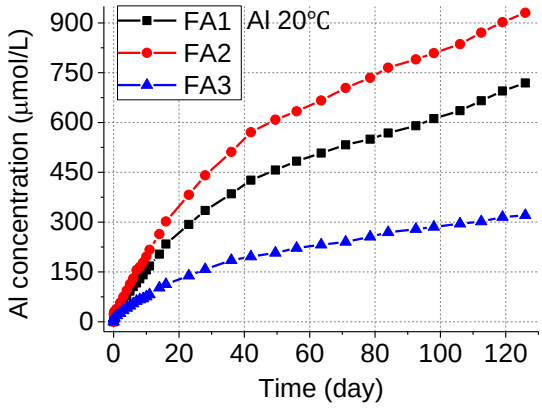

(a) Al concentrations of fly ashes at 20 °C

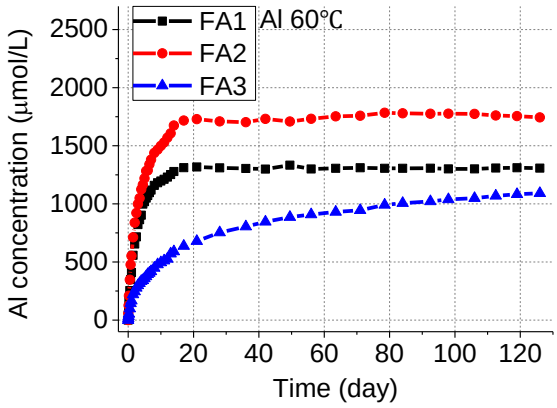

(b) Al concentrations of fly ashes at 60 °C

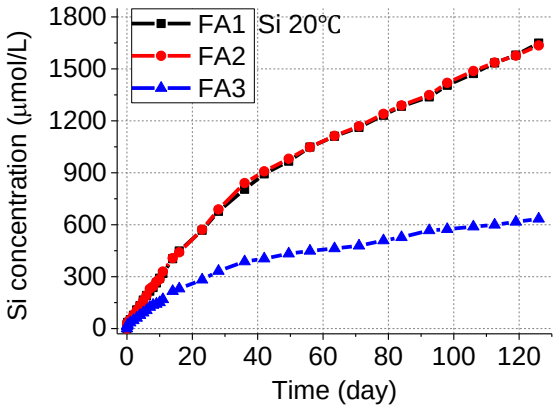

(c) Si concentrations of fly ashes at 20 °C

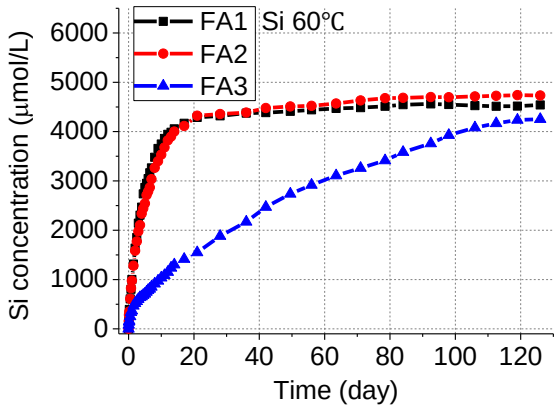

(d) Si concentrations of fly ashes at 60 °C

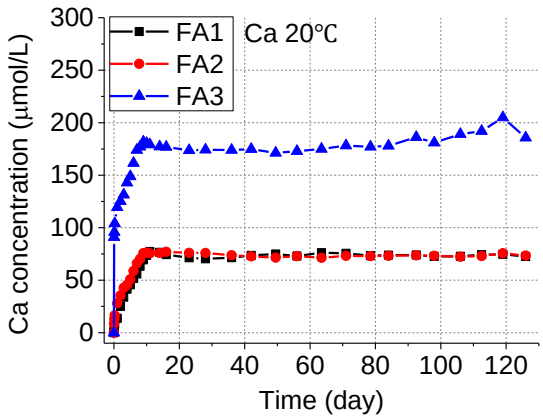

(c) Si concentrations of fly ashes at 20 °C

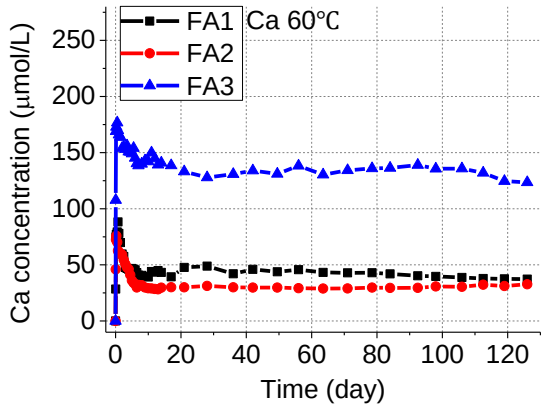

(d) Si concentrations of fly ashes at 60 °C

Fig. 5.3 Measurement result of dissolved element concentrations in alkaline dissolution test

5.2.2 Induvial composition dissolution process

5.2.2.1 Bulk oxide solids

To further study the dissolution process of fly ash, individual oxide solids dissolution degrees of SiO_2 and Al_2O_3 were calculated by silicon and aluminium aqueous concentrations in alkali solutions (Eqs. (5.1) and (5.2)).

$$D_{Al_2O_3}^{Bulk} = \frac{m_{Al_2O_3}}{m_s c_{Al_2O_3}^{Bulk}} \tag{5.1}$$

$$D_{SiO_2}^{Bulk} = \frac{m_{SiO_2}}{m_s c_{SiO_2}^{Bulk}} \tag{5.2}$$

where m_s is the mass of fly ash powder added in NaOH solution and; $m_{Al_2O_3}$ is the dissolved Al_2O_3 content estimated by the concentration of Al ion in alkali solution and $c_{Al_2O_3}^{Bulk}$ is the weight ratio of bulk oxide chemical composition of Al_2O_3 of the specified fly ash according to SEM-EDS mapping result (Table. 4.2). Similar definitions are used for the other compositions of SiO_2 as well. Here the chemical composition of fly ashes was used the SEM-EDS mapping result rather than XRF analysis result.

The reason for this decision was as follows. Although EDS and XRF both are semi-quantitative analysis, the testing conditions (e.g. flat and smooth surface) and amount of data of EDS is obviously better than XRF, therefore, EDS result is believed more reliable. Another reason is that SEM-EDS mapping will be used to study the reactivity of fly ashes in alkaline condition and cement systems. Therefore, the chemical composition determined by SEM-EDS mapping is more convenient and potential.

Fig. 5.4 showed the dissolution degrees of bulk oxide chemical composition among the three different siliceous fly ashes. It can be seen that dissolution rates of Al_2O_3 and SiO_2 composition are all different in all fly ashes. For example, FA1 and FA2 have a higher dissolution rate and FA3 is slower. Moreover, the relationship between dissolution rates of Al_2O_3 and SiO_2 composition are also different in different fly ashes (Fig. 5.4). The reason might be because fly ash have crystal and amorphous solids but only the amorphous solids are dissoluble in alkaline solution. Therefore, the dissolution process of induvial oxide

composition of amorphous solids will be discussed in next section.

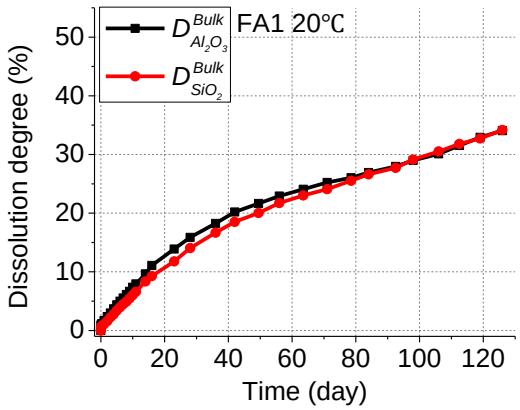

(a) dissolution processes of FA1 at 20 °C

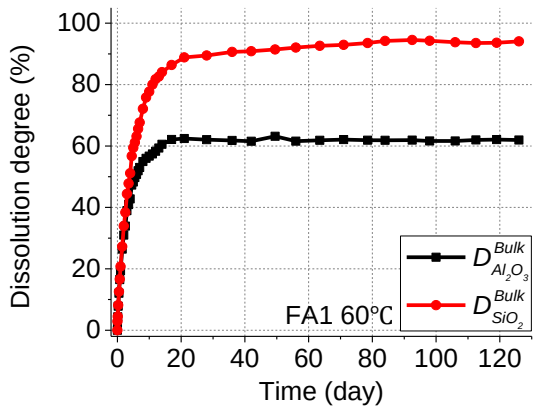

(b) dissolution processes of FA1 at 60 °C

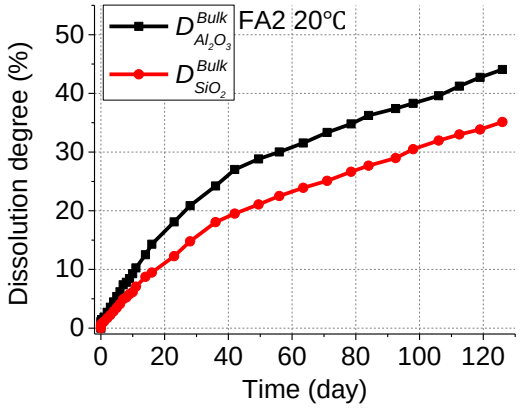

(c) dissolution processes of FA2 at 20 °C

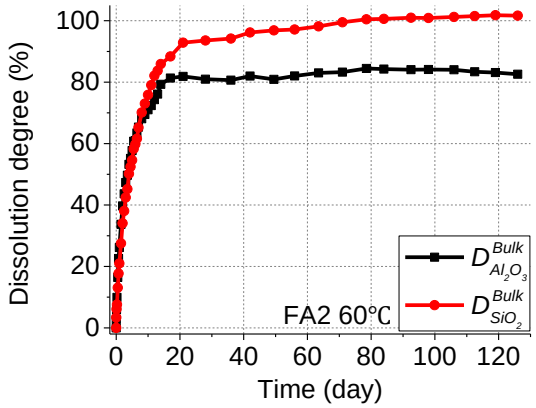

(d) dissolution processes of FA2 at 60 °C

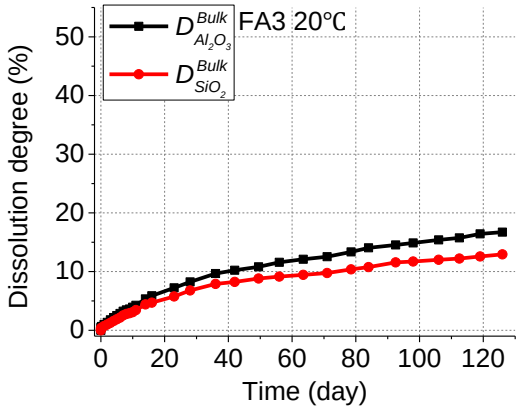

(e) dissolution processes of FA3 at 20 °C

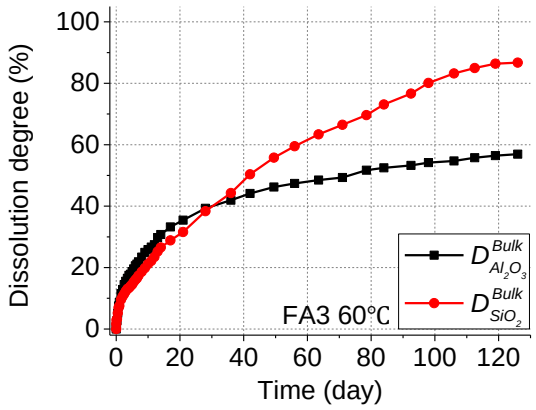

(f) dissolution processes of FA3 at 60 °C

Fig. 5.4 Dissolution processes of individual oxide chemical composition of fly ash

5.2.2.2 Individual amorphous oxide solids

To eliminate the influence of crystal solids, the oxide chemical composition of amorphous solids was determined by abstracting the oxide composition of crystal solids (Table. 4.6) from bulk oxide compositions (Table. 4.2). Table. 5.3 is the calculation result of oxide compositions of amorphous solids. With the help of Table. 5.3, the amorphous oxide dissolution degrees were re-calculated by Eqs. (5.3) and (5.4) and illustrated in Fig. 5.5 as well.

$$D_{Al_2O_3}^{Amor} = \frac{m_{Al_2O_3}}{m_s c_{Al_2O_3}^{Amor}} \tag{5.3}$$

$$D_{SiO_2}^{Amor} = \frac{m_{SiO_2}}{m_s c_{SiO_2}^{Amor}} \tag{5.4}$$

where: $c_{Al_2O_3}^{Amor}$ and $c_{SiO_2}^{Amor}$ are the mass ratio of Al_2O_3 and SiO_2 of bulk amorphous phase of a fly ash in Table. 5.3.

Table. 5.3 Oxide chemical compositions of amorphous solid (mass %)

	Al_2O_3	SiO_2	CaO
FA1	13.33	47.68	2.36
FA2	16.88	49.18	2.46
FA3	8.58	43.97	3.33

After eliminating the influence of crystal solids, Fig. 5.5 clearly shows that the Al_2O_3 dissolution rate of amorphous solid is faster than SiO_2 both at 20 and 60 °C. This agrees with Haha's observation at room temperature and Durdzinski's finding that Al-silicate amorphous solid dissolves faster than silicate amorphous solid [28, 54]. It might be because amorphous Al-silicate is reactive than amorphous silicate, which will be discussed in following sections.

Moreover, it can be seen that the dissolution processes are significantly promoted by rising temperature. Most amorphous content of FA1 and FA2 was dissolved after 2 weeks at 60 °C. Although the dissolution rate of FA3 was slower than FA1 and FA2, the amorphous content was still completely dissolved after 120 days. It is also interesting found that the maximum dissolution degrees of Al_2O_3 were around 100% but the dissolution degrees of SiO_2 were all higher than 100%. That means that crystalline mullite was not dissolved but at least some amount of quartz was dissolved at high temperature. This phenomena will be further

discussed in the SEM-EDS mapping result of alkaline dissolution test.

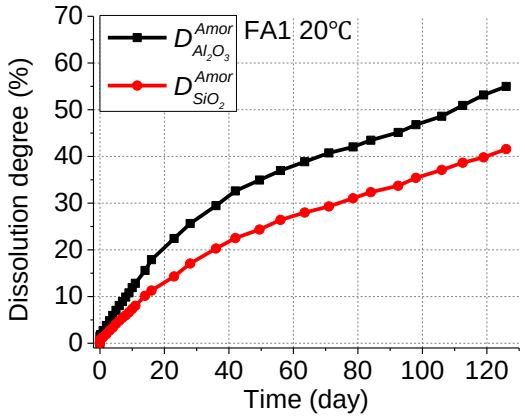

(a) dissolution processes of FA1 at 20 °C

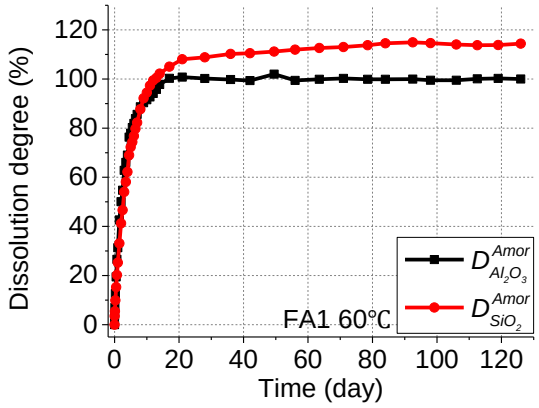

(b) dissolution processes of FA1 at 60 °C

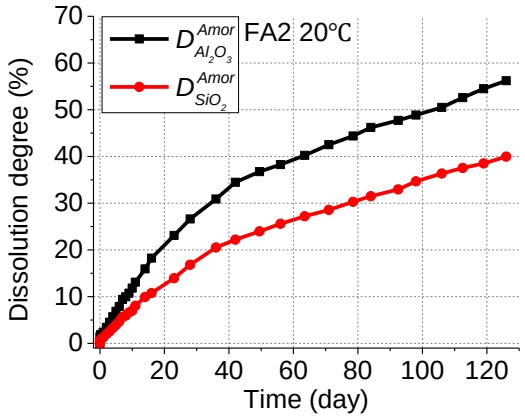

(c) dissolution processes of FA2 at 20 °C

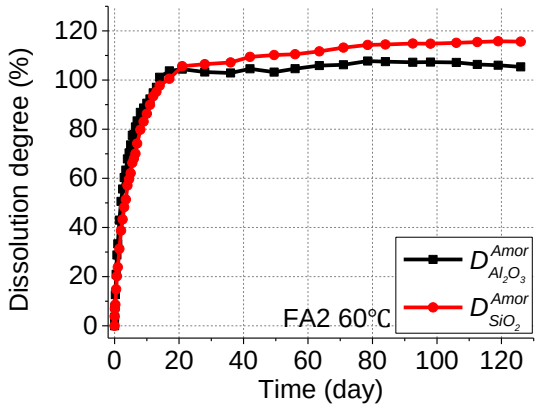

(d) dissolution processes of FA2 at 60 °C

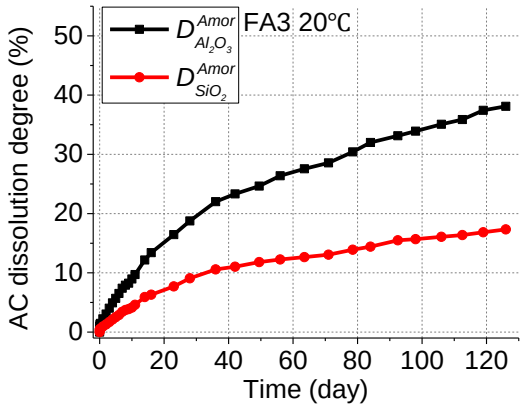

(e) dissolution processes of FA2 at 20 °C

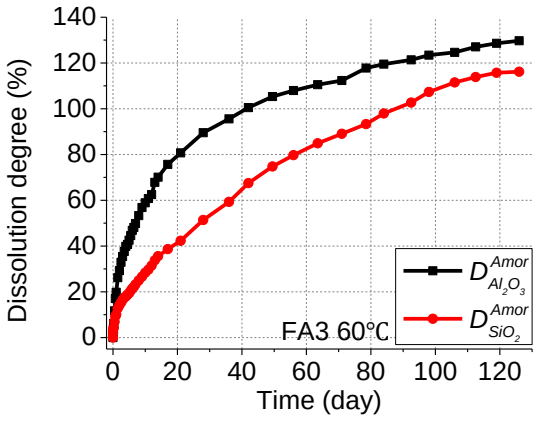

(f) dissolution processes of FA2 at 60 °C

Fig. 5.5 Dissolution processes of individual oxide chemical composition of amorphous solid

5.2.3 Composite dissolution process

Because different oxide compositions have different dissolution rates as discussed in last section, any individual composition dissolution process is not proper to be used to describe the reactivity of fly ash. Therefore, the composite dissolution degree D_{com} was proposed herein to study the reactivity of fly ash, i.e. Eq. (5.5).

$$D_{com} = \frac{m_{Al_2O_3} + m_{SiO_2} + m_{CaO}}{m_s \left(c_{Al_2O_3}^{Bulk} + c_{SiO_2}^{Bulk} + c_{CaO}^{Bulk} \right)} \tag{5.5}$$

where the symbols m_{CaO} and c_{CaO}^{Bulk} used similar definitions in Eqs. (5.1) and (5.2); and the definition of symbols $m_{Al_2O_3}$, m_{SiO_2}, $c_{Al_2O_3}^{Bulk}$ and $c_{SiO_2}^{Bulk}$ are same to Eqs. (5.1) and (5.2).

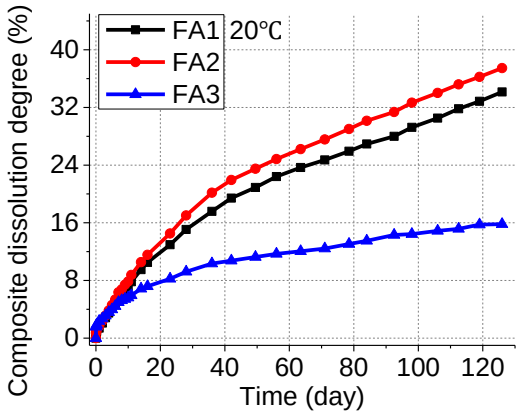

(a) 20 ℃

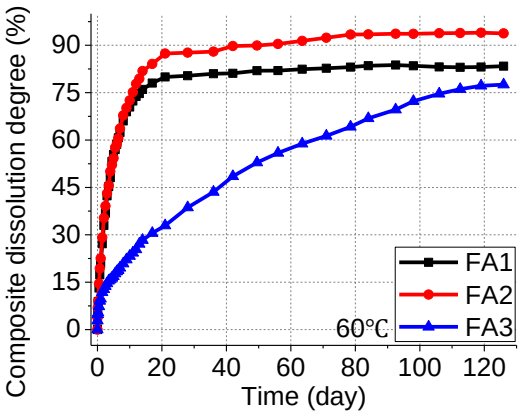

(b) 60 °C

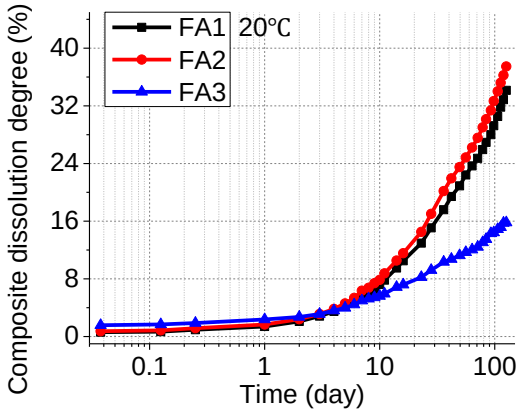

(c) 20 °C (log10 scale)

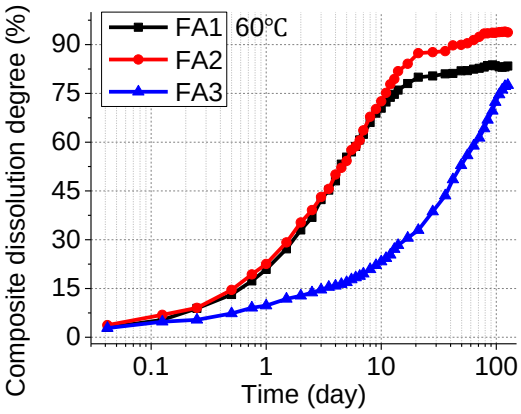

(d) 60 °C (log10 scale)

Fig. 5.6 Dissolution processes of fly ashes in alkaline system

Fig. 5.6 presents the composite dissolution degree among these three different fly ashes at different temperatures. Generally speaking, FA1 and FA2 have similar reactivity but FA3 is less reactive than FA1 and FA2 both at 20 and 60 °C. At room temperature of 20 °C, FA3 dissolved faster than FA1 and FA2 at the first day (Fig. 5.6 (c)). That is because FA3 has a higher CaO content and its reactivity is higher than other compounds (Table. 4.1). After most of the CaO content was dissolved, the dissolution degree of FA3 was rapidly exceeded by FA1 and FA2 and the differences become more and more. At 120 days, FA1 and FA2 had almost 2 times dissolution degree of FA3. At high temperature of 60 °C, all fly ashes dissolution process were significantly promoted. FA1 and FA2 rapidly dissolved in NaOH solution and most dissolution process had already finished and reached up to the plateau stage in the first two weeks. FA2 had a slightly higher dissolution degree than FA1, which coincides with the higher amorphous content of FA2 (Table. 4.6). Regarding to FA3, the dissolution process fell behind FA1 and FA2 from the beginning (Fig. 5.6 (d)). It shows that, even at high temperature, the reactivity of FA3 is still smaller than FA1 and FA2.

According to these alkali dissolution tests, it can be seen that the reactivities of siliceous fly ash are different, even they had been carefully selected according to the classification of type II fly ash in Japanese standard [23]. Therefore, current fly ash classifications are not enough to describe the reactivity of fly ash and more fundamental studies are needed.

5.3 Microscopic evaluation on fly ash after alkali dissolution test

5.3.1 Dissolution mechanism of fly ash

To further investigate the status of fly ash in alkaline system, the morphology of fly ash particles after alkali dissolution test was observed by SEM of ZEISS Merlin with accelerating voltage of 15 kV at SUSTech.

Fig. 5.7 and Fig. 5.8 are the BSE images of fly ash particles after alkali dissolution test of 210 days at 20 and 60 °C respectively. It can be seen that amorphous solids dissolved and the crystalline solids inside the particles exposed after alkali dissolution tests. At room temperature of 20 °C (Fig. 5.7), the dissolution processes had not completed, therefore some amorphous solids still can be found inside or around fly ash particles. At high temperature of

60 °C (Fig. 5.8), the dissolution processed was significantly promoted and it had finished, the crystalline solids inside the fly ash particles thus completely and clearly appeared in BSE observations.

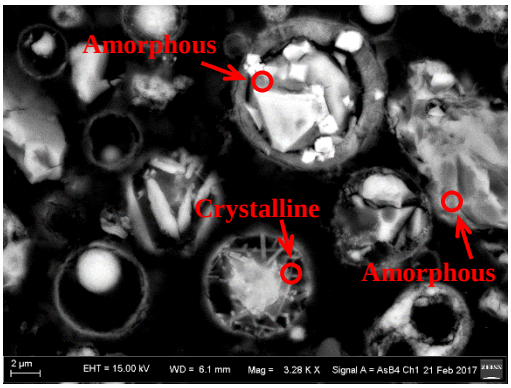

(a) overview

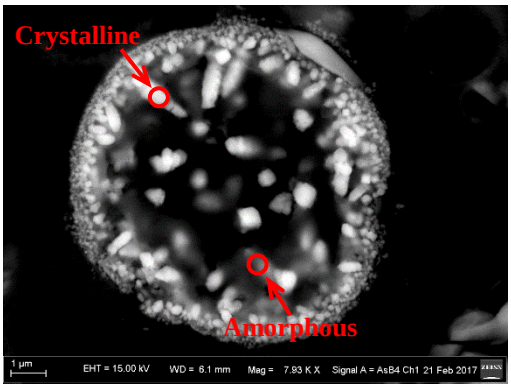

(b) detail 1

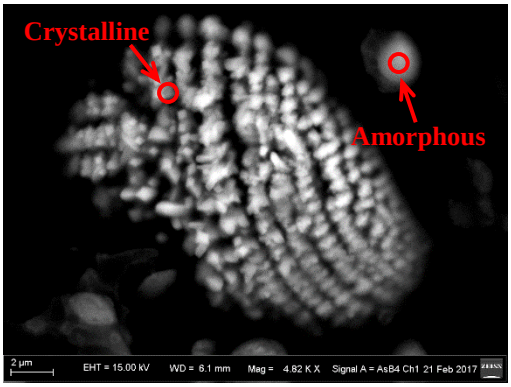

(c) detail 2

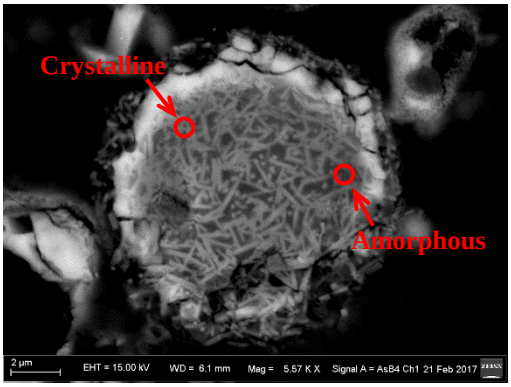

(b) detail 3

Fig. 5.7 BSE pictures of fly ash particles after alkali dissolution test of 210 day at 20 °C

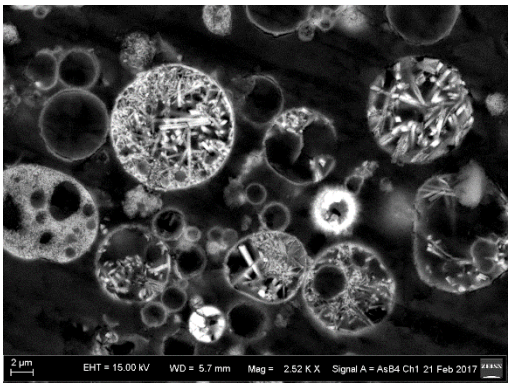

(a) overview

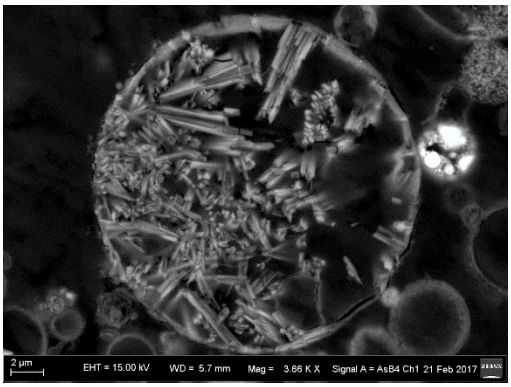

(b) detail 1

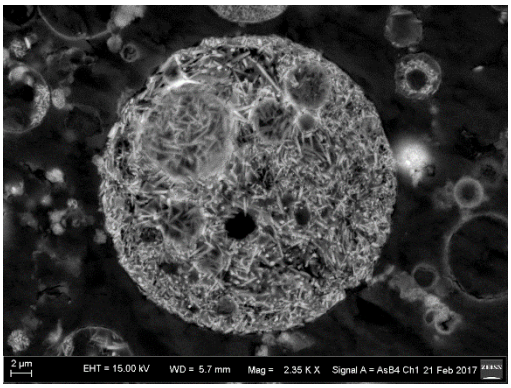

(c) detail 2

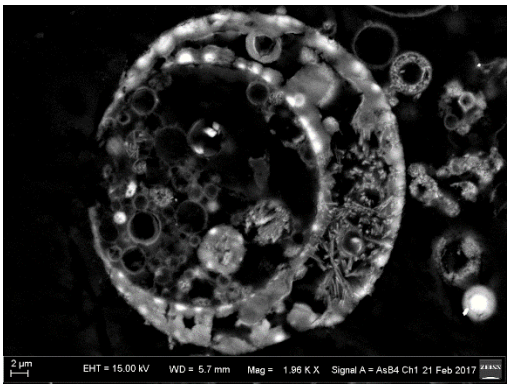

(b) detail 3

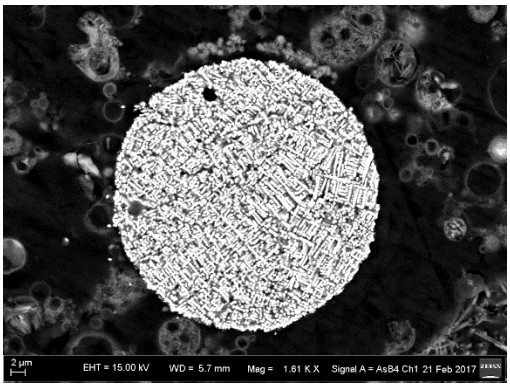

(e) detail 4

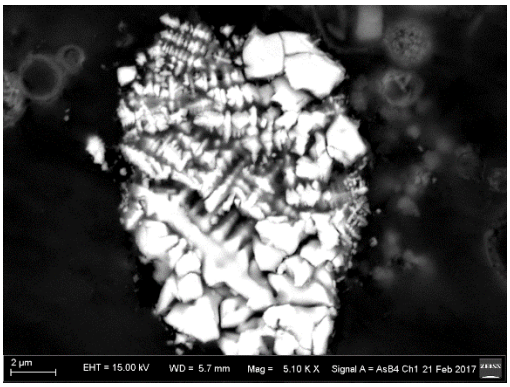

(f) detail 5

Fig. 5.8 BSE pictures of fly ash particles after alkali dissolution test of 210 day at 20 °C

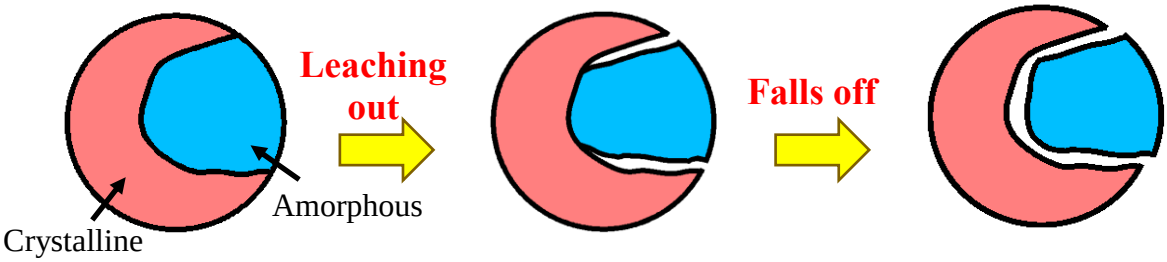

Fig. 5.9 Proposed dissolution mechanism of fly ash particles

According to these observations, it can be seen that the crystalline solids of fly ash particles are hardly dissolved but amorphous solids are dissolvable in alkali systems, which agrees with previous research conclusions [12, 19]. It also can be reasonably assumed that, under the erosion of hydroxyl in the alkaline system, the amorphous solids gradually leaches out from fly ash particles and finally falls off from it, as schematically illustrated in Fig. 5.9. That is also why it was observed that some amorphous content remained inside or existed

around fly ash particles at 20 °C (Fig. 5.7).

5.3.2 SEM-EDS mapping result and discussions

5.3.2.1 SEM-EDS mapping result

In chapter 4, based on the new segmentation criteria, the phase assemblages of the three siliceous fly ashes had been satisfactorily distinguished and quantified. Therefore, this section is going to further study and discuss the kinetic properties of these different phases in alkaline systems by SEM-EDS mapping analysis.

The remained fly ash powders after alkali dissolution test of 210 days both at 20 and 60 °C were collected by filtrating through a dried and weighted Whatman GF/B filter (minimum particle size retained 1.0 μm) and rinsing with deionized water, ethanol and deionized water successively. The filter and residue were dried at 105 °C for 4 hour to remove physically absorbed water and weighted by the same method in selective dissolution test. The mass percentages of remained fly ash powders compared to original one are listed in Table. 5.4. After that, the remained fly ashes particles were made into epoxy sample and measured by SEM-EDS mapping following the same procedures described in section 4.2.2.1. The phase remapping results were shown from Fig. 5.10 to Fig. 5.12. The phase assemblage of fly ash after alkali dissolution test were summarized in Table. 5.5.

Table. 5.4 Mass percentages of remained fly ash powders after alkali dissolution test (%)

	FA1	FA2	FA3
20 °C	62.46	57.46	83.32
60 °C	36.07	31.36	41.13

Table. 5.5 Phase assemblage of fly ashes after alkali dissolution tests (mass %)

	Quartz	Amorphous silicate	Amorphous Al-silicate	Semi-mullite	Mullite	Magnetite	Lime
FA1 20 °C	9.49	14.99	32.50	42.75	0.10	0.16	0.00
FA1 60 °C	1.90	4.29	26.70	66.55	0.22	0.29	0.05
FA2 20 °C	9.64	17.02	39.45	32.57	0.09	1.20	0.03
FA2 60 °C	3.30	8.09	37.98	46.92	1.52	2.18	0.01
FA3 20 °C	11.87	15.33	36.65	35.32	0.10	0.73	0.00
FA3 60 °C	2.87	14.47	17.58	63.18	0.30	1.57	0.02

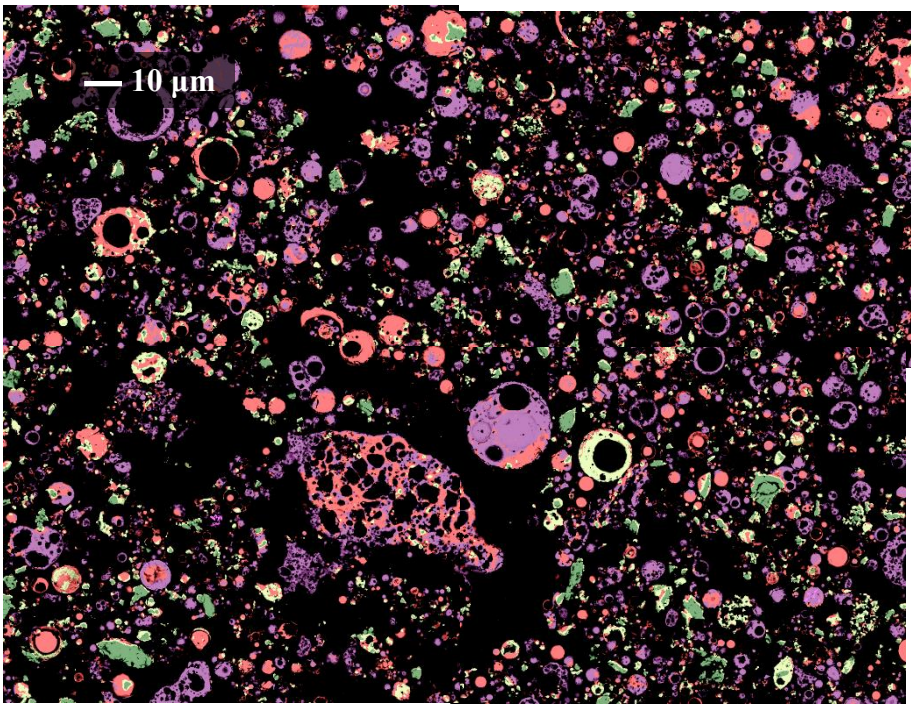

(a) FA1 at 20 °C after 210 days

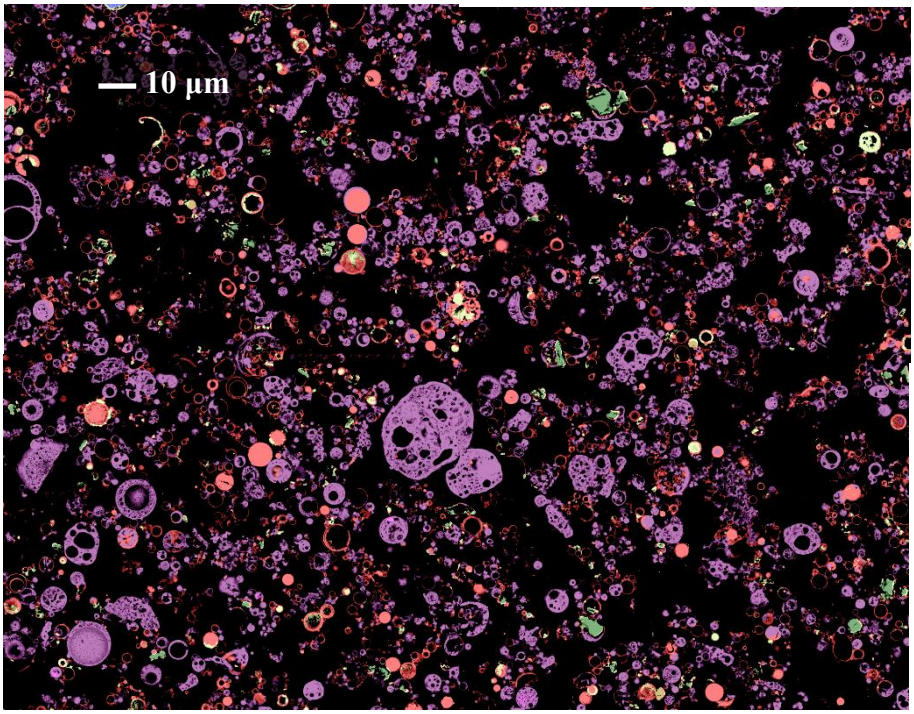

(b) FA1 at 60 °C after 210 days

Fig. 5.10 Mineralogical mapping result of FA1 after alkali dissolution test

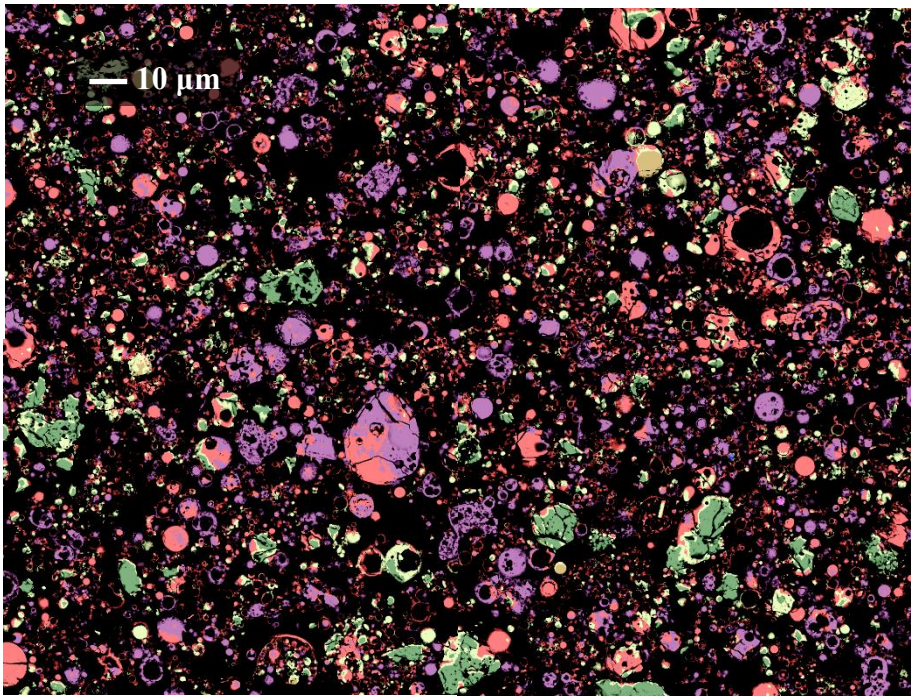

(a) FA2 at 20 °C after 210 days

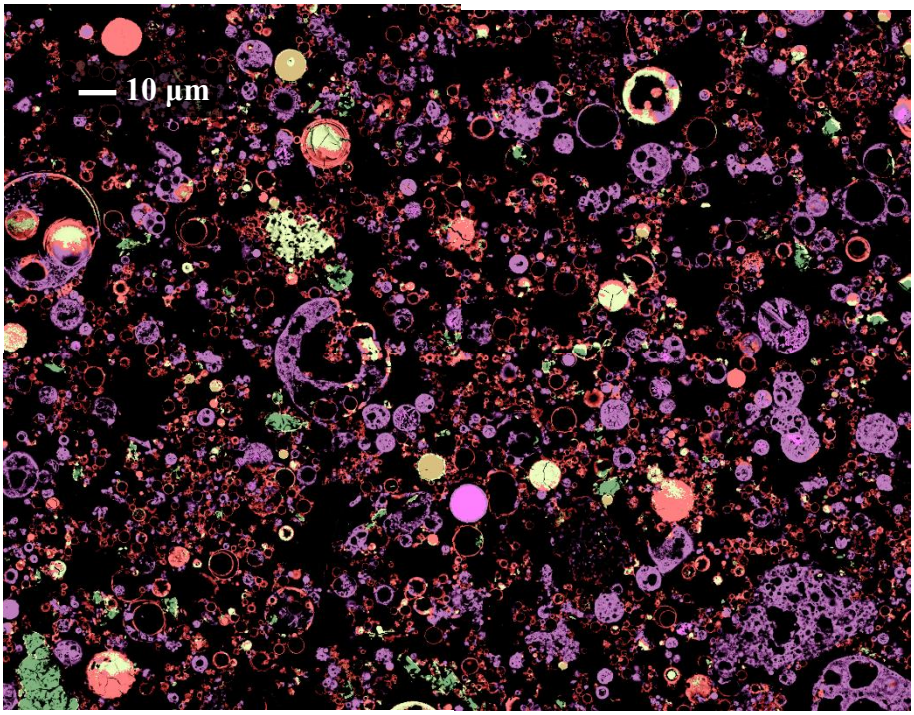

(b) FA2 at 60 °C after 210 days

Fig. 5.11 Mineralogical mapping result of FA2 after alkali dissolution test

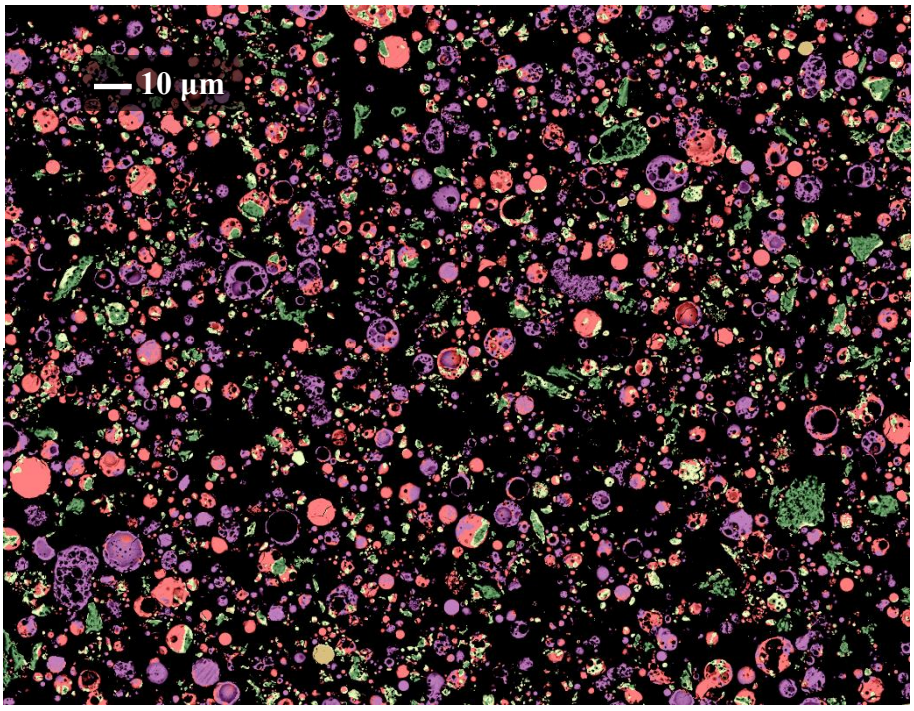

(a) FA3 at 20 °C after 210 days

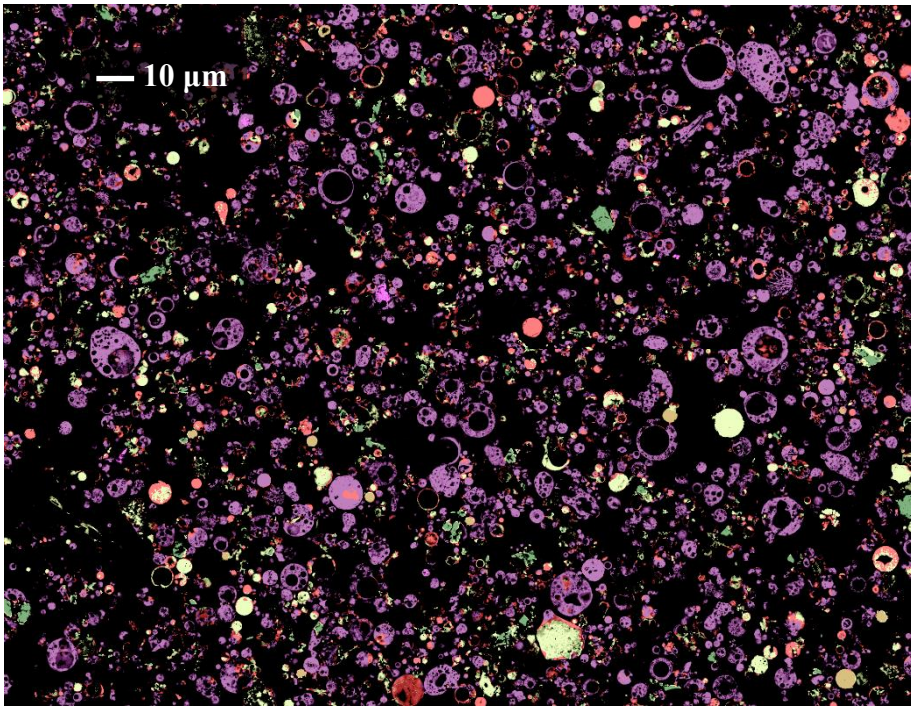

(b) FA3 at 60 °C after 210 days

Fig. 5.12 Mineralogical mapping result of FA3 after alkali dissolution test

5.3.2.2 Reactivity of mineralogical phase in alkaline system

(a) Dissolvable phases in alkaline system

Substitution of mass percentages of remained fly ash powders (Table. 5.4) into the phase assemblage of fly ashes after alkali dissolution test (Table. 5.5), it gives us the actual remained content of each phase of fly ash after alkali dissolution test. All the content are determined and summarized in Table. 5.6.

Table. 5.6 Mass fractions of each phase of fly ashes before and after alkali dissolution tests (%)

	Quartz	Amorphous silicate	Amorphous Al-silicate	Semi-mullite	Mullite	Magnetite	Lime
FA1 raw	7.56	10.79	48.03	33.46	0.01	0.14	0.02
FA1 20 °C	5.93	9.36	20.30	26.70	0.07	0.10	0.00
FA1 60 °C	0.69	1.55	9.63	24.01	0.08	0.10	0.02
FA2 raw	7.41	10.30	44.64	36.67	0.05	0.85	0.08
FA2 20 °C	5.54	9.78	22.67	18.71	0.05	0.69	0.01
FA2 60 °C	1.03	2.54	11.91	14.71	0.48	0.68	0.00
FA3 raw	10.97	13.59	45.72	29.27	0.05	0.26	0.13
FA3 20 °C	9.89	12.78	30.53	29.43	0.08	0.61	0.00
FA3 60 °C	1.18	5.95	7.23	25.98	0.12	0.65	0.01

Table. 5.6 shows that the amorphous silicate and amorphous Al-silicate are dissoluble phases. However, these two phases cannot be completed dissolved even at high temperature of 60 °C. That is probably because the network of amorphous solids varies with coal source and combustion conditions and some amorphous solids may have quite repeated geometric constituent molecules (e.g. Fig. 2.7). In case of these systematic solids, they are more like crystalline solids and thus hardly dissolved even at high temperature.

Table. 5.7 Comparison of dissolution degrees between Al-silicate and semi-mullite at 60 °C

	Dissolution degree (%)		Mullite content (mass %)
	Al-silicate	Semi-mullite	
FA1	79.95%	28.24%	11.40
FA2	73.32%	59.87%	6.49
FA3	84.19%	11.24%	15.28

Table. 5.6 also shows that semi-mullite can partially dissolve in alkaline systems. The dissolved content of semi-mullite probably comes from its exposed amorphous Al-silicate

solids. Therefore, its dissolution degrees was significantly smaller than amorphous Al-silicate phase and inversely proportional to the mullite content of fly ashes as well (see Table. 5.7).

Compared to these dissoluble amorphous phases, the contents of crystalline mullite and magnetite were almost the same or even a little increased after alkali dissolution test (Table. 5.6). That is because crystalline phase mullite and magnetite are almost insoluble in alkaline system [48] and their contents accordingly increased as other amorphous phases were dissolved.

Unlike crystalline phases mullite and magnetite, the crystalline phase quartz also can dissolve in alkaline system. Therefore, its content decreased after alkali dissolution test, as shown in Table. 5.6. Moreover, it is also found that the free lime content decreased after alkali dissolution tests as well. That could be the free lime (CaO) can directly react with water and become calcium hydroxide. However, because the content of free lime is quite low in fly ashes, its influence can be ignored.

In conclusion, the major dissolvable phases of siliceous fly ash are crystalline quartz and amorphous silicate and Al-silicate. They are therefore also believed to be the reactive phases of siliceous fly ash in cement system.

(b) Reactivity and thermal dependency of dissolvable phases

Since the major dissolvable phases of siliceous fly ash are quartz, amorphous silicate and Al-silicate, their kinect properties will be further studied and discussed in this section. The dissolution degrees of these there phases at 20 and 60 °C were calculated according to Table. 5.6 and summarized in Fig. 5.13.

It can been seen that the dissolution degree of amorphous Al-silicate is higher than the amorphous silicate, which means that the reactivity of amorphous Al-silicate is higher than amorphous silicate as well. A similar observation is also found in the work of Durdziński et al. [9, 28]. They studied the initial dissolution rate of synthetic glasses and found that the dissolute rate of amorphous Al-silicate solids (C, red) is higher than amorphous silicate solids (A, green) as well, as shown in Fig. 5.14.

As outlined in section 2.2.2.2(b), amorphous Al-silicate phases forms as a modification

result of either a polymeric network substitution or a polymeric network modifier addition. The higher the modifier concentration, the more matrix will be depolymerized. For example, after the Al^{3+} is introducing into Si^{4+} network to form amorphous Al-silicate phase, some Si-O-Si bonds break and consequently modified element as well as non-bridging oxygen atoms (NBO) will coexist (see Fig. 2.10 and Fig. 2.11). These modifications further extend and disorder the network, so the network becomes progressively depolymerized and the amorphous Al-silicate phase will finally consist of small alumina-silicate oligomers with a large number of negatively charged NBO's [18]. In the alkaline system, these modified bridging tends to act like a somewhat "defect" and thus more easily be broken under the erosion of hydroxyl. Therefore, amorphous Al-silicate phase is more reactive than amorphous silicate. That may be also the reason of the dissolution rate of amorphous Al_2O_3 is faster than amorphous silicate as shown in Fig. 5.5.

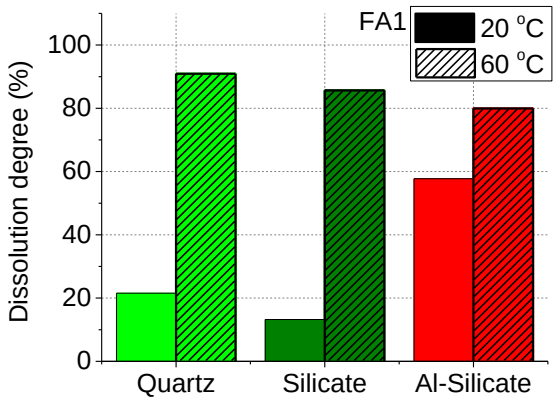

(a) FA1

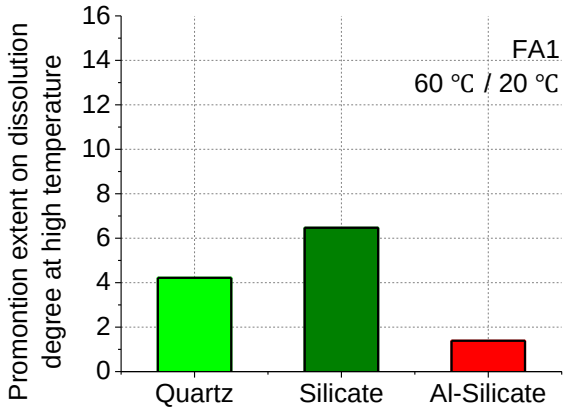

(b) temperature-dependent effect of FA1

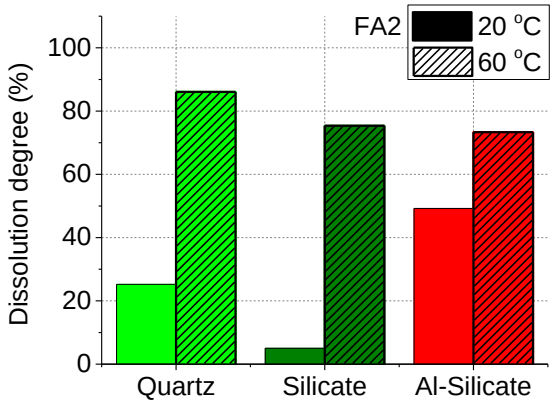

(c) FA2

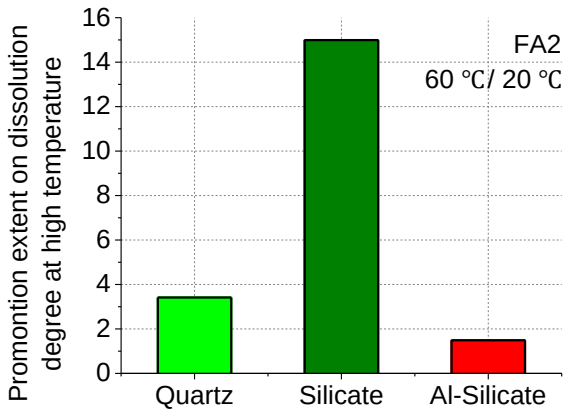

(d) temperature-dependent effect of FA2

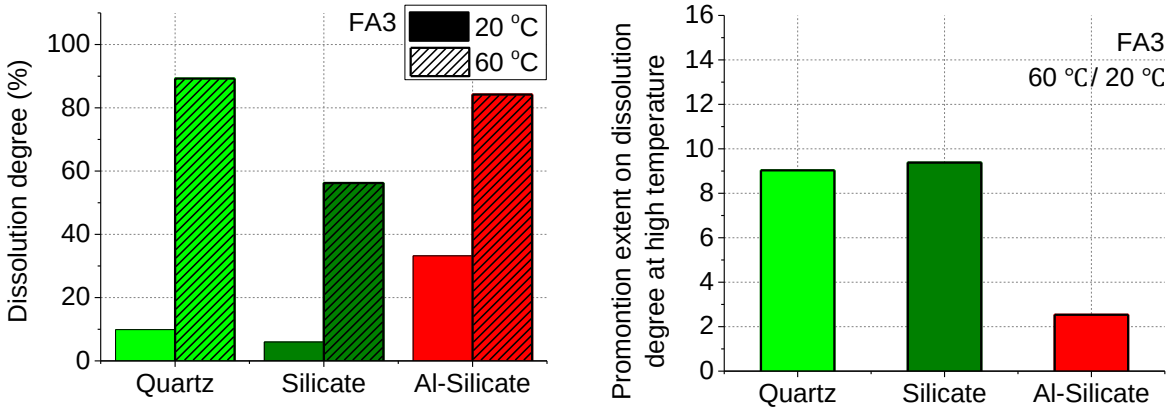

(e) FA3 (f) temperature-dependent effect of FA3

Fig. 5.13 Comparisons of different mineralogical passes at different temperatures

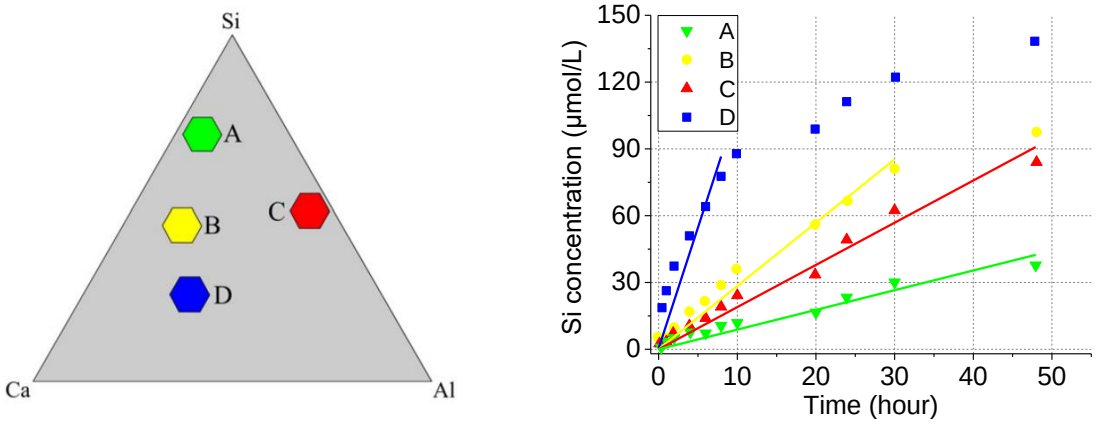

(a) synthetic glasses (b) silicon concentrations

Fig. 5.14 Dissolution process of synthetic glasses in alkaline solution [28]

Moreover, it is also interesting to note that the dissolution degree amorphous silicate phase is more significantly promoted by high temperature of 60 °C compared to amorphous Al-silicate phase. In other words, amorphous silicate phase is more sensitive to temperature than amorphous Al-silicate phase.

At last, regrading the crystalline quartz phase, it can be seen from Fig. 5.13 that its behaviors are very similar to amorphous silicate phase both at room and high temperature. Considering the content of crystalline quartz phase are limited, the crystalline quartz phase is classified into amorphous silicate phase for simplification in this study.

In conclusion, amorphous Al-silicate phase is more reactive than amorphous silicate but less sensitive to temperature.

5.4 Fly ash reactivity and its material properties

5.4.1 Introduction

The material properties characterization of fly ashes had been carried out in chapter 4. The reactivity of fly ashes is also investigated and discussed in this chapter. Therefore, this section is going to discuss the relationship between reactivity of fly ash and its material properties.

Table. 5.8 summarized the major material properties of fly ashes and the dissolution processes were redrew in Fig. 5.15 for discussions. It is known that the amorphous Al-silicate phase is more reactive than amorphous silicate phase but less sensitive to temperature. However, this information is insufficient to explain the varication of dissolution processes in Fig. 5.15. Specifically speaking, FA1 and FA2 had similar contents of amorphous silicate and Al-silicate but FA1 has a higher specific surface area. It is therefore reasonably expected that dissolution process of FA1 should be faster than FA2. However, the experiment result showed that the dissolution degree of FA2 were actually a little higher than FA1 from the beginning. Therefore, something should be still missed in previous discussions.

Table. 5.8 Summarization of fly ash material properties

	Total amorphous (mass %)	Amorphous silicate (mass %)	Amorphous Al-silicate (mass %)	Specific surface area (cm^2/g)	Al-silicate /Mullite	Silicate /Quartz
FA1	81.07	10.79	48.03	7894	4.23	1.52
FA2	87.90	10.30	44.64	5648	6.90	2.09
FA3	73.03	13.59	45.72	5623	3.01	1.28

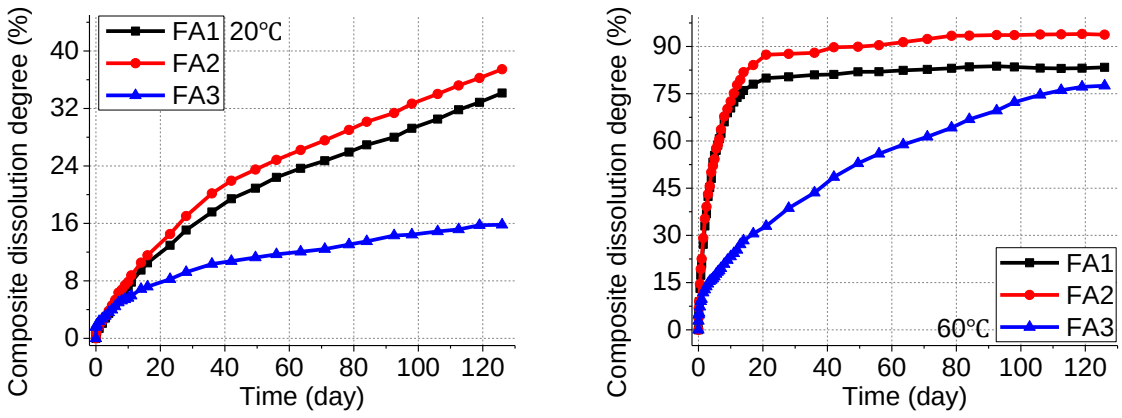

(a) 20 ℃ (b) 60 °C

Fig. 5.15 Redrawing of dissolution processes of fly ashes in alkaline system

5.4.2 Intrinsic reactivity of amorphous phase

As pointed out in section 2.2.2, the network of amorphous solids has different structures and it varies as type of coal, combustion temperature and cooling history changes [56]. Generally speaking, a higher combustion temperature and a more rapid cooling process in thermal furnace results in a higher amount of amorphous solids. Meanwhile, the intrinsic reactivity of amorphous phase (i.e. the actual reactivity of amorphous phase without fineness influence) is very likely to be promoted in this condition as well because it has a higher energy. In contrast, the intrinsic reactivity of amorphous phase could be suppressed with a lower combustion temperature and a slower cooling process. This relationship is schematically illustrated in Fig. 5.16.

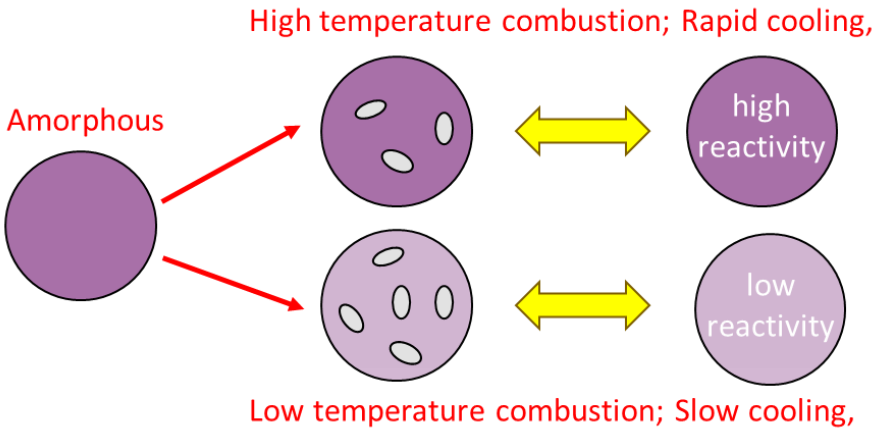

Fig. 5.16 Schematic representation of the relationships between the intrinsic reactivity of amorphous phases and the combustion conditions

Therefore, a supplementary hypothesis is proposed herein that the intrinsic reactivity of the amorphous phase are affected by combustion conditions and it may be different in different fly ashes. Since a proper combustion condition will both promote the production of amorphous solids and its intrinsic reactivity, the amorphous-crystalline ratio can be used to describe the intrinsic reactivity of amorphous phases, i.e. a higher value of amorphous-crystalline ratio means a higher intrinsic reactivity of an amorphous phase.

Considering the the major crystalline solids of amorphous silicate and amorphous Al-silicate are quartz and mullite, two amorphous-crystalline ratio R_{Si}^{Amor} and R_{Al-Si}^{Amor} for amorphous

silicate and amorphous Al-silicate phases were proposed herein, as Eqs. (5.6) and (5.7) show.

$$R_{Si}^{Amor} = \frac{c_{Si}^{Amor}}{c_{quartz}} \tag{5.6}$$

$$R_{Al-Si}^{Amor} = \frac{c_{Al-Si}^{Amor}}{c_{mullite}} \tag{5.7}$$

where: c_{Si}^{Amor} is the mass ratio of amorphous silicate phase and c_{quartz} is the mass ratio of crystalline quartz. Similar definitions are used for the other compositions of c_{Al-Si}^{Amor} and $c_{mullite}$ as well. All the calculation results are all summarized in Table. 5.8.

Table. 5.9 Material properties of amorphous silicate and Al-silicate phases in FA2 and FA3

	Total (cm2/g)	Silicate (cm2/g)	Al-Silicate (cm2/g)	Silicate/ Quartz	Al-silicate/ Mullite
FA2	5648	5202	6510	2.09	6.90
FA3	5623	6926	6296	1.28	3.01

Because FA2 and FA3 have very similar specific surface areas (see Table. 5.9), their alkali dissolution result was selected to validate this hypothesis. It can be seen that because the amorphous silicate of FA3 has a higher surface area than FA2 but its amorphous-crystalline ratio (i.e. Silicate/Quartz) is smaller than FA2, the dissolution degrees of amorphous silicate are very similar between these two fly ashes. In addition, because the specific surface area of amorphous Al-silicate of FA2 and FA3 are similar but the amorphous-crystalline ratio (i.e. Al-silicate/Mullite) of FA2 is higher than FA3, the dissolution degree of amorphous Al-silicate of FA2 is higher than FA3. That shows that intrinsic reactivity of amorphous phases are different in different fly ashes and it can be described by the amorphous-crystalline ratios.

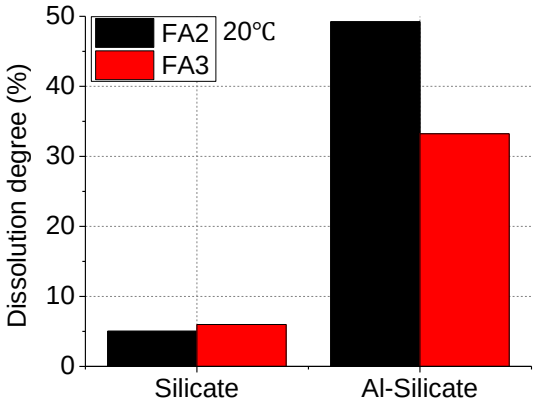

Fig. 5.17 Comparisons between FA2 and FA3 for amorphous silicate and Al-silicate

5.4.3 Explanation on the reactivity variation of studied fly ashes

According to Eqs. (5.6) and (5.7), the amorphous-crystalline ratios of amorphous silicate and Al-silicate phases for different fly ashes were determined and summarized in Table. 5.8. Combined with these reactivity indexes, the dissolution processes can be reasonably explained now.

Specially speaking, FA1 has a higher specific surface area but a smaller reactivity indexes than FA2, therefore FA1 and FA2 have the similar dissolution processes both at 20 and 60 °C. Compared to FA1 and FA2, FA3 has the lowest specific surface area and reactivity indexes and the dissolution process is therefore the lowest among these three fly ashes.

In conclusion, the reactivity of siliceous fly ash depends on its amorphous phase assemblage, surface areas and intrinsic reactivity of amorphous phases; the instinct reactivity of amorphous phase can be described by amorphous-crystalline ratio.

5.5 Summary and conclusions

The temperature-dependent reactivity of fly ashes was investigated by alkali dissolution test in this chapter. The microscopic evaluation of the fly ashes after alkali dissolution test was also conducted. Based on these works, the conclusions of this chapter are summarized in the following points:

1. A sample treatment method and measurement procedures was developed for the ICP-OES measurement of fly ash alkali dissolution test. This method provides a satisfied measurement result of element aqueous concentrations in fly ash alkali dissolution tests;

2. It is found the dissolution rate of oxide compound Al_2O_3 in amorphous solid is faster than SiO_2 both at 20 and 60 °C;

3. The dissolvable phase of siliceous fly ash are crystalline quartz and amorphous silicate and Al-silicate;

4. Amorphous Al-silicate is more reactive than amorphous silicate but less sensitive to temperature;

5. It is found that the reactivity of amorphous phase are different in different fly ashes. It can be described by the corresponding amorphous-crystalline ratio; and

6. With the help of amorphous-crystalline ratio, the dissolution processes can be reasonably explained now. FA1 has a higher specific surface area but a smaller amorphous-crystalline ratio than FA2, therefore FA1 and FA2 have the similar dissolution processes both at 20 and 60 °C. Compared to FA1 and FA2, FA3 has the lowest specific surface area and amorphous-crystalline ratio, the dissolution process is therefore the lowest among these three fly ashes.

6 Temperature-dependent reactivity of fly ash in cement system

Contents:

6.1 Introduction 104
6.2 Sample preparation 105
6.3 Fly ash reaction degree 107
6.3.1 Selective dissolution test procedures 107
6.3.2 Selective dissolution test results 109
6.4 Calcium hydroxide and bound water content 111
6.4.1 TGA test procedures and analysis method 112
6.4.2 TGA test result 119
6.5 Hydration degrees of cement clinkers 122
6.5.1 XRD test and Rietveld refinement analysis procedures 123
6.5.2 Cement clinkers hydration degrees 123
6.5.3 Interaction between cement clinkers and fly ash 125
6.6 Summary and conclusions 133

6.1 Introduction

In chapter 5, the temperature-dependent reactivities of the three siliceous fly ashes had been investigated by alkali dissolution tests. Experiment results showed that these three fly ashes have different temperature-dependent reactivities because they have different amorphous phase assemblages, surface areas and intrinsic reactivities of amorphous phases.

The microscopic evaluation for fly ashes after alkali dissolution test was also conducted. It showed that amorphous Al-silicate is more reactive than amorphous silicate but less sensitive to temperature. The instinct reactivity of amorphous phase can be described by amorphous-crystalline ratio.

Although alkali dissolution test provides us a direct and fundamental understanding on fly ash reactivity, the most concern for civil engineers is still its pozzolanic reaction processes and their various influences in cement systems. Therefore, the temperature-dependent reaction processes of these three siliceous fly ashes and its effect on cement hydration will be investigated in cement systems in this chapter.

Selective dissolution methods are common techniques to determine the reaction degree of fly ash in a hardened cement paste. These methods aim at dissolving the hydrates and the unhydrated clinkers without dissolving the unreacted fly ash and the unreacted fly ash remains as residue and so that can be quantified [54]. Several dissolving agents had been reported in previous literatures. Among these dissolving agents, ethylene diamine tetra acetic acid (EDTA) with NaOH is believed the most suitable agents to determine the degree of reaction of the siliceous fly ash in hydrated FA blended cement pastes [54]. Therefore, EDTA with NaOH is used in this study to determine the reaction degree of fly ash in blended cement paste.

The pozzolanic reaction of fly ash consumes calcium hydroxide (CH) to produce C-S-H gel. Thus the consumption trend of calcium hydroxide and the bound water content of hydration products are important factors to access and study the pozzolanic reaction of fly ash. In addition, the calcium hydroxide content also affects the morphology of C-S-H gel. Therefore, in this chapter, these two contents were both evaluated by TGA tests with a modified analysis method as well.

Previous researches points out that dicalcium silicate (C_2S, belite) hydration process was retarded by supplementary pozzolanic materials, such as slag [57] and fly ash [32]. Kawabata et al. found that this retarded effect was promoted at high temperature curing [37]. Therefore, the hydration degrees of fly ash blended cement paste were also investigated by XRD-Rietveld method in this study. Based on the experiment data, the mechanism and hypothesis on the interaction between cement and pozzolanic materials was discussed at the last of this chapter as well.

6.2 Sample preparation

To better investigate the interaction between cement and pozzolanic materials, besides ordinary portland cement (OPC), the low heat portland cement (LPC) was also used in this test for study. The bulk chemical and physical properties of cement were summarized in Table. 6.1. The material properties of fly ash can be found in Chapter 4.

Table. 6.1 Material properties of cement

	C_2S (wt. %)	C_3S (wt. %)	C_3A (wt. %)	C_4AF (wt. %)	Blaine fineness (cm^2/g)	Specific gravity
OPC	15.90	65.50	8.07	8.77	3350	3.15
LPC	62.53	26.33	2.10	6.30	3750	3.24

Two series of fly ash cement pastes with a water to cementitious materials ratio of 0.4 and a fly ash mass replacement ratio of 0.3 were prepared for sealed curing at 20 and 60 °C respectively. Another two series of referenced cement paste with the water to cementitious materials ratio of 0.4 was also prepared in this test for comparison. To ensure the consistency of pastes, samples were prepared by following procedures according to ASTM 305 [58] and practical guidance proposed by EPFL [45].

1. For the fly ash cement paste, a specific fly ash of 165 g and cement of 385 g were first blended using a paint mixer for 2 min at 200 rpm to obtain homogenous dry powders;

2. Placed the dry paddle and the dry bowl in the central mixing position in the lab mixer (Eurostar 60 digital, IKA). The lower end of the paddle and the bottom of the bowl was not greater than 1.5 mm and not less than 0.8 mm.

3. Added pure water of 200 g into the bowel. Started the lab mixer at 400 rpm and the dry powders of 500 g prepared before was then carefully and gradually added into the bowel to ensure the powders fully absorbed the water. All actions were done in 30 s;

4. Accelerated the lab mixer to the high speed of 1600 rpm and mixed for 60 s. Then stopped the mixer for 15 s and during this time scraped down into the batch any paste that may have collected on sides of the bowl;

5. Started the lab mixer at 1600 rpm and mixed for another 60 s to complete the mixing procedures;

6. Placed the paste into polypropylene petri dishes (40×13 mm) for sealed curing. To control the bleeding, the paste was gently re-scooped at 30 min, 1 h, 2 h, 3 h and 4 h again after placing the paste. Then all petri dishes were sealed by para film and stored in sealed plastic boxes; and

7. The batch of samples for 20 °C curing were stored in a curing room of 20 ± 2 °C. The batch of samples for 60 °C curing was first cured at 20 °C for 1 day and then gradually heated to 60 °C in a warm water bath with a heating speed of 10 °C/hour (ICC control, IKA). After that, the batch of samples for 60 °C were continuously cured at an environment chamber of 60 ± 0.1 °C.

At the designated times (7, 14, 28, 56, 91 and 182 days), samples were unmolded from the petri dishes and immersed into isopropanol to stop hydration by solvent exchange. The storage in isopropanol lasted 7 days and the isopropanol was replaced one time after 3 days. The samples were then stored in a desiccator with silica gel beads and dried under vacuum for another 7 days to completely evacuate the isopropanol. This dehydration method with isopropanol and vacuum was used because it was less destructive to microstructure and phase assemblage than other methods [9, 45]. Part of the samples was manually ground into powders in a mortar and passed through a sieve of 0.1 mm for future selective dissolution test, TGA test and XRD-Rietveld test. Any type of machine grinding was not used in this test because it has significant effect on phase assemblage and then the microstructural analysis of cement paste [45, 59-61]. All samples were stored in a vacuum condition to avoid any carbonations.

6.3 Fly ash reaction degree

6.3.1 Selective dissolution test procedures

As mentioned previously, several dissolving agents had been reported in previous literatures and EDTA with NaOH is believed the most suitable one [54]. Table. 6.2 and Table. 6.3 summarize the mass percentage of residue of fly ash, cement and hydration products to initial mass after selective dissolution test. It can seen that dissolving agent of EDTA with NaOH satisfactorily dissolved the hydrate products and the unhydrated cement clinkers but without dissolving fly ashes. Therefore, EDTA with NaOH was used in this test as dissolving agent.

Table. 6.2 Residue of raw material to initial mass after selective dissolution test

OPC	LPC	FA1	FA2	FA3
0.50%	0.26%	96.12%	97.10%	92.50%

Table. 6.3 Residue of hydrated products to anhydrous cement after selective dissolution test

OPC 20 °C	OPC 60 °C	LPC 20 °C	LPC 60 °C
4.03%	2.90%	2.95%	1.86%

Note: These hydrated powders comes form the referenced cement paste of 182 days.

Based on previous researches [54, 62, 63], a modified experiment method with dissolving agent of EDTA with NaOH was developed in this test as follows. 500 ml dissolving solvent with disodium EDTA of 0.025 M was prepared by dissolving the disodium EDTA solids of 4.653 g in 500 ml NaOH solution of 0.05 M. 25 ml of 1:1 triethanolamine of H_2O mixture (volume ratio) was added to prevent agglomeration and coating of the powder. The pH was adjusted to 11.6 ± 0.1 to maximize the efficiency of EDTA by adding analytical grade NaOH solution of 1 M. Then a treated sample of around 0.5 g was added into the dissolving solvent and stirred for 1 hour at 1500 rpm by magnetic stirrer. After mixing, the suspension was filtrated through a dried and weighted Whatman GF/B filter (minimum particle size retained 1.0 μm). The residue was washed seven times with around 40 ml deionized water followed by three washes with 20 ml ethanol.

Because the filter paper absorbs the moisture of air and it significantly affects the experiment data, a new measurement procedures were proposed to eliminate the moisture effect and obtain the accurate mass of residue. The filter paper was first dried at 105 °C until

a constant mass was reached. Then the mass of filter paper was immediately weighted as m_1^F . Keep the filter paper in a constant temperature (20 ± 2 °C) and humidity (60 ± 5 %) room for 2 hours to allow it fully absorbs moisture. The mass of filter paper was then weighted again and recorded as m_2^F . The same procedures were also applied to the residue and filter after selective dissolution test and the two masses were recorded as m_1^{R+F} and m_2^{R+F} . All the weighting actions were conducted in a constant temperature and humidity room to ensure the quality of measurement result and the precision of mass was up to 0.0001 g. The average mass of residue m_{Avg}^R was finally determine by Eq. (6.1).

$$m_{Avg}^R = \frac{\left(m_1^{R+F} - m_1^F\right) + \left(m_2^{R+F} - m_2^F\right)}{2} \tag{6.1}$$

If assuming that all phases decompositions complete at 1000 °C, the status between the treated sample and raw materials should be same at 1000 °C. Therefore the initial mass of raw materials of treated sample m_s^{raw} can be determined by Eq. (6.2).

$$m_s^{raw} = \frac{m^{TS} LOI^{TS}}{F^{FA} LOI^{FA} + F^{CE} LOI^{CE}} \tag{6.2}$$

where m^{TS} is the mass of treated sample; F^{FA} and F^{CE} are the mass fraction ratio of fly ash and cement of the blended cement paste; and LOI^{TS}, LOI^{FA} and LOI^{CE} are the losses of ignition of treated sample, fly ash and cement at 1000 °C in TGA tests. The LOI^{FA} and LOI^{CE} are summarized in Table. 6.4.

Table. 6.4 Loss of ignition of raw material at 1000 °C

OPC	LPC	FA1	FA2	FA3
2.10%	0.64%	0.83%	1.45%	1.38%

In realistic condition, cement clinkers and hydrated products cannot be completely dissolved (e.g. Table. 6.2 and Table. 6.3) but fly ash can be a little dissolved in dissolving solvent of EDTA with NaOH (e.g. Table. 6.2) [54], the average mass of residue m_{Avg}^R had to be corrected to obtain the actual mass of unreacted fly ash of treated sample $m_{unreacted}^{FA}$ according to Eq. (6.3).

$$m_{unreact}^{FA} = \frac{m_{Avg}^{R} - m_{undissolved}^{CE,HP}}{R^{FA}} \tag{6.3}$$

$$m_{undissolved}^{CE,HP} = m_s^{Raw} F^{CE} \left[\left(1.0 - H^{CE}\right) R^{CE} + H^{CE} R^{HP} \right] \tag{6.4}$$

where $m_{undissolved}^{CE,HP}$ is the mass of undissolved cement and hydration products, which is determined by Eq. (6.4); H^{CE} is the average hydration degree of cement clinkers of blended cement paste, which is determined by XRD-Rietveld tests; and R^{CE}, R^{HP} and R^{FA} are the residue mass percentage of cement clinkers, hydrated products and fly ash after selective dissolution tests, which can be found in Table. 6.2 and Table. 6.3. R^{HP} was approximately estimated by the referenced cement paste of 182 days.

With the actual mass of unreacted fly ash of treated sample $m_{Act}^{R,FA}$ and corresponding mass of raw materials of treated sample m_c^{Raw}, the pozzolanic reaction degree of fly ash can be finally determined by Eq. (6.5).

$$R^{FA} = \left(1.0 - \frac{m_{unreacted}^{FA}}{F^{FA} m_s^{Raw}}\right) \times 100\% \tag{6.5}$$

6.3.2 Selective dissolution test results

Following the test procedures described above, the extent of pozzolanic reaction degrees of these three fly ashes in cement systems were measured by selective dissolution tests with dissolving agent EDTA and NaOH.

Fig. 6.1 presents the comparisons of reaction degrees of different fly ashes at different temperatures. It can be seen that the pozzolanic reaction degrees in cement systems are in good agreement with dissolution processes in alkaline conditions. FA1 and FA2 have similar pozzolanic reactivity and FA2 is a little higher. FA3 is more inactive compared to FA1 and FA2 both at 20 and 60 °C.

This result shows that the dissolution step is the rate-controlling step of pozzolanic reaction of fly ash in cement systems. Therefore, the conclusions and findings in alkali dissolution test should be applied for cement systems as well.

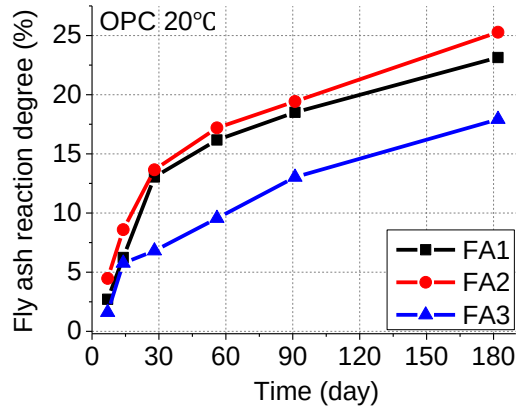

(a) OPC 20 °C

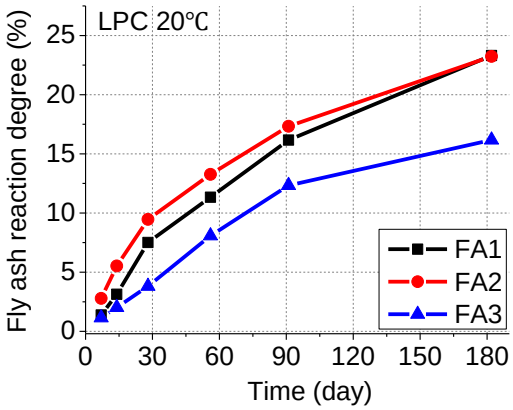

(b) LPC 20 °C

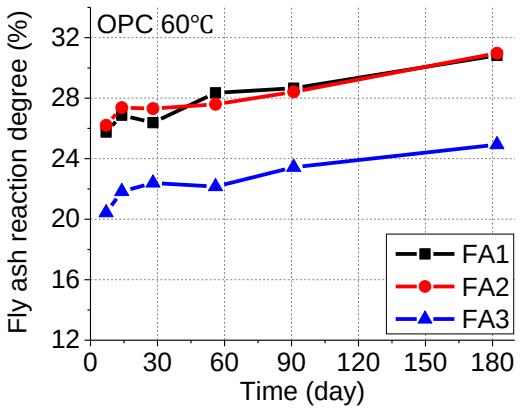

(c) OPC 60 °C

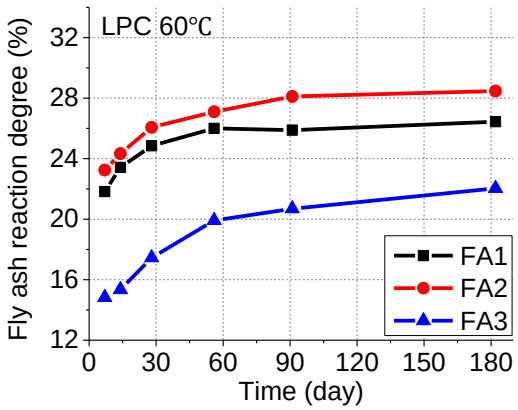

(d) LPC 60 °C

Fig. 6.1 Comparison of fly ash reaction degrees among different fly ashes

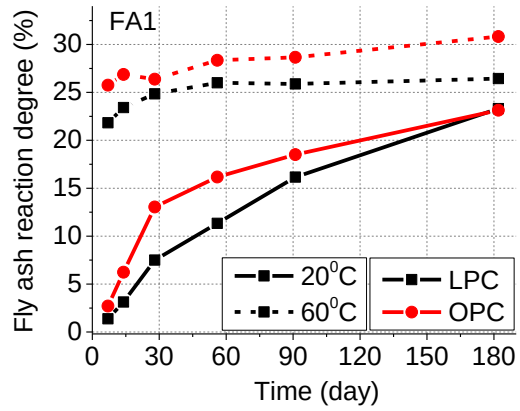

(a) FA1

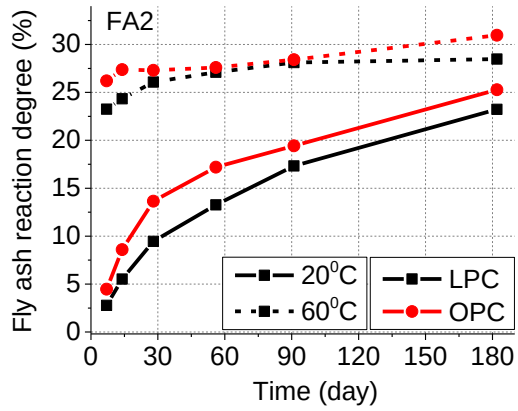

(b) FA2

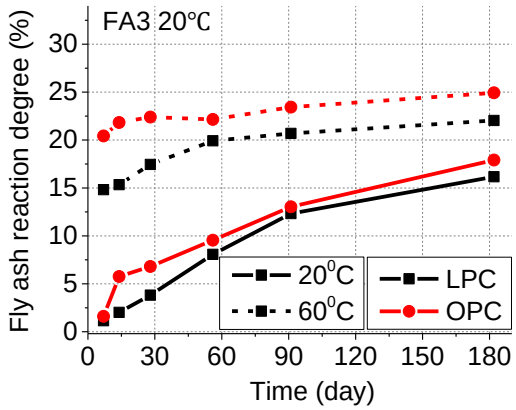

(c) FA3

Fig. 6.2 Comparison of fly ash reaction degrees between OPC and LPC

The temperature effect the influence of cement types were also studied in Fig. 6.2. It can be seen that the pozzolanic reactions of fly ash is temperature sensitive and the pozzolanic reaction processes can be significantly promoted by high temperature at early age. However, the promotion effect of temperature is not obvious in later age and the differences of reaction degrees between different temperatures gradually decreased with time. It is also noted that that pozzolanic reaction degree of fly ash in OPC system is higher than LPC system. These phenomena are probably because the consumption of calcium hydroxide in blended cement paste. A lower calcium hydroxide content results in a smaller possibilities of pozzolanic reaction of fly ash and a more dense C-S-H gel and then a lower diffusion rate of ion. Therefore, the promotion effect of temperature reduces in later age and the pozzolanic reaction degree of fly ash is lower in LPC systems because the calcium hydroxide contents are smaller compared to the referenced cases.

6.4 Calcium hydroxide and bound water content

The calcium hydroxide (CH) and bound water content (BW) content are two important factors to access of the extent of pozzolanic reaction degree of fly ash. In this test, these two parameters were analyzed and determined by TGA tests. Based on the latest researches, a new test procedure and analysis method for TGA test was also developed herein to obtain the accurate test result.

6.4.1 TGA test procedures and analysis method

6.4.1.1 TGA test procedures

The preparation procedures of sample powders had been described in section 6.2. The dehydration method with isopropanol and vacuum was used to keep the phase assemblage intact and avoid any unexpected carbonation as much as possible [9, 45, 64]. A strict protocol on test method was also developed and followed to ensure the comparability of test results.

These tests were conducted using a TGA analyzer of Thermo plus EVO2 (Rigaku) at Saitama University. Approximately 38 mg of powdered sample was placed in 100 μL alumina crucible without a lid. Because powdered sample has a high surface area, a certain amount of isopropanol and physically absorbed water was still remained even under a vacuum drying. Therefore, before testing, similar to the Nitrogen absorption test, tested sample was degassing for 1 hour at 30 °C under a N_2 flow of 50 mL/min to evacuate the remained isopropanol and physically absorbed water. Fig. 6.3 presents the comparison of test result between with and without degassing. It can be seen that this effect significantly affect the test results and it should be taken into account in TGA tests.

After that, heating from 30 to 1000 °C at a heating rate of 15 °C/min was carried out under a protective 50 mL/min N_2 protective gas flow to minimize sample carbonation. An intense sampling of one point per 0.2 s was adopted for future analysis.

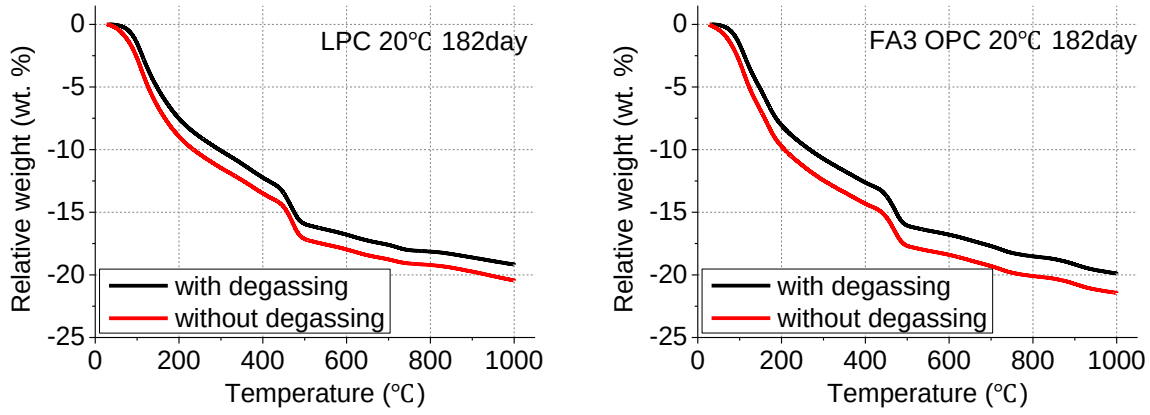

(a) LPC 20 °C 182day (b) FA3-OPC-20 °C 182day

Fig. 6.3 Comparison of TGA test result with and without degassing

6.4.1.2 Analysis method

(a) Data smoothing

Thermogravimetric test is a dynamical progress accompanying with a series of complicated phases decompositions. Therefore, the raw data of TGA test, especially for differential thermogravimetric curve (DTG) and second differential thermogravimetric curve (DDTG), are apparently full with noises (Fig. 6.4) and have to be smoothed by mathematical methods before the chemical analysis.

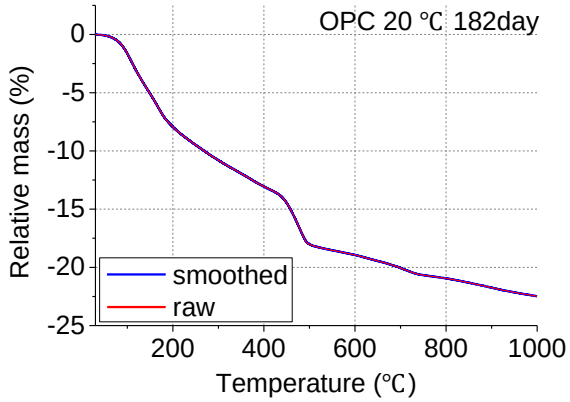

(a) TG curve

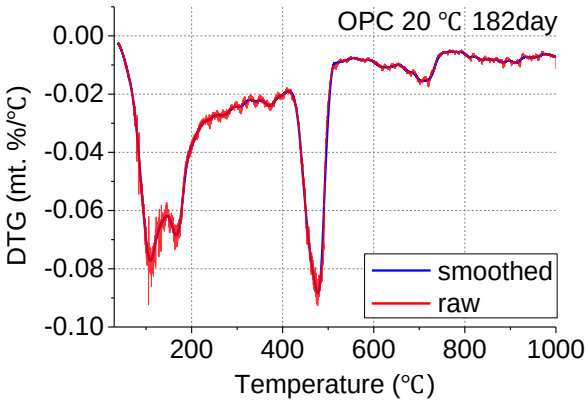

(b) DTG curve

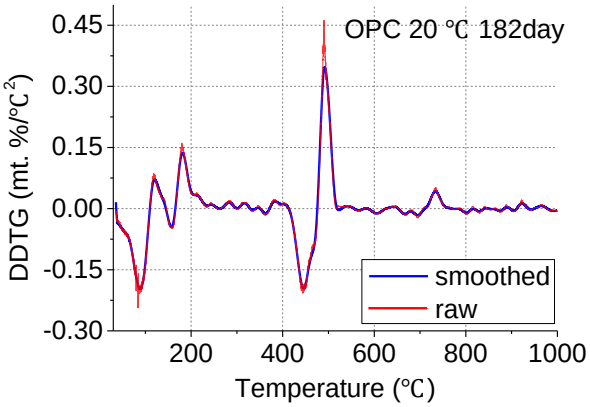

(c) DDTG curve

Fig. 6.4 Comparison of TGA test result before and after data smoothing

Therefore, a smoothing program based on Savitzky-Golay filter with a span of 900 was consequently developed in this test to smooth the experiment result. Fig. 6.4 presented the comparison of TGA test result before and after post-data smoothing. It can be seen that the

noises in experiment result, especially for the DTG and DDTG curves, had been satisfactorily filtered out after post-data smoothing, which paved the way for next step chemical analysis.

(b) Calcium hydroxide content

The pozzolanic reaction of fly ash consumes calcium hydroxide to produce C-S-H gel. The content of calcium hydroxide in paste therefore is an important parameter to access the pozzolanic reactivity of fly ash in cement systems. Besides that, the morphology of C-S-H gel is significantly affected by calcium hydroxide content as well, which will be introduce in next section. Therefore, an accurate estimation for calcium hydroxide content is indispensable for modelling of pozzolanic reaction of fly ash in cement systems. This section is to discuss how to determine calcium hydroxide content in cement pastes by TGA tests.

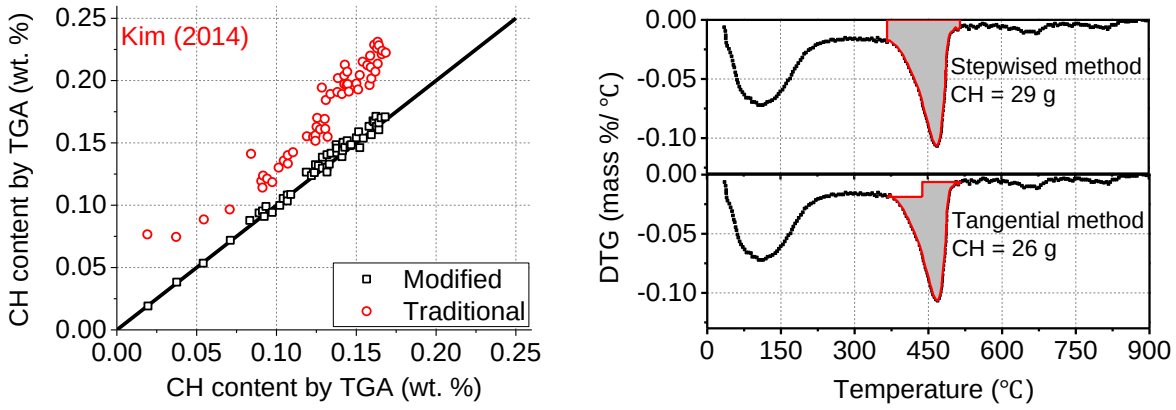

(a) Kim et al experiment [64] (b) Lothenbach et al experiment [45]

Fig. 6.5 Comparison of different analysis method for TGA tests

Calcium hydroxide generally decomposes between 400 and 550 °C to become CaO and H_2O. In literatures, there are usually two methods to quantify the calcium hydroxide content, the traditional stepwise method and the tangential method developed recently. The stepwise method is the simplest method and it often assumes that calcium hydroxide decomposes from 400 and 550 °C and the corresponding mass difference is accordingly used to determine the content of calcium hydroxide according to chemical equation. However, this assumption is highly controversial because the decomposition temperature usually varies with sample preparation, sample mass, atmosphere pressure, heating rate et al [45]. More

importantly, this method overestimates the real calcium hydroxide content as it includes not only the mass loss of the calcium hydroxide but also the mass loss of the C-S-H and any other phases which might lose water in this temperature region. The tangential method assumes that the mass changes due to the presence of C-S-H or other hydrates region is linear in the calcium hydroxide decomposition region. With such a correction, the quantification of the calcium hydroxide mass is the peak area of calcium hydroxide decomposition region, as shown in Fig. 6.5 (b) [45].

Fig. 6.5 shows the previous researches on the comparisons of different methods on determination of calcium hydroxide content in TGA test. For example, Kim et al. verified different methods by differential scanning calorimetry tests (DSC). It was found that stepwise method (traditional interpretation) overestimated the calcium hydroxide content of cement paste and the tangential method (modified interpretation) was in good agreement with DSC tests [64]. Moreover, Lothenbach et al. studied the differences between stepwise method, and tangential method by analyzing a sample containing 75 wt. % of synthetic C-S-H (without calcium hydroxide) and 23 wt. % of calcium hydroxide. Analysis result showed that the stepwise method overestimated the calcium hydroxide content and the tangential method provides the accurate estimation on calcium hydroxide content [45].

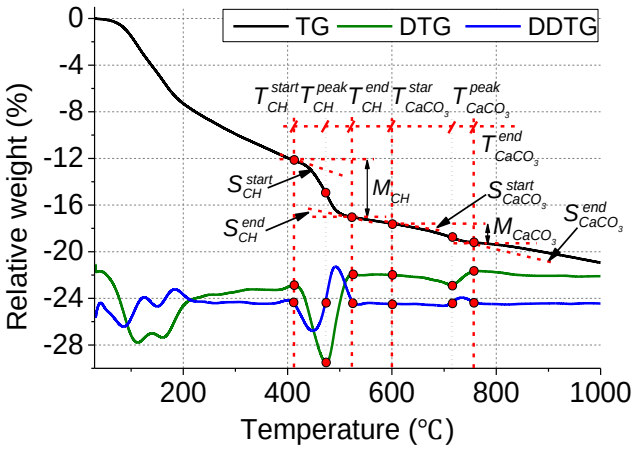

Fig. 6.6 Interpretation of calculation method of calcium hydroxide content in TGA tests

Based on these previous researches [45, 64], a modified tangential method was developed in this test as follows. To accurately determine the calcium hydroxide content, the first step is to find out the decomposition starting point T_{CH}^{start}, peak point T_{CH}^{peak}, and ending point

T_{CH}^{end}. Since these points are the inflection points of thermogravimetric, they can be determined by finding the zero point of the second differential thermogravimetric curve in the decomposition region, as shown in Fig. 6.6. After these points were known, the content of decomposed calcium hydroxide w_{CH1} can be determined by Eq. (6.6) with the assumption that other hydration productions decompose linearly.

$$w_{CH1} = \frac{74.1}{18.0}\left[M_{CH} - S_{CH}^{start}\left(T_{CH}^{end} - T_{CH}^{peak}\right) - S_{CH}^{end}\left(T_{CH}^{end} - T_{CH}^{peak}\right)\right] \tag{6.6}$$

$$M_{CH} = M_{CH}^{start} - M_{CH}^{end} \tag{6.7}$$

where M_{CH} is the mass difference between temperature T_{CH}^{start} and T_{CH}^{end}, which is determined by Eq. (6.7); M_{CH}^{start} and M_{CH}^{end} are the masses of tested sample at temperature T_{CH}^{start} and T_{CH}^{end}; S_{CH}^{start} and S_{CH}^{end} are the slopes of the tangential lines of the starting and ending points of decomposition of calcium hydroxide at temperature T_{CH}^{start} and T_{CH}^{end}, which are determined by averaging the slope values over a short temperature interval $T_{CH}^{start} - 0.5\,°C$ and $T_{CH}^{start} + 0.5\,°C$ respectively.

Although a strict protocol was used to minimize the carbonation, a certain amount of calcium hydroxide still probably carbonates to calcium carbonate during the curing stage and sample preparation. Therefore, this carbonated calcium hydroxide should be taken into account as well. The decomposed calcium carbonate w_{CaCO_3} was computed with the same procedure as that used for calcium hydroxide, i.e. Eq. (6.8), as shown in Fig. 6.6. Because cement and fly ash always contains limestone, the initial calcium carbonate $w_{CaCO_3}^{CE}$ of anhydrous cement and fly ash $w_{CaCO_3}^{FA}$ was also considered in this method, which is measured from the same method for hydrated sample. With these two calcium carbonate content, the content of carbonated calcium hydroxide w_{CH2} can be determined by Eq. (6.8).

$$w_{CH2} = \begin{cases} \dfrac{74.1}{100.1}\left(w_{CaCO_3} - w_{CaCO_3}^{CE+FA}\right) & w_{CaCO_3} \geq w_{CaCO_3}^{CE+FA} \\ 0 & w_{CaCO_3} < w_{CaCO_3}^{CE+FA} \end{cases} \tag{6.8}$$

$$w_{CaCO_3} = \frac{100.1}{44.0}\left[M_{CaCO_3} - S^{start}_{CaCO_3}\left(T^{peak}_{CaCO_3} - T^{start}_{CaCO_3}\right) - S^{end}_{CaCO_3}\left(T^{end}_{CaCO_3} - T^{peak}_{CaCO_3}\right)\right] \tag{6.9}$$

$$M_{CaCO_3} = M^{start}_{CaCO_3} - M^{end}_{CaCO_3} \tag{6.10}$$

$$w^{CE+FA}_{CaCO_3} = F^{CE} w^{CE}_{CaCO_3} + F^{FA} w^{FA}_{CaCO_3} \tag{6.11}$$

where w_{CaCO_3} is the mass of decomposed calcium carbonate determined by Eq. (6.9) according to tangential method as shown in Fig. 6.6; $w^{CE+FA}_{CaCO_3}$ is the initial content of calcium carbonate of blended cement paste, which is determined by Eq. (6.11); $w^{CE}_{CaCO_3}$ and $w^{FA}_{CaCO_3}$ are initial content of calcium carbonate of anhydrous cement and unreacted fly ash; F^{FA} and F^{CE} are the mass fraction ratio of fly ash and cement of the blended cement paste. M_{CaCO_3} is the mass difference between temperature $T^{start}_{CaCO_3}$ and $T^{end}_{CaCO_3}$, which is determined by Eq. (6.10); $M^{start}_{CaCO_3}$ and $M^{end}_{CaCO_3}$ are the masses of tested sample at temperature $T^{start}_{CaCO_3}$ and $T^{end}_{CaCO_3}$; and $S^{start}_{CaCO_3}$ and $S^{end}_{CaCO_3}$ are the slopes of the tangential lines of the starting and ending points of decomposition of calcium carbonate at temperature $T^{start}_{CaCO_3}$ and $T^{end}_{CaCO_3}$, which are determined by averaging the slope values over a short temperature interval $T^{start}_{CaCO_3} - 0.5\,°C$ and $T^{start}_{CaCO_3} + 0.5\,°C$;

With the two decomposed calcium hydroxide content w_{CH1} and carbonated calcium hydroxide content w_{CH2}, the calcium hydroxide content of raw materials (i.e. anhydrous cement and unreacted fly ash) w_{CH} is consequently determined by

$$w_{CH} = \frac{w_{CH1} + w_{CH2}}{m^s_{raw}} \times 100\% \tag{6.12}$$

where m^s_{raw} is the corresponding mass of raw materials of treated sample, which is determined by Eq. (6.2).

A verification test for OPC samples was conducted by comparing the TGA result (TGA-50, Shimadzu) and DSC (DSC-60, Shimadzu). Fig. 6.7 shows the comparison of decomposed calcium hydroxide content. It can be seen that the developed method provides a good consistency between TGA and DSC results.

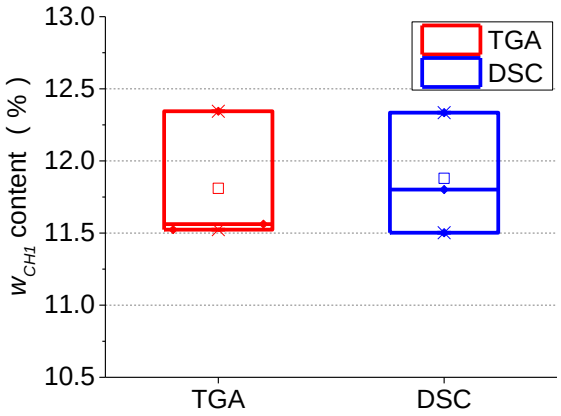

Fig. 6.7 Verification of the proposed tangential method in determining decomposed calcium hydroxide content in TGA test

(c) Bound water content

Bound water is another important parameter to access the hydration of cement and pozzolanic reaction of fly ash. This section is to discuss how to determine the bound water content of blended cement paste by TGA tests.

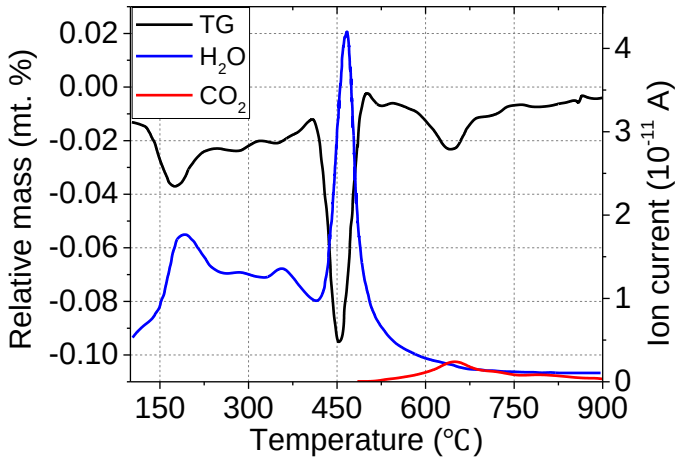

Fig. 6.8 Experiment result of TGA-FTIR test [65]

De Weerdt et al. analyzed the type and the amount of gaseous reaction products in TGA test by Fourier transform infrared spectroscopy (FTIR). They found that mass loss up to the ending of decomposition of calcium hydroxide is generally related to the loss of water and after that mainly to the release of CO_2 [65]. Therefore, the definition of bound water in this

study is the masses loss from 30 °C to the ending point of the decomposition of calcium hydroxide T_{CH}^{end} with the bound water content of carbonated calcium hydroxide w_{CH2} .

$$w_{BW} = M_d^{30°C} - M_{CH}^{end} + \frac{18.0}{74.1} w_{CH2} \tag{6.13}$$

where $M_d^{30°C}$ is the mass of tested sample at 30 °C after degassing. M_{CH}^{end} and w_{CH2} are the same definition in Eq. (6.7) and Eq. (6.8).

6.4.2 TGA test result

6.4.2.1 Calcium hydroxide content

All cement pastes and fly ash blended cement pastes from 7 to 182 days were analyzed by TGA tests following the procedures described above. The second differential thermogravimetric curves are all summarized in appendix. B. With the modified tangential method, the calcium hydroxide content was determined, as shown in Fig. 6.9 and Fig. 6.10.

Fig. 6.9 shows the calcium hydroxide content of cement paste. It is interesting to note that the calcium hydroxide content at high temperature of 60 °C is lower than room temperature of 20 °C both in OPC and LPC systems. That is very likely because the Ca/Si ratio of C-S-H gel increases as curing temperature increases. Elkhadiri et al. analyzed the Ca/Si ratio of the inner and outer C-S-H products of cement paste at a water-cement ratio of 0.3 under different curing temperatures. They found that Ca/Si ratio increased as the temperature increased [66]. Therefore, less calcium hydroxide is produced at high temperature since the Ca/Si ratio of C-S-H gel increases. In other words, more calcium element participates to produce C-S-H gel and then the calcium hydroxide content accordingly decreases at high temperature.

Table. 6.5 Ca/Si ratio of C-S-H gel for cement paste (CEM I 42.5R) [66]

2 day	4 ℃	22 ℃	40 ℃	85 ℃
Outer	1.90 ± 0.23	2.00 ± 0.23	2.24 ± 0.24	2.30 ± 0.30
Inner	2.10 ± 0.33	2.15 ± 0.15	2.17 ± 0.18	2.23 ± 0.25
28 day	4 ℃	22 ℃	40 ℃	85 ℃
Outer	1.74 ± 0.22	1.78 ± 0.13	1.84 ± 0.17	2.39 ± 0.36
Inner	2.02 ± 0.34	1.93 ± 0.15	1.98 ± 0.14	2.14 ± 0.27

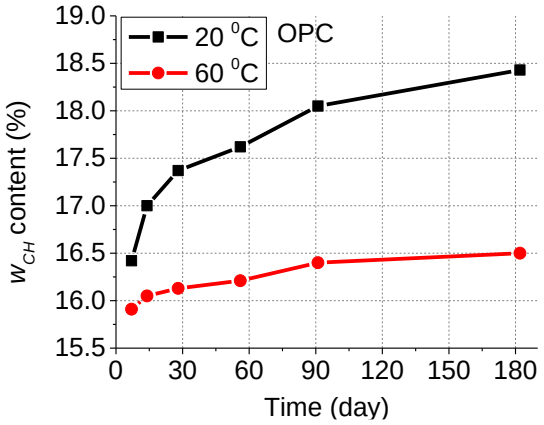

(a) OPC

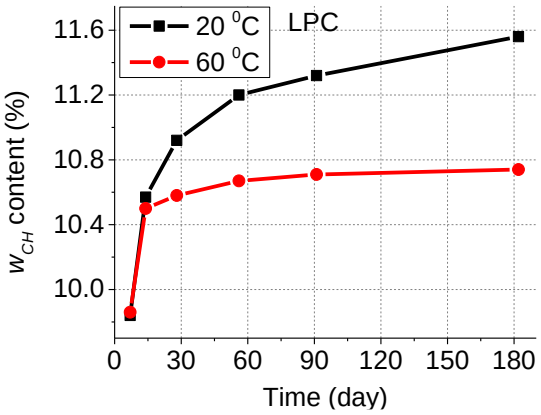

(b) LPC

Fig. 6.9 Calcium hydroxide content of cement pastes

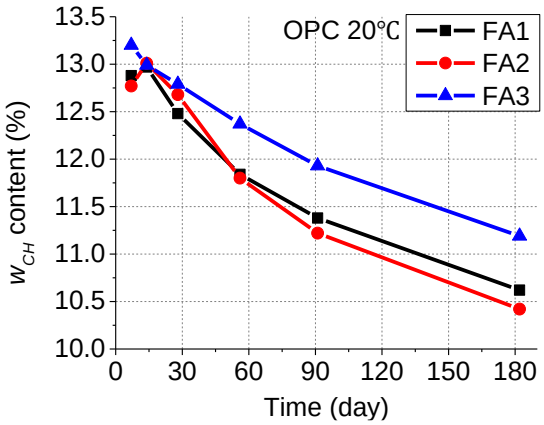

(a) FA OPC 20 °C

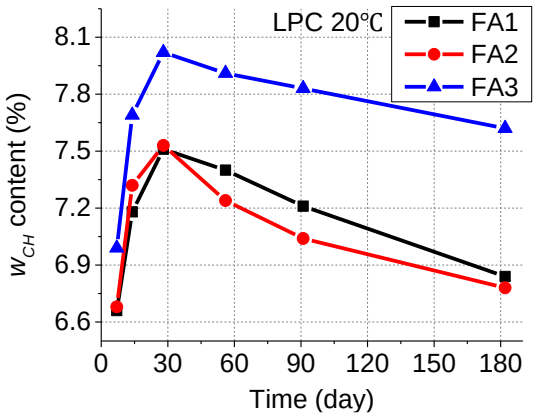

(b) FA LPC 20 °C

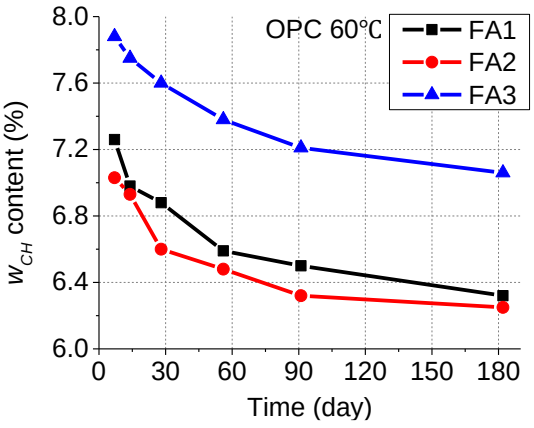

(c) FA OPC 60 °C

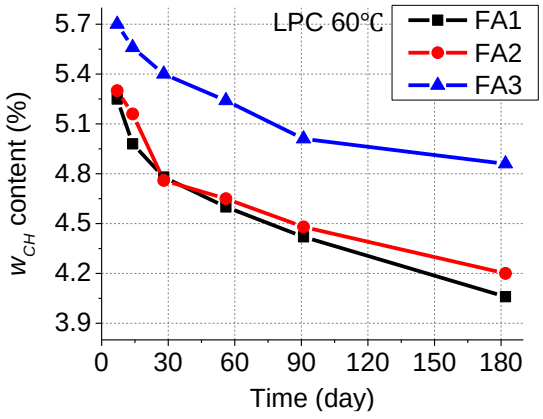

(d) FA LPC 60 °C

Fig. 6.10 Calcium hydroxide content of blended FA cement pastes

The calcium hydroxide content of FA blended cement pastes were illustrated in Fig. 6.10. It showed that FA1 and FA2 has similar calcium hydroxide content but FA3 is higher. In other words, the FA1 and FA2 have a similar pozzolanic reactivity but FA3 is less reactive, which is in good agreement with the selective dissolution test and alkali dissolution test as well.

6.4.2.2 Bound water content

The bound water content of cement paste and FA blended cement paste were analyzed by TGA tests and the modified method described above. Fig. 6.11 shows the result of cement paste. It can be seen that the bound water content of OPC and LPC cement paste both increased at room temperature of 20 °C with time. In contrast, at high temperature, the bound water continuously decreased after 28 days both in OPC and LPC cement paste. That is because some hydration products, like ettringite, continuously loss their bound water during long-term high temperature curing even the curing temperature has not reach up to the decomposition temperatures of these hydration products.

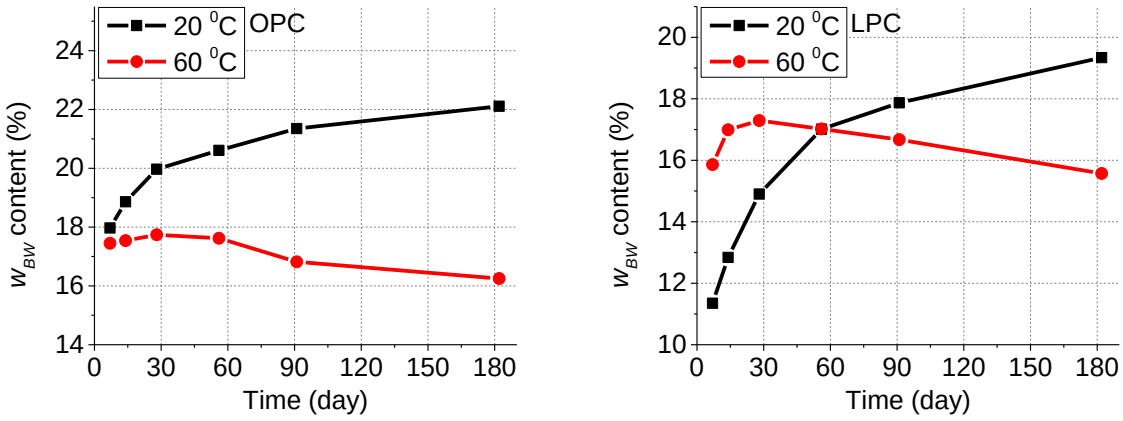

(a) OPC (b) LPC

Fig. 6.11 Bound water content of cement pastes

The bound water of FA blended cement pastes are illustrated in Fig. 6.12. It can be seen that the three fly ashes had similar bound water contents. That is because most bound water content comes from the hydration products of cement clinkers. The differences due to fly ashes are relatively small and covered by cement hydration products. Similar to cement pastes, the bound water of FA blended cement paste also continuously decreased at later age

under high temperature curing. Therefore, bound water content is not suitable to access pozzolanic reactivity of fly ash in cement systems.

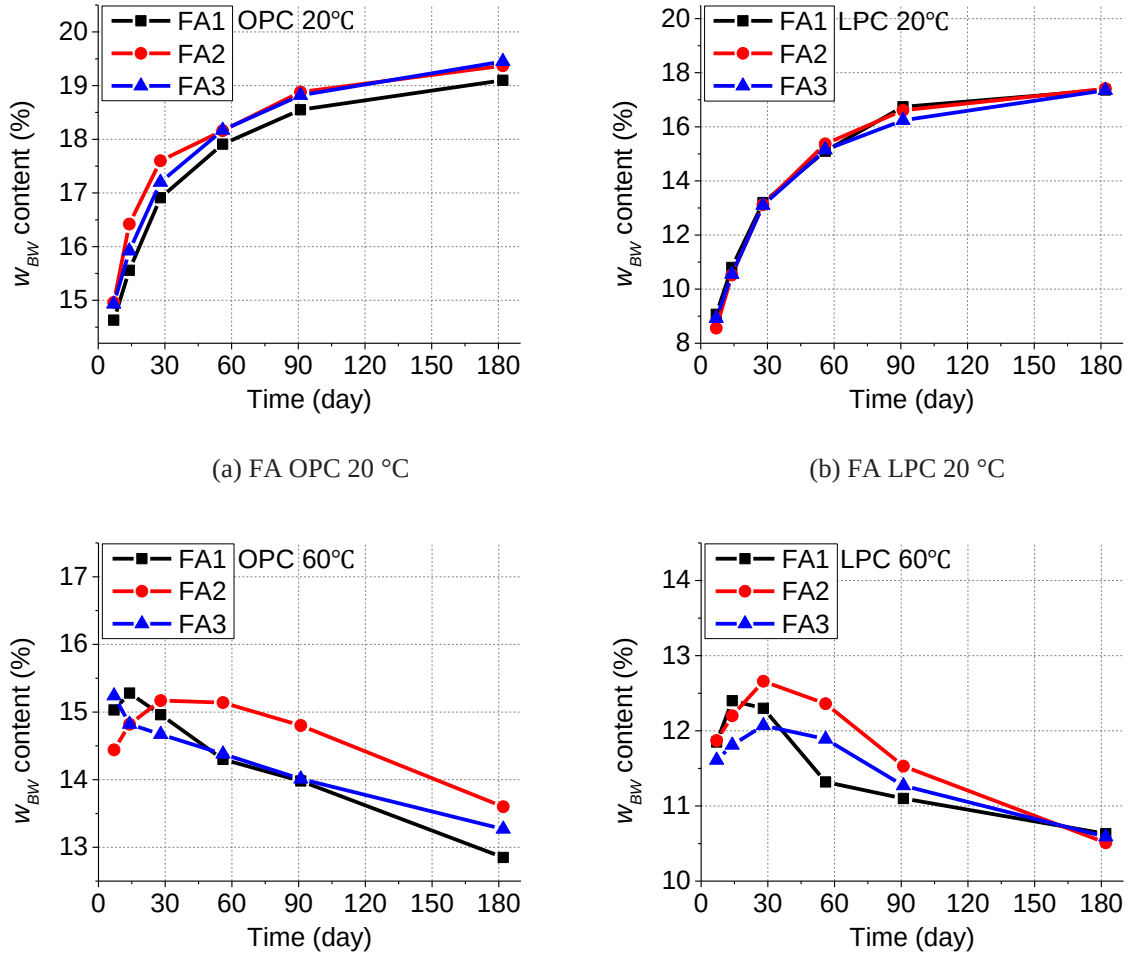

(a) FA OPC 20 °C

(b) FA LPC 20 °C

(c) FA OPC 60 °C

(d) FA LPC 60 °C

Fig. 6.12 Bound water content of FA blended cement pastes

6.5 Hydration degrees of cement clinkers

Previous researches points out that the hydration processes were retarded by fly ash. Therefore, the hydration degrees of fly ash blended cement paste were investigated by XRD-Rietveld method in this test. Based on the experiment data and previous researches, the mechanism and hypothesis on this phenomenon was discussed in this section as well.

6.5.1 XRD test and Rietveld refinement analysis procedures

In this test, X-ray diffraction with Rietveld refinement analysis was used to determine the hydration degrees of cement clinkers in cement paste and FA blended cement paste. XRD tests on powdered sample mixed with 10 mass % corundum as internal standard was conducted by X-ray diffractometer of Shimadzu XRD 6100 under test conditions mentioned in section 3.2.3.

Rietveld analysis was carried out after measurement by software Siroquant version 3. Alite (C_3S, Belov and mono.), belite (C_2S, Beta), aluminate phase (C_3A, cubic and ortho.), ferrite phase (C_4AF), ettringite ($C_3A{\cdot}3C\$\cdot H_{32}$), portlandite (CH), monosulfate ($C_3A{\cdot}C\$\cdot H_{12}$), monocarbonate ($C_3A{\cdot}Cc\cdot H_{11}$), hemicarbonate ($C_3A{\cdot}Cc_{0.5}\cdot H_{12}$), katoite ($C_3AH_6$) calcite (Cc) and corundum (α-A) was selected into Rietveld refinement analysis of cement paste. For FA blended cement paste, silicated katoite ($C_3A{\cdot}S_{2.16}\cdot H_{1.6}$), mullite (3A·2S), quartz (S), free-lime (C), magnetite (F) were also selected. More technician details can be referred to section 3.2.3.

To improve the experiment quality, each sample were done 3 times XRD tests and the average masses of anhydrous cement clinkers were accordingly obtained and then used to determine the hydration degrees. With the average Rietveld refinement analysis result, the hydration degrees of each cement clinker phases were determined by Eq. (6.14)

$$H_I^{CE} = \left(1.0 - \frac{m_{I,unhydrated}^{CE}}{F^{CE} m_s^{Raw} C_I^{CE}}\right) \times 100\% \tag{6.14}$$

$$m_{I,unhydrated}^{CE} = M_d^{30°C} f_{Ava,i}^{c} \tag{6.15}$$

where $m_{I,unhydrated}^{CE}$ is the mass of unhydrated cement clinker phase I in powdered sample according to Eq. (6.15); C_I^{CE} is the mass ratio of cement clinker phase I of the specified cement, which can be referred to Table. 6.1; and $f_{Ava,i}^{c}$ is the average mass fraction of unhydrated cement clinker phase I in powdered sample. The symbols m_s^{Raw} and $M_d^{30°C}$ are same to Eqs. (6.2) and (6.13).

6.5.2 Cement clinkers hydration degrees

According to Eqs. (6.14) and (6.15), the hydration degrees of cement paste and FA blended

cement paste were determined by and summarized in appendix. C. To study the FA effect on cement clinkers, comparisons on alite and belite at different temperatures were made and illustrated in Fig. 6.14 and Fig. 6.13 respectively. It can be seen that the extent of alite hydration degrees of FA blended cement paste were lower than LPC cement paste at 60 °C.

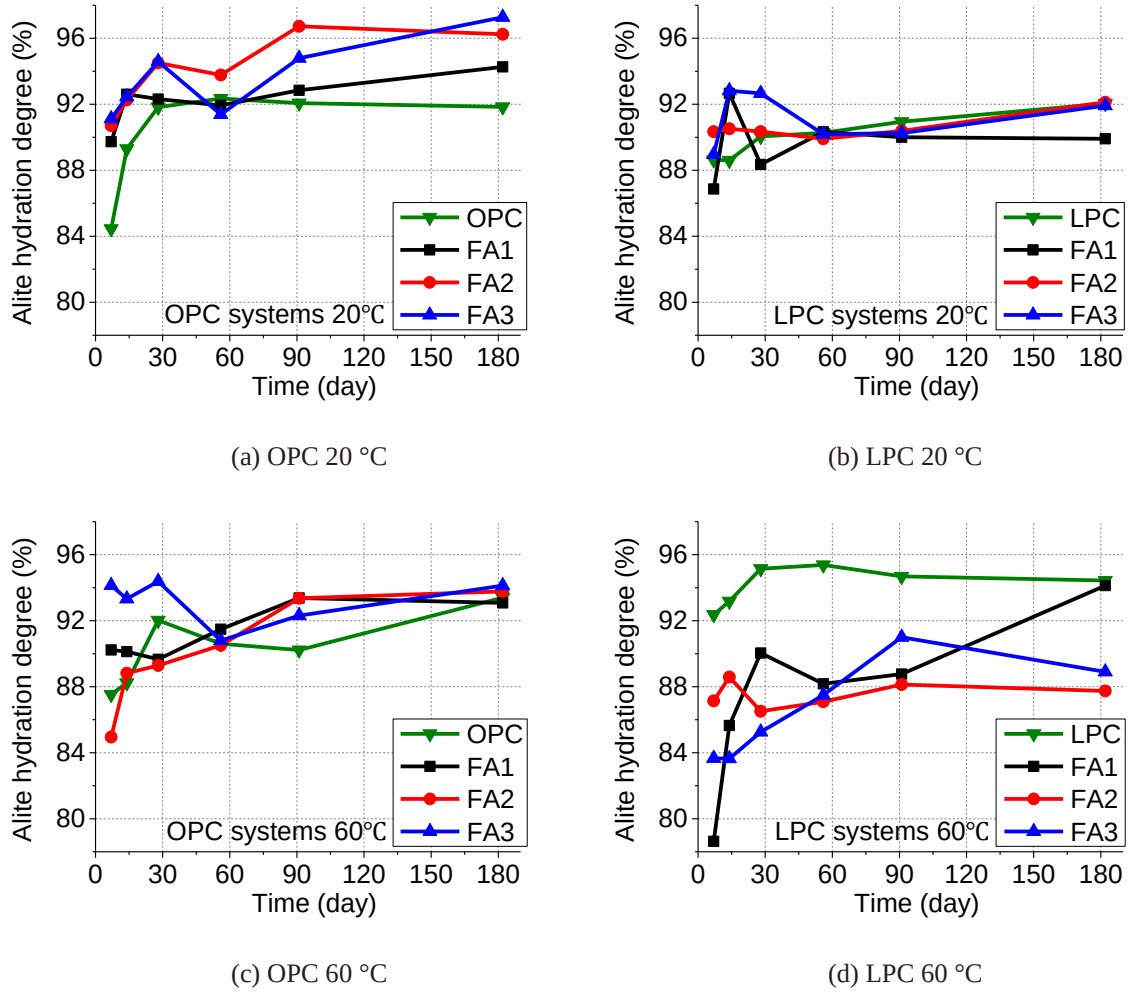

(a) OPC 20 °C

(b) LPC 20 °C

(c) OPC 60 °C

(d) LPC 60 °C

Fig. 6.13 Comparison of Alite hydration processes between cement and FA blended paste

Compared to alite, the influence of fly ash on belite is clearer. Fig. 6.13 clearly shows that the extent of belite hydration degrees of FA blended cement paste is higher than both OPC and LPC cement paste at room temperature of 20 °C but lower than cement pastes at high temperature of 60 °C. Similar phenomenon were found in previous researches as well. For example, Sakai et al. found that belite hydration process was retarded by fly ash at later age at 20 °C (Fig. 2.16 (a)) [32]. Kawabta et al. found that this retarded effect was promoted at high temperature. The belite hydration in FA blended cement paste was only around one third of

cement paste in 91 day at 40 °C (Fig. 2.16 (b)) [37].

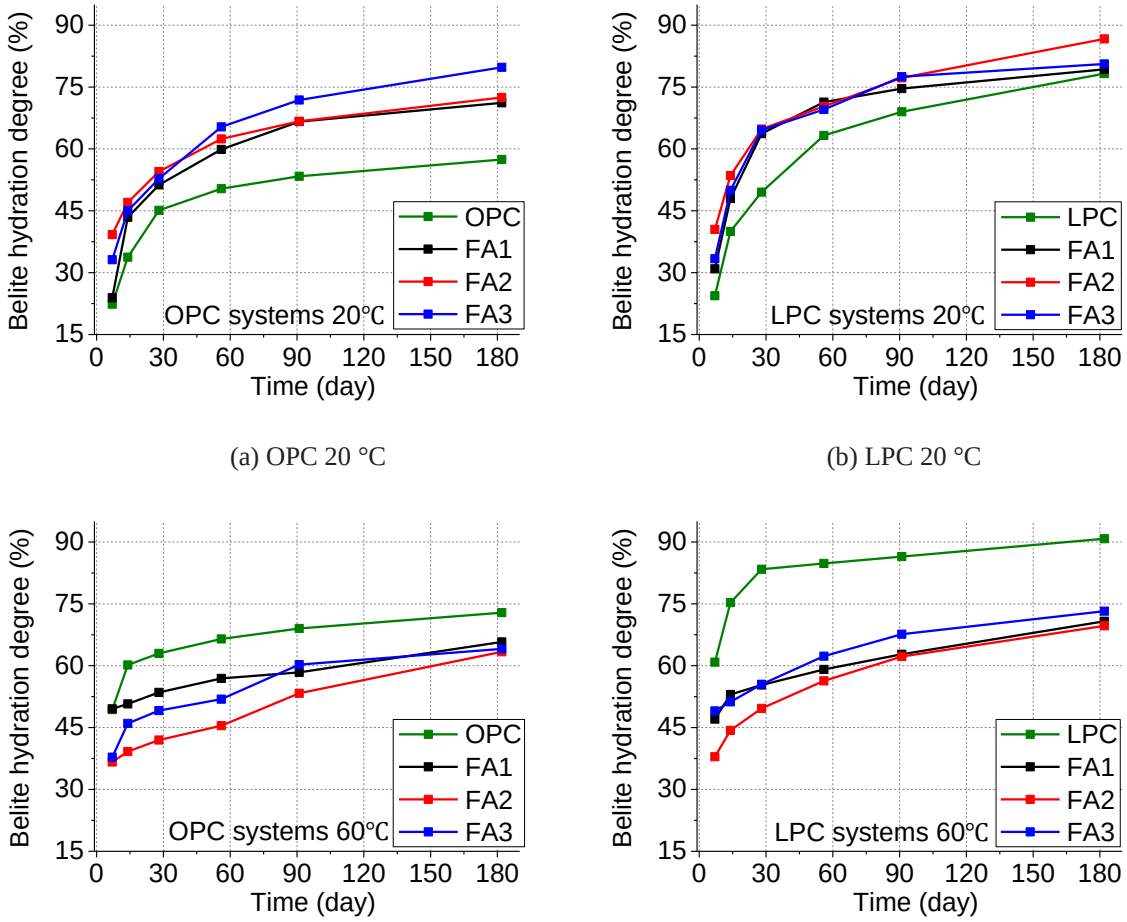

(a) OPC 20 °C

(b) LPC 20 °C

(c) OPC 60 °C

(d) LPC 60 °C

Fig. 6.14 Comparison of Belite hydration processes between cement and FA blended paste

6.5.3 Interaction between cement clinkers and fly ash

Last section compared the extent of hydration degrees of cement clinkers of cement paste to FA blended cement paste. It is found that the alite hydration was retarded by fly ash at high temperature in LPC system. Compared to alite, the belite hydration was promoted by fly ash at room temperature of 20 °C but retarded at high temperature of 60 °C. Such phenomena are believed as the result of the competition between filler effect and dilute effect and the morphology effect induced by consumption of calcium hydroxide. This section is going to study the mechanism of the interaction between cement clinkers and fly ash at length.

6.5.3.1 C-S-H gel morphology effect

As we well know, the hydration rate of cement clinkers gradually decreases and follows a dissymmetric sigmoid law (Fig. 6.15). This is because the fact that C-S-H gel grows on the surface of anhydrous cement grains and builds a diffusion barrier between cement grains and pore solutions. Therefore, diffusion is the controlling process of cement hydration at later age.

Nonat et al. studied the effect of C-S-H gel layer on belite and alite hydration processes by investigating the hydration rate of synthetic tricalcium and dicalcium silicate (i.e. synthetic C_3S and C_2S) in prepared solutions with different calcium hydroxide concentrations [36]. They found that although the calcium hydroxide suppressed the dissolution of synthetic grains, the hydration rate of synthetic grains interestingly increased as calcium hydroxide concentration increased in later age (Fig. 6.15) [34].

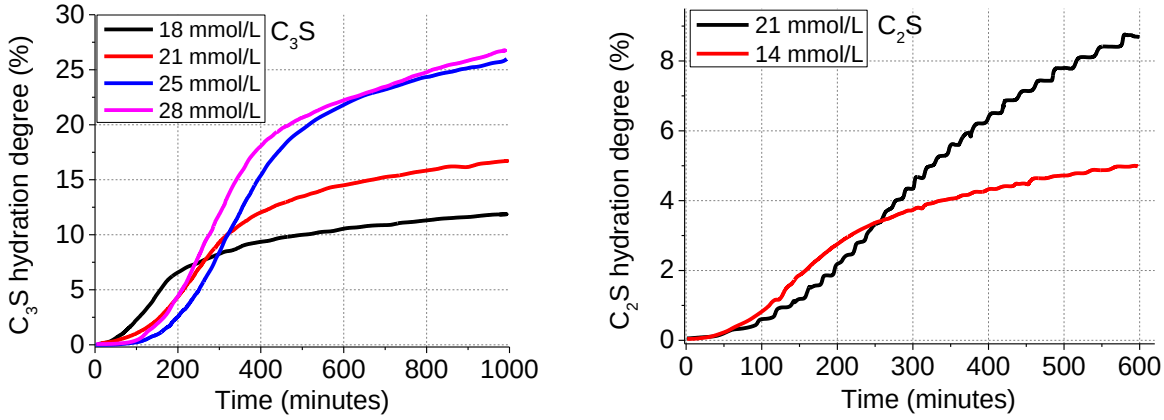

(a) synthetic tricalcium silicate hydration process (b) synthetic dicalcium silicate hydration process

Fig. 6.15 Comparison of hydration processes of synthetic belite and alite in different calcium hydroxide concentrations [34]

The reason is that morphology of C-S-H gel precipitated on the surface of anhydrous synthetic grains varies with calcium hydroxide concentrations. It is found that the C-S-H gel tends to growth parallel to the surface of anhydrous cement grains at low calcium hydroxide content but perpendicular to the surface at high calcium hydroxide content [36], which was further confirmed by the surface representation of C-S-H gel measured by atomic force microscope (AFM) (Fig. 6.17) in later research [33]. Therefore, the diffusion processes between pore solution and anhydrous cement grains becomes more difficult and the hydration

processes of cement grains are accordingly suppressed at low calcium hydroxide content at later age because the C-S-H more completely covers the surface of anhydrous cement grains.

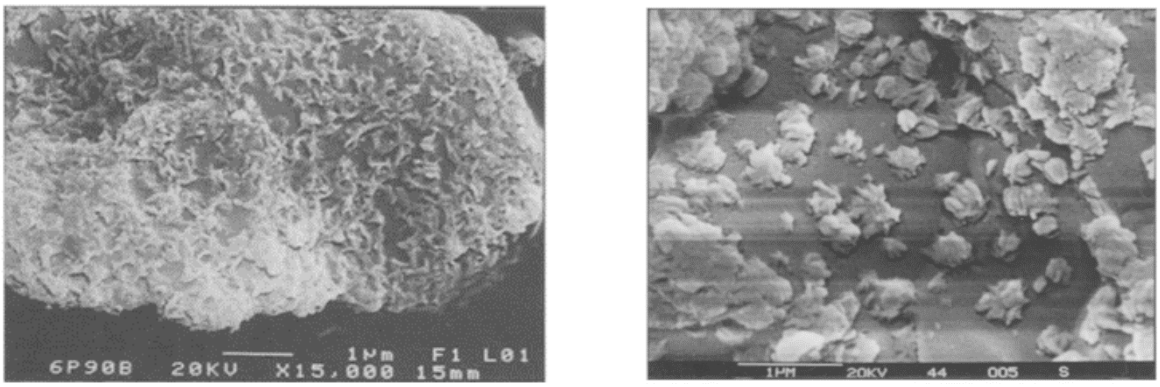

(a) low CH concentration (b) high CH concentration

Fig. 6.16 Morphologies of C-S-H on the surface of synthetic tricalcium silicate [34]

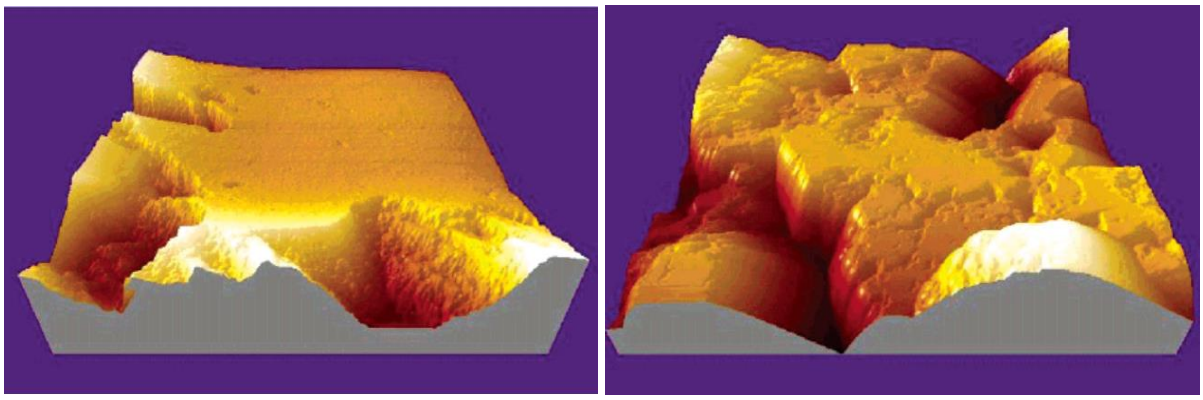

(a) low CH concentration (b) high CH concentration

Fig. 6.17 Surface representation of C-S-H on the surface of synthetic tricalcium silicate gel measured by AFM [33]

Nonat et al. further pointed out the varication of morphology of C-S-H gel was induced by the complicate interaction of C-S-H gel in nono-scale [33]. They measured the nano-interaction between C-S-H gel by AFM in different solutions, as shown in Fig. 6.18 (a) [33]. Experiment result showed that the interaction is purely repulsive at lowest calcium hydroxide concentration of 3.15 mmol/L and attraction-repulsion interactions appeared when the calcium hydroxide concentration was over than 3.15 mmol/L. For the high calcium hydroxide concentration, the nano-interaction become purely attractive [33]. This such variation is

because the nano-interaction is a resultant force of born repulsion, van der Walls attraction, electrostatic repulsion and DLVO potential (Fig. 6.18 (b)) [67]. The latter two nano-force are varied with ionization degrees and charge density of the C-S-H gel particles, which depend on solution condition and chemical composition [33, 36, 68-70]. The maximum adhesion force of C-S-H gel thus increases with increase of pH and calcium concertation (pH effect is more dominated), as shown in Fig. 6.19. Therefore, the C-S-H gel tends to parallelly growth at low calcium hydroxide content but perpendicularly at high calcium hydroxide content, as shown in Fig. 6.16 and Fig. 6.17.

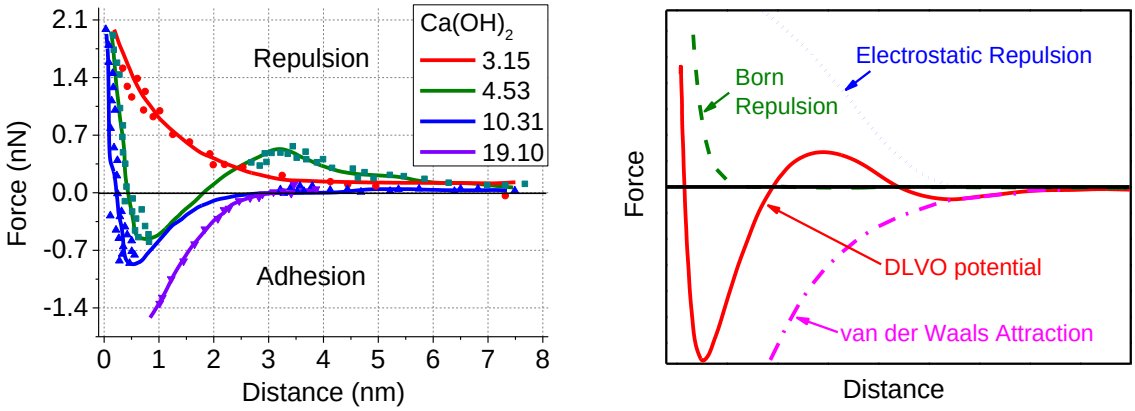

(a) interaction forces of C-S-H gel [33] (b) schematic illustration diagram [69]

Fig. 6.18 Interaction forces of C-S-H gel and the schematic illustration [33, 69]

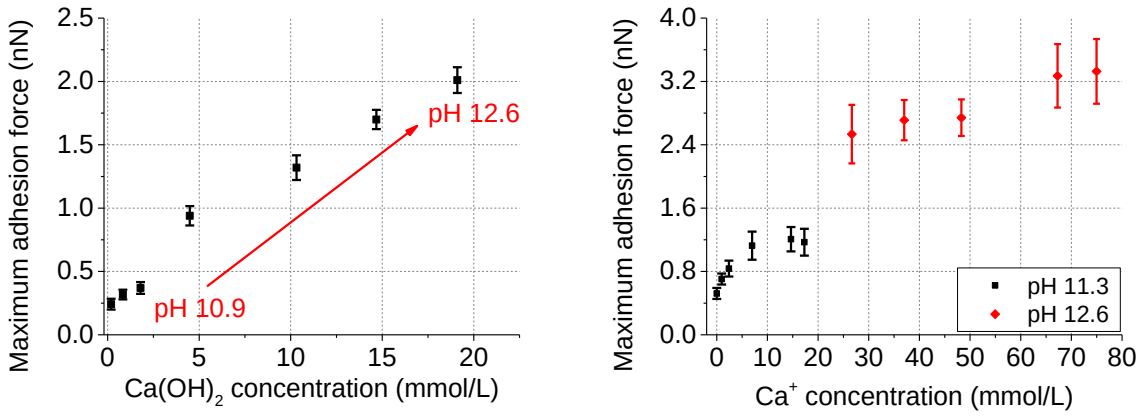

(a) pH effect (b) Ca concentration effect

Fig. 6.19 Maximum adhesion force in different conditions [33]

Based on previous findings and discussions, Ioannidou et al. investigated the

development of gels and its corresponding effect on cement hydration in different calcium hydroxide concentrations by molecular dynamics (MD) simulations with Grand Canonical Monte Carlo method [69, 70]. The simulation result showed that the C-S-H did tend to locally aggregate at high calcium hydroxide concentration but elongatedly and branchedly growth at low calcium hydroxide concentration (Fig. 6.20). The hydration rate therefore decelerate at later age is due to the compact cover of C-S-H gel at low calcium hydroxide concentration, as shown in Fig. 6.21. [69, 70].

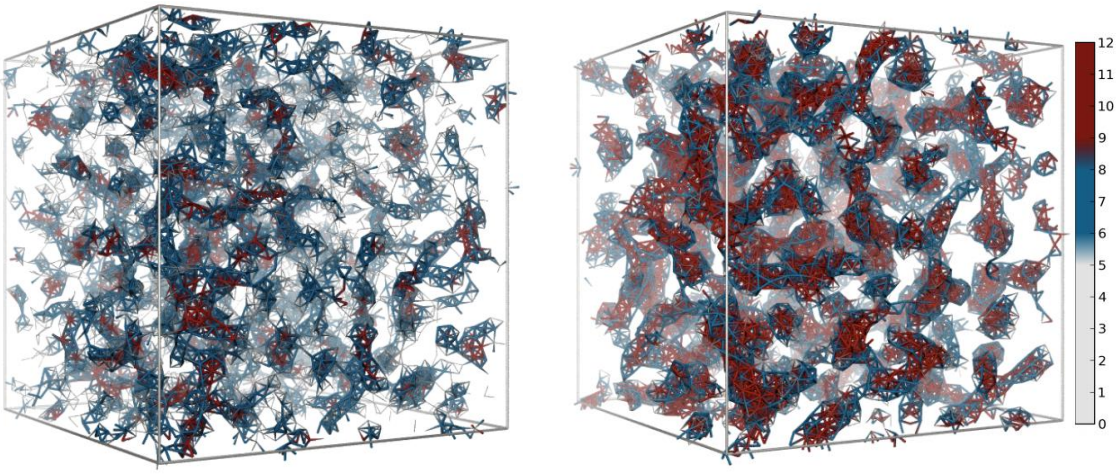

(a) low pH (b) high pH

Fig. 6.20 Simulated bond representations of C-S-H at low and high pH by MD methods. The color code corresponds to the particle coordination number. [70]

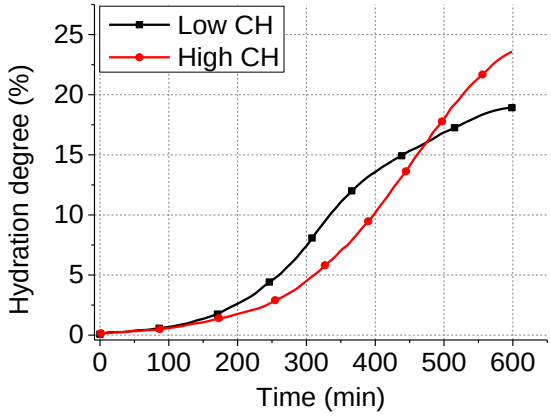

Fig. 6.21 Simulated hydration processes at low and high pH by MD methods [70]

6.5.3.2 C-S-H gel morphology test

Previous research had theoretically explained the mechanism on precipitation and gelation of C-S-H gel and its corresponding effect on cement clinker hydration processes, however, there is still lack of a direct observation on the pore solution influence on the morphology of C-S-H gel. Therefore, a C-S-H gel morphology test was conducted in this study to further verify previous mechanism.

According to Nonat et al. research, the most important parameter on C-S-H gel morphology is the pH of the solution. Therefore, this test is focused on the pH effect. Two tested solution simulated the pore solution of cement paste were prepared by mixing the low heat Portland cement of 20 g with deionized water of 1 L in plastic bottles at 1500 rpm for 30 minutes respectively. The tested solution was stood for 6 hours to ensure the anhydrous cement particles mostly precipitate on the bottom. Two 600 ml of tested solution was then carefully extracted into a plastic bottle and 300 ml water or NaOH of 1 M were subsequently added into to adjust the pH to 11.90 and 13.05 respectively. These two tested solution therefore had the same calcium concertation and nuclei quantity but different pH. The two tested solutions were stood for another 24 hours again to let the C-S-H growth. After that, the C-S-H gel was collected by filtrating through a Whatman GF/B filter (minimum particle size retained 1.0 μm) and rinsed by deionized water and isopropanol subsequently.

(a) low pH (b) high pH

Fig. 6.22 Collected C-S-H gel from different pH conditions

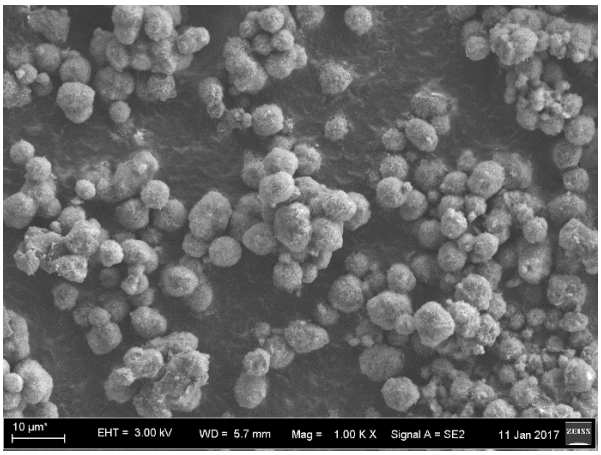

(a) low pH (1000x)

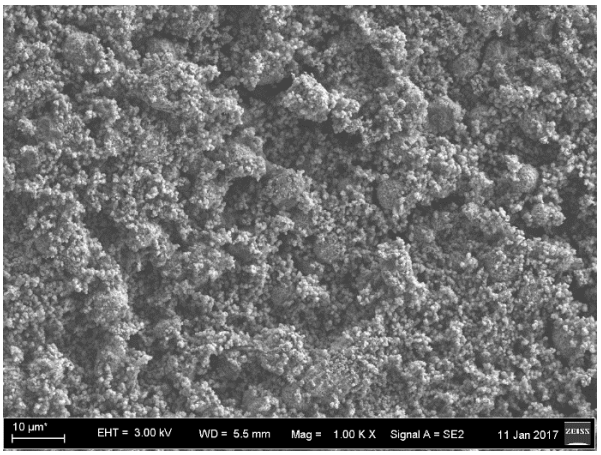

(b) high pH (1000x)

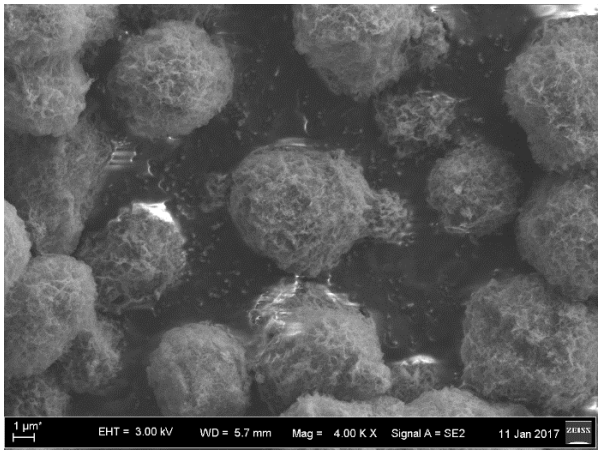

(c) low pH (4000x)

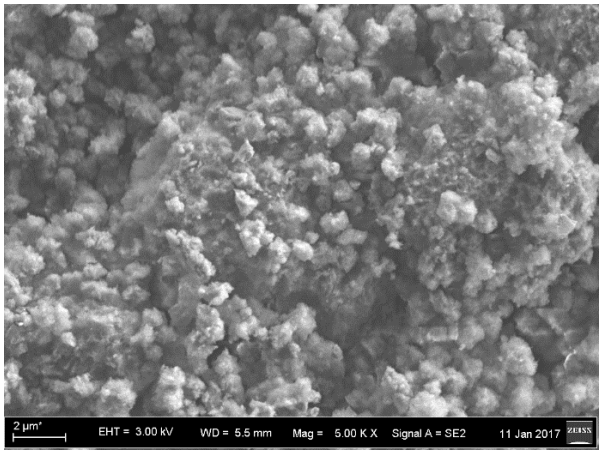

(d) high pH (5000x)

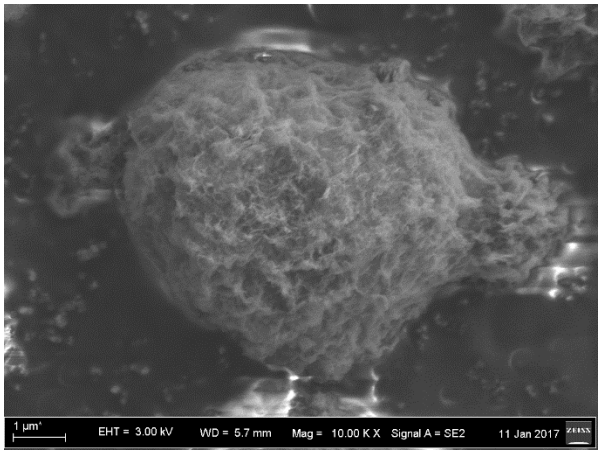

(e) low pH (10000x)

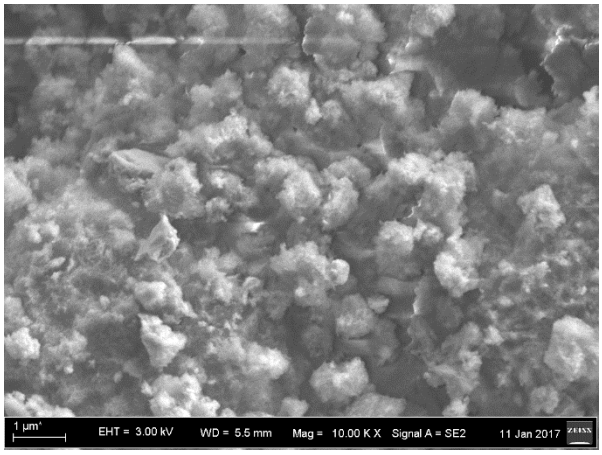

(f) high pH (10000x)

Fig. 6.23 Micro observation of C-S-H gel from different pH conditions

Fig. 6.22 showed the collected C-S-H gel from different pH solutions. The difference between these two C-S-H gels already can be distinguished by naked eyes. The C-S-H gel from high pH was more like “gel” and “moist” and the color was whiter but the C-S-H gel from low pH was “drier” and “grayer”.

These two different C-S-H gel were further investigated and observed by SEM of ZEISS Merlin at SUSTech as well. Fig. 6.23 showed the micro details of these C-S-H gel at magnification from 1000 to 10000. It can be seen that, at high pH, the C-S-H gel aggregated together and a lot of small particles predicated on the bigger one. Compared to the high pH case, the C-S-H gel at low pH tended to exist alone and homogenously growth in all directions and then more like a sphere. The surface of low pH C-S-H gel was cleaned and clear and there was no small C-S-H gel predicated. Such observation are in good agreement with previous theoretical expectation that the C-S-H gel tends to growth parallel to the surface of nuclei at low pH but perpendicular to the surface at high pH.

6.5.3.3 Hypothesis for Interaction between fly ash and cement clinkers

Based on previous discussion, the fly ash influence on hydration process of cement clinkers is believed as the result of the competition between filler effect and dilute effect and the morphology effect. As we know, hydration of cement clinkers in blended cement paste is promoted by fly ash due to the dilute effect (i.e. W/C ratio increases under same W/B ratio) and filler effect (i.e. fly ash particles provide additional precipitate sites for hydration products). In the other hand, as the calcium hydroxide is continuously consumed by fly ash, the pH and calcium concentration of pore solution decreases and C-S-H gel prefers to growth parallel to the surface of anhydrous cement grains and more densely cover, which finally results in a slower hydration rate of inner cement grains. Therefore, the cement hydration is accelerated or retarded that depends on which effect is dominated in the hydration kinetics.

For example, at high temperature curing, the fly ash reaction is significant promoted and calcium hydroxide is consumed much from the beginning. It results in a dense cover of C-S-H over the surface of anhydrous cement grains. Therefore, the retarded effect induced by C-S-H gel is dominated and the hydration of cement clinkers decelerates at high temperature.

Unlike the case of high temperature, the reaction rate of fly ash is much slower and calcium hydroxide is abundant. The morphology of C-S-H gel on the surface of anhydrous cement grains is consequently loose and the filler and dilute effect of fly ash is accordingly dominated and the hydration rate is accelerated at low temperature. This mechanism was schematically illustrated in Fig. 6.24.

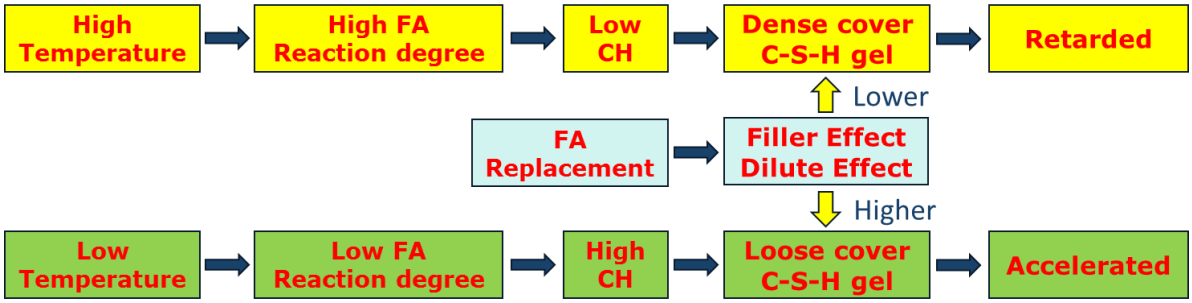

Fig. 6.24 Schematic illustration on influence of fly ash on cement hydration process

Therefore, for the cement past test in this study the hydration degree of belite was accelerated at low temperature but retarded at high temperature and the retarded effect is more significant for LPC due its lower calcium hydroxide content. Compared to belite, the hydration rate of alite is much faster, therefore the influence of fly ash was not clearly captured but still was observed in the case of LPC at high temperature of 60 °C.

6.6 Summary and conclusions

The extent of pozzolanic reaction degree of the siliceous fly ashes in cement systems was investigated by selective dissolution test in this chapter. The calcium hydroxide content and bound water content were accessed by TGA test with modified analysis method as well. The fly ash influence on cement hydration processes was studied by XRD-Rietveld method and the corresponding mechanism was discussed at the end of this chapter. Based on these works, the conclusions of this chapter are summarized in the following points:

1. A modified sample preparation method on fly ash blended paste was developed in this study;

2. A modified selective dissolution test method was developed in this study to access extent of pozzolanic reaction degree of the siliceous fly ashes in cement paste;

3. Selective dissolution test result showed that FA1 and FA2 have similar pozzolanic activities and FA3 is less reactive compared to FA1 and FA2 both at 20 and 60 °C, which is in good agreement with dissolution processes in alkaline conditions. It shows that dissolution is the rate-controlling step of pozzolanic reaction of fly ash in cement system and alkali dissolution test can be used to study and estimate pozzolanic reactivities of fly ash;

4. A modified TGA test procedures and analysis method was developed in this study to determine the calcium hydroxide content and bound water content of cement paste;

5. TGA test result showed that FA1 and FA2 had similar calcium hydroxide content but FA3 had a higher one, which was in good agreement with the selective dissolution test and alkali dissolution test as well;

6. The hydration degrees of cement paste and fly ash blended cement paste were investigated by XRD-Rietveld method. Experiment showed that cement hydration was promoted in room temperature but retarded at high temperature, especially for belite;

7. The mechanism of C-S-H gel morphology variation was discussed in this chapter. It is the result of a series of complicated nano-interaction, including born repulsion, van der Walls attraction, electrostatic repulsion and DLVO potential. A C-S-H gel morphology test was conducted to provide direct observation on C-S-H gel morphology variation at different pH conditions; and

8. Based previous research and C-S-H morphology test, the influence of fly ash on cement hydration is the result of the competition between filler effect and dilute effect and the morphology effect induced by calcium hydroxide content.

7 Modeling of pozzolanic reaction of fly ash in cement systems

Contents:

7.1 Introduction 136
7.2 Current DuCOM multi-heat model 137
7.2.1 Multi-component hydration model of Portland cement 137
7.2.2 Current fly ash pozzolanic reaction model in cement systems 139
7.2.3 Current model verification on cement paste tests 141
7.3 Modified multi-heat model 147
7.3.1 Modified multi-component hydration model of Portland cement 147
7.3.2 Modified fly ash pozzolanic reaction model 150
7.4 Modified model verification 158
7.4.1 Cement paste test 158
7.4.2 Hanehara's experiment [14] 168
7.5 Parameter analysis 169
7.6 Summary and conclusions 172

7.1 Introduction

Fly ash is one of the most widely used supplementary materials in cement industry. It has been broadly recognized that fly ash concrete has many advantages, including lower permeability, better chloride resistance and higher strength at later ages [4, 71, 72]. Although these potential for using fly ash as a supplementary cementitious material in concrete has been well known almost for a long time, the current application of fly ash is limited in engineering practices around the world due to its intrinsic and significant heterogeneity and variability varied with coal, combustion temperature and production processes. Another shortcoming of siliceous fly ash is the slow pozzolanic reaction compared to cement hydration. High temperature curing therefore is often used in fly ash concrete to accelerate its reaction. Although numerous studies had been carried out to investigate the pozzolanic reactivity of fly ash [14, 16, 31, 73, 74], current information regarding material properties, temperature-dependent reactivity of fly ash and its interaction between cement clinkers is still insufficient to understand the behavior of fly ash and its effect in cement systems.

To solve these problems, three different types of siliceous fly ashes are first selected based on its solubility in NaOH solution. A comprehensive material characterization had been carried out in chapter 4 based on the developed full element EDS mapping and image analysis method. The long-term temperature-dependent dissolution processes in alkaline systems were also investigated in chapter 5. These three fly ashes are further studied in cement systems by preparing blended cement pastes under sealed curing conditions at 20 and 60 °C. The extent of pozzolanic reaction, calcium hydroxide consumption trend and hydration processes were determined and studied in chapter 6. Based on these experiment works, the mechanisms on fly ash reactivity variation and the interaction between fly ash and cement clinker were correspondingly studied and discussed.

Based on previous experiment works and discussions, this chapter is going to develop a unified model on the basis of current DuCOM multi-heat model to predict the pozzolanic reaction of different siliceous fly ash at different temperatures. It is hoped that this model can help us to better understand the behavior of siliceous fly ash and its effect in cement systems and finally provide us operable guidances for siliceous fly ash application in concrete engineering practices.

7.2 Current DuCOM multi-heat model

7.2.1 Multi-component hydration model of Portland cement

At the Concrete Lab of the University of Tokyo, a computational system called DuCOM-COM3, which couples thermo–hygro–physical information of cementitious composites with a multi-scale constitutive model, has been developed by Maekawa et al [75]. In this model, the total hydration heat of cement components H_c including alite (C_3S), belite (C_2S), aluminate (C_3A), ferrite (C_4AF) are simulated by following equations:

$$\begin{aligned} H_c &= \sum p_i H_i \\ &= p_{C_3A}\left(H_{C_3AET} + H_{C_3A}\right) + p_{C_4AF}\left(H_{C_4AFET} + H_{C_4AF}\right) + p_{C_3S}H_{C_3S} + p_{C_2S}H_{C_2S} \end{aligned} \tag{7.1}$$

where H_i is the heat-generation rate of cement components *i* per unit mass; p_i is the mass fraction ratio of cement components *i* ; and H_{C_3AET} and H_{C_4AFET} are the heat-generation rate of ettringite produced from aluminate (C_3A), ferrite (C_4AF) respectively.

For each component, the heat-generation rate H_i was expressed by an exothermic equation with considering mutual interactions as follows:

$$H_i = \gamma_i \cdot \beta_i \cdot \mu_i \cdot H_{i,T_0}\left(Q_i\right)\exp\left\{-Z_i\left(\frac{1}{T}-\frac{1}{T_0}\right)\right\} \tag{7.2}$$

where H_{i,T_0} is the referenced heat-generation rate of cement components *i* at referenced temperature T_0 ; Q_i is the accumulated heat released from hydrated cement components *i*; Z_i is the thermal active energy of cement components *i* ; T_0 is the referenced temperature of 20 °C; T is the environment temperature of concrete element; γ_i is a coefficient considering delaying effect of chemical admixture; β_i is a coefficient considering delaying effect due to lack of free water; and μ_i is a coefficient considering considering interactions of alite and belite.

Among above different factors, the factor β_i is one of the important controlling coefficient of cement hydration to consider diffusion processes between free water and

unhydrated cement grains in hardened cement paste. It is determined by the amount of free water w_{free} and the thickness of hydrated layer η_i on cement grains as follows:

$$\beta_i = 1 - \exp\left\{-2.0\left[\left(\frac{w_{free}}{100\eta_i}\right)\Big/\sqrt{SSA_{CE,i}^N}\right]^{2.5}\right\} \tag{7.3}$$

$$\eta_i = 1.0 - \left(1.0 - Q_i/Q_{i,\infty}\right)^{\frac{1}{3}} \tag{7.4}$$

where $SSA_{CE,i}^N$ is the normalized specific surface area of cement components *i*.

Free water is essential for continuous hydration and also provides available space for precipitation of hydrated product. Lack of free water would induce the stagnation of cement hydration and fly ash reaction as well. Under sealed condition, the free water w_{free} can be determined by Eq. (7.5):

$$w_{free} = \frac{W_{Initial} - \sum W_i}{C} \tag{7.5}$$

where $W_{Initial}$ is the initial water mass amount; and W_i is the mass amount of water consumed by various components in the cementitious binder and C is the unit mass of cement in the paste.

With the Eq. (7.2), the hydration degree of cement components *i* at interested time *t*, α_i^t can be determined by Eq. (7.6)

$$\alpha_i^t = \frac{\int_0^t H_i dt}{Q_{i,\infty}} \tag{7.6}$$

where $Q_{i,\infty}$ is the total heat of cement components *i*.

The water consumption for cement hydration and the hydration product such as C-S-H gel and calcium hydroxide can be determined by the chemical reactions. In current model, the chemical reactions are expressed as follows

$$C_2S + 2H = C_{1.5}SH_{1.5} + 0.5CH \tag{7.7}$$

$$C_3S + 3H = C_{1.5}SH_{1.5} + 1.5CH \tag{7.8}$$

$$C_3A + 6H = C_3AH_6 \tag{7.9}$$

$$C_4AF + 2CH + 10H = C_3AH_6 + C_3FH_6 \tag{7.10}$$

7.2.2 Current fly ash pozzolanic reaction model in cement systems

Similar to cement hydration model, the fly ash pozzolanic reaction model is also simulated by an exothermic equation with considering various factors such as calcium hydroxide content, free water, temperature and material fineness as follows:

$$H_{FA} = \min(\beta_{FA}, \lambda_{FA}) H_{FA,T_o}\left(Q^c_{FA}\right) \exp\left[-Z_{FA}\left(\frac{1}{T} - \frac{1}{T_0}\right)\right] \tag{7.11}$$

$$H_{FA,T_o}\left(Q_{FA}\right) = f_s \times 0.005 \times \left(1 - Q^c_{FA}/Q_{FA,MAX}\right)^{2.0} \quad Q^c_{FA} \le Q_{FA,MAX} \tag{7.12}$$

$$f_s = \left(1.2SSA^N_{FA} - 0.2\right) \tag{7.13}$$

where H_{FA} is the heat-generation rate of pozzolanic reaction of fly ash in cement systems; H_{FA,T_0} is the referenced heat-generation rate of pozzolanic reaction of fly ash at referenced temperature T_0 of 20 °C; f_s is reaction index considering the influence of specific surface area of fly ash; SSA^N_{FA} is the referenced specific surface area of fly ash, which is determined by $SSA_{FA}/3380$; SSA_{FA} is the specific surface area of fly ash; Q_{FA} is the accumulated heat released from reacted fly ash; Z_{FA} is the thermal active energy of fly ash (it is assumed as 12000 WK/kg in current model); T is the environment temperature of concrete element; β_{FA} is the reaction reduction factor of fly ash due to insufficiency of free water; and λ_{FA} is the reaction reduction factor of fly ash due to insufficiency of calcium hydroxide.

With Eq. (7.11), the temperature-dependent pozzolanic reaction degree of fly ash α^t_{FA} at interested time *t* can be therefore determined by Eq.(7.11):

$$\alpha^t_{FA} = \frac{\int_0^t H_{FA} dt}{Q_{FA,\infty}} \tag{7.14}$$

where $Q_{FA,\infty}$ is the total heat of fly ash and it is assumed as 50 kJ/kg in current model [75].

Besides temperature effect, β_{FA} and λ_{FA} are another two important factors that significantly affect fly ash reaction degree in DuCOM model. The reaction reduction factor of fly ash due to insufficiency of free water had been improved by Kinomura et al. [76] based on the ion transport effect proposed by Luan et al. [77]:

$$\beta_{FA} = \left\{1 - \exp\left\{-r\left[\left(\frac{w_{free}}{7.0}\right)\Big/\sqrt{S_{FA}^{N}}\right]^{s}\right\}\right\}\chi_{FA} \tag{7.15}$$

where S_{FA}^{N} is the normalized surface area of fly ash; and w_{free} is the same definition to Eq. (7.5).

In Eq. (7.15), the variation of diffusion properties between inner and outer hydrated layer was also taken into account by introducing a reduction diffusion factor χ, which is determined by Eqs. (7.16), (7.17) and (7.18) with fly ash replacement ratio P_{FA}:

$$\chi_{FA} = \exp\left(-a\omega_{FA}{}^{b}\right) \tag{7.16}$$

$$\omega_{FA} = \begin{cases} \eta_{FA} - 0.02P_{FA} & \eta_{FA} \geq 0.02P_{FA} \\ 0 & \eta_{FA} < 0.02P_{FA} \end{cases} \tag{7.17}$$

$$\begin{cases} a = 75.0P_{FA} \\ b = 0.25\Big/\sqrt{p_{FA}} + 0.50 \end{cases} \tag{7.18}$$

where η_{FA} is the normalized cluster thickness of the inner hydrated layer and it is determined by Eq. (7.19)

$$\eta_i = 1.0 - \left(1.0 - Q_{FA}/Q_{FA,\infty}\right)^{\frac{1}{3}} \tag{7.19}$$

At last, the reaction reduction factor of fly ash λ_{FA} due to insufficiency of calcium hydroxide was determined by Eq. (7.20)

$$\lambda_{FA} = 1 - \exp\left[-2.0\left(\frac{F_{CH}}{R_{FACH}}\right)^{1.5}\right] \tag{7.20}$$

where F_{CH} is the calcium hydroxide content in the cement paste and R_{FACH} is the amount of calcium hydroxide required for fully reaction of fly ash in next step.

7.2.3 Current model verification on cement paste tests

7.2.3.1 Fly ash reaction degree

The comparisons between experiment result and current model predictions with different fineness (i.e. image analysis and Bliane value) are made in Fig. 7.1. It can be seen that the fineness of image analysis result provided a better prediction, which means an accurate estimation of fly ash fineness is essential to simulate its pozzolanic reaction in cement system.

Table. 7.1 Fineness values used for model simulation

	FA1	FA2	FA3
Blaine	3940	3730	4070
Image analysis	5893	5803	5567

However, even with the fly ash fineness determined by image analysis, current model still cannot accurately capture the pozzolanic reactivity variation among different fly ashes (e.g. FA2 and FA3) and overestimated the pozzolanic reaction degrees of fly ashes at high temperature of 60 °C as well. That is because the fly ash material properties, such as pozzolanic reactivity, mineralogical phase, thermal activation energy etc., have not been properly considered in current model. Therefore, based on all the works and discussions in previous chapters, this section is going to develop a modified model on the basis of current DuCOM multi-heat model. This modified model will be verified by cement paste test and Hanehara's experiment [14] in next section.

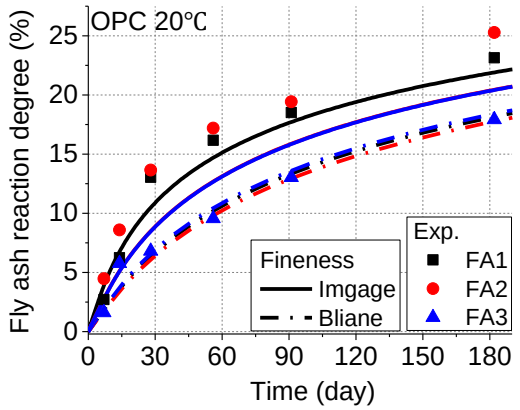

(a) FA OPC 20 °C

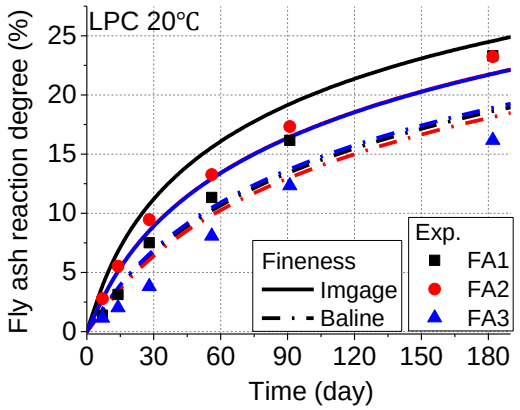

(b) FA LPC 20 °C

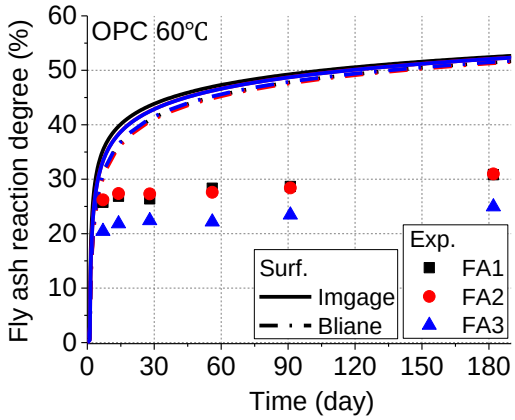

(c) FA OPC 60 °C

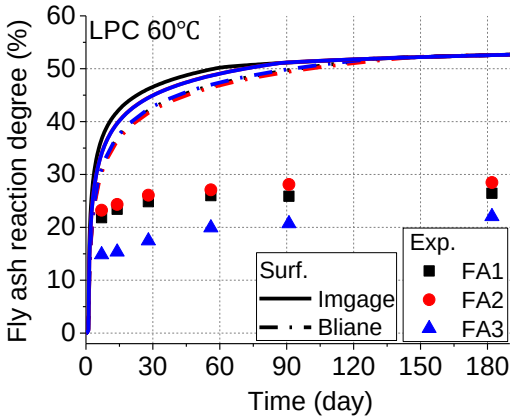

(d) FA LPC 60 °C

Fig. 7.1 Comparison of fly ash reaction degrees between cement paste test result and current model simulations

7.2.3.2 Cement hydration

Fig. 7.2 presents the comparisons of alite and belite hydration processes between cement paste experiment results and current model simulation predictions at room temperature of 20 °C. It can be seen that, although the belite hydration degree were underestimated in LPC cases, which might be the sensitivity of free water has not been so properly considered so far, current model still can capture the general extent of alite and belite hydration degrees and filler effect of fly ash at room temperature.

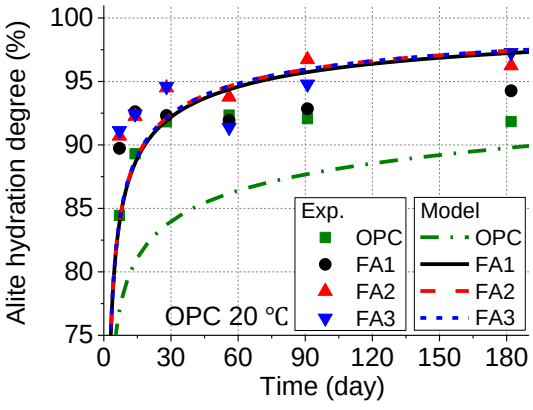

(a) Alite OPC 20 °C

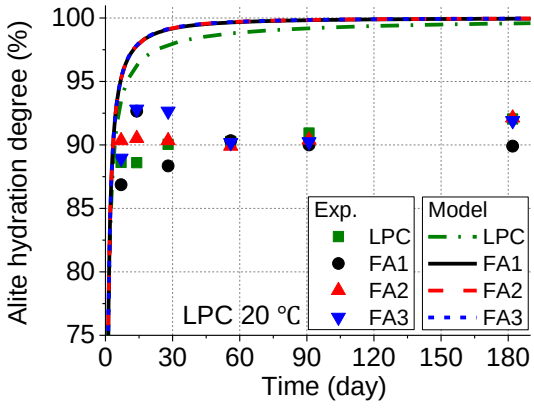

(b) Alite LPC 20 °C

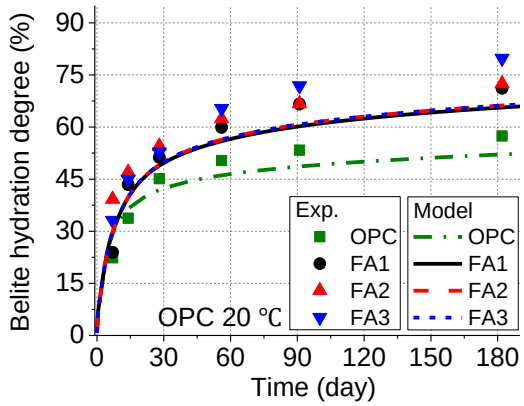

(c) Belite OPC 20 °C

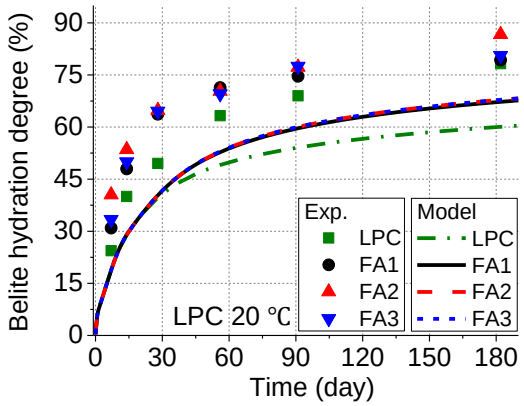

(d) Belite LPC 20 °C

Fig. 7.2 Comparison of hydration processes between cement paste test result and current model simulations at room temperature of 20 °C

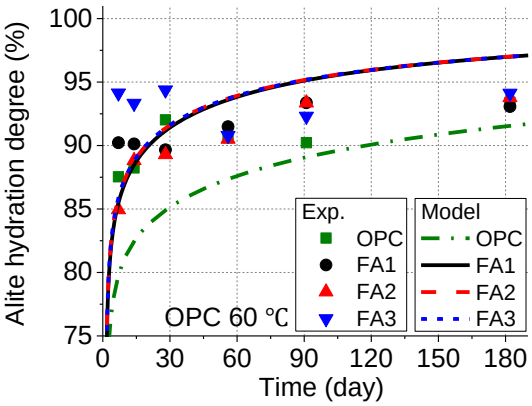

(a) Alite OPC 60 °C

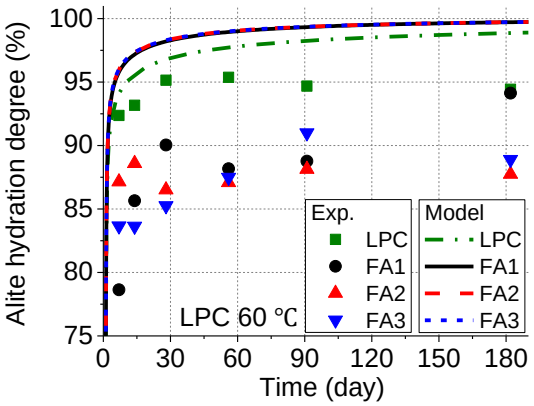

(b) Alite LPC 60 °C

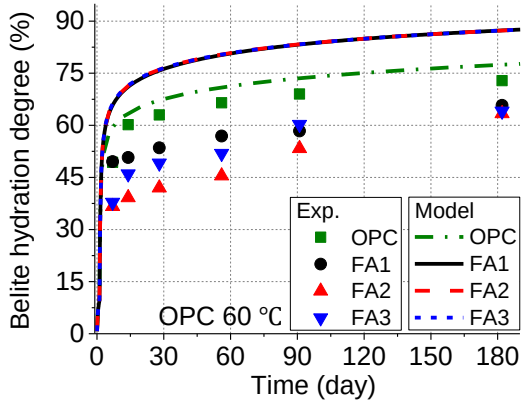

(c) Belite OPC 20 °C

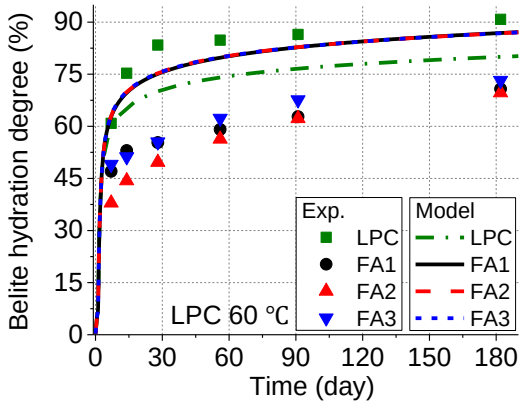

(d) Belite LPC 20 °C

Fig. 7.3 Comparison of hydration processes between cement paste test result and current model simulations at high temperature of 60 °C

Regarding the high temperature of 60 °C (Fig. 7.3), the hydration processes of cement paste were also satisfactorily predicted. However, for fly ash blended cement paste, because the retarded effect on cement hydration induced by C-S-H gel morphology which was discussed in section 6.5 has not been considered in current model, the hydration degrees of belite and alite of fly ash blended cement paste were higher than the ones in cement paste (Fig. 7.3). Therefore, this issue will be studied and modified in the following sections.

7.2.3.3 Calcium hydroxide content

Fig. 7.4 compared the calcium hydroxide content of cement paste to simulation results. It can be seen that current model overestimated the calcium hydroxide content and it was more closed to the traditional stepwise analysis result for TGA test at room temperature (referred to section 6.4.2.1). It is also noted that calcium hydroxide contents at high temperature were higher than the ones at room temperature in current model, which was different from the experiment result of cement paste. The reasons for these problems are because the Ca/Si ratio of C-S-H gel are not properly considered and it will be discussed in the modified model.

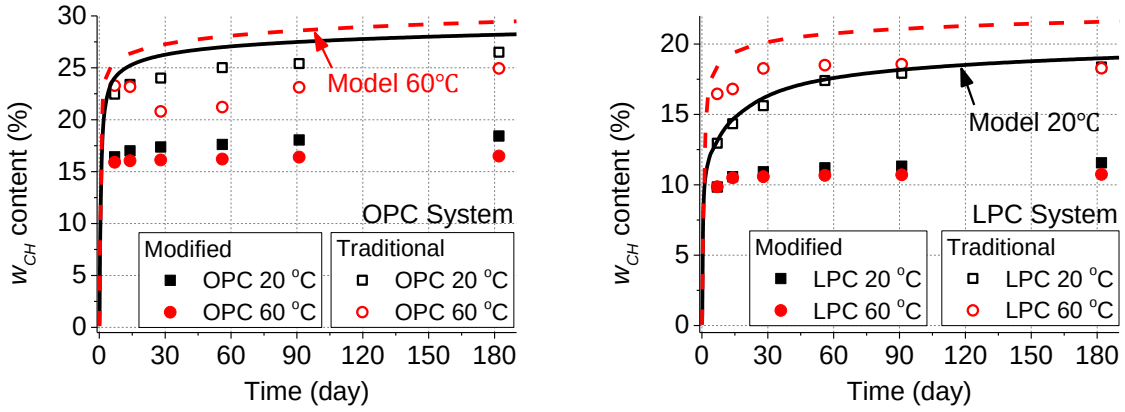

(a) OPC (b) LPC

Fig. 7.4 Comparison of calcium hydroxide content between cement paste test result and current model simulations

Regarding the fly ash blended cement paste, the situations were more complicated. For example, the calcium hydroxide content was overestimated in OPC at 20 °C (Fig. 7.5 (a)) but it was underestimated in LPC at 60 °C (Fig. 7.5 (b)). That is because the pozzolanic reaction

degrees of fly ashes and calcium hydroxide content of cement matrix are not properly simulated as discussed before. Besides these two reasons, the calcium hydroxide consumption rate of fly ash is another possible reason. These issues will be all reviewed in the modified model as well.

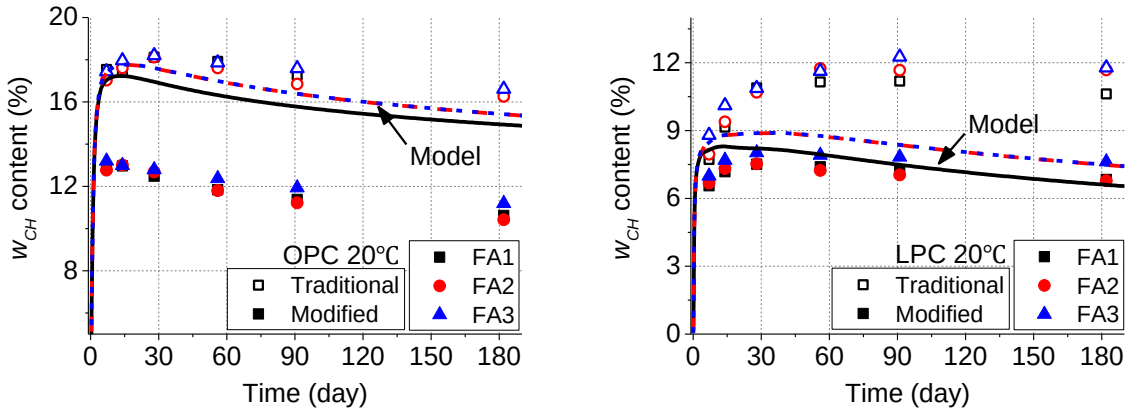

(a) FA OPC 20 °C

(b) FA LPC 20 °C

(c) FA OPC 60 °C

(d) FA LPC 60 °C

Fig. 7.5 Comparison of calcium hydroxide content between FA blended cement paste test result and current model simulations

7.2.3.4 Bound water content

Fig. 7.6 compares the bound water between simulation results and cement paste experiment result. It shows that current model satisfactorily predicted the bound water content of cement paste at room temperature but overestimated at high temperature.

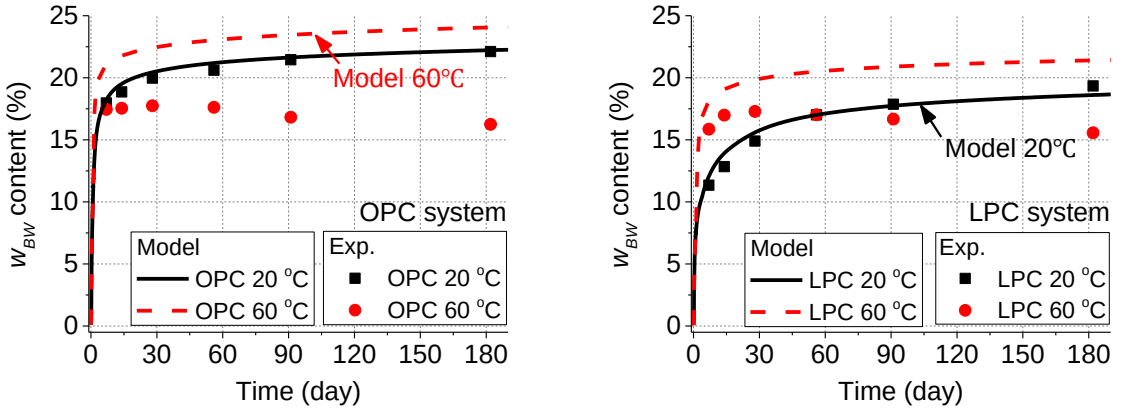

(a) OPC (b) LPC

Fig. 7.6 Comparison of bound water content between cement paste test result and current model simulations

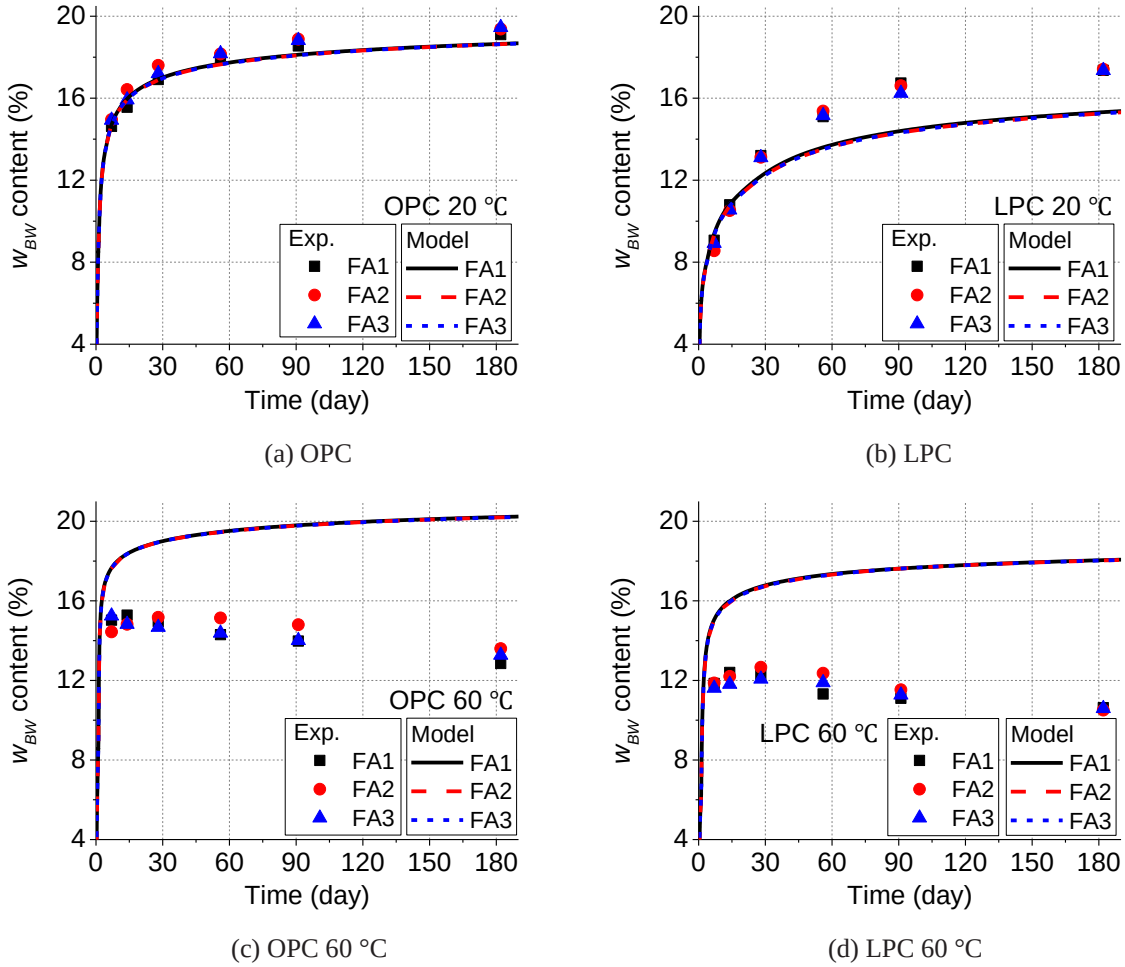

(a) OPC (b) LPC

(c) OPC 60 °C (d) LPC 60 °C

Fig. 7.7 Comparison of bound water content between FA cement paste test result and current model simulations

Fig. 7.7 presents the comparison of the bound water between simulation predictions and FA blended cement paste experiment result. It shows that current model can predicted the bound water content of FA blended cement paste at room temperature. However, it overestimated the bound water content of fly ash blended cement paste at high temperature as well. Therefore, this issue will be also reviewed in the modified model.

7.3 Modified multi-heat model

7.3.1 Modified multi-component hydration model of Portland cement

Last section showed that the calcium hydroxide content and bound water content of cement paste have not been properly simulated by current model. That is because the Ca/Si ratio of C-S-H gel of current model is 1.5 (see Eqs. (7.7) and (7.8)) and it is smaller than the actual ratio of C-S-H gel in cement paste. Recent researches pointed out that the Ca/Si ratio of C-S-H gel usually varied in the range of 1.70 and 1.80 [49, 78-81]. For example, Jennings proposed his well known colloid model of C-S-H and its Ca/Si ratio is 1.70.

Moreover, as mentioned in Chapter 6.4.2.1, Elkhadiri et al. analyzed the Ca/Si ratio of the inner and outer C-S-H products of cement paste at a water-cement ratio of 0.3 under different curing temperatures. They found that Ca/Si ratio increased as the temperature increased as shown in Table. 6.5 [66].

Based on these previous works, the Ca/Si ratio of C-S-H gel is modified herein and tentatively proposed to linearly increase with temperature as Eqs. (7.21) and (7.22) shows (Fig. 7.8)

$$\begin{cases} C/S_{C_2S} = 1.70, \quad C/S_{C_3S} = 1.80 & T \le 5\,^{\circ}C \\ C/S_{C_2S} = 1.85, \quad C/S_{C_3S} = 2.20 & T \ge 60\,^{\circ}C \end{cases} \tag{7.21}$$

$$\begin{cases} C/S_{C_2S} = 1.70 + (1.85-1.70)/(60.0-5.0)\times(T-5.0) \\ C/S_{C_3S} = 1.80 + (2.20-1.80)/(60.0-5.0)\times(T-5.0) \end{cases} \tag{7.22}$$

where C/S_{C_2S} and C/S_{C_3S} are the Ca/Si ratios of C-S-H gel produced by belite and alite respectively.

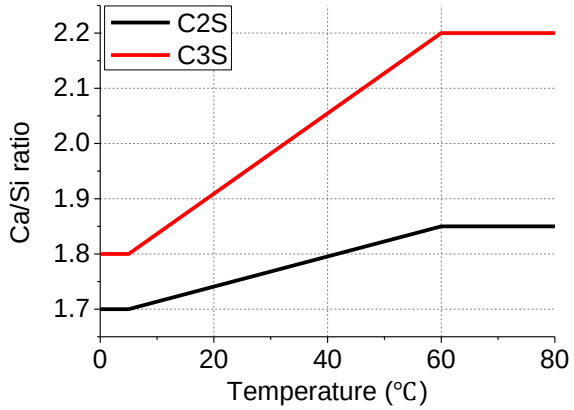

Fig. 7.8 Proposed Ca/Si ratio of C-S-H gel with temperature

With these Ca/Si ratios, the production rates of calcium hydroxide PCH_{C_2S} and PCH_{C_3S} and consumption rates of free water CW_{C_2S} and CW_{C_3S} for cement components belite and alite per gram can be therefore determined by Eqs. (7.24) and (7.25) according to chemical reaction equations Eq. (7.23).

$$\begin{cases} C_2S + \left(2.0 - C/S_{C_2S} + BW_{CSH}\right)H = C_{C/S_{C_2S}}SH_{BW_{CSH}} + \left(2.0 - C/S_{C_2S}\right)CH \\ C_3S + \left(3.0 - C/S_{C_3S} + BW_{CSH}\right)H = C_{C/S_{C_3S}}SH_{BW_{CSH}} + \left(3.0 - C/S_{C_2S}\right)CH \end{cases} \tag{7.23}$$

$$\begin{cases} PCH_{C_2S} = \left(2.0 - C/S_{C_2S}\right) \times M_{CH}/M_{C_2S} \\ PCH_{C_3S} = \left(3.0 - C/S_{C_3S}\right) \times M_{CH}/M_{C_3S} \end{cases} \tag{7.24}$$

$$\begin{cases} CW_{C_2S} = \left(2.0 - C/S_{C_2S} + BW_{CSH}\right) \times M_W/M_{C_2S} \\ CW_{C_3S} = \left(3.0 - C/S_{C_3S} + BW_{CSH}\right) \times M_W/M_{C_3S} \end{cases} \tag{7.25}$$

Where M_{CH}, M_W, M_{C_2S} and M_{C_3S} are the molar mass density of calcium hydroxide, water, belite and alite and they are 74.0930 g/mol, 18.0153 g/mol, 172.2348 g/mol and 228.3132 g/mol respectively; and BW_{CSH} is the bound water index of C-S-H gel. Since the definition of C-S-H gel in DuCOM model is the index at 105 °C, it still used the same index 1.50 of current model according to Jennings and Taylor suggestions [49, 79].

Taking these modifications, the simulations were re-calculated and illustrated in Fig. 7.10. It can be seen that prediction on calcium hydroxide were significantly improved both at

OPC and LPC system and the reduction effect at high temperature curing can be captured as well.

Regarding the bond water content (Fig. 7.10), although the cases at high temperature curing were still overestimated since the decomposition of hydration products at high temperature has not been considered, which should be considered in the future, this modified model still provided a reasonable estimations for cement pastes. Therefore, the fly ash pozzolanic reaction model will further reviewed and discussed based on this modified model.

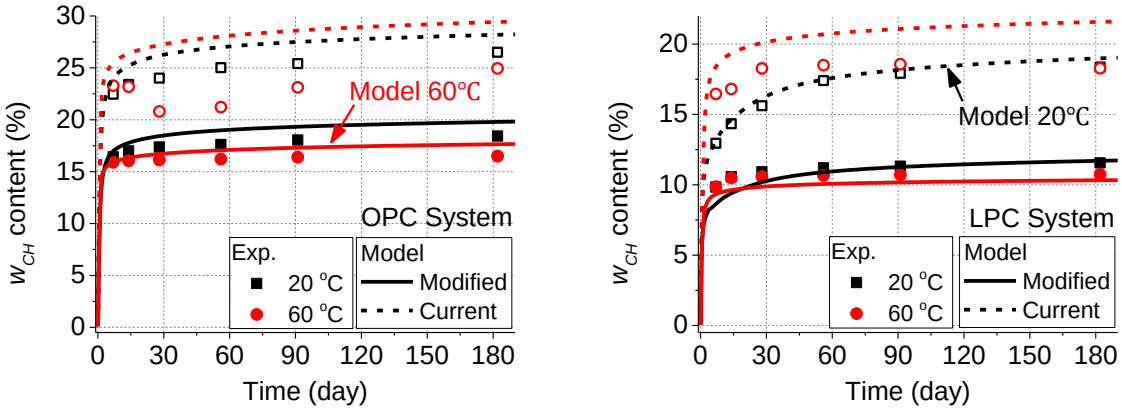

(a) OPC (b) LPC

Fig. 7.9 Comparison of calcium hydroxide content between cement paste test result and modified model predictions

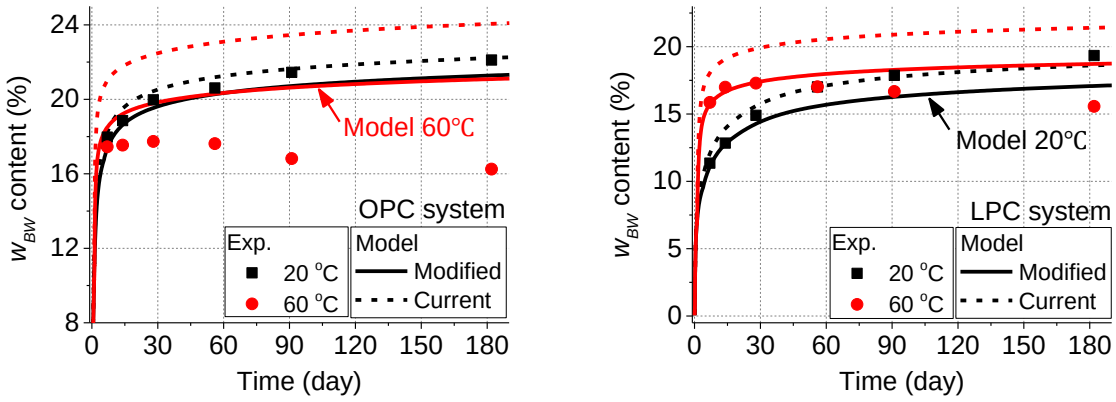

(a) OPC (b) LPC

Fig. 7.10 Comparison of bound water content between cement paste test result and modified model predictions

7.3.2 Modified fly ash pozzolanic reaction model

Chapter 5 discussed the dissolution mechanism of fly ash in alkaline system. It is found that the major dissoluble phases are amorphous silicate and Al-silicate. Although crystalline quartz and semi-mullite are partially dissoluble, the amount contents and dissolution degrees of these crystalline phases are relatively small compared to amorphous phases. Therefore, it is assumed that all crystalline phases are insoluble and their actual influences are considered by amorphous silicate and Al-silicate phase in the proposed model. Based on this assumption, a two-phase reaction model, i.e. amorphous silicate and Al-silicate phase, is consequently proposed in this study and developed as follows.

7.3.2.1 Two-phase reaction model

(a) Reaction activity of different phases

In chapter 5, the reactivity of different amorphous phases had been studied by EDS full element mapping analysis. Table. 7.2 shows the dissolution degrees of amorphous phases at 20 °C in alkaline system. It can be seen that the dissolution rate of amorphous Al-silicate is significantly faster than amorphous silicate in all three fly ashes. This observation also aggress with the work of Durdziński et al that they studied the initial dissolution rate of synthetic glasses and found that the dissolute rate of Al-silicate is higher than silicate.

Table. 7.2 Dissolution degrees of amorphous phases at 20 °C in alkaline system

	Silicate (mt. %)	Al-Silicate (mt. %)	Comparison
FA1	13.24	57.73	4.36
FA2	5.03	49.22	9.79
FA3	6.00	33.23	5.54
Ava.			6.56

Therefore, this model assumes that the siliceous fly ash have two different reactivity phases, i.e. the high reactivity phase amorphous Al-silicate and the low reactivity phase amorphous silicate and their relative reactivity can be determined by the dissolution degrees at 20 °C in alkaline system, as shown in Table. 7.2. Considering the reactivity of amorphous phases are also affected by many parameters, such as surface area, geometrical shape etc., this study is conservatively assumed that the reactivity of amorphous Al-silicate phase is 8 times

of amorphous silicate for the sake of simplification.

(b) Thermal activation energy of different amorphous phases

Alkali dissolution test is a good potential approach to estimate the temperature-dependent reactivity properties of fly ash. Although alkali dissolution processes are nonlinear since fly ash has different reactivity phases, they still can be approximately represented by two liner stages, i.e. the initial stage and the second stage, as shown in Fig. 7.11.

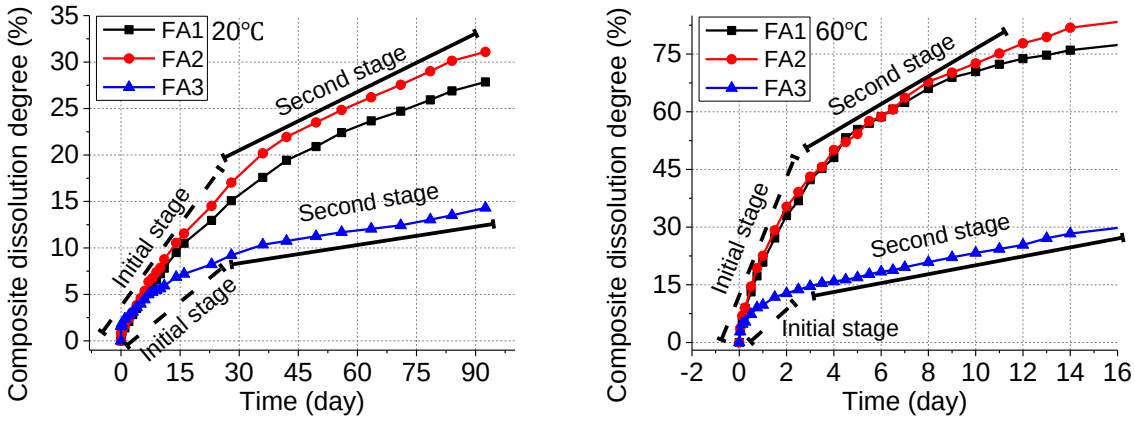

(a) 20 ℃ (b) 60 ℃

Fig. 7.11 Illustration of two dissolution stages of fly ash

Based on this simplified model, the slopes of these two different linear stage can be estimated by liner regressions of alkali dissolution test result. The regression result can be found in appendix D. With these regression analysis result, the thermal activation energy of two different stages can be therefore approximately estimated by the slopes of initial stage and the slopes of second stage according to Arrhenius equation (i.e. Eq. (7.26)).

$$Z_I = \ln \frac{S_I^{T_2}}{S_I^{T_1}} \Bigg/ \left(\frac{1}{(273+T_1)} - \frac{1}{(273+T_2)} \right) \tag{7.26}$$

where $S_I^{T_1}$ and $S_I^{T_2}$ are the slopes of stage I at temperature T_1 and T_2 respectively.

Table. 7.3 summarizes all calculation results. It can be seen that the thermal activation energy varies in different stages and second stage seems higher than initial stage. That is probably because the reactivity of amorphous Al-silicate is higher than amorphous silicate but

less sensitive to temperature as discussed in chapter 6. Therefore, the dominated phase of initial stage is amorphous Al-silicate and the thermal activation energy is smaller. As amorphous Al-silicate continuously dissolves, the less reactive amorphous silicate gradually poses the dominate place at the second stage of dissolution processes and the thermal activation energy correspondingly increases.

Based on these alkali dissolution test results, this study tentatively assumes the thermal activation energy of amorphous Al-silicate is 6000 WK/kg and amorphous silicate is 8000 WK/kg respectively.

Table. 7.3 Thermal activity energies of different stages (WK/kg)

	Initial stage	Second stage
FA1	7526	8199
FA2	7188	8000
FA3	5651	7201
Ava.	6789	7800

(c) Relative intrinsic reactivity of fly ash

In chapter 5, we had discussed that the intrinsic reactivity of amorphous solids not only depends on their chemical compositions, but it also will be affected by the fly ash production processes, like combustion temperature and cooling history, and it therefore varies in different fly ashes. Since a higher combustion temperature and a more rapid cooling process in thermal furnace not only results in a higher amount of amorphous solids itself but also promotes the intrinsic reactivity of amorphous solids, chapter 5 proposed to use amorphous-crystalline ratio to describe the combustion conditions effect on intrinsic reactivity of amorphous phases.

Considering the amount of amorphous Al-silicate and silicate phase have to be determined by SEM-EDS mapping analysis, this study tentatively proposed another ratio of crystalline mullite to total amorphous to represent the combustion effect on relative intrinsic reactivity of fly ash R_{FA} for engineering practice (Eq. (7.27)). In other words, this model assumes the combustion conditions effect are same to amorphous Al-silicate and silicate phases. The reason chose crystalline mullite but not quartz because mullite is the crystallization product of amorphous phase and it seems to be better to represent the combustion effect.

$$R_{FA} = \frac{c_{Amorphous}}{15 \times c_{mullite}} \tag{7.27}$$

where $c_{Amorphous}$ and $c_{mullite}$ are the mass ratio of amorphous content and mullite content determined by XRD tests.

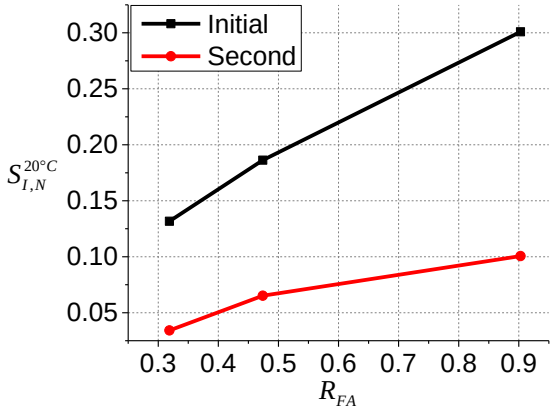

Fig. 7.12 Comparison of two different reactivity indexed of fly ash

Since the dissolution is the controlling step of fly ash pozzolanic reactions in cement systems, the slopes of two linear stage in last section can be used to approximately represent the pozzolanic reactivity of fly ash. To eliminate the influence of specific surface area, the normalized reactivity of fly ash $R_{I,N}^{20°C}$ was determined by Eq. (7.28) with the help of surface reaction index f_s proposed by DuCOM model (i.e. Eq. (7.13)).

A comparison between these two different reactivity indexes is made in Fig. 7.12. It can be seen that relative reactivity of fly ash R_{FA} linearly agrees with normalized reactivity of fly ash $R_{I,N}^{20°C}$ well, which means that relative reactivity of fly ash R_{FA} can be used to describe the activity variation of fly ash:

$$R_{I,N}^{20°C} = S_I^{20°C} / f_r \tag{7.28}$$

where $S_I^{20°C}$ is the slopes of stage *I* of dissolution processes of fly ash at temperature 20 °C.

(d) Calcium hydroxide and free water consumption rate of fly ash

Section 7.2.3.3 and 7.2.3.4 had examined the simulation results of calcium hydroxide content

and bound water content in current model, it can be seen that current model cannot properly predict calcium hydroxide content and bound water content of fly ash blended cement paste. Besides the reason that the calcium hydroxide production rate and free water consumption rate of cement matrix were not properly considered as discussed in section 7.3.1, the calcium hydroxide and free water consumption rate of fly ash were also another possible reasons.

As we know, the Ca/Si ratio of C-S-H gel is not a constant value and it varies as chemical composition of cement, curing temperature, water-binder ratio etc. Moreover, Richadson et al. had studied the Ca/Si of slag cement paste and they found that the Ca/Si ratio decrease as slag replacement ratio increases since more silicon was supplied into pore solution at high replacement ratio. This mechanism is believed also happened in fly ash blended cement paste. Therefore, the calcium hydroxide consumption rate of fly ash FA_{CH} was tentatively proposed to be relative the potential calcium hydroxide amount of cement CH_{CE}^{Pot} and the fly ash replacement percentage P_{FA} as Eqs. (7.29) and (7.30) show. Regarding the free water consumption rate of fly ash CW_{FA}, since the information on the bound water of C-S-H gel produced from the fly ash pozzolanic reaction is still insufficient, it is therefore given a constant value of 0.5 for the sake of simplification in this modified model.

$$FA_{CH} = 0.035CH_{CE}^{Pot} - P_{FA}/100 \tag{7.29}$$

$$CH_{CE}^{Pot} = P_{C_2S} \times PCH_{C_2S}^{20\,^{\circ}C} + P_{C_3S} \times PCH_{C_3S}^{20\,^{\circ}C} \tag{7.30}$$

$$CW_{FA} = 0.50 \tag{7.31}$$

where P_{C_2S} and P_{C_3S} are the mass percentage of belite and alite in cement; and $PCH_{C_2S}^{20\,^{\circ}C}$ and $PCH_{C_3S}^{20\,^{\circ}C}$ are the production rates of calcium hydroxide of belite and alite at 20 °C, which can be determined by Eq. (7.24).

(e) Summarization on modified model

According to previous discussions, a tentative two-phase reaction model, amorphous silicate and Al-silicate, was proposed based on current DuCOM model and summarized herein as follows:

$$H_{silicate}^{20℃} = f_r \times \frac{0.025}{R_p} \times \left(1 - \frac{Q_{silicate}^c}{Q_{FA,\infty}}\right)^{2.0} \tag{7.32}$$

$$H_{Al-silicate}^{20℃} = f_r \times 0.025 \times \left(1 - \frac{Q_{Al-silicate}^c}{Q_{FA,\infty}}\right)^{2.0} \tag{7.33}$$

$$f_r = R_{FA} \times \left(1.2 SSA_{FA}^N - 0.2\right) \tag{7.34}$$

$$R_{FA} = \frac{c_{Amorphous}}{15 \times c_{mullite}} \tag{7.27}$$

$$H_{silicate}^T = H_{silicate}^{20℃} \times exp\left(-Z_{silicate}\left(\frac{1}{273+T} - \frac{1}{293}\right)\right) \tag{7.35}$$

$$H_{Al-silicate}^T = H_{Al-silicate}^{20℃} \times exp\left(-Z_{Al-silicate}\left(\frac{1}{273+T} - \frac{1}{293}\right)\right) \tag{7.36}$$

$$H_{FA}^T = P_{silicate} H_{silicate}^T + P_{Al-silicate} H_{Al-silicate}^T \tag{7.37}$$

$$FA_{CH} = 0.035 CH_{CE}^{Pot} - P_{FA}/100 \tag{7.29}$$

$$CH_{CE}^{Pot} = P_{C_2S} \times PCH_{C_2S}^{20\,°C} + P_{C_3S} \times PCH_{C_3S}^{20\,°C} \tag{7.30}$$

$$CW_{FA} = 0.50 \tag{7.31}$$

where $H_{silicate}^{20℃}$ and $H_{Al-silicate}^{20℃}$ are the heat-generation rate of pozzolanic reaction of amorphous silicate and Al-silicate at 20° C respectively; $H_{silicate}^T$ and $H_{Al-silicate}^T$ are the heat-generation rate of pozzolanic reaction of amorphous silicate and Al-silicate at temperature *T*; H_{FA}^T is the total heat-generation rate of pozzolanic reaction of fly ash at temperature *T*; f_r is the pozzolanic reaction factor of fly ash considering the influence of normalized specific surface area of fly ash SSA_{FA}^N and relative reactivity of fly ash R_{FA}, which are the same definition to the Eqs. (7.13) and (7.27); R_p is the reaction reduction factor between amorphous silicate and Al-silicate and it is assumed as 8.0 according to alkali dissolution test; $Q_{silicate}^c$ and $Q_{Al-silicate}^c$ are the accumulated release-heat of amorphous silicate and Al-silicate; $Q_{FA,\infty}$ is the total heat of fly ash and it is still assumed as 50 kJ/kg in this modified model; $P_{silicate}$ and $P_{Al-silicate}$ are the mass

fraction of amorphous silicate and Al-silicate; and $Z_{silicate}$ and $Z_{Al-silicate}$ are the thermal activation energies of amorphous silicate and Al-silicate and they are assumed as 6000 WK/kg and 8000 WK/kg respectively. Moreover, Eqs. (7.27), (7.29), (7.30) and (7.31) are also repeated herein for summarization and their symbol definitions can be referred to the original ones in this chapter.

7.3.2.2 Fly ash and cement interaction model

Section 6.5.2 investigated the hydration degrees of cement clinkers in fly ash blended cement paste and it is found that the hydration degree is promoted in room temperature but retarded at high temperature. This phenomenon is the result of the competition between filler effect and dilute effect and the morphology effect induced by calcium hydroxide contents. More detailed explanation can be referred to section 6.5.3. Since the filler effect and dilute effect of fly ash had been considered in the current model, this section is going to discuss the C-S-H gel morphology model.

As discussed in section 6.5.3, the morphology of C-S-H gel varied with calcium hydroxide content. The C-S-H gel prefers to growth parallel to the surface of anhydrous cement grains at low calcium hydroxide content but to perpendicularly at high calcium hydroxide content. Therefore, the calcium hydroxide content of fly ash blended cement paste seems a good index to describe the morphology effect. Consequently, a possible modification on cement hydration thickness is keeping the original equation β_i (i.e. Eq. (7.3)) unchanged but introduce a C-S-H gel morphology factor χ_{mor} to modify it, which is depended on calcium hydroxide content. Considering the extent of cement hydration degrees can be properly simulated at room temperature of 20 °C (see Fig. 7.2) in current model, the calcium hydroxide content of the cement matrix at 20 °C is accordingly a good reference value to describe the morphology effect. Moreover, it should be noted that the pH of pore solution decreases at high temperature since the ionization constant of water increases but solubility of calcium hydroxide decreases as temperature increases [82]. Therefore, the C-S-H gel morphology factor χ_{mor} should be temperature-dependent as well.

In conclusion, a tentative model based on the original hydrated layer thickness model

β_i (i.e. Eq. (7.3)) was proposed as follows:

$$\beta_i = \left\{1 - \exp\left\{-2.0\left[\left(\frac{w_{free}}{100\eta_i}\right)\Big/\sqrt{SSA_{CE,i}^{N}}\right]^{2.5}\right\}\right\}\chi_{mor} \tag{7.38}$$

$$\chi_{mor} = \exp\left[-4.0\left(\eta_{CH}\right)^{6.0}\right] \tag{7.39}$$

$$\eta_{CH} = 1.0 - \left(R_{paste}^{CH}\right)^{\frac{T}{15}} \tag{7.40}$$

$$R_{paste}^{CH} = CH_{paste}^{current} / CH_{paste}^{ref} \tag{7.41}$$

$$CH_{paste}^{ref} = \left(\alpha_{C3S} \times P_{C3S} \times CH_{C3S}^{20°C} + \alpha_{C2S} \times P_{C2S} \times CH_{C2S}^{20°C}\right) \times P_{CE} \tag{7.42}$$

where η_{CH} is a temperature-dependent factor to describe the influence of calcium hydroxide content on C-S-H gel morphology; T is the temperature of concrete element; and R_{paste}^{CH} is the relative ratio of calcium hydroxide content, which compares the current calcium hydroxide content in cement paste $CH_{paste}^{current}$ to the referenced calcium hydroxide content of cement matrix under same hydration degrees at 20 °C, CH_{paste}^{ref}. The relationship between C-S-H gel morphology factor χ_{mor} and relative ratio of calcium hydroxide content R_{paste}^{CH} at different temperatures were shown in Fig. 7.13 for reference.

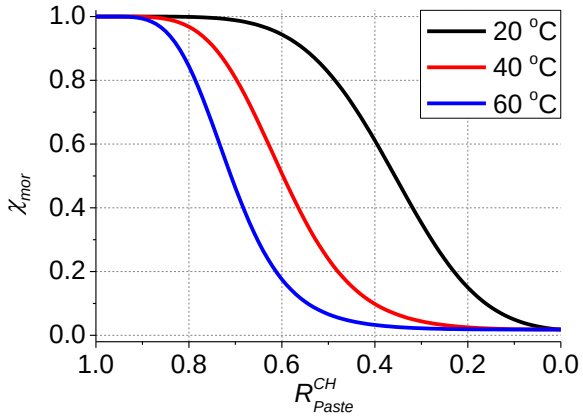

Fig. 7.13 Relationship between factors χ_{mor} and R_{paste}^{CH}

7.4 Modified model verification

7.4.1 Cement paste test

The modified model was verified by the experimental results from the cement paste described above. The material properties required for the modified model are listed in Table. 7.4. In this verification, the mass fractions of amorphous silicate and Al-silicate for all three fly ashes are used constant values of 0.15 and 0.45 for sake of simplification. The fly ash pozzolanic reaction degrees, hydration degrees, calcium hydroxide content and bound water were validated in following sections.

Table. 7.4 Fly ash material properties used in proposed model

	R_{FA}	Silicate (mass. %)	Al-silicate (mass. %)	Specific surface area (cm^2/g)
FA1	0.47	0.15	0.45	7894
FA2	0.90	0.15	0.45	5648
FA3	0.32	0.15	0.45	5623

7.4.1.1 Fly ash pozzolanic reaction degrees

Fig. 7.14 presents the comparison of fly ash pozzolanic reaction degrees predicted by current and modified model. It can be seen that the predictions were all improved and in good agreement with experimental results. The reactivity variation of these three fly ashes can be simulated by introducing the relative intrinsic reactivity of fly ash with the proper estimations of fineness of fly ashes. Compared to the the significant overestimation of current model at high temperature, the proposed model with two different reactivity phases provides a profound improvements.

However, it should be also noted that the predictions of fly ash reaction degree in modified model is still somewhat overestimated in LPC system. That is probably because the sensitivity on insufficiency of calcium hydroxide is still not enough in LPC system. Moreover, although the predictions at high temperature had been profoundly improved in modified model, the fly ash pozzolanic reaction degrees were still a little overestimated as well. One of the possible reasons is that the retarded effect induced by C-S-H gel morphology also happened on the fly ash but it has been taken into account in the modified model. Therefore, the fly ash

pozzolanic reaction degrees were overestimated. These issues should be reviewed and studied in the future.

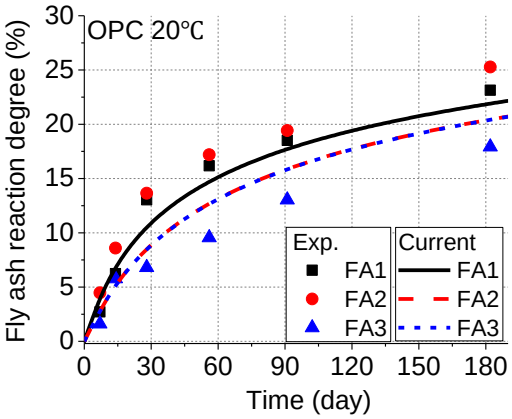

(a) current model (OPC 20 °C)

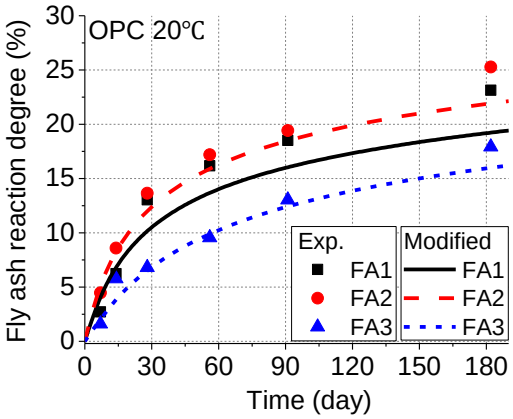

(b) modified model (OPC 20 °C)

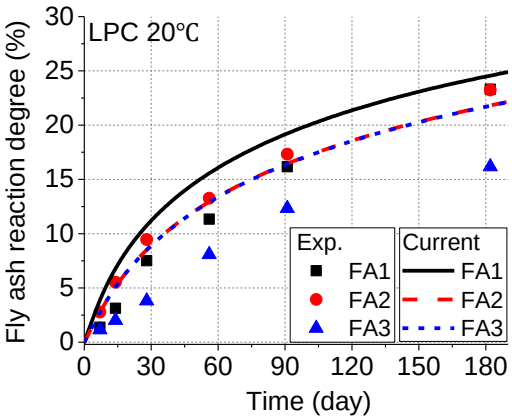

(c) current model (LPC 20 °C)

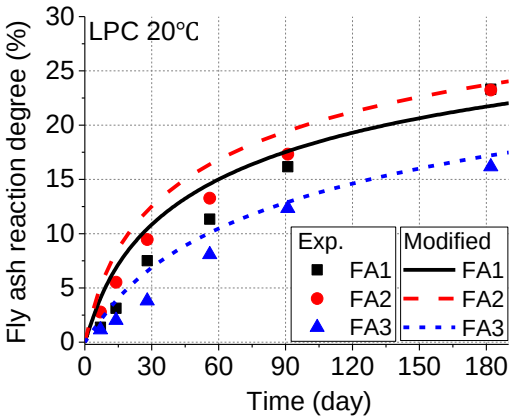

(d) modified model (LPC 20 °C)

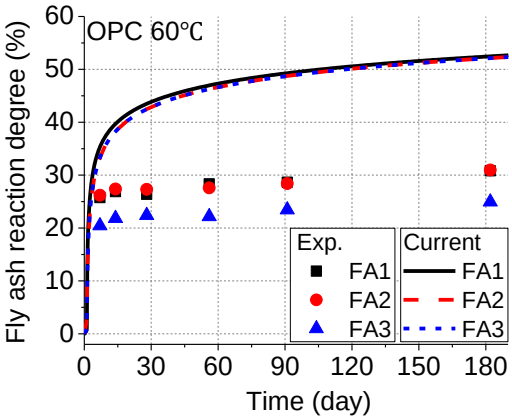

(e) current model (OPC 60 °C)

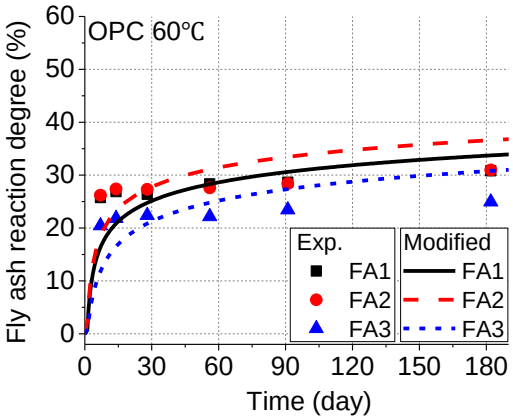

(f) modified model (OPC 60 °C)

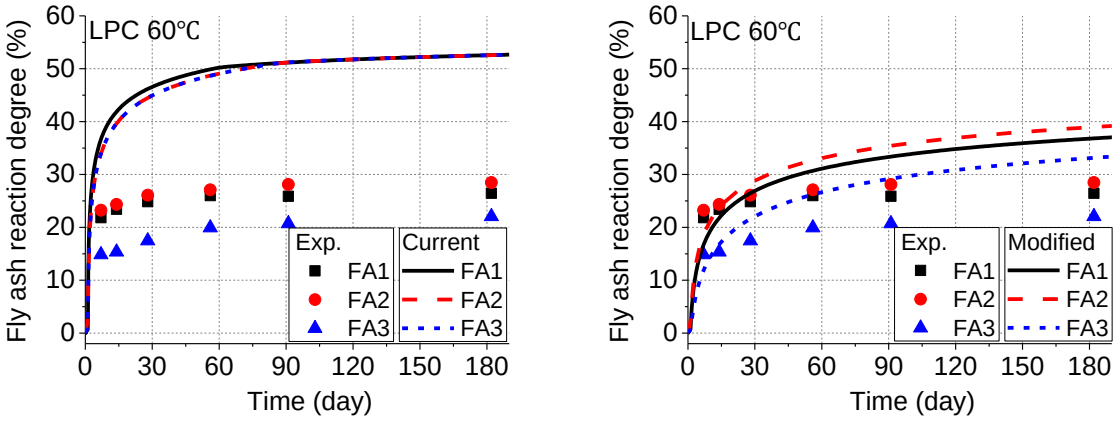

(h) current model (LPC 60 °C) (i) modified model (LPC 60 °C)

Fig. 7.14 Comparison of fly ash reaction degrees predicted by current and modified model

7.4.1.2 Cement clinkers hydration degrees

(a) Room temperature of 20 °C

The comparisons on cement hydration processes at 20 °C between current and modified model are made in Fig. 7.15. It can be seen that he simulation results of modified model are very similar to the current model at room temperature of 20 °C. However, the predicted hydration degrees of modified model is a little higher than current model. That is because the free water consumption reduces in modified model (i.e. Eq. (7.25)) since the Ca/Si ratio increases (i.e. Eq. (7.23)) and more free water therefore precipitates to the cement hydration, as Fig. 7.16 (a) and (b) shown.

Moreover, the cement hydration degree variations was also exhibited in the modified model right now. That is because the fly ash reaction degrees varies in the modified model (see Fig. 7.14) so that the free water contents were also different in different fly ashes (see Fig. 7.16 (c) and (d)).

In conclusion, the modified model can satisfactorily predict the filler effect and dilute effect of fly ahs in cement systems. This modified model also can predict the differences of cement clinker hydration degrees induced by the reactivity variation of siliceous fly ash right now.

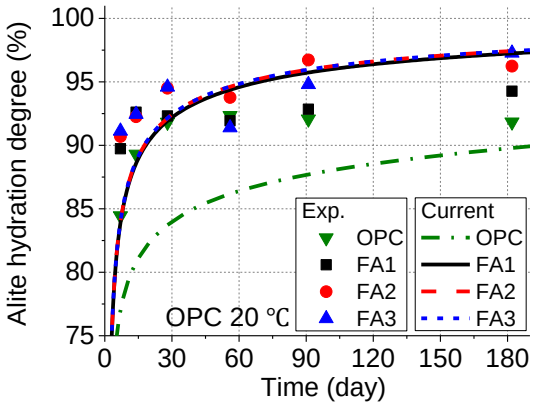

(a) current model (alite OPC 20 °C)

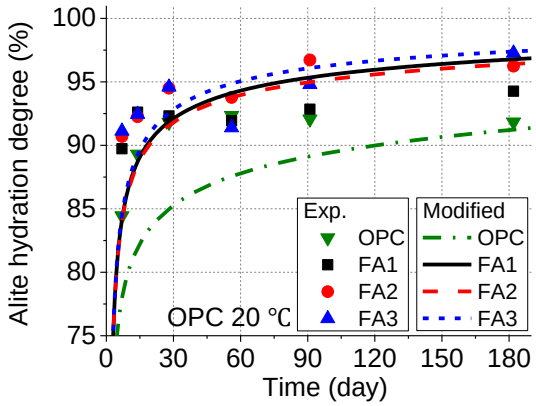

(b) modified model (alite OPC 20 °C)

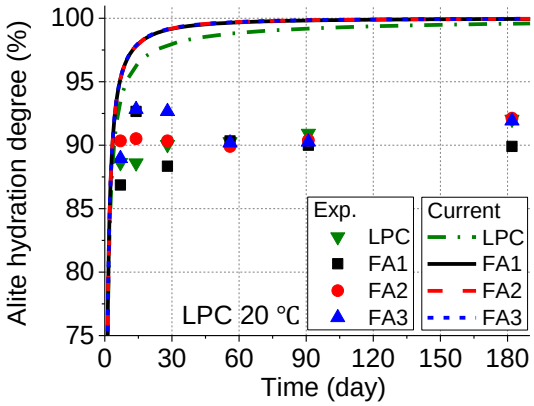

(c) current model (alite LPC 20 °C)

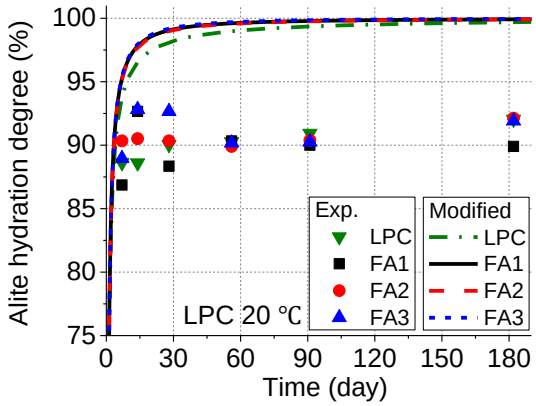

(d) modified model (alite LPC 20 °C)

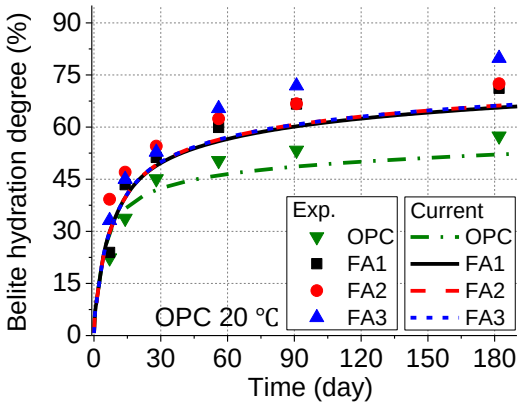

(e) current model (belite OPC 20 °C)

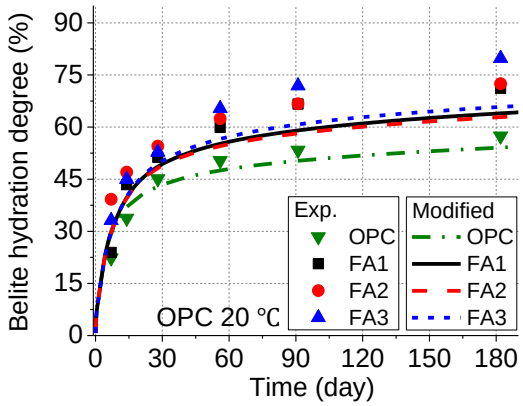

(f) modified model (belite OPC 20 °C)

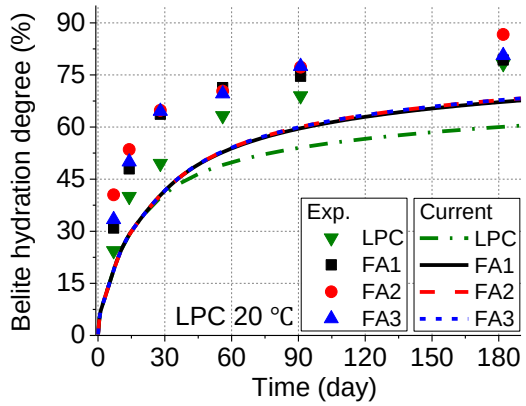

(h) current model (belite OPC 20 °C)

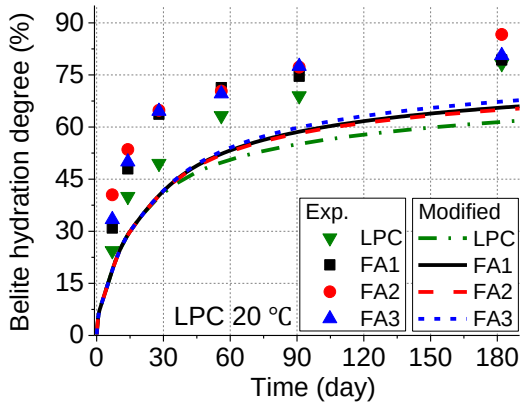

(i) modified model (belite OPC 20 °C)

Fig. 7.15 Comparison of alite and belite hydration degrees at 20 °C predicted by current model and modified model

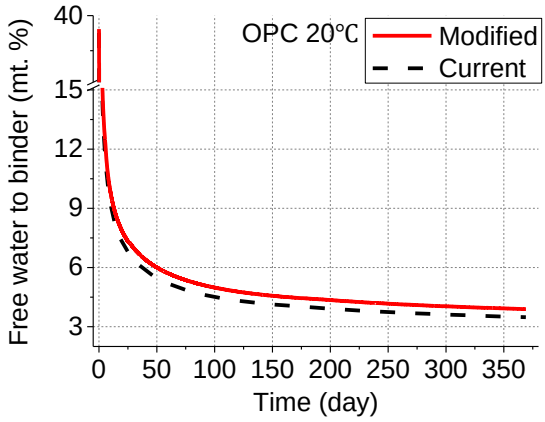

(a) OPC 20 °C

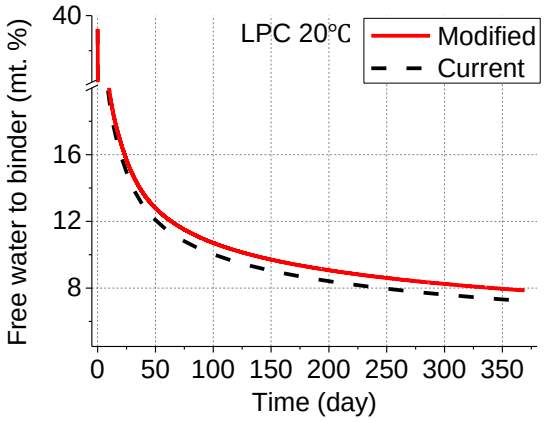

(b) LPC 20 °C

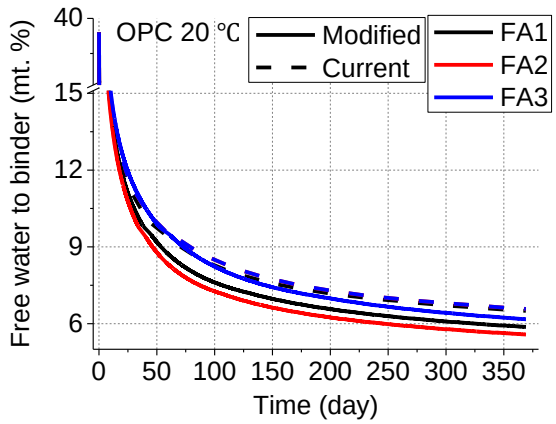

(c) FA OPC 20 °C

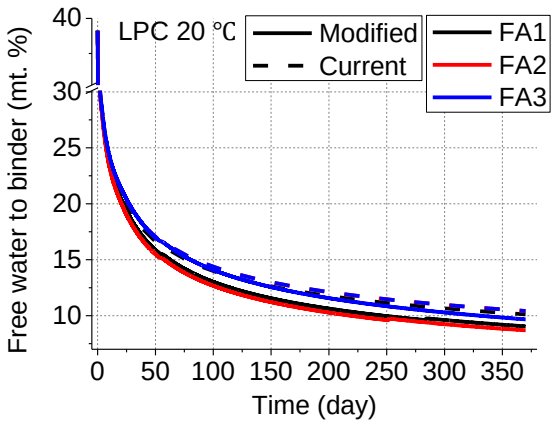

(d) FA LPC 20 °C

Fig. 7.16 Comparison of free water content of fly ash blended cement paste at 20 °C predicted by current and modified model

(b) High temperature of 60 °C

Fig. 7.17 presents the comparison of cement hydration degrees at 60 °C between current and modified model. It can be seen that, compared to current model, retarded phenomena on cement hydration can be simulated by modified model with introducing the C-S-H gel morphology effect (Fig. 7.18), especially for belite hydration processes at 60 °C in LPC systems (Fig. 7.17 (e)).

However, it should be noted that, although the general trend of alite hydration processes were also improved in the modified model, some differences still existed between simulation predictions and simulation results. Many possible reasons will result in this problem, such as C-S-H gel morphology effect, hydration model of alite or the interaction between alite and blite and they should be comprehensively reviewed in the future.

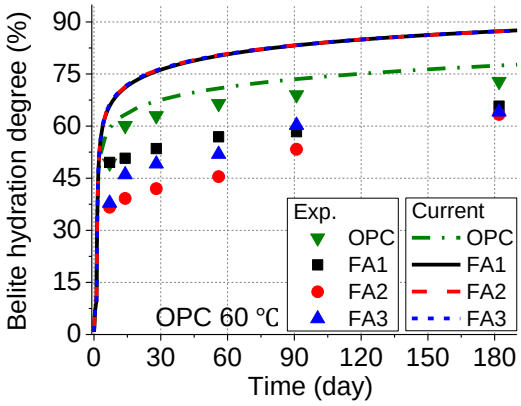

(a) current model (belite OPC 60 °C)

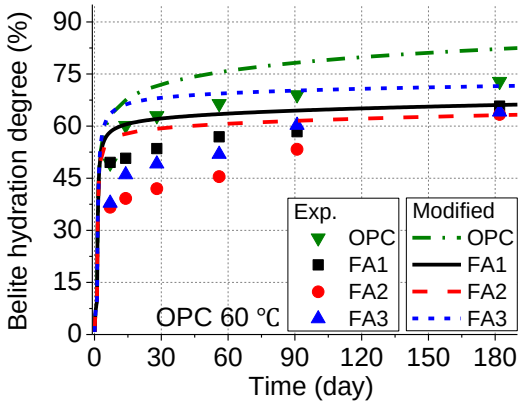

(b) modified model (belite OPC 60 °C)

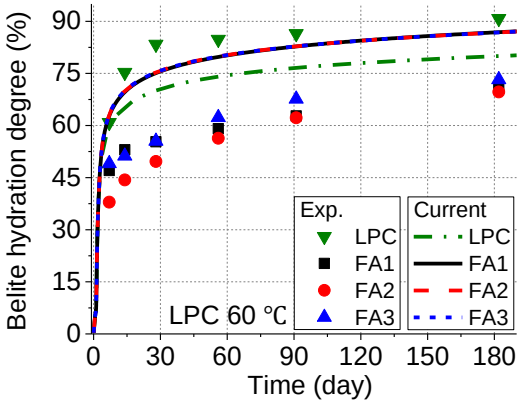

(c) current model (belite LPC 60 °C)

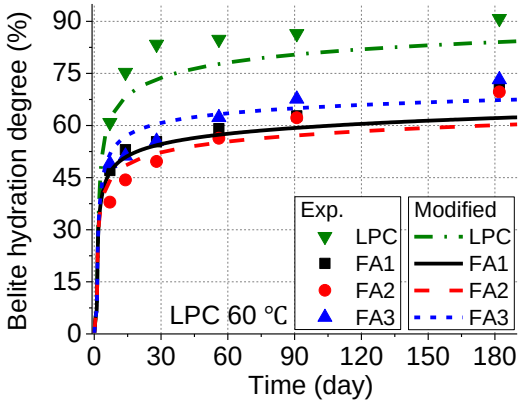

(d) modified model (belite LPC 60 °C)

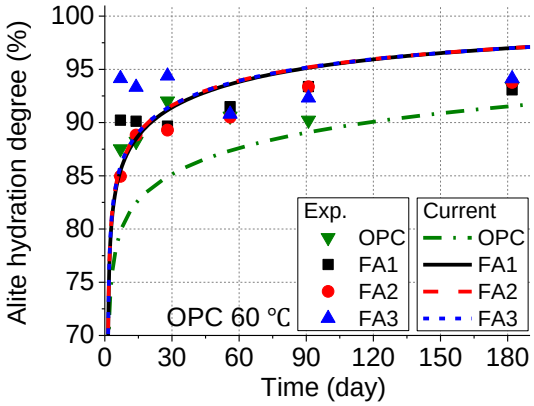

(e) current model (alite OPC 60 °C)

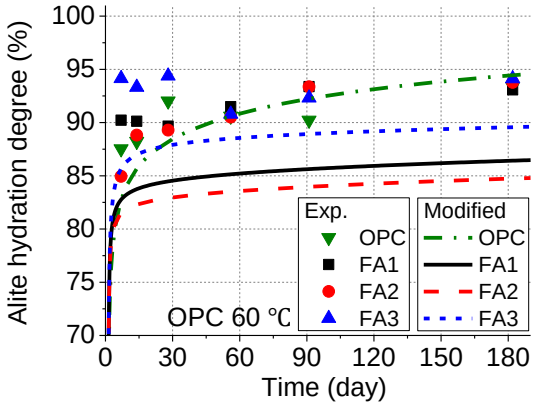

(f) modified model (alite OPC 60 °C)

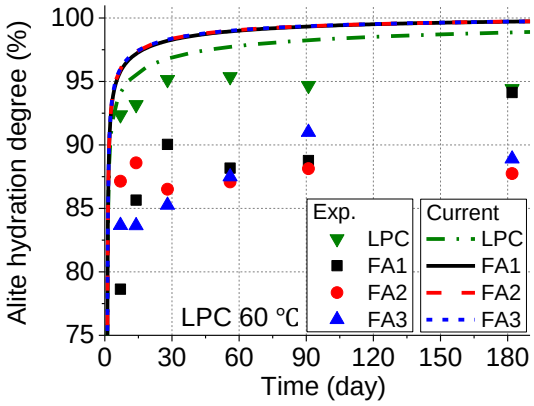

(h) current model (alite LPC 60 °C)

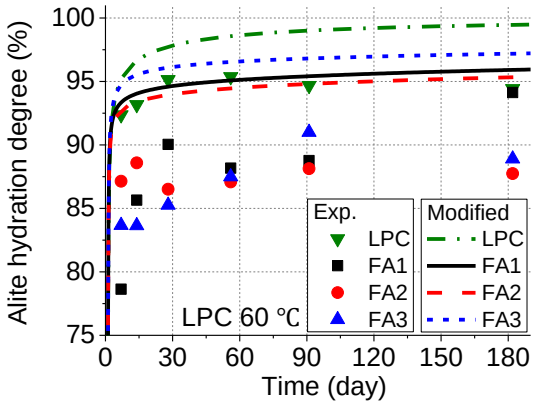

(i) modified model (alite LPC 60 °C)

Fig. 7.17 Comparison of alite and belite hydration degrees at 60 °C predicted by current model and modified model

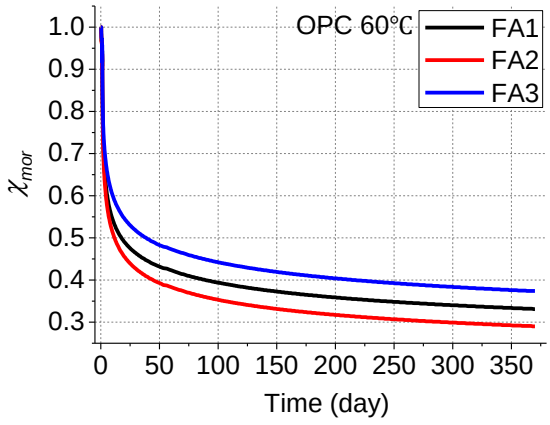

(a) OPC 60 °C

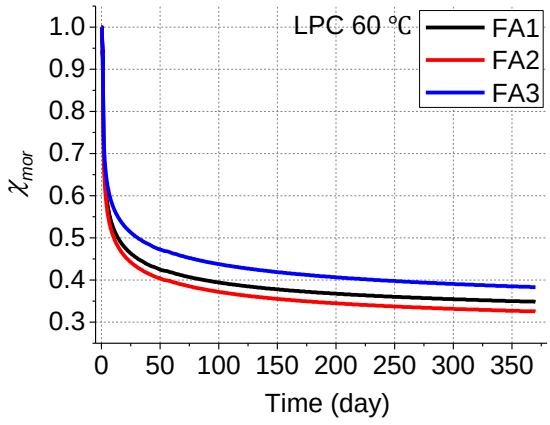

(b) LPC 60 °C

Fig. 7.18 C-S-H gel morphology factor χ_{mor} in fly ash blended cement paste at 60 °C

7.4.1.3 Calcium hydroxide content and bound water content

Fig. 7.19 compares calcium hydroxide content predicted by current model and modified model as well. It can be seen that all simulation results were significantly improved in the modified model, especially for the cases of OPC pastes at 20 °C and LPC pastes 60 °C. However, it is still noted that the calcium hydroxide content of LPC still tended to be underestimated because the fly ash reaction degrees were overestimated (Fig. 7.14).

The bound water was also used to verify the proposed model. It can be seen that the simulation results were also improved in the modified model. However, similar to cement paste, the bound water of fly ash blended paste were still overestimated at high temperature because the corresponding decomposition of hydration products has not been taken into account in modified model.

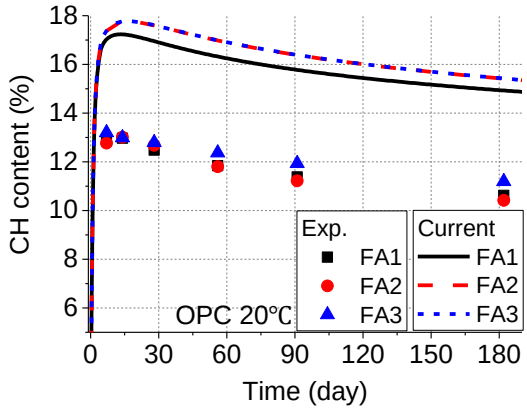

(a) current model (OPC 20 °C)

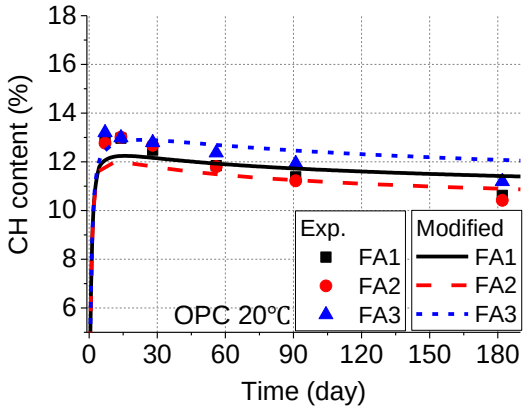

(b) modified model (OPC 20 °C)

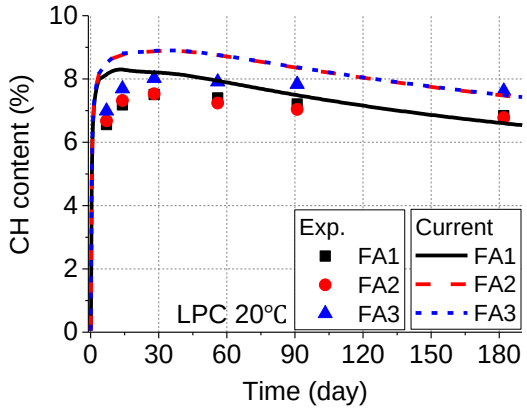

(c) current model (LPC 20 °C)

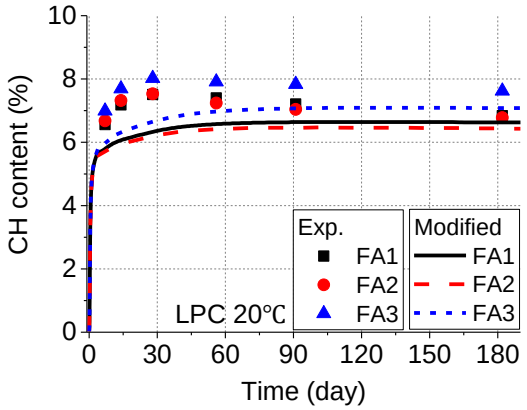

(d) modified model (LPC 20 °C)

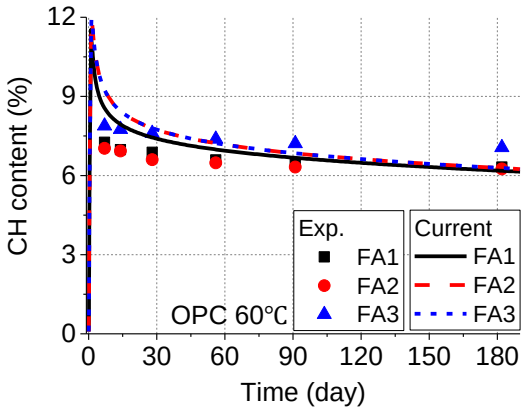

(e) current model (OPC 60 °C)

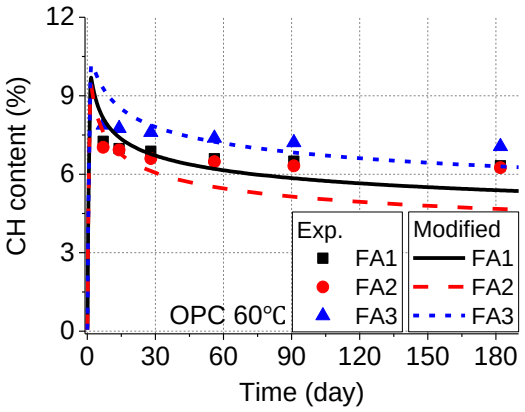

(f) modified model (OPC 60 °C)

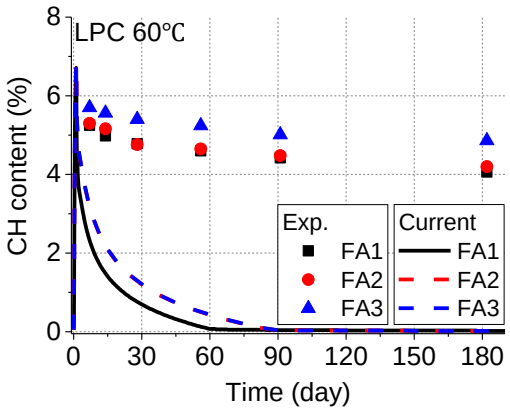

(h) current model (LPC 60 °C)

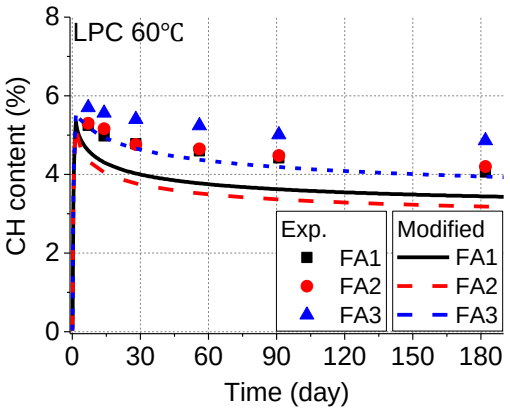

(i) modified model (LPC 60 °C)

Fig. 7.19 Comparison of calcium hydroxide content predicted by current model and modified model

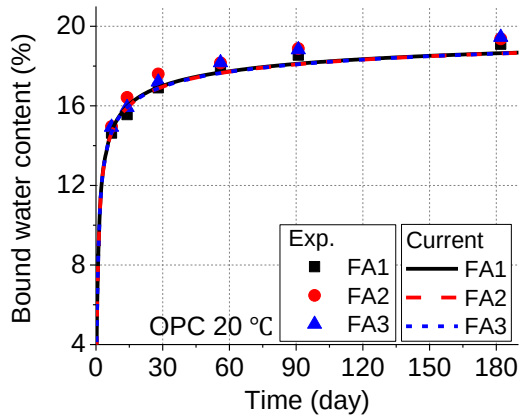

(a) current model (OPC 20 °C)

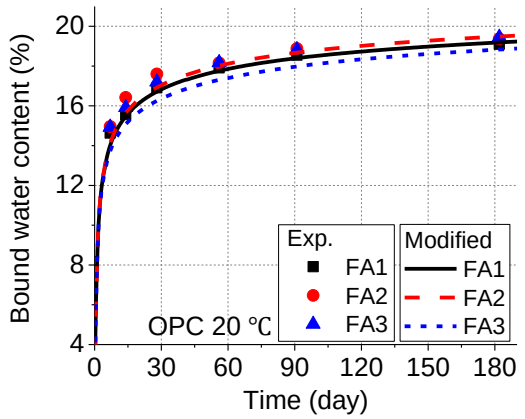

(b) modified model (OPC 20 °C)

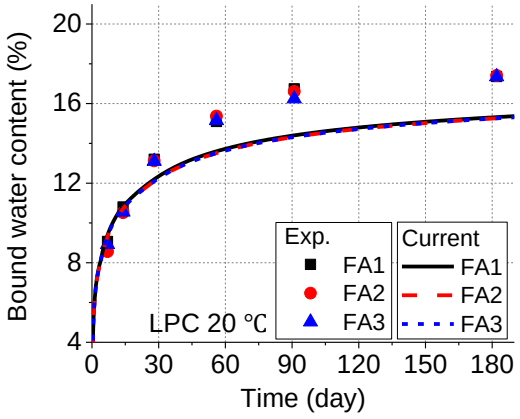

(c) current model (LPC 20 °C)

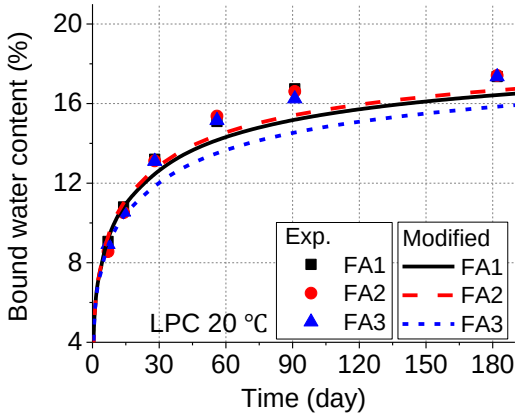

(d) modified model (LPC 20 °C)

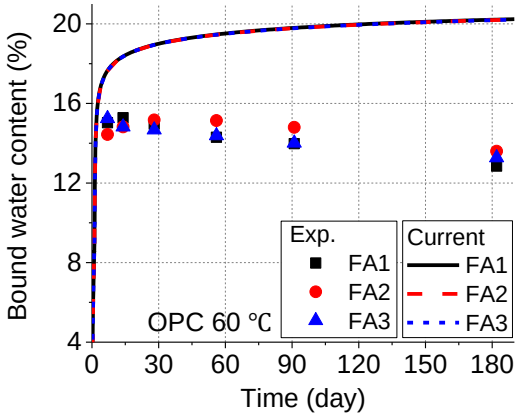

(e) current model (OPC 60 °C)

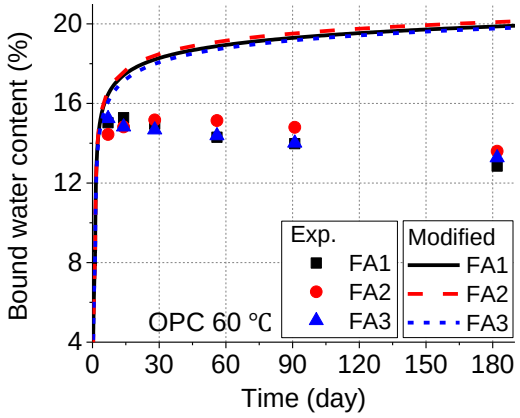

(f) modified model (OPC 60 °C)

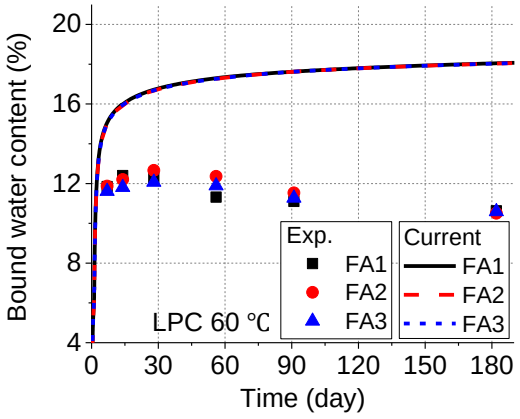

(h) current model (LPC 60 °C)

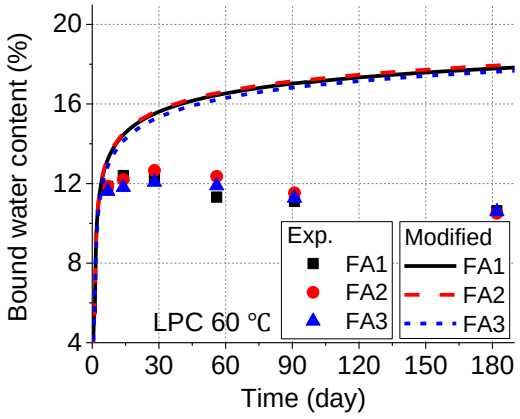

(i) modified model (LPC 60 °C)

Fig. 7.20 Comparison of bound water content predicted by current model and modified model

7.4.2 Hanehara's experiment [14]

Furthermore, Hanehara's experiment was also used to verify the proposed model. The variables in this experiment included the temperature (20°C and 40°C), the water to cementitious materials ratio (30% and 50%) and the fly ash replacement ratio (from 10% to 60%). Other experimental details can be found in reference 9.

Because the fly ash material properties required for proposed model are unknown, a trial and error simulation was carried out to determine the proper material parameters by fitting the experiment data of one case first (i.e. W/C of 50 %, fly ash replacement ratio of 20 % and sealed curing at 40 °C, Fig. 7.21). The regression result was listed in Table. 7.5. After that, these material parameters were submitted back to the proposed model to check other cases.

Table. 7.5 Fly ash material properties used in proposed model

	R_{FA}	Silicate (mt. %)	Al-silicate (mt. %)	Specific surface area (cm^2/g) *
Hanehara	1.00	0.20	0.65	4000

Note *: The specific surface area is used the blain value of fly ash in the original paper [14].

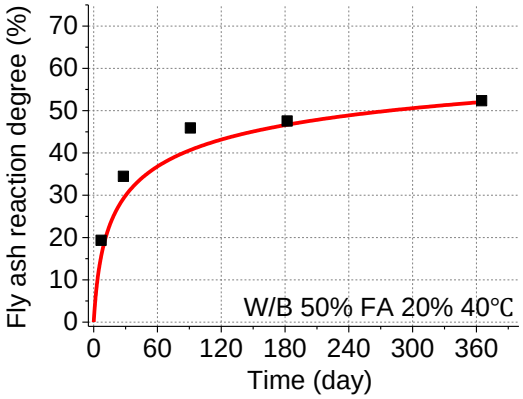

Fig. 7.21 Trial-error simulation for determination of fly ash material parameters of Hanehara's experiment used in the modified model

The comparison between the predictions using proposed model and the experimental results are presented in Fig. 7.22. It can be seen that theoretical predictions are all in good agreement with experiment results among different conditions. In conclusion, the proposed two-phase reaction model can be used to simulate the temperature-dependent pozzolanic reaction of fly ash in cement systems.

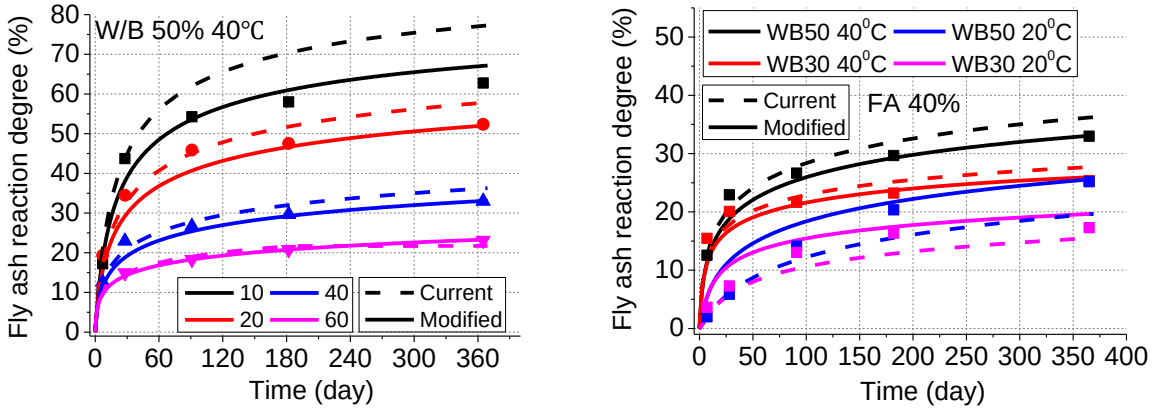

(a) W/B 50% 40°C (b) FA 40%

Fig. 7.22 Comparison between simulation predictions and Hanehara's experimental results

7.5 Parameter analysis

To better understand how the fly ash material properties affect the concrete performance, based on the proposed model, fly ash FA1 were selected to carry out a long-term (1 year) parametric analyses to investigate the influence of fly ash pozzolanic reaction on concrete compression strength.

It can be seen from Fig. 7.23 and Fig. 7.24 that pozzolanic reaction degrees increased as fly ash replacement ratio decreased, which is coincides previous result. A higher amount of amorphous phase also provides a higher pozzolanic reaction degree. The influence of high reactivity phase Al-silicate is higher than silicate as well. Correspondingly, the compression strength of concrete increased as the amount of high reactivity phase increased and fly ash replacement ratio decreased (Fig. 7.25 and Fig. 7.26).

It is noted that compression strength of fly ash concrete after 1 year will be higher than normal concrete when fly ash replacement ratio is smaller than 30% both at low and high temperature and the promotion effect on strength seems more profound at low temperature. Therefore, to archive a higher compression strength than OPC concrete, it seems that the fly ash replacement ratio should not be higher than 30%.

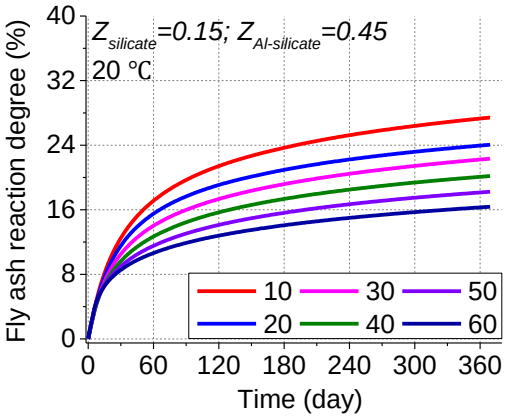

(a) $Z_{silicate}$ = 0.15; $Z_{Al\text{-}silicate}$ = 0.45 at 20 °C

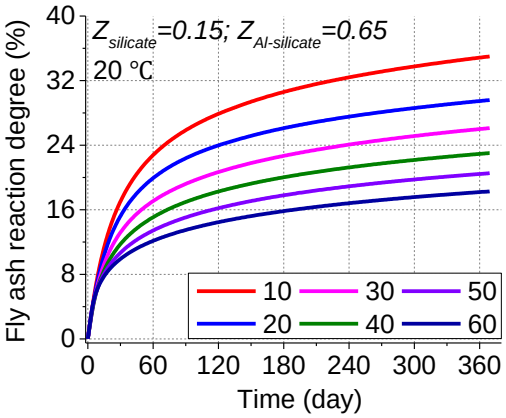

(b) $Z_{silicate}$ = 0.15; $Z_{Al\text{-}silicate}$ = 0.65 at 20 °C

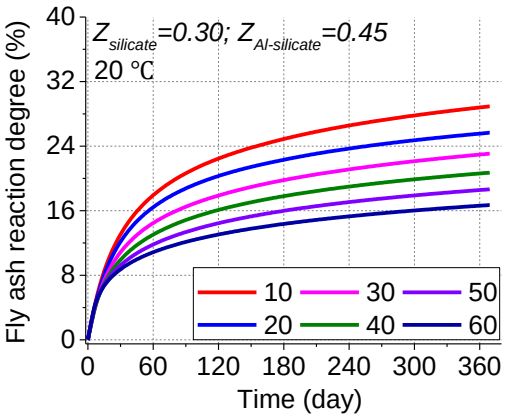

(c) $Z_{silicate}$ = 0.30; $Z_{Al\text{-}silicate}$ = 0.45 at 20 °C

Fig. 7.23 Parametric analyses on pozzolanic reaction degree of fly ash at 20 °C

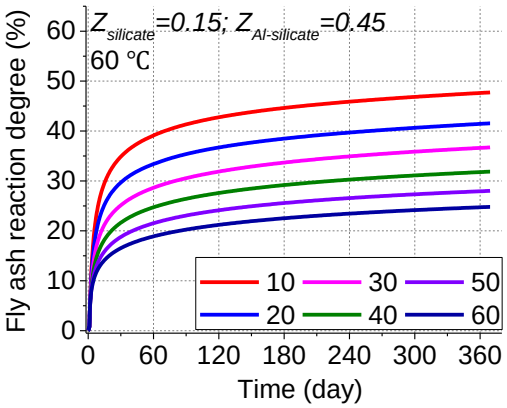

(a) $Z_{silicate}$ = 0.15; $Z_{Al\text{-}silicate}$ = 0.45 at 60 °C

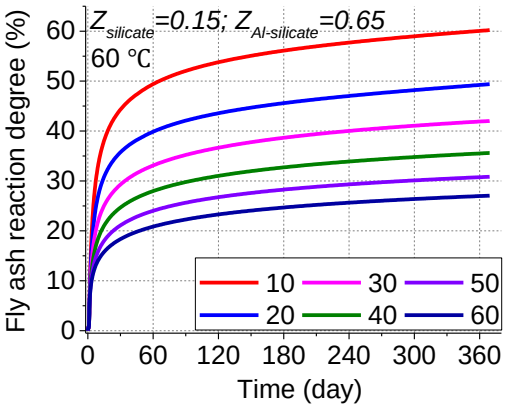

(b) $Z_{silicate}$ = 0.15; $Z_{Al\text{-}silicate}$ = 0.65 at 60 °C

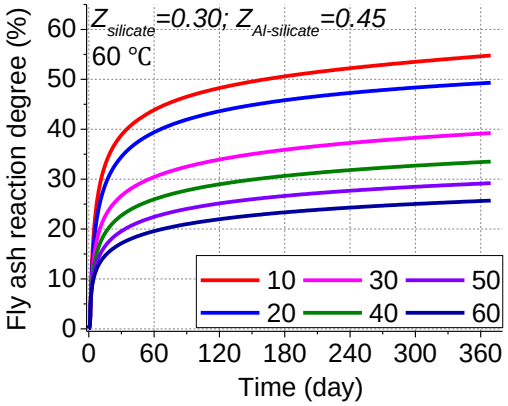

(c) $Z_{silicate}$ = 0.30; $Z_{Al\text{-}silicate}$ = 0.45 at 60 °C

Fig. 7.24 Parametric analyses on pozzolanic reaction degree of fly ash at 60 °C

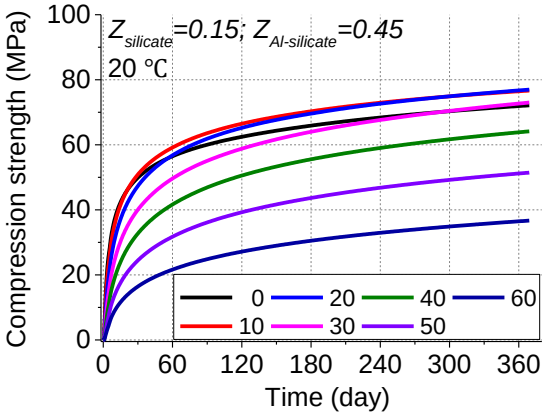

(a) $Z_{silicate}$ = 0.15; $Z_{Al\text{-}silicate}$ = 0.45 at 20 °C

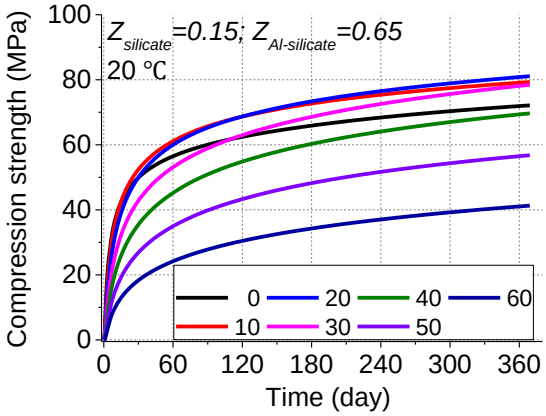

(b) $Z_{silicate}$ = 0.15; $Z_{Al\text{-}silicate}$ = 0.65 at 20 °C

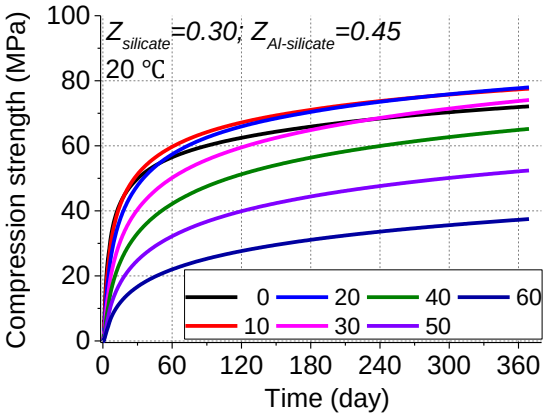

(c) $Z_{silicate}$ = 0.15; $Z_{Al\text{-}silicate}$ = 0.45 at 20 °C

Fig. 7.25 Parametric analyses on compression strength of fly ash concrete at 20 °C

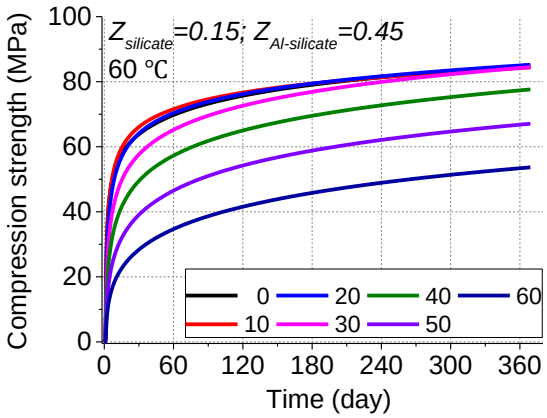

(a) $Z_{silicate}$ = 0.15; $Z_{Al\text{-}silicate}$ = 0.45 at 60 °C

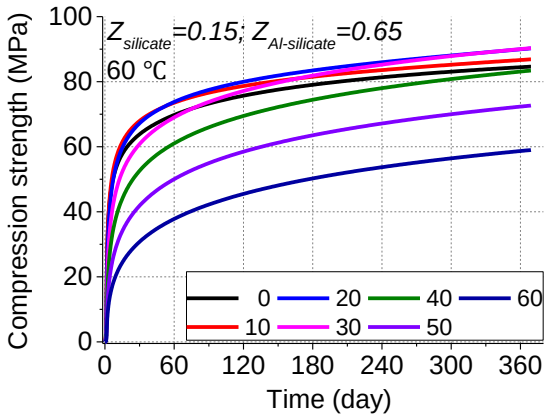

(b) $Z_{silicate}$ = 0.15; $Z_{Al\text{-}silicate}$ = 0.65 at 60 °C

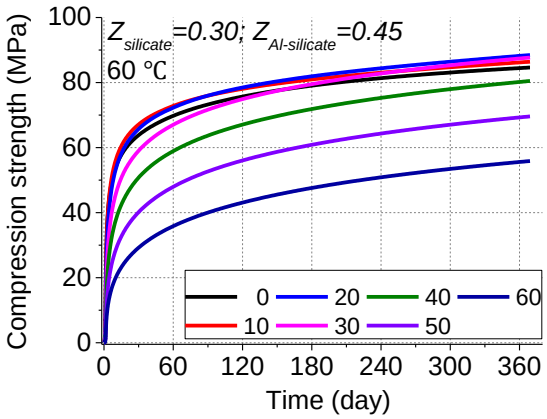

(c) $Z_{silicate}$ = 0.15; $Z_{Al\text{-}silicate}$ = 0.45 at 60 °C

Fig. 7.26 Parametric analyses on compression strength of fly ash concrete at 60 °C

7.6 Summary and conclusions

With previous experiment works and discussions, on the basis of current DuCOM multi-heat model, this chapter is going to develop a unified model to predict the pozzolanic reaction of different siliceous fly ash at different temperatures. The conclusions of this chapter are summarized in the following points:

1. A temperature-dependent Ca/Si ratio model was proposed in this chapter. Numerical analysis showed that the prediction on calcium hydroxide content in cement paste and FA blended cement paste were both improved in modified model;

2. A two-phase reaction model for siliceous pozzolanic reaction model considering variation of fly ash material properties was proposed in this chapter. Numerical analysis showed that this modified model can predict the temperature-dependent pozzolanic reaction of different siliceous fly ash in cement system now;

3. A interaction model between cement clinkers and fly ash was proposed in chis chapter. Numerical analysis showed that, with this modified model, DuCOm model can simulate the retarded effect on cement hydration due to fly ash pozzolanic reaction right now; and

4. Based on the proposed model, fly ash FA1 were selected to carry out a long-term (1 year) parametric analyses to investigate the influence of fly ash pozzolanic reaction on concrete compression strength. Numerical analysis showed that, to archive a higher compression strength than OPC concrete, the fly ash replacement ratio seems should not be higher than 30%.

8 Conclusions and perspectives

The work presented in this thesis was developed in several directions to improve the understanding of material properties of and temperature-dependent reactivity of siliceous fly ash and then modelling its behavior in cement systems. On this respect, this chapter is going to summarize the major achievements as follows:

8.1 Conclusions

8.1.1 Fly ash material characterization

A new segmentation criteria both considering chemical and mineralogical influence was developed to identify and quantity the amount of reactive amorphous phase through SEM-EDS mapping. This criteria provide us with a new and fundamental way to characterize a siliceous fly ash. Based on this criteria, a fly ash can be satisfactorily distinguished by serval fundamental crystalline and amorphous phases in a micro-scale with the help of full element SEM-EDS mapping analysis. Therefore, this criteria is a powerful approach which can cover any types of siliceous fly ash. More importantly, this criteria has a great potential to be extended to other pozzolanic materials, such class C fly ash, slag, silica fume and so on.

SEM-EDS mapping analysis result showed that fly ash are mainly composed of

amorphous silicate and amorphous Al-silicate. SEM-EDS mapping result showed that crystalline mullite usually exists as a small solid and widely distributes in fly ash particles due to local crystallization of amorphous Al-silicate phase. Compared to mullite, quartz tends to exist along and and it is usually covered by amorphous silicate. Because quartz comes from the parent coal and the temperature of furnace is not enough to melt all the quartz, the outside part of quartz is melted and becomes amorphous silicate and finally cover the inside crystalline quartz core.

Moreover, experiment showed that Blaine air permeability method, laser diffraction method and nitrogen absorption method all have their own drawbacks on estimation of fly ash fineness. Therefore, a new image analysis method based on the new segmentation criteria was developed in this study. Based on this new image analysis method, the specific surface area of induvial phase and the whole particles can be accurately estimated without the morphology influence.

8.1.2 Reactivity of siliceous fly ash

The pozzolanic reactivity of fly ash depends on its phase assemblage, fineness and its intrinsic reactivity. Alkali dissolution test result showed that the reactive phases of siliceous fly ash are amorphous silicate and Al-silicate; amorphous Al-silicate is more reactive than amorphous silicate but less sensitive to temperature.

Alkali dissolution test result further showed that the intrinsic reactivity of the amorphous phase are affected by combustion conditions and it may be different in different fly ashes. Since a proper combustion condition will both promote the production of amorphous solids and its intrinsic reactivity, the amorphous-crystalline ratio can be used to describe the intrinsic reactivity of amorphous phases.

With the help of amorphous-crystalline ratio, the dissolution processes of the studied fly ashes can be reasonably explained. FA1 has a higher specific surface area but a smaller amorphous-crystalline ratio than FA2, therefore FA1 and FA2 have the similar dissolution processes both at 20 and 60 °C. Compared to FA1 and FA2, FA3 has the lowest specific surface area and amorphous-crystalline ratio, the dissolution process is therefore the lowest among

these three fly ashes.

8.1.3 Interaction between cement and fly ash

Previous research and C-S-H mopholgoy test result showed that C-S-H gel tends to growth parallel to the surface of anhydrous cement grains at low calcium hydroxide content but perpendicular to the surface at high calcium hydroxide content. Besides the dilute effect and filler effect of fly ash which promotes the cement hydration rate at early age, the later hydration process will be retarded in fly ash blended cement paste because C-S-H gel becomes denser with continuous consumption of calcium hydroxide of fly ash. Therefore, the influence of fly ash on cement hydration is the result of the competition between filler effect and dilute effect and the morphology effect.

8.1.4 Modelling of pozzolanic reaction of siliceous fly ash

TGA experiment showed that calcium hydroxide content decreased as curing temperature increases. That is because the Ca/Si ratio increases as curing temperature increases. Moreover, simulation result showed that current model overestimate the calcium hydroxide content of cement paste. Therefore, a temperature-dependent Ca/Si ratio model was proposed in this chapter. Numerical analysis showed that this modified model can satisfactorily predict the calcium hydroxide content of cement paste.

On the basis of this modified cement model, a two-phase reaction model for siliceous pozzolanic reaction model with considering the amount of amorphous phase assemblage, surface areas and relative intrinsic reactivity of fly ash was proposed to predict the temperature-dependent pozzolanic reaction of siliceous fly ash in cement system. The interaction between cement clinkers and fly ash was taken into account by introducing C-S-H morphology effect to cement hydration model.

Numerical results show that the proposed two-phase reaction model can be used to predict temperature-dependent pozzolanic reaction of various siliceous fly ash in cement systems with reasonable accuracy.

8.2 Perspectives

This thesis developed the material characterization method on siliceous fly ash; discussed the the mechanism on pozzolanic reaction of siliceous fly ash and interaction between cement and fly ash; and finally proposed a two-phase reaction model to predict temperature-dependent pozzolanic reaction of siliceous fly ash. In the future, the research will be further conducted at least in following directions

1. Experimentally study the influence of the fly ash production processes to the intrinsic reactivity of amorphous phase, such as combustion temperature, cooling rate, coal chemical composition etc.,;

2. Study the influence of pozzolanic reaction of siliceous fly ash to the microstructure of fly ash cement paste;

3. Study the influence of pozzolanic reaction of siliceous fly ash to the fly ash concrete performance, including strength, shrinkage, creep, chloride ingression etc.; and

4. Based on the framework developed in this study, generalize and develop current research method to be capable of applying for other pozzolanic materials and finally build a unified pozzolanic reaction model to cover all the pozzolanic materials.

A Two-dimension hamming window

As outlined before, EDS data is affected by the proximity of epoxy resin and the adjacent particles with different chemical composition and consequently full with noises. Therefore, the raw EDS data should be smoothed before chemical analysis.

To account of this effect, Durdzinski suggested to use Hamming window to smooth data [9]. However, typical hamming window is one-dimensional. In other words, the EDS data should be horizontally smoothed first (step 1) and then vertically smoothed (step 2) or inversely (Fig. A.1 (a)) [9]. This is obviously inconsistent with the real situation that the EDS data of the interested point will be affected by all of its neighbor points (Fig. A.1 (b)).

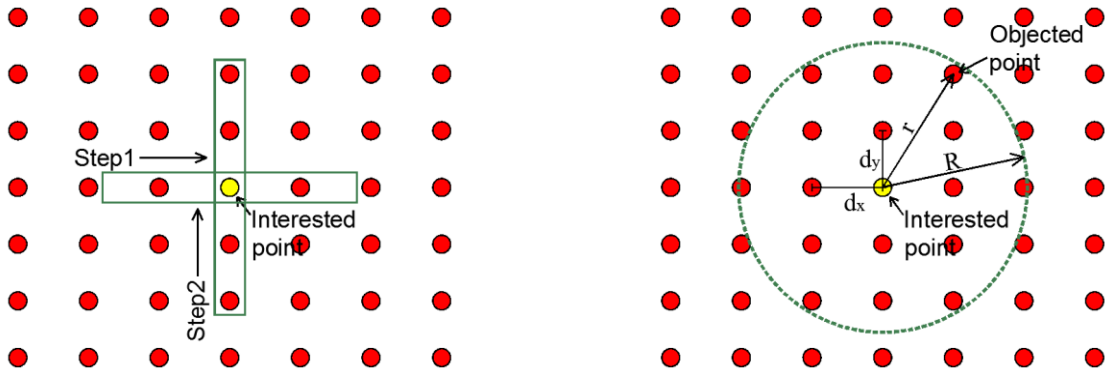

(a) one dimension (b) two dimension

Fig. A.1 Schematic illustration on dimension-reduction algorithm of hamming window

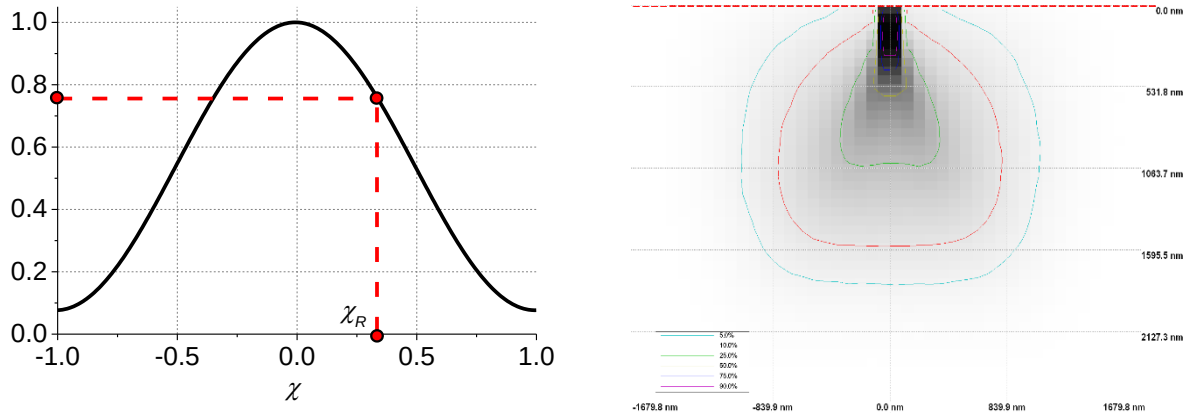

(a) hamming window (b) energy distribution

Fig. A.2 Schematic illustration on algorithm of hamming window smooth method

Therefore, a new dimension-reduction algorithm was proposed herein for hamming window as follows. With respect to hamming window, the most important parameter is the normalized distance of χ (Fig. A.2 (a)). For the two-dimension EDS data matrix (Fig. A.1 (b)), because the radium of interaction volume *R* is limited, the data of interested point (yellow one) only will be affected by the neighbor points within the interaction volume (green circle). Therefore, if we introduced a relative distance χ_R to submit into the hamming window (Fig. A.2 (a)), which is the ratio of the distance of the interested point and the objected point *r* and the radium of interaction volume *R* (i.e. Eq. (A.1)), the two-dimension problem can be reduced to the one-dimension issue and all smooth methods for one-dimension window can be directly used again.

$$\chi_R = r / R \tag{A.1}$$

$$r = \sqrt{\left(n_x d_x\right)^2 + \left(n_y d_y\right)^2} \tag{A.2}$$

where χ_R is the ratio of distance of interested point and objected point *r* and radium of interaction volume *R; R* is the radium of interaction volume, which can be determined by the energy distribution simulated by Casino Monte Carlo simulation software (Fig. A.2 (b)); n_x and n_y are the horizontal and vertical layers between the interested point and the objected point; and d_x and d_y are the horizontal and vertical spacing distance of data matrix.

B Thermogravimetric curves

B.1 Cement paste

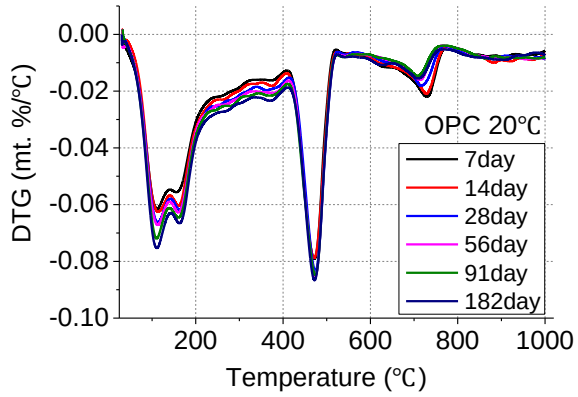

(a) OPC 20°C

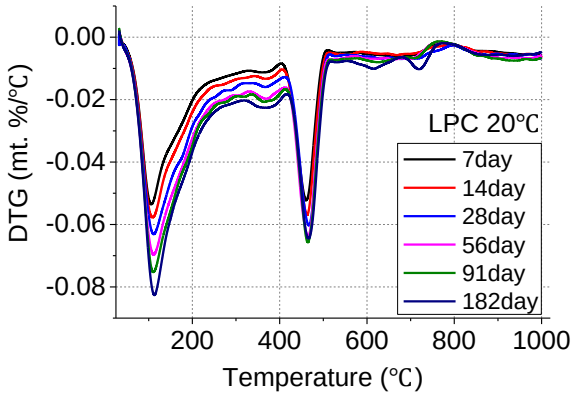

(b) LPC 20°C

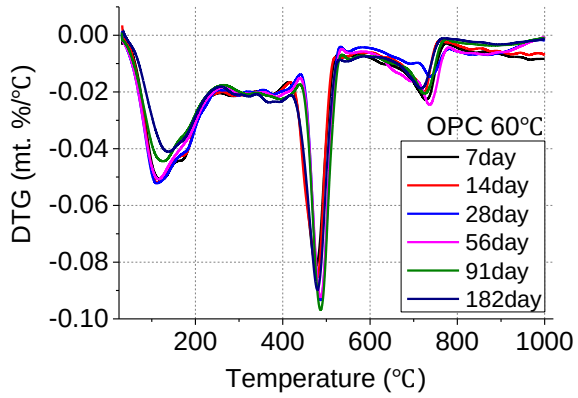

(c) OPC 60°C

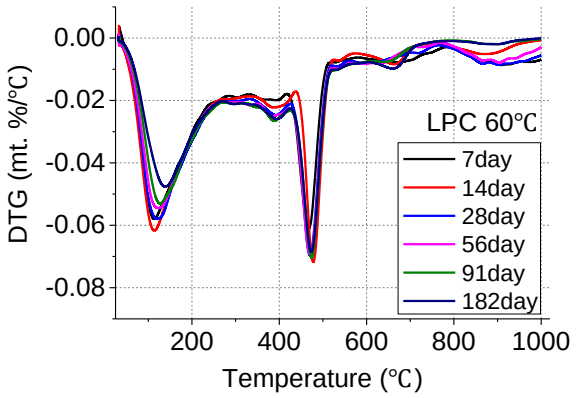

(d) LPC 60°C

Fig. B.1 Differential thermogravimetric curves of cement paste

B.2 FA1 blended cement paste

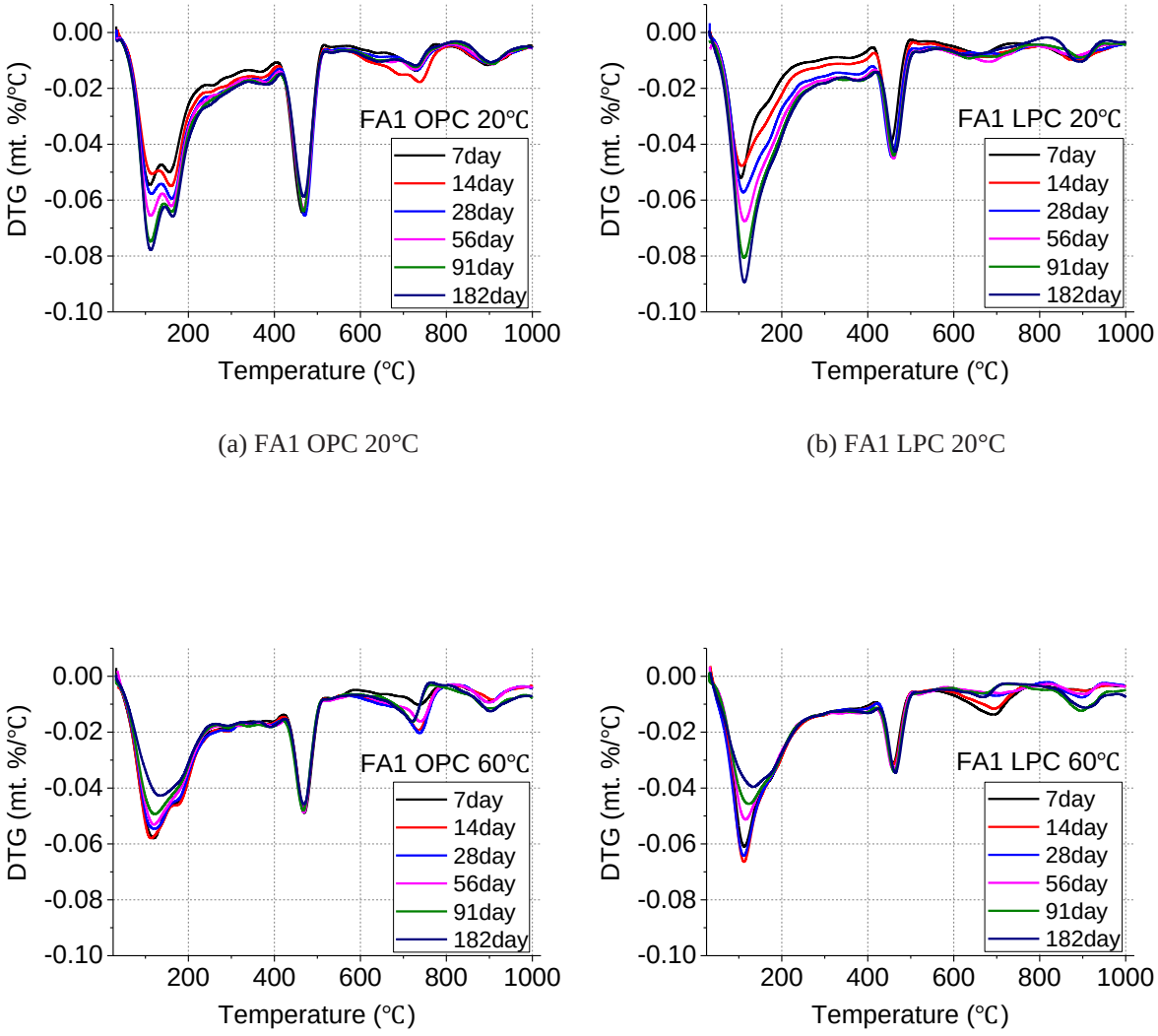

(a) FA1 OPC 20°C

(b) FA1 LPC 20°C

(c) FA1 OPC 60°C

(d) FA1 LPC 60°C

Fig. B.2 Differential thermogravimetric curves of FA1 blended cement paste

B.3 FA2 blended cement paste

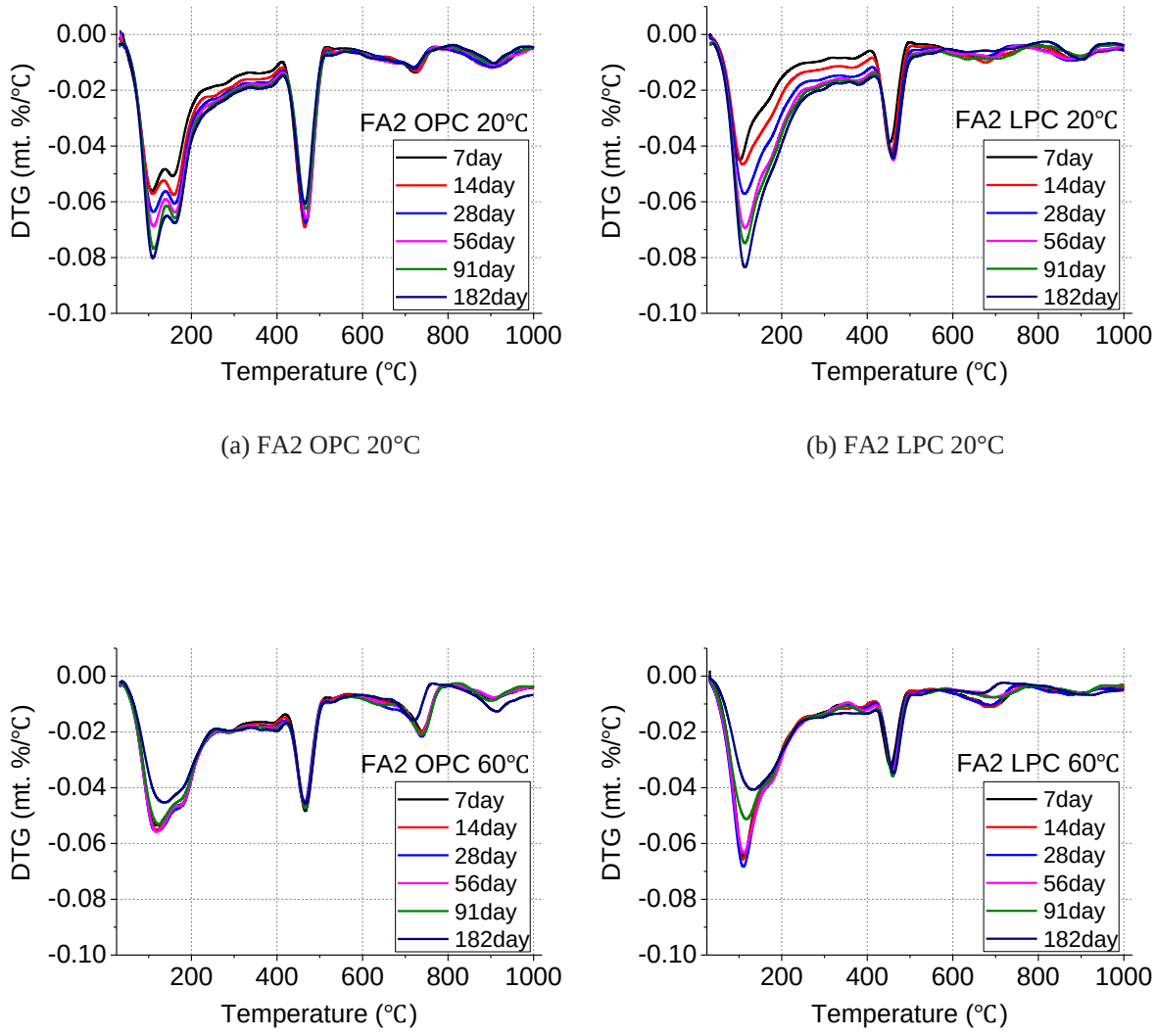

(a) FA2 OPC 20°C

(b) FA2 LPC 20°C

(c) FA2 OPC 60°C

(d) FA2 LPC 60°C

Fig. B.3 Differential thermogravimetric curves of FA2 blended cement paste

B.4 FA3 blended cement paste

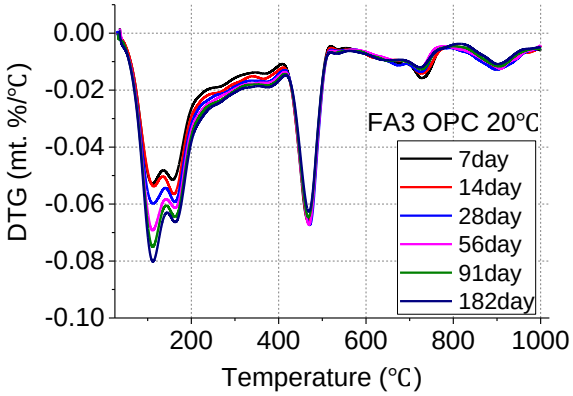

(a) FA3 OPC 20°C

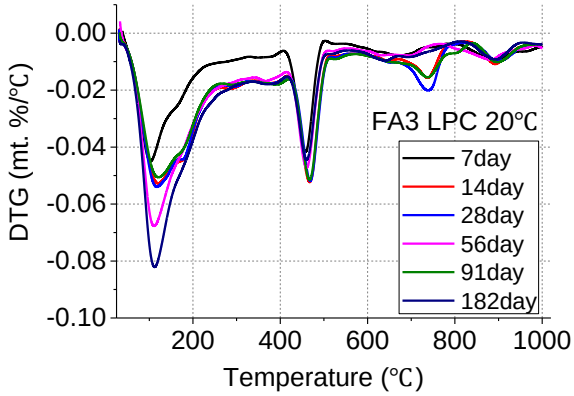

(b) FA3 LPC 20°C

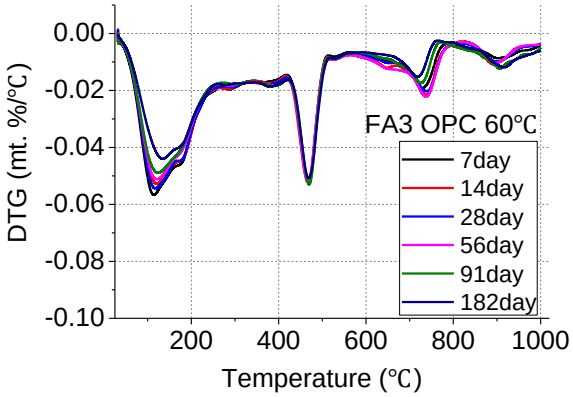

(c) FA3 OPC 60°C

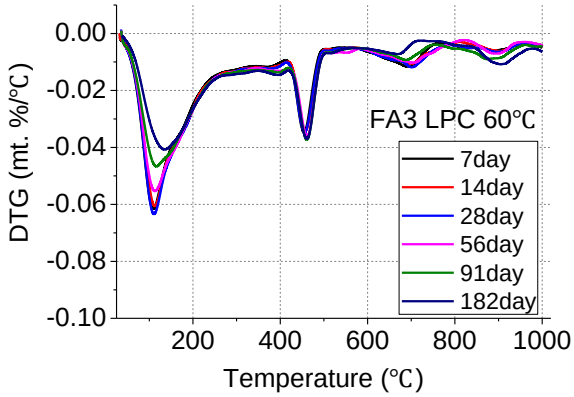

(d) FA3 LPC 60°C

Fig. B.4 Differential thermogravimetric curves of FA3 blended cement paste

C Hydration degrees

C.1 Cement paste

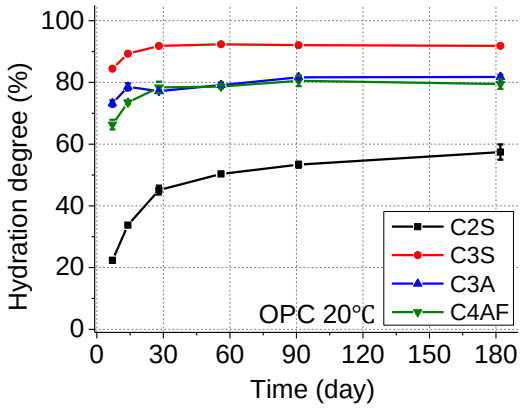

(a) OPC 20°C

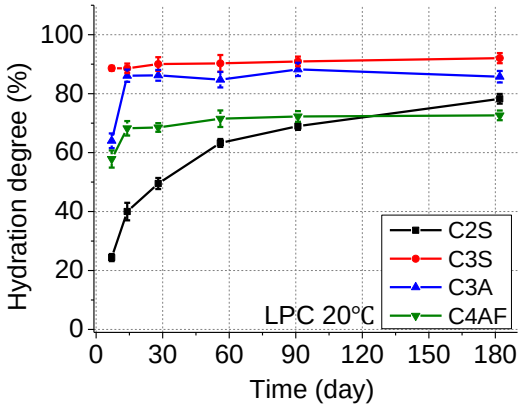

(b) LPC 20°C

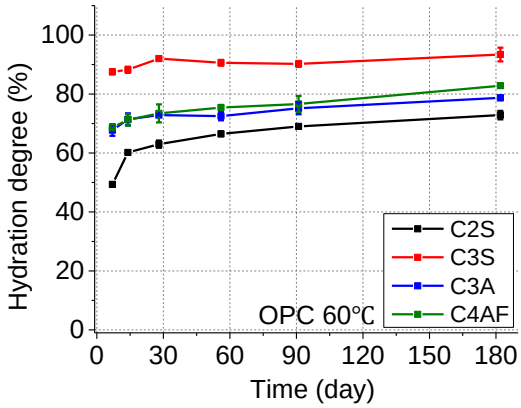

(c) OPC 60°C

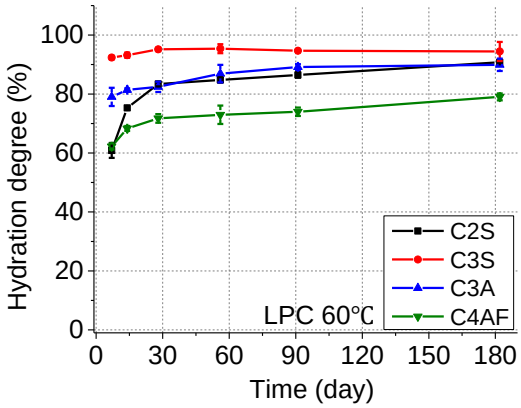

(d) LPC 60°C

Fig. C.1 Hydration degrees of cement paste

C.2 FA1 blended cement paste

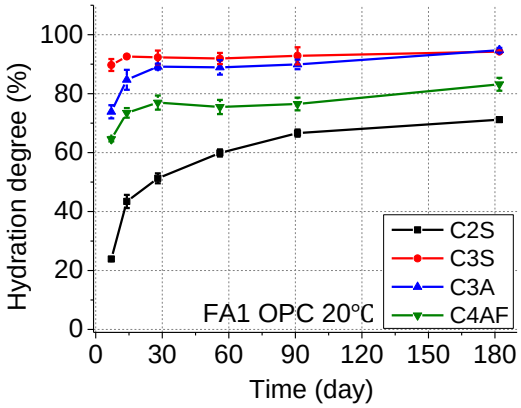

(a) FA1 OPC 20°C

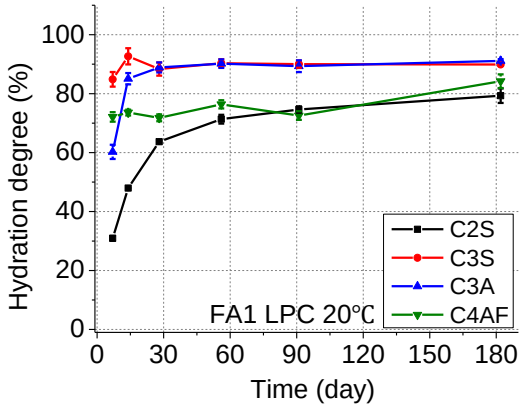

(b) FA1 LPC 20°C

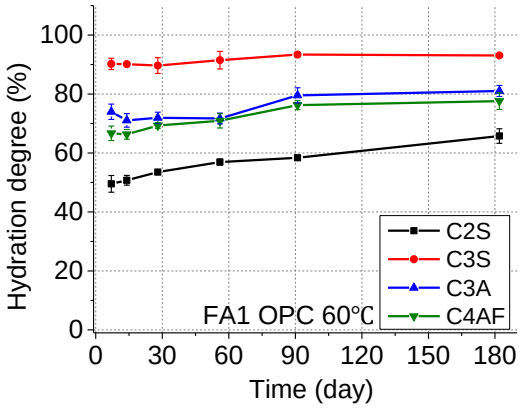

(c) FA1 OPC 60°C

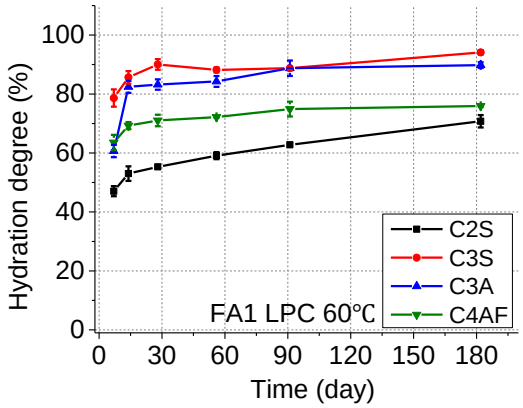

(d) FA1 LPC 60°C

Fig. C.2 Hydration degrees of FA1 blended cement paste

C.3 FA2 blended cement paste

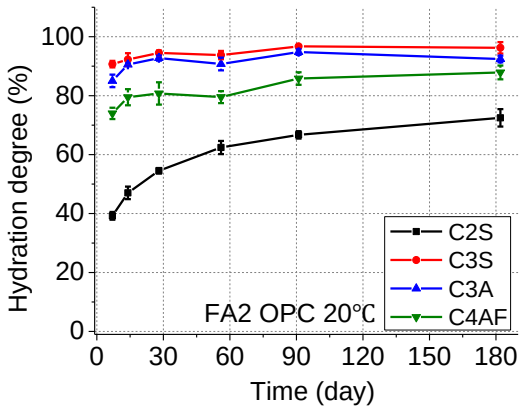

(a) FA2 OPC 20°C

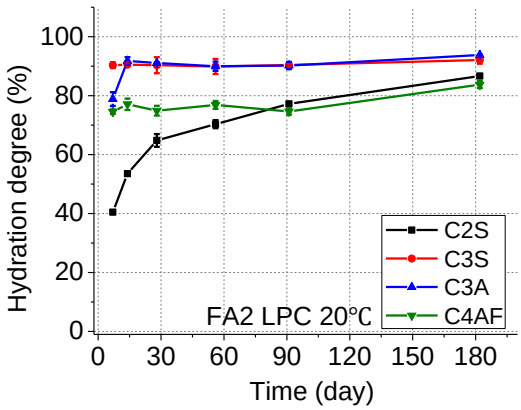

(b) FA2 LPC 20°C

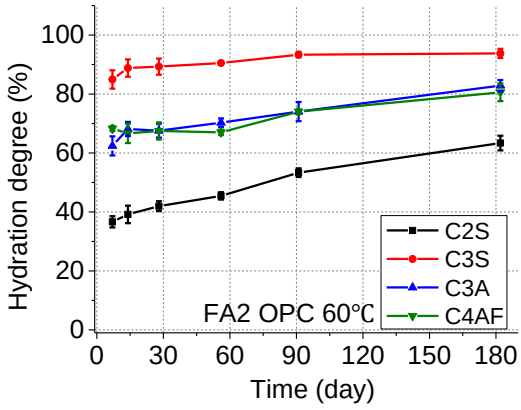

(c) FA2 OPC 60°C

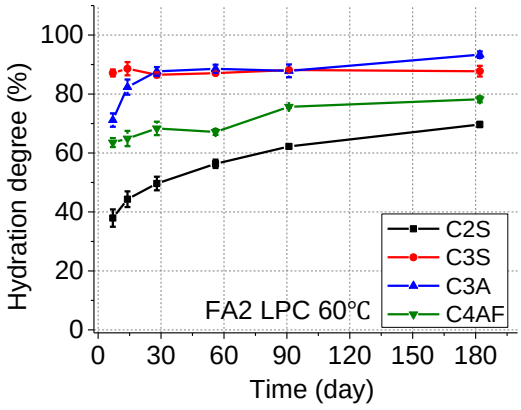

(d) FA2 LPC 60°C

Fig. C.3 Hydration degrees of FA2 blended cement paste

C.4 FA3 blended cement paste

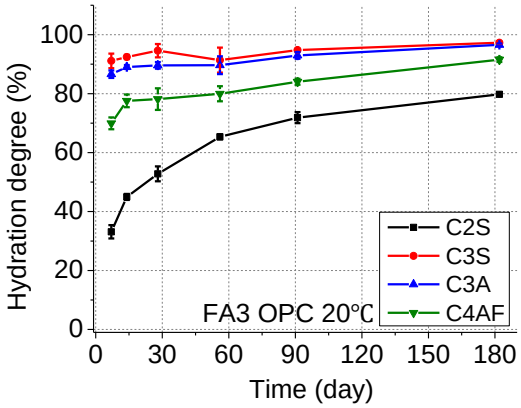

(a) FA3 OPC 20°C

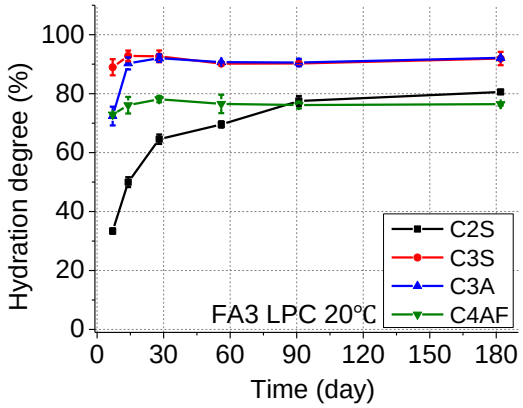

(b) FA3 LPC 20°C

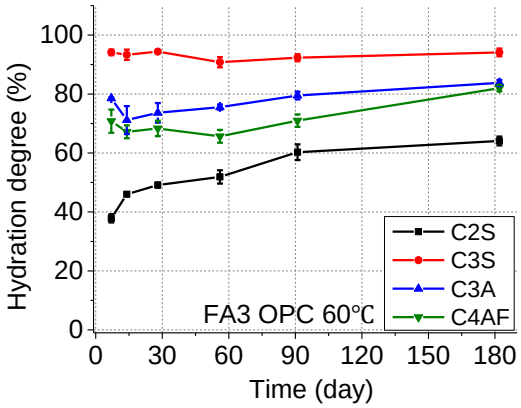

(c) FA3 OPC 60°C

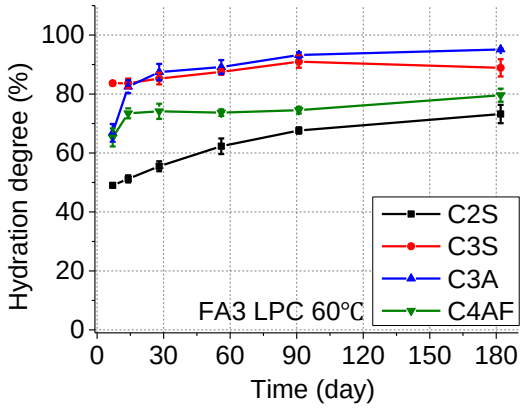

(d) FA3 LPC 60°C

Fig. C.4 Hydration degrees of FA3 blended cement paste

D Regression analyses for alkali dissolution tests

D.1 Introduction

This section is to illustrate the regression analyses result for the alkali dissolution test. Because the current information on the kinetic mechanism of amorphous phases are still insufficient, the range of initial and second stage is experimentally determined by author right now as follows. All linear regression analysis result are summarized in Fig. D.1 and Fig. D.2.

1. 20 °C: Initial stage 2 ~ 28 day; second stage 36 ~ 126 day; and
2. 60 °C: Initial stage 0.75 ~ 3 day; second stage 3 ~ 7 day.

D.2 Linear regression analyses result

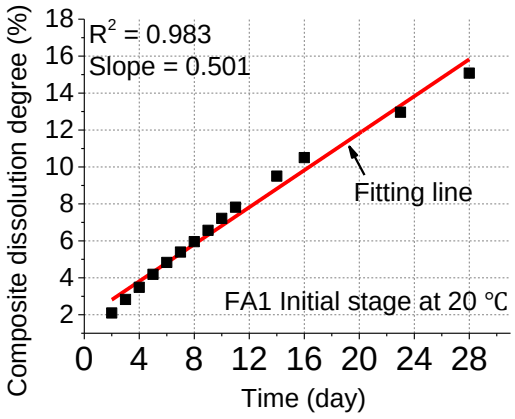

(a) FA1 Initial stage at 20 °C

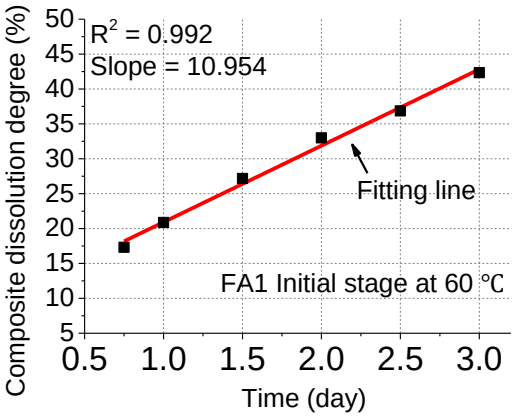

(b) FA1 Initial stage at 60 °C

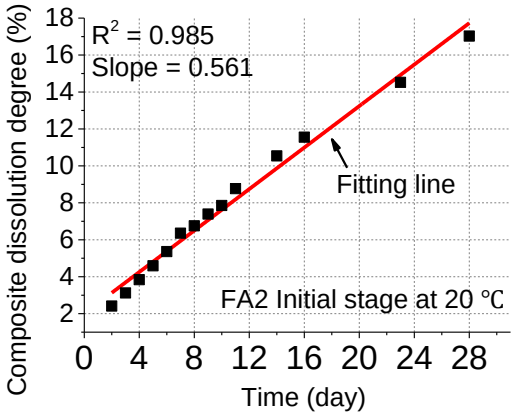

(c) FA2 Initial stage at 20 °C

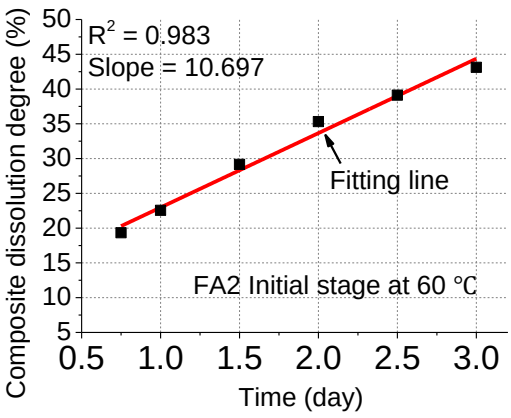

(d) FA2 Initial stage at 60 °C

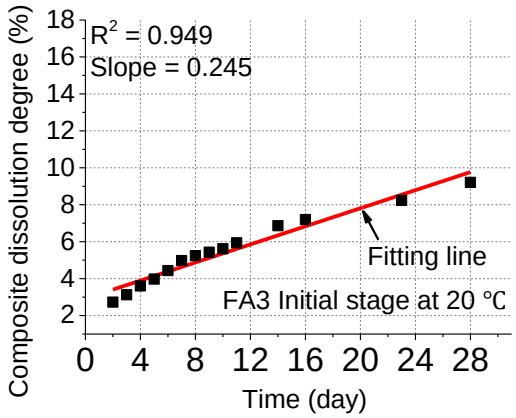

(e) FA3 Initial stage at 20 °C

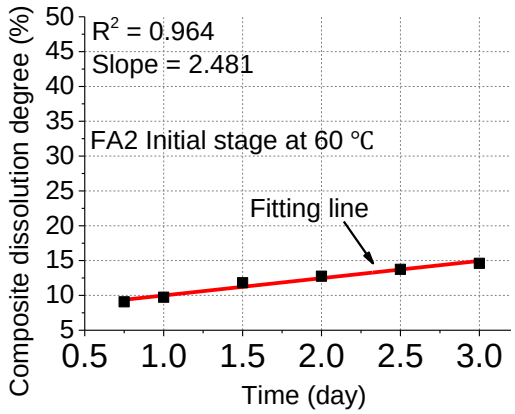

(f) FA3 Initial stage at 60 °C

Fig. D.1 Linear regression analyses result for intimal stage

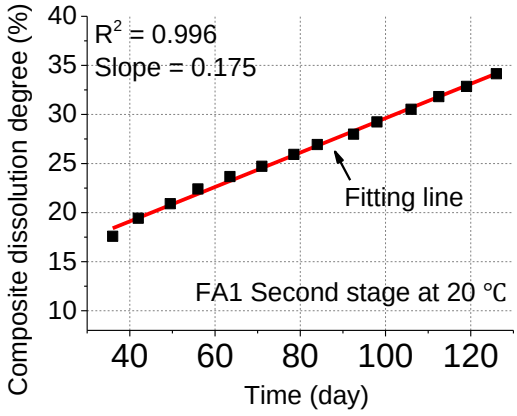

(a) FA1 Second stage at 20 °C

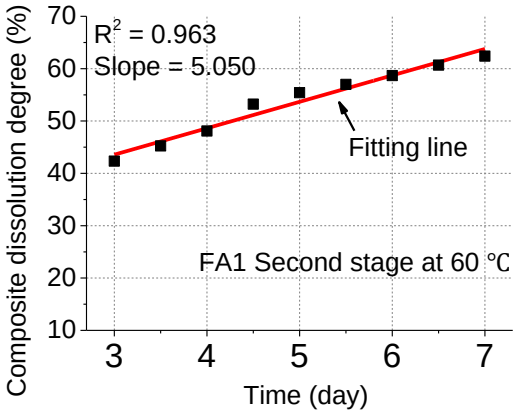

(b) FA1 Second stage at 60 °C

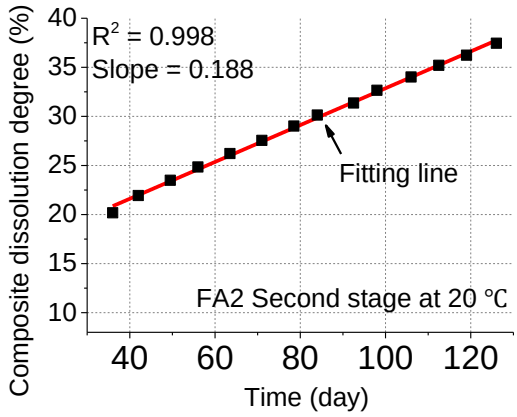

(c) FA2 Second stage at 20 °C

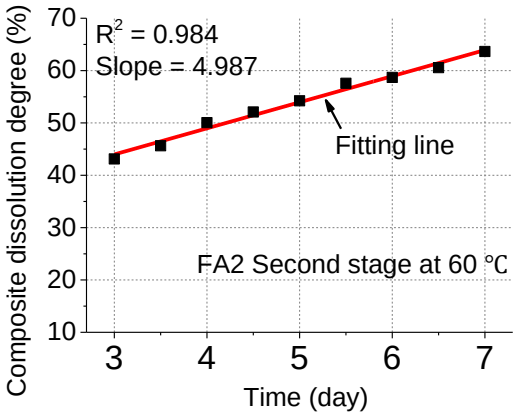

(d) FA2 Second stage at 60 °C

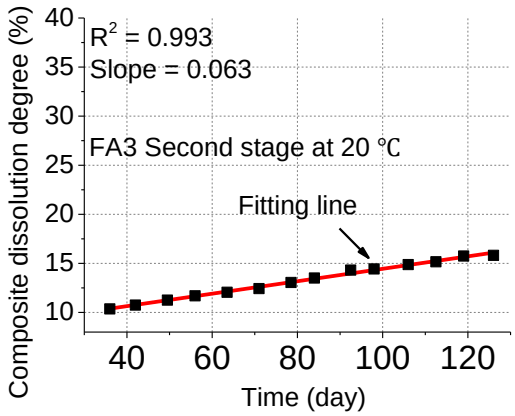

(e) FA3 Second stage at 20 °C

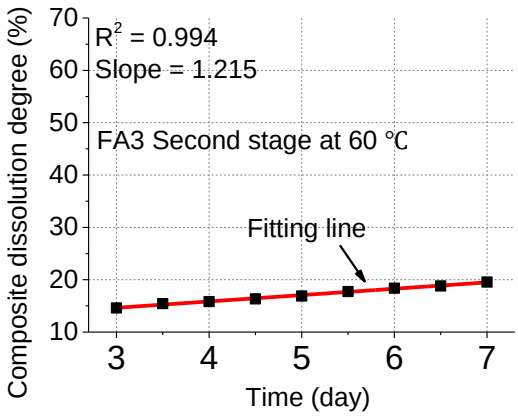

(f) FA3 Second stage at 60 °C

Fig. D.2 Linear regression analyses result for intimal stage

Bibliography

[1] P.K. Mehta, P.J. Monteiro, "Concrete: microstructure, properties, and materials (4th Edition)", McGraw-Hill Education, NewYork, (2006).

[2] Daffodils Minerals, "Fly ash" Url: http://www.daffodilminerals.com/OurProducts/FlyAsh.aspx

[3] S. Schlorholtz, K. Bergeson, T. Demirel, "Monitoring of fluctuations in the physical and chemical properties of a high-calcium fly ash", MRS Proceedings, Cambridge Univ Press, 1987, pp. 107-116.

[4] M. Thomas, "Optimizing the use of fly ash in concrete", Portland Cement Association Skokie, IL, (2007).

[5] J.S. Damtoft, J. Lukasik, D. Herfort, D. Sorrentino, E.M. Gartner, "Sustainable development and climate change initiatives", Cement and Concrete Research, 38 (2008), pp. 115-127.

[6] J.E. Anderson, "Sustainable cement using fly ash: an examination of the net role of high volume fly ash cement on carbon dioxide emissions", Ecocity World Summit 2008 Proceedings, (2008).

[7] H.S. Pietersen, "Reactivity of fly ash and slag in cement", Ph.D. Thesis (1993), Delft University of Technology, Netherlands.

[8] N. Koukouzas, J. Hämäläinen, D. Papanikolaou, A. Tourunen, T. Jäntti, "Mineralogical and elemental composition of fly ash from pilot scale fluidised bed combustion of lignite, bituminous coal, wood chips and their blends", Fuel, 86 (2007), pp. 2186-2193.

[9] P.T. Durdzinski, "Hydration of multi-component cements containing cement clinker, slag, calcareous fly ash and limestone", Ph.D. Thesis (2016), École polytechnique fédérale de Lausanne, Switzerland.

[10] Japan Coal Energy Center, "Survey on coal ash applicaion in japan (2017)", (2017), URL: http://www.jcoal.or.jp/ashdb/ashstatistics/upload/H28_ashstatistics_r2.pdf.

[11] P.K. Mehta, W.S. Langley, "Monolith foundation: built to last a 1000 years", Concrete International, 22 (2000), pp. 27-32.

[12] H. Pietersen, A. Fraay, J. Bijen, "Reactivity of fly ash at high pH", MRS Online Proceedings Library Archive, 178 (1989).

[13] A. Fraay, J. Bijen, Y. De Haan, "The reaction of fly ash in concrete a critical examination", Cement and Concrete Research, 19 (1989), pp. 235-246.

[14] S. Hanehara, F. Tomosawa, M. Kobayakawa, K. Hwang, "Effects of water/powder ratio, mixing ratio of fly ash, and curing temperature on pozzolanic reaction of fly ash in cement paste", Cement and Concrete Research, 31 (2001), pp. 31-39.

[15] M. Narmluk, T. Nawa, "Effect of curing temperature on pozzolanic reaction of fly ash in blended cement paste", International Journal of Chemical Engineering and Applications, 5 (2014), pp. 31-35.

[16] M. NARMLUK, "Hydration Kinetics of Fly Ash-Portland Cement Paste with Low Water to Cementitious Powder Ratio", Ph.D. Thesis (2011), Hokkaido University, Japan.

[17] M. Thomas, J. Matthews, "Performance of PFA concrete in a marine environment—10-year results", Cement and Concrete Composites, 26 (2004), pp. 5-20.

[18] H.S. Pietersen, "Reactivity of fly ash and slag in cement", Ph.D. Thesis (1993), Delft University of Technology, Netherlands.

[19] R.T. Chancey, "Characterization of crystalline and amorphous phases and respective reactivities in a class F fly ash", Ph.D. Thesis (2008), The University of Texas at Austin, United States.

[20] H. Takahashi, K. Yamada, "Critical characters of fly ash suppressing ASR", Proceedings of 14th International Conference on Alkali-Aggregate Reaction in Concrete, 2012.

[21] H. Takahashi, K. YAMADA, "Characterization of fly ash dominating ASR suppressing effects by using SEM-EDS and EBSD (in Japanese)", Concrete Research and Technology, 23 (2012), pp 1-11.

[22] R. Roy, "Metastable liquid immiscibility and subsolidus nucleation", Journal of the American Ceramic Society, 43 (1960), pp. 670-671.

[23] Japanese Industrial standard, "Fly Ash for Use Concrete (in Japanese)", (2008), Japan.

[24] P.T. Durdziński, C.F. Dunant, M.B. Haha, K.L. Scrivener, "A new quantification method based on SEM-EDS to assess fly ash composition and study the reaction of its individual components in hydrating cement paste", Cement and Concrete Research, 73 (2015), pp. 111-122.

[25] R.T. Chancey, P. Stutzman, M.C. Juenger, D.W. Fowler, "Comprehensive phase characterization of crystalline and amorphous phases of a class F fly ash", Cement and Concrete Research, 40 (2010), pp. 146-156.

[26] EN. 197-1, "2011-Cement-Part 1: Compositions, Specifications and Conformity Criteria for Common Cement", (2011).

[27] ASTM Standard, C618-15, "Standard Specification for Coal Fly Ash and Raw or Calcined Natural Pozzolan for Use in Concrete", (2015).

[28] P.T. Durdziński, R. Snellings, C.F. Dunant, M.B. Haha, K.L. Scrivener, "Fly ash as an assemblage of model Ca–Mg–Na-Aluminosilicate glasses", Cement and Concrete Research, 78 (2015), pp. 263-272.

[29] E.C. Arvaniti, M.C. Juenger, S.A. Bernal, J. Duchesne, L. Courard, S. Leroy, J.L. Provis, A. Klemm, N. De Belie, "Determination of particle size, surface area, and shape of supplementary cementitious materials by different techniques", Materials and Structures, 48 (2015), pp. 3687-3701.

[30] S. Mantellato, M. Palacios, R.J. Flatt, "Reliable Specific surface area measurements on anhydrous cements", Cement and Concrete Research, 67 (2015), pp. 286-291.

[31] M. Narmluk, T. Nawa, "Effect of fly ash on the kinetics of portland cement hydration at different curing temperatures", Cement and Concrete Research, 41 (2011), pp. 579-589.

[32] E. Sakai, S. Miyahara, S. Ohsawa, S.-H. Lee, M. Daimon, "Hydration of fly ash cement", Cement and Concrete Research, 35 (2005), pp. 1135-1140.

[33] C. Plassard, E. Lesniewska, I. Pochard, A. Nonat, "Nanoscale experimental investigation of particle interactions at the origin of the cohesion of cement", Langmuir, 21 (2005), pp. 7263-7270.

[34] S. Garrault, E. Finot, E. Lesniewska, A. Nonat, "Study of C-S-H growth on C_3S surface during its early hydration", Materials and Structures, 38 (2005), pp. 435-442.

[35] A. Nonat, "The structure and stoichiometry of C-S-H ", Cement and Concrete Research, 34 (2004), pp. 1521-1528.

[36] S. Garrault, A. Nonat, "Hydrated layer formation on tricalcium and dicalcium silicate surfaces: experimental study and numerical simulations", Langmuir, 17 (2001), pp. 8131-8138.

[37] Y. Kawabata, K. Yamada, "Evaluation of alkalinity of pore solution based on the phase composition of cement hydrates with supplementary cementitious materials and its relation to suppressing asr expansion", Journal of Advanced Concrete Technology, 13 (2015), pp. 538-553.

[38] Chemiasoft, Inductively Coupled Plasma Optical Emission Spectrometry (ICP-OES), Url: Http://Www.Chemiasoft.Com/Chemd/Node/52.

[39] M. Huang, G.M. Hieftje, "Simultaneous measurement of spatially resolved electron temperatures, electron number densities and gas temperatures by laser light scattering from the ICP", Spectrochimica Acta Part B: Atomic Spectroscopy, 44 (1989), pp. 739-749.

[40] Equipco, X-Ray Fluorescence (XRF) Spectrometry Url: Http://Www.Equipcoservices. Com/Support/Tutorials/Introduction-to-Xrf-Spectrometry/, 2017.

[41] R. Blaine, "A simplified air permeability fineness apparatus", ASTM Bull, 123 (1943), pp. 51-55.

[42] ASTM Standard. C204-11, "Standard test methods for fineness of hydraulic cement by air permeability apparatus", (2011).

[43] Y.C. Agrawal, I.N. McCave, J.B. Riley, "Laser diffraction size analysis, in: principles, methods and application of particle size analysis", Cambridge University Press, (1991).

[44] Wikipedia, Scanning Electron Microscope, Url: Https://En.Wikipedia.Org/Wiki/ Scanning_Electron_Microscope, (2017).

[45] K. Scrivener, R. Snellings, B. Lothenbach, "A practical guide to microstructural analysis of cementitious materials", CCR Press, (2016).

[46] N.B. Winter, "Scanning electron microscopy of cement and concrete", WHD Microanalysis, (2012).

[47] EDAX, "Edax Team Manual", (2014).

[48] H. Schneider, J. Schreuer, B. Hildmann, "Structure and properties of mullite—a review", Journal of the European Ceramic Society, 28 (2008), pp. 329-344.

[49] H.F. Taylor, "Cement Chemistry (2nd Edition)", Thomas Telford, (1997).

[50] I. Abe, S. Iwasaki, Y. Iwata, H. Kominami, Y. Kera, "Relationship between production method and adsorption property of charcoals", Tanso, (1998), pp. 277-284.

[51] E.R. Weibel, "Stereological principles for morphometry in electron microscopic cytology", International review of cytology, 26 (1969), pp. 235-302.

[52] C.S. Smith, L. Guttman, "Measurement of internal boundaries in three-dimensional structures by random sectioning", Trans. Aime, 197 (1953), pp. 81-87.

[53] R. Snellings, "Solution‐controlled dissolution of supplementary cementitious material glasses at pH 13: the effect of solution composition on glass dissolution rates", Journal of the American Ceramic Society, 96 (2013), pp. 2467-2475.

[54] M.B. Haha, K. De Weerdt, B. Lothenbach, "Quantification of the degree of reaction of fly ash", Cement and Concrete Research, 40 (2010), pp. 1620-1629.

[55] B. DENG, "Atomic absorption spectrometry: principle, technology and application (in Chinese)", Tsinghua University Press, (2004).

[56] H.S. Pietersen, "Reactivity of fly ash and slag in cement", Ph.D. Thesis (1993), Delft University of Technology, Netherlands.

[57] T. Sagawa, T. Nawa, "Quantitative hydration analysis of blast furnace slag cement by rietveld method", Concrete Research and Technology, 17 (2006), pp. 1-11.

[58] ASTM Standard, C305-14, "Standard Practice for Mechanical Mixing of Hydraulic Cement Pastes and Mortars of Plastic Consistency", (2014).

[59] J. Pourchez, F. Valdivieso, P. Grosseau, R. Guyonnet, B. Guilhot, "Kinetic modelling of the thermal decomposition of ettringite into metaettringite", Cement and Concrete Research, 36 (2006), pp. 2054-2060.

[60] B. Lothenbach, F. Winnefeld, C. Alder, E. Wieland, P. Lunk, "Effect of temperature on the pore solution, microstructure and hydration products of portland cement pastes", Cement and Concrete Research, 37 (2007), pp. 483-491.

[61] G. Le Saoût, V. Kocaba, K. Scrivener, "Application of the rietveld method to the analysis of anhydrous cement", Cement and Concrete Research, 41 (2011), pp. 133-148.

[62] K. Luke, F.P. Glasser, "Internal chemical evolution of the constitution of blended cements", Cement and Concrete Research, 18 (1988), pp. 495-502.

[63] K. Luke, F.P. Glasser, "Selective dissolution of hydrated blast furnace slag cements", Cement and Concrete Research, 17 (1987), pp. 273-282.

[64] T. Kim, J. Olek, "Effects of sample preparation and interpretation of thermogravimetric curves on calcium hydroxide in hydrated pastes and mortars", Transportation Research Record: Journal of the Transportation Research Board, (2012), pp. 10-18.

[65] K. De Weerdt, M.B. Haha, G. Le Saout, K.O. Kjellsen, H. Justnes, B. Lothenbach, "Hydration mechanisms of ternary portland cements containing limestone powder and fly ash", Cement and Concrete Research, 41 (2011), pp. 279-291.

[66] I. Elkhadiri, M. Palacios, F. Puertas, "Effect of curing temperature on cement hydration", Ceram Silik, 53 (2009), pp. 65-75.

[67] A. Ioannidou, "Precipitation, gelation and mechanical properties of calcium-silicate-hydrate gels", Ph.D. Thesis (2014), Eidgenössische Technische Hochschule Zürich, Switzerland.

[68] R.J.M. Pellenq, N. Lequeux, H. van Damme, "Engineering the bonding scheme in C–S–H: the iono-covalent framework", Cement and Concrete Research, 38 (2008), pp. 159-174.

[69] A. Ioannidou, "Precipitation, gelation and mechanical properties of calcium-silicate-hydrate gels", Ph.D. Thesis (2014), Eidgenössische Technische Hochschule Zürich, Switzerland.

[70] K. Ioannidou, R.J.-M. Pellenq, E. Del Gado, "Controlling local packing and growth in calcium–silicate–hydrate gels", Soft matter, 10 (2014), pp. 1121-1133.

[71] V.M. Malhotra, M.-H. Zhang, P.H. Read, J. Ryell, "Long-term mechanical properties and durability characteristics of high-strength/high-performance concrete incorporating supplementary cementing materials under outdoor exposure conditions", ACI Materials Journal, 97 (2000), pp. 518-525.

[72] T.R. Naik, B.W. Ramme, R.N. Kraus, R. Siddique, "Long-Term performance of high-volume fy ash concrete pavements", ACI Materials Journal, (2003), pp.

[73] X. Wang, "Properties prediction of fly ash blended concrete using hydration model", Science China Technological Sciences, 56 (2013), pp. 2317-2325.

[74] X.-Y. Wang, H.-S. Lee, "Modeling the hydration of concrete incorporating fly ash or slag", Cement and Concrete Research, 40 (2010), pp. 984-996.

[75] K. Maekawa, T. Ishida, T. Kishi, "Multi-Scale Modeling of Structural Concrete", CRC Press, (2008).

[76] K. Kinomura, T. Ishida, "Enhanced modeling of multi-component hydration model for fly ash blended cement at normal temperature", Proceedings of the Japan Concrete Institute, 38 (2016), pp. 99-104.

[77] Y. Luan, T. Ishida, T. Nawa, T. Sagawa, "Enhanced model and simulation of hydration process of blast furnace slag in blended cement", Journal of Advanced Concrete Technology, 10 (2012), pp. 1-13.

[78] H.M. Jennings, "Refinements to colloid model of C-S-H in cement: CM-II", Cement and Concrete Research, 38 (2008), pp. 275-289.

[79] H.M. Jennings, "A model for the microstructure of calcium silicate hydrate in cement paste", Cement and Concrete Research, 30 (2000), pp. 101-116.

[80] I. Maruyama, G. Igarashi, "Cement reaction and resultant physical properties of cement paste", Journal of Advanced Concrete Technology, 12 (2014), pp. 200-213.

[81] I. Maruyama, G. Igarashi, "Numerical approach towards aging management of concrete structures: material strength evaluation in a massive concrete structure under one-sided heating", Journal of Advanced Concrete Technology, 13 (2015), pp. 500-527.

[82] F. Xiancai, "Physical chemistry (5th Edition) (in Chinese)", Higher Education Press, (2006).